



**DGK Deutsche Geodätische Kommission**  
der Bayerischen Akademie der Wissenschaften

---

Reihe C

Dissertationen

Heft Nr. 756

**Balaji Devaraju**

**Understanding filtering on the sphere**

**– Experiences from filtering GRACE data –**

**München 2015**

---

**Verlag der Bayerischen Akademie der Wissenschaften  
in Kommission beim Verlag C. H. Beck**

ISSN 0065-5325

ISBN 978-3-7696-5168-3





Understanding filtering on the sphere  
– Experiences from filtering GRACE data –

Von der Fakultät Luft- und Raumfahrttechnik und Geodäsie  
der Universität Stuttgart  
zur Erlangung der Würde eines  
Doktors der Ingenieurwissenschaften (Dr.-Ing.)  
genehmigte Abhandlung

Vorgelegt von  
**Balaji Devaraju**  
aus Tirupathi, Indien

München 2015

---

Verlag der Bayerischen Akademie der Wissenschaften  
in Kommission beim Verlag C. H. Beck

Adresse der Deutschen Geodätischen Kommission:



Deutsche Geodätische Kommission

Alfons-Goppel-Straße 11 • D – 80 539 München

Telefon +49 – 89 – 23 031 1113 • Telefax +49 – 89 – 23 031 - 1283 / - 1100

e-mail hornik@dgfi.badw.de • <http://www.dgk.badw.de>

Hauptberichter: Prof. Dr.-Ing. Nico Sneeuw

Mitberichter: Prof. Dr. Volker Michel, Universität Siegen

Tag der mündlichen Prüfung: 14.08.2015

Diese Dissertation ist auf dem Server der Deutschen Geodätischen Kommission unter <<http://dgk.badw.de/>>  
sowie auf dem Server der Universität Stuttgart unter <<http://elib.uni-stuttgart.de/opus/doku/e-diss.php>>  
elektronisch publiziert

---

© 2015 Deutsche Geodätische Kommission, München

Alle Rechte vorbehalten. Ohne Genehmigung der Herausgeber ist es auch nicht gestattet,  
die Veröffentlichung oder Teile daraus auf photomechanischem Wege (Photokopie, Mikrokopie) zu vervielfältigen.



*Dedicated to my teachers*

*Mr. Durai, Ms. Jayalakshmi, Prof. Sanjeevi & Prof. Sneeuw*



## ABSTRACT

---

GEODESISTS employ signal processing techniques on the sphere to analyse gravity field data, and the primary mathematical tool of choice has been the *spherical harmonics*. Harmonic analysis and synthesis were the predominant signal processing techniques that were employed. However, with the launch of the Gravity Recovery And Climate Experiment (GRACE) satellite mission, there was a strong need for low-pass filtering techniques as the GRACE data is heavily contaminated with noise. Now, after a decade since the launch there is a garden of filters that have been proposed, which has brought with it the problem of *filter choice*. It is in this context that this study would like to understand the anatomy of low-pass linear filters, their mechanics of filtering, and measure their performance that will enable consistency in the choice of a filter for the problem in hand.

The central idea behind these filters is the moving weighted averaging using weighting windows defined on the sphere. The filter functions belong to a broad class of functions called the *two-point functions*, similar to the covariance functions. The weighting functions provide weights to the data points on the sphere depending on the direction and distance of the data points with respect to the point where the filter is located, called the calculation point. Since the provision of a weight requires the knowledge of the calculation point and the data points, the weight functions, and eventually the filter functions, are two-point functions.

Special forms of the filter functions can be generated by applying certain restrictions on the structure of the weights with respect to the location of filter and direction and distance of the data points to the calculation point. These special forms are characterized by the properties of *isotropy* and *homogeneity*. The windows are *isotropic* if the weights vary only with the angular distance, and are *homogeneous* if and only if the weight structure is one and the same at all the calculation points. The former is also referred to as *direction invariant* and the latter as *translation invariant*. Convolution, in the classical sense, on the sphere is guaranteed if and only if homogeneity is ensured.

The weighting windows are designed either in a deterministic manner or using stochastic information, and sometimes data-driven techniques are also employed. The simplest class of windows that can be defined on the sphere are the homogeneous isotropic windows as they only depend on the spherical distance in the spatial domain and the spherical harmonic degree in the spectral domain. However, the complexity of the design multiplies manifold and deterministic design of inhomogeneous and/or anisotropic filters becomes difficult if not impossible. This difficult realm is filled-in by the stochastic and data-driven designing methods. While stochastic methods are borne out of the optimization principles, the data-driven techniques do not follow a specific principle, for example, polynomial fitting methods and empirical orthogonal functions.

When applying filters there is always a question of choice, and from the experiences in filtering GRACE, it can be said that the output is heavily influenced by the chosen filter. Irrespective of the filter chosen, filtering smudges part of the signal in addition to smoothing out noise, and the amount of signal lost depends on the filter. In order to assess the suitability of a filter and to understand its behaviour, a framework has been developed. The framework consists of a set of metrics designed

on the basis of the energy of the filters and log-normal of the filter weights.

Filtering smothers the data, eventually changing its resolution. Resolution turns out to be important information when combining/comparing two different datasets, and it directly affects the filter choice. To this end an empirical method has been developed to ascertain the *ideal resolution* of any given filter, and further, a metric for quantifying the contrast, called the *modulation transfer function*, has also been devised. The latter concept is an adaptation of the modulation transfer functions used in optics. Applying these methods to both the isotropic and anisotropic filters, it is clear that the resolving power of anisotropic filters depends heavily on the direction, and for inhomogeneous filters it is based on the calculation point as well.

Since the filtering method follows a weighted average approach, strong signals that are far away from the calculation point, sometimes, contribute significantly to the filtered value. This is termed as *signal leakage*, and it is an undesirable effect of filtering. Although leakage is inevitable with low-pass filtering, it can be quantified when the true signal is known or with a model that is nearly as good as the true signal. A generic estimate of leakage can be computed by considering energy contribution beyond the ideal resolution as leakage.

This thesis elucidates a number of attributes of the filters and filtering on the sphere, but is far short of a comprehensive treatment. Only the low-pass linear filters have been studied, which leaves out high-pass and band-pass filters. Having said that this work makes positive strides in the direction of understanding the mechanics of linear low-pass filtering on the sphere, especially with respect to resolution and leakage. Further, it also puts forth a set of metrics that provide a generic understanding of the filter in hand, enabling appropriate filter choice.

UM SCHWEREFELDDATEN zu analysieren, wenden Geodäten üblicherweise Methoden der Signalverarbeitung auf einer Kugel an, was mit Hilfe von Kugelflächenfunktionen ermöglicht wird. Hierbei sind die harmonische Analyse und Synthese die gängigsten Signalverarbeitungsmethoden. Zusätzlich werden jedoch seit dem Start des *Gravity Recovery and Climate Experiment* (GRACE) spezielle Tiefpaß-Filter-Methoden benötigt, da GRACE-Daten üblicherweise stark fehlerbehaftet sind. In den vergangenen 10 Jahren seit dem Start von GRACE wurde daher eine Vielzahl von Filtern entwickelt, was die Nutzer vor die Wahl einer geeigneten Filtermethode stellt. In dieser Studie soll daher die Anatomie von linearen Tiefpaß-Filtern und ihre speziellen Filtermechaniken untersucht sowie ihre Effizienz bestimmt werden. Dies soll einen konsistenten Vergleich und letztendlich die Wahl eines problemspezifisch geeigneten Filters zulaßen.

Das zugrunde liegende Prinzip aller Filter ist eine gewichtete gleitende Mittelung, welche auf der Kugel definiert ist, mit Hilfe einer Gewichtsfunktion. Die Filterfunktionen gehören, ähnlich wie die Kovarianzfunktionen, zur Klasse der *Zwei-Punkt-Funktionen*. Die Gewichtsfunktionen liefern hierbei die Gewichte zu den einzelnen Datenpunkten auf der Kugel, abhängig von Richtung und Entfernung zu dem Ort, wo der Filter angewendet wurde (dem sog. *Berechnungspunkt*). Für die Berechnung dieser Gewichte müssen somit sowohl der Berechnungspunkt, als auch die Datenpunkte bekannt sein, was die Zugehörigkeit von Gewichts- und Filterfunktionen zu den Zwei-Punkt-Funktionen verdeutlicht.

Spezielle Formen der Filterfunktionen können durch Einschränkungen der räumlichen Struktur der Gewichte im Bezug auf die Position des Filters sowie Richtung und Entfernung der Datenpunkte zum jeweiligen Berechnungspunkt erzeugt werden. Diese speziellen Formen werden durch die Eigenschaften *Isotropie* und *Homogenität* beschrieben. Dabei hängen die (räumlichen) Gewichte bei einem isotropen Fenster lediglich vom Winkelabstand zwischen Daten- und Berechnungspunkt ab. Falls die Struktur der Gewichte in allen Berechnungspunkten identisch ist, spricht man von einem homogenen Fenster. Daher bezeichnet man isotrope Fenster auch als richtungsinvariant und homogene als translationsinvariant. Eine Faltung auf der Kugel ist somit ausschließlich bei Homogenität durchführbar.

Die Gewichtsfenster werden entweder deterministisch oder stochastisch bestimmt, in manchen Fällen kommen auch datenbasierte Methoden zum Einsatz. Die einfachste Klasse von Filtern, welche auf einer Kugel angewendet werden können, sind die homogenen isotropen Filter, da diese lediglich vom Winkelabstand im Ortsraum bzw. sphärisch harmonischen Grad im Spektralbereich abhängen. Der Aufbau von Filtern kann aber beliebig komplex gestaltet werden und die deterministische Bestimmung von inhomogenen und/oder anisotropen Filtern ist äußerst schwierig, wenn nicht sogar unmöglich. Hier gewinnen daher die stochastischen und datenbasierten Ansätze an Bedeutung. Während stochastische Filter auf Optimierungsprinzipien basieren, leiten sich die datenbasierten Ansätze aus einer Vielzahl von Methoden, wie z.B. der Schätzung von Polynomen oder den Empirischen Orthogonalen Funktionen, ab.

Die Filterung von GRACE-Daten hat deutlich gezeigt, daß die gefilterten Daten maßgeblich vom gewählten Filter beeinflusst werden. Somit steht man immer vor der schwierigen Wahl eines problemspezifisch geeigneten Filters. Unabhängig von dem eingesetzten Filter wird neben der Verringerung des Rauschens immer auch ein Teil des Signals verwischt. Der Anteil des Signals, welcher durch die Filterung verloren geht, hängt dabei stark von dem eingesetzten Filter ab. Um daher die problemspezifische Eignung eines Filters zu beurteilen und dessen Eigenschaften besser zu verstehen, wurde in dieser Studie ein entsprechendes Rahmenkonzept aus Filtermetriken entwickelt. Diese Metriken basieren auf der Energie der Filter und den log-normalen Filter-Gewichten.

Durch Anwendung eines Filters werden Daten geglättet, wobei sich aber auch deren Auflösung ändern kann. Da bei einem Vergleich oder der Kombination zweier Datensätze die Auflösung eine entscheidende Rolle spielt, muß diese natürlich auch bei der Wahl eines entsprechenden Filters berücksichtigt werden. Hierfür wurde ein empirischer Ansatz entwickelt, mit welchem sich die *ideale Auflösung* eines beliebigen Filters bestimmen lässt. Darüber hinaus wurde auch eine Metrik zur Beschreibung des Kontrasts entwickelt, die sogenannte *Modulationsübertragungsfunktion*. Das zugrunde liegende Konzept basiert auf den Modulationsübertragungsfunktionen, welche in Bereichen der Optik eingesetzt werden. Eine Analyse von isotropen und anisotropen Filter mit Hilfe der entwickelten Metriken zeigt, dass das Auflösungsvermögen der anisotropen Filter stark richtungsabhängig ist und bei den inhomogenen Filtern von der Lage des Berechnungspunktes abhängt.

Da die Filterung einer gewichteten Mittelung entspricht, können starke Signale, welche weit vom Berechnungspunkt entfernt sind, unter gewissen Umständen den gefilterten Wert maßgeblich beeinflussen. Dieser unerwünschte, bei einer Tiefpaß-Filterung aber unvermeidbare, Nebeneffekt wird als *Signal Leakage* bezeichnet. Dessen Einfluss kann bestimmt werden, wenn das wahre Signal bekannt ist oder ein Modell vorliegt, welches das wahre Signal ausreichend gut approximiert. Eine allgemeingültige Schätzung hingegen erhält man, wenn der Energiebeitrag jenseits der idealen Auflösung als *Leakage* betrachtet wird.

In dieser Arbeit wurden etliche Eigenschaften von Filtern beschrieben und erläutert. Die dargestellten Ergebnisse sind somit ein wichtiger Schritt zum Verständnis von linearen Tiefpaß-Filtern auf der Kugel, vor Allem in Hinblick auf Auflösung und Leakage. Des Weiteren wurde eine Reihe von Metriken entwickelt, mit deren Hilfe Filter konsistent analysiert und verglichen werden können, was die Wahl problemspezifisch geeigneter Filter erheblich erleichtert.

# CONTENTS

---

ABSTRACT	VII
ZUSAMMENFASSUNG	IX
EPIGRAPH	XIII
1 INTRODUCTION	1
2 SMOOTHING KERNELS ON THE SPHERE	6
2.1 Spatial smoothing	6
2.2 Alternative representation of weighting functions	11
2.3 Classification of smoothing kernels	13
2.4 Amplitude and phase spectrum of the filtered field	25
3 DESIGN OF SMOOTHING KERNELS	31
3.1 Some trivial designs of smoothing kernels	31
3.2 Classification of filter design	34
3.3 Gaussian smoothing operator	36
3.4 Destriping filter	39
3.5 Regularization filter	43
4 PERFORMANCE METRICS FOR ANALYSING SMOOTHING KERNELS	47
4.1 Damping factor	48
4.2 Main-lobe half-width	50
4.3 Main-lobe energy concentration	54
4.4 Spatial resolution	55
4.5 Spatial leakage	58
4.6 Highest side-lobe level	59
4.7 Side-lobe roll-off ratio	59
5 PERFORMANCE ANALYSIS OF SMOOTHING KERNELS	60
5.1 Homogeneous isotropic filters	60
5.2 Inhomogeneous anisotropic filters	74
5.3 Discussion	86
6 GRACE OBSERVATIONS OF WATER STORAGE CHANGE	92
6.1 Gravity to mass	92

6.2	Signal covariance of mass anomalies	93
6.3	Amplitude and phase of the filtered GRACE data	102
7	CONCLUDING REMARKS	105
	BIBLIOGRAPHY	109
A	SPHERICAL HARMONICS	114
A.1	Surface spherical harmonics	114
A.2	Associated Legendre functions	115
A.3	Rotation of spherical harmonics	116
A.4	Spherical harmonic spectrum	118
B	INTEGRAL OF THE PRODUCT OF WIGNER- $d$ SYMBOLS	120
C	POLAR FORM OF THE SPHERICAL HARMONIC SPECTRUM	122
	LIST OF SYMBOLS	124
	LIST OF ABBREVIATIONS	126
	ACKNOWLEDGEMENTS	127
	EPILOGUE	131



“It was both odd and unjust, said Gauss, a real example of the pitiful existence, that you were born into a particular time and held prisoner there whether you wanted it or not. It gave you an indecent advantage over the past and made you a clown vis-à-vis the future. ... in another two hundred years each and every idiot would be able to make fun of him and invent the most complete nonsense about his character.”

– Daniel Kehlmann  
*(Measuring the world)*



THE GLOBAL GEODETIC OBSERVING SYSTEM (GGOS) proposed by the International Association of Geodesy (IAG) defines geodesy as the science that determines the geometry, gravity field and rotation of the Earth and also their evolution in time [Plag and Pearlman, 2009, pg. xiii]. Evolution of the Earth's geometry, gravity field and rotation around the polar axis is driven by the mass transport and redistribution that is continuously taking place between the lithosphere, hydrosphere, atmosphere, cryosphere, the mantle and the core. By frequently or continuously monitoring the evolution of the Earth's geometry, gravity field and rotation, the geophysical phenomena behind the mass transport and redistribution can be studied. This ability of geodetic measurement tools and techniques casts them as *geodetic sensors*. However, this role of geodetic methods has been possible largely due to the advent of *space-geodetic techniques* like satellite altimetry, satellite interferometry, satellite ranging and positioning and satellite gravimetry. Space-geodetic techniques have brought with them global coverage and uniform accuracy [Rummel, 2010], and have established themselves as an indispensable tool for Earth system science [Jin et al., 2013].

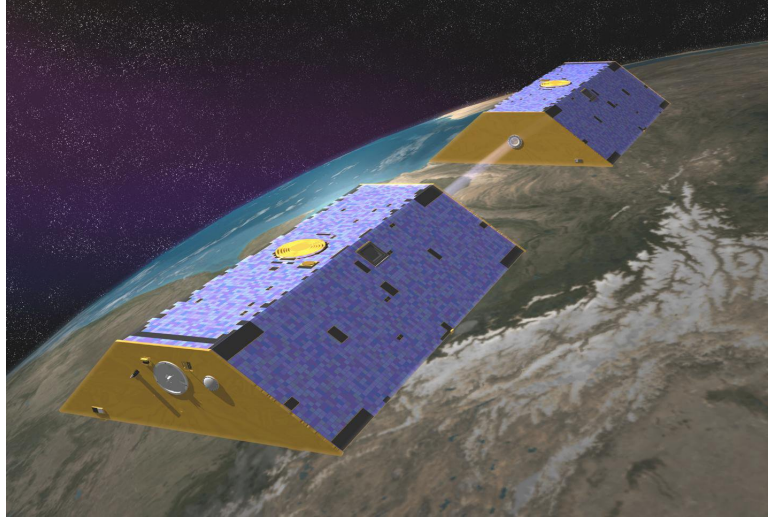
Traditionally, remote sensing of the Earth has been carried out by satellites equipped with active and passive electromagnetic radiation sensors. With the advent of *satellite gravimetry* missions such as the CHAllenging Minisatellite Payload (CHAMP) [Reigber et al., 2002], Gravity Recovery and Climate Experiment (GRACE) [Tapley et al., 2004] and Gravity field and steady-state Ocean Circulation Explorer (GOCE) [Rummel et al., 2011] a novel method of Earth observation has been introduced.

In particular, the GRACE satellite mission, with more than a decade of observations, has been an overwhelming success, particularly for climatology and global hydrology. This is supported by vast literature on those areas of research: Estimation of basin- to continental-scale water storage [Crowley et al., 2006; Schmidt et al., 2008] or evapotranspiration [Rodell et al., 2004]; regional weather analysis [Seitz et al., 2008]; large-scale moisture flux divergences [Swenson and Wahr, 2006a; Fersch et al., 2012]; groundwater depletion in India [Rodell et al., 2009]; runoff from landmasses [Syed et al., 2009; Lorenz et al., 2014; Sneeuw et al., 2014] and polar ice mass loss monitoring [Schrama and Wouters, 2011]. For this reason GRACE mission has been identified as an important mission for climate studies [Gleick et al., 2013].

## THE GRACE SATELLITE MISSION

The GRACE satellite mission is a twin satellite mission that fly in an *in-line* orbit configuration (cf. Figure 1.1), and in a near-polar sun-synchronous orbit. The two satellites are linked by a micrometer precise K-band ranging radar instrument, and are further tracked by global

navigation satellite systems. The satellites were launched into a 500 km near-circular orbit within the Earth's gravity field. Due to orbital decay and ageing of the instruments, the satellites currently fly at an altitude of  $\approx 390$  km. The inter-satellite distance is maintained between 170–270 km. The distance between the satellites is perturbed by the changes in the gravity field caused by the distribution and redistribution of mass in the system Earth. By precisely tracking these low-earth orbiting satellites, their positions can be inverted for gravity field mapping.



**Figure 1.1:** Artists impression of the GRACE satellite mission. *Courtesy: Wikipedia*

One of the primary intentions of the GRACE mission is to study the changes in continental water storage [Tapley et al., 2004]. Water storage changes over landmasses is part of the hydrologic cycle and it is what remains after the precipitated water ( $P$ ) is transported back to the oceans via runoff ( $R$ ) and to the atmosphere as evapotranspiration ( $E$ ).

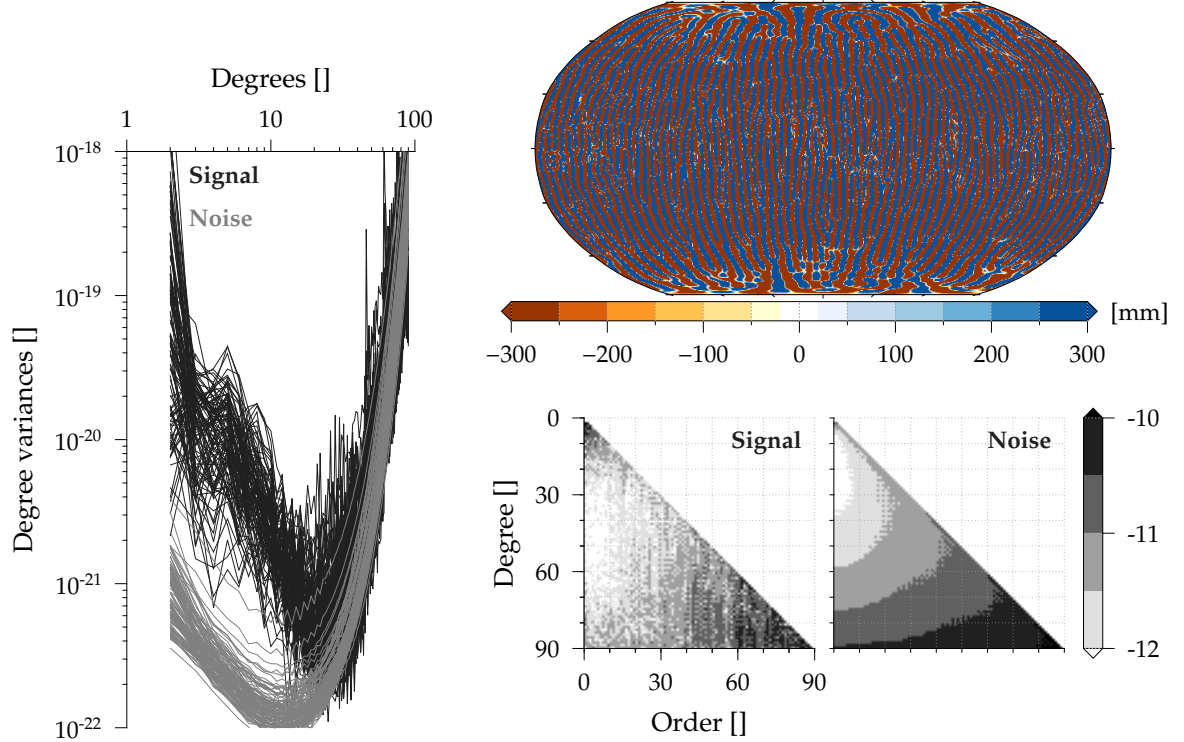
$$P - R - E = \frac{dS}{dt}, \quad (1.1)$$

where  $S$  is the water storage over landmasses. The water storage constitutes only 3.5 % of the hydrologic cycle, but has a greater influence on climate and weather. Up until the launch of GRACE, the measurements of water storage were sparse both in space and time [Rodell and Famiglietti, 1999]. For the first time, after the launch of the GRACE satellites, hydrologers were able to close the global water balance equation (1.1) using observations [Trenberth et al., 2007].

## MAJOR SOURCES OF ERROR IN GRACE DATA

Nevertheless, the GRACE data, being novel, comes with its own problems. The most persistent of them being the noise that manifests itself as *stripes* (cf. top right panel of Figure 1.2), which is mainly caused by the in-line orbit configuration of the GRACE mission [Kusche et al., 2009]. The effect of the noise is particularly severe on the higher spherical harmonic degrees of the monthly gravity field estimated from GRACE: The higher degree spherical harmonics contain more energy than their lower degree counterparts, which is not realistic (cf. left panel of Figure 1.2). The in-line configuration of the GRACE satellites causes the sectorial and

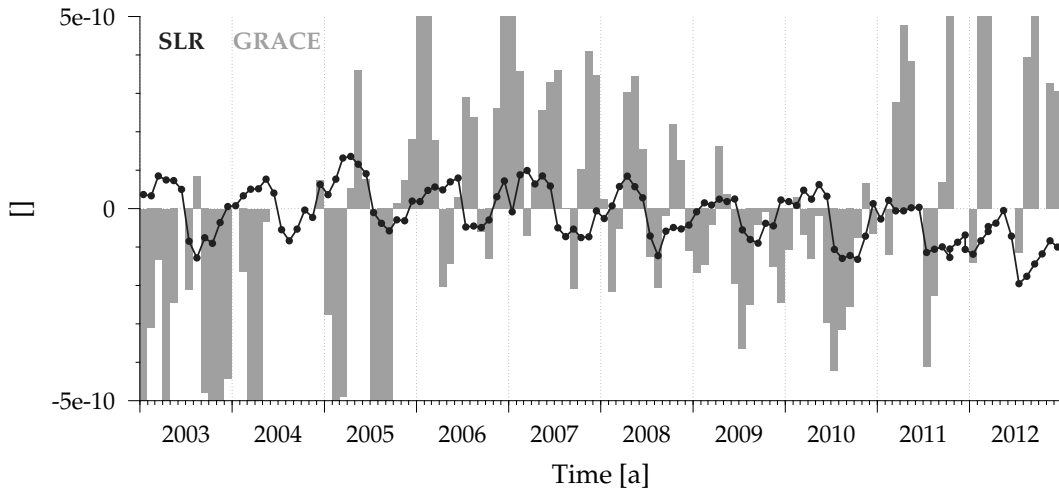
the near-sectorial elements of the spherical harmonic coefficients (cf. Figure A.1) to be more sensitive to the noise. This is shown by their higher noise levels compared to the noise levels of the tesseral and zonal harmonics for a given spherical harmonic degree (cf. bottom right panel of Figure 1.2). The signal amplitudes also show the impact of the GRACE orbit, where the sectorial coefficients have higher amplitudes compared to the tesseral and zonal coefficients for a given harmonic degree (cf. bottom right panel of Figure 1.2).



**Figure 1.2:** Unfiltered temporal gravity field variations retrieved from GRACE observations. The degree variances of the spectrum (left panel) shows the typical high frequency (higher harmonic degrees) noise, and its spatial manifestation, the characteristic “stripe” like noise (map in the top right panel).

The orbit configuration of GRACE also does not allow it to retrieve the spherical harmonic degree 2 and order 0 coefficient,  $C_{20}$ , (Figure 1.3), which is the single largest coefficient in the spherical harmonic series of the gravity field. This problem is currently remedied by replacing the GRACE  $C_{20}$  with the ones estimated from SLR observations [Cheng and Ries, 2013].

The above problems are exacerbated by another source of major errors: mismodelling of dealiasing models. Changes in gravity are brought in by the sum total of all the sources of mass changes. In order to retrieve the mass changes from a particular source, the other well known sources are modelled and removed from the observations. Further, there are also mass changes that are shorter than the temporal sampling of GRACE and these also have to be modelled and removed. This procedure is called *dealiasing* and is reliant upon *a priori* knowledge of the sources. The known sources of mass changes include tides (atmospheric, ocean and solid earth) and non-tidal mass variations of the atmosphere and ocean. Improving these models is an ongoing process, as they are one of the stumbling blocks for the accurate estimation of mass changes from satellite gravimetry [Murböck et al., 2014].



**Figure 1.3:** Time-series of the degree 2 order 0 ( $C_{20}$ ) coefficient estimated from GRACE and SLR observations.

### THE NEED FOR FILTERING GRACE DATA

While the improvement of the dealiasing models is a work of the larger scientific community, mitigation of stripes are user manageable. The standard method of removing stripes is by way of spectral filtering or by spatial averaging of the GRACE gravity field. Much of the progress in scientific understanding that has been made relies upon this filtering as GRACE data is nearly unusable without proper filtering. A whole garden of filters has been proposed to mitigate the striping behaviour and retrieve mass changes: [Wahr et al., 1998; Swenson and Wahr, 2002; Han et al., 2005; Swenson and Wahr, 2006a; Sasgen et al., 2006; Chen et al., 2006; Wouters and Schrama, 2007; Klees et al., 2008; Wu et al., 2009; Zhang et al., 2009]. This has brought with it the problem of filter choice and a few studies have attempted at providing (mostly subjective) solutions [e.g., King et al., 2006; Werth et al., 2009]. Filtering brings with it certain side-effects, namely, signal loss, leakage and poor spatial resolution, which limit the utility of GRACE data only to catchments with a sizeable area, for example,  $\approx 200,000 \text{ km}^2$  or more [Longuevergne et al., 2010]. These side-effects have also been studied extensively [e.g., Klees et al., 2007, 2008; Landerer and Swenson, 2012], but again mostly in a subjective perspective.

### OBJECTIVES

Although the majority of the scientific understanding from GRACE data hinges on filtering, there has not been a definitive effort, except for the early effort of Jekeli [1981], to study filtering and approach it from a data agnostic manner. It is this void that this work will fill with the following salient objectives:

- i. to understand the mechanics of filtering on the sphere
- ii. to provide metrics for analysing the performance of filters in order to make an informed choice with the filters

## ORGANISATION OF CHAPTERS

The second chapter will deal with the idea of filtering on the sphere, where we will deal with filters of different spatial and spectral structures. Thereafter, the design elements of some of the widely used filters in the GRACE community will be discussed in the third chapter. In the fourth chapter, ways to evaluate the performance of a given filter prior to its usage in the real world will be dealt with. The focal point of the sixth chapter will be filtering of GRACE data, where we will also discuss couple of not so well-known issues concerning GRACE and filtering. In chapter 7, the work will be summarised and conclusions drawn.

SMOOTHING a dataset given on a sphere can be achieved by taking a weighted mean at each data-point, where the weights are provided by a kernel function defined on the sphere. Any square integrable scalar function defined on the sphere can be transformed into a more compact spherical harmonic spectrum and the smoothing operations can be performed in the spectral domain as well. Smoothing operations on the sphere are quite different to their Fourier counterparts on the planar domain or on the line, where they are convolution operations. It will be shown here that the smoothing operations on the sphere are convolutions only under specific conditions. Nevertheless, smoothing operations are compact and computationally efficient in the spherical harmonic spectral domain as in the Fourier domain. In order to differentiate the spatial and spectral operations, hereafter smoothing operations in the spatial domain will be referred to as smoothing, and the corresponding operation in the spectral domain will be referred to as filtering. Due to this differentiation the spectral representation of the smoothing kernel will be called a filter, and the kernel itself will also be referred to as the smoothing operator.

In this chapter, a general representation of smoothing kernels on the sphere and their spherical harmonic spectrum representations will be provided after which particular cases of the kernels will be discussed. The particular cases are arrived at after imposing some restrictions on the degrees of freedom of the general case. Due to the compactness and easiness of filtering compared to smoothing, filtering is the preferred method of computation in physical geodesy. During the course of the discussion we will also elaborate, where possible, the analytical formulae in terms of matrix algebra.

## §2.1 SPATIAL SMOOTHING

Given a square integrable scalar function (e.g., gravity field)  $f(\theta, \lambda)$  on a sphere ( $\Omega$ ), it can be represented in terms of a spherical harmonic spectrum as

$$f(\theta, \lambda) = \sum_{l=0}^{\infty} \sum_{m=-l}^l F_{lm} Y_{lm}(\theta, \lambda) = \sum_{l,m} F_{lm} Y_{lm}(\theta, \lambda), \quad (2.1a)$$

$$F_{lm} = \frac{1}{4\pi} \int_{\Omega} f(\theta, \lambda) Y_{lm}^*(\theta, \lambda) d\Omega, \quad F_{lm} \in \mathbb{C} \quad (2.1b)$$

$$d\Omega = \sin \theta d\theta d\lambda, \quad (2.1c)$$



$$Y_{lm}(\theta, \lambda) = \begin{cases} N_{lm} P_{lm}(\cos \theta) e^{im\lambda}, & m \geq 0 \\ (-1)^m Y_{l,-m}^*(\theta, \lambda), & m < 0 \end{cases}, \quad Y_{lm}(\cdot) \in \mathbb{C} \quad (2.1d)$$

$$N_{lm} = (-1)^m \sqrt{(2l+1) \frac{(l-m)!}{(l+m)!}}, \quad N_{lm} \in \mathbb{R}. \quad (2.1e)$$

where

$Y_{lm}(\theta, \lambda)$  – Geodetic normalised complex surface spherical harmonics of degree  $l$  and order  $m$  with  $|m| \leq l$ .

$\theta, \lambda$  – Co-latitude and longitude of a point on the sphere.

$F_{lm}$  – Geodetic normalised spherical harmonic coefficients of degree  $l$  and order  $m$ .

$P_{lm}(\cos \theta)$  – Associated Legendre functions of degree  $l$  and order  $m$ .

$N_{lm}$  – Normalisation factor.

The above analytical expressions can be expressed in matrix form as well to facilitate computational understanding.

$$\mathbf{f} = \mathbf{Y} \mathbf{F}, \quad (2.2a)$$

$$\mathbf{F} = (\mathbf{Y}^\dagger \mathbf{Y})^{-1} \mathbf{Y}^\dagger \mathbf{f}, \quad (2.2b)$$

where  $\mathbf{Y}$  is the matrix of geodetic normalised complex surface spherical harmonics,  $\mathbf{Y}^\dagger$  is the *Hermitian* of  $\mathbf{Y}$  and  $\mathbf{K}$  is the vector of spherical harmonic coefficients of the field  $\mathbf{f}$ . The equations (2.2) together represent the computational form of spherical harmonic analysis (2.1a) and synthesis (2.1b), where we have used least-squares approach to spherical harmonic analysis. Henceforth, it will be used as the standard technique for spherical harmonic analysis.

### Smoothing kernels

Our aim is to smooth the field  $f(\theta, \lambda)$ , and one of the methods employed to smooth a field is to take a weighted average of the field at the point whose smoothed value is sought. Weighting functions that are defined on the sphere carry the information of the weights. These weights vary according to the distance and direction from the point whose smoothed value needs to be calculated. Before we move further we need a few definitions for our discussion: The point whose smoothed value is sought will be called the *calculation point*, and the rest of the points that are involved in the smoothing operation will be called the *data points* (cf. Figure 2.2). Since we always need the calculation point and the data points to specify the weighting functions, these weighting functions are called *two-point weighting functions*. It should be noted that the term *point(s)* is merely used as a *figure of speech*. The two-point functions  $b(\cdot, \cdot)$  and the field  $f(\cdot)$  are all continuous functions, and the term *point(s)* is used here to provide an intuitive understanding to the computations. The two-point weighting functions we will use throughout this document are all scalar unless and otherwise specified.

*Remark* The smoothing operation is similar to the ideas of moving average and convolution. Looked at it from the point of view of convolution in the classical Fourier sense, there is a point of departure from those concepts. The point of departure is that the weighting function for each of the calculation points is completely different, but in moving average and convolution the weighting function remains the same for all calculation points.

A general two-point scalar weighting function  $w(\cdot, \cdot)$  defined on the sphere can be represented in terms of a spherical harmonic transform pair, which is given as [e.g., Rummel and Schwarz, 1977]

$$\begin{aligned} w(\theta, \lambda, \theta', \lambda') &= \sum_{l=0}^{\infty} \sum_{m=-l}^l Y_{lm}(\theta, \lambda) \sum_{n=0}^{\infty} \sum_{k=-n}^n W_{lm}^{nk} Y_{nk}^*(\theta', \lambda'), \\ &= \sum_{l,m} Y_{lm}(\theta, \lambda) \sum_{n,k} W_{lm}^{nk} Y_{nk}^*(\theta', \lambda'), \end{aligned} \quad (2.3a)$$

$$W_{lm}^{nk} = \frac{1}{16\pi^2} \iint_{\Omega, \Omega'} w(\theta, \lambda, \theta', \lambda') Y_{lm}^*(\theta, \lambda) Y_{n'k'}(\theta', \lambda') d\Omega d\Omega'. \quad (2.3b)$$

The matrix form of the transform pair is given as follows

$$\mathbf{w} = \mathbf{Y} \mathbf{W} \mathbf{Y}^\dagger, \quad (2.4a)$$

$$\mathbf{W} = (\mathbf{Y}^\dagger \mathbf{Y})^{-1} \mathbf{Y}^\dagger \mathbf{w} \mathbf{Y} (\mathbf{Y}^\dagger \mathbf{Y})^{-1}. \quad (2.4b)$$

Smoothing the field  $f(\theta, \lambda)$  with a general two-point weighting function  $w(\theta, \lambda, \theta', \lambda')$  results in the smoothed field  $\bar{f}(\theta, \lambda)$ :

$$\bar{f}(\theta, \lambda) = \frac{\frac{1}{4\pi} \int_{\Omega'} f(\theta', \lambda') w(\theta, \lambda, \theta', \lambda') d\Omega'}{\frac{1}{4\pi} \int_{\Omega'} w(\theta, \lambda, \theta', \lambda') d\Omega'}, \quad (2.5a)$$

$$\begin{aligned} &= \frac{1}{4\pi} \int_{\Omega'} f(\theta', \lambda') \frac{w(\theta, \lambda, \theta', \lambda')}{\bar{w}(\theta, \lambda)} d\Omega', \\ &= \frac{1}{4\pi} \int_{\Omega'} f(\theta', \lambda') b(\theta, \lambda, \theta', \lambda') d\Omega', \end{aligned} \quad (2.5b)$$

where

$$\begin{aligned} \bar{w}(\theta, \lambda) &= \frac{1}{4\pi} \int_{\Omega'} w(\theta, \lambda, \theta', \lambda') d\Omega', \\ &= \frac{1}{4\pi} \int_{\Omega'} \sum_{l,m} Y_{lm}(\theta, \lambda) \sum_{n,k} W_{lm}^{nk} Y_{nk}^*(\theta', \lambda') d\Omega', \quad \because (2.3a), \\ &= \sum_{l,m} Y_{lm}(\theta, \lambda) \sum_{n,k} W_{lm}^{nk} \delta_{n0} \delta_{k0}, \end{aligned}$$

$$= \sum_{l,m} Y_{lm}(\theta, \lambda) W_{lm}^{00}, \text{ and} \quad (2.5c)$$

$$b(\theta, \lambda, \theta', \lambda') = \frac{w(\theta, \lambda, \theta', \lambda')}{\bar{w}(\theta, \lambda)}. \quad (2.5d)$$

Here,  $b(\cdot, \cdot)$  is the smoothing kernel, and it is clear from (2.5b) that  $b(\cdot, \cdot)$  is the normalised form of the two-point weighting function  $w(\cdot, \cdot)$  and the entire operation is a weighted average. Pellinen [1966] used such a formulation to spatial smoothing, and thereafter Jekeli [1981] used the terms weighting function to denote  $w(\cdot, \cdot)$  and smoothing kernel for  $b(\cdot, \cdot)$ , and this convention is followed here as well.

The two-point smoothing kernel being a scalar, it can also be expanded in terms of spherical harmonics, and therefore, it has its own spectrum:

$$b(\theta, \lambda, \theta', \lambda') = \sum_{l,m} Y_{lm}(\theta, \lambda) \sum_{n,k} B_{lm}^{nk} Y_{nk}^*(\theta', \lambda'). \quad (2.6)$$

The relationship between the spectra of the weighting function and the smoothing kernel can be derived as follows:

$$\begin{aligned} b(\theta, \lambda, \theta', \lambda') &= \frac{w(\theta, \lambda, \theta', \lambda')}{\bar{w}(\theta, \lambda)}, \\ \Rightarrow w(\theta, \lambda, \theta', \lambda') &= \bar{w}(\theta, \lambda) b(\theta, \lambda, \theta', \lambda'), \end{aligned} \quad (2.7a)$$

$$\begin{aligned} \frac{1}{16\pi^2} \iint_{\Omega, \Omega'} w(\theta, \lambda, \theta', \lambda') Y_{l'm'}^*(\theta, \lambda) Y_{n'k'}(\theta', \lambda') d\Omega' d\Omega &= \\ \frac{1}{16\pi^2} \iint_{\Omega, \Omega'} \bar{w}(\theta, \lambda) b(\theta, \lambda, \theta', \lambda') Y_{l'm'}^*(\theta, \lambda) Y_{n'k'}(\theta', \lambda') d\Omega' d\Omega, \end{aligned} \quad (2.7b)$$

$$\begin{aligned} W_{lm}^{nk} &= \frac{1}{16\pi^2} \iint_{\Omega, \Omega'} \bar{w}(\theta, \lambda) b(\theta, \lambda, \theta', \lambda') Y_{l'm'}^*(\theta, \lambda) Y_{n'k'}(\theta', \lambda') d\Omega' d\Omega, \\ &= \frac{1}{16\pi^2} \iint_{\Omega, \Omega'} \sum_{p,q} Y_{pq}(\theta, \lambda) W_{pq}^{00} \times \sum_{l,m} Y_{lm}(\theta, \lambda) \sum_{n,k} B_{lm}^{nk} Y_{nk}^*(\theta', \lambda') \times \\ &\quad Y_{l'm'}^*(\theta, \lambda) Y_{n'k'}(\theta', \lambda') d\Omega' d\Omega, \\ &= \frac{1}{4\pi} \int_{\Omega} \sum_{p,q} Y_{pq}(\theta, \lambda) W_{pq}^{00} \times \sum_{l,m} Y_{lm}(\theta, \lambda) \sum_{n,k} B_{lm}^{nk} \delta_{nn'} \delta_{kk'} \times Y_{l'm'}^*(\theta, \lambda) d\Omega, \\ &= \sum_{p,q} W_{pq}^{00} \sum_{l,m} B_{lm}^{nk} \times \frac{1}{4\pi} \int_{\Omega} Y_{pq}(\theta, \lambda) Y_{lm}(\theta, \lambda) Y_{l'm'}^*(\theta, \lambda) d\Omega, \\ &= \sum_{p,q} W_{pq}^{00} \sum_{l,m} B_{lm}^{nk} \left[ \sqrt{\frac{(2l+1)(2p+1)}{2l'+1}} C_{l0p0}^{l'0} C_{lmpq}^{l'm'} \right], \end{aligned} \quad (2.7c)$$

where  $C_{l0p0}^{l'0}$  and  $C_{lmpq}^{l'm'}$  are the Clebsch-Gordan coefficients [Varshalovich et al., 1988, p.148].

The relationship derived in (2.7) is done purely for academic purposes as it only provides a way to relate the spectra of the weighting and smoothing kernels, but it is impractical for computational purposes. The impracticality is explained by the fact that one needs to know both the spectra,  $W_{lm}^{nk}$  and  $B_{lm}^{nk}$ , to calculate one from the other, which negates the whole purpose of the relationship. However, given a weighting kernel the corresponding smoothing kernel can be computed numerically as follows:

$$\mathbf{b} = (\bar{\mathbf{w}})^{-1} \mathbf{w}, \quad (2.8a)$$

$$\mathbf{Y} \mathbf{B} \mathbf{Y}^\dagger = (\bar{\mathbf{w}})^{-1} \mathbf{Y} \mathbf{W} \mathbf{Y}^\dagger,$$

$$\mathbf{Y} \mathbf{B} \mathbf{Y}^\dagger \mathbf{Y} (\mathbf{Y}^\dagger \mathbf{Y})^{-1} = (\bar{\mathbf{w}})^{-1} \mathbf{Y} \mathbf{W} \mathbf{Y}^\dagger \mathbf{Y} (\mathbf{Y}^\dagger \mathbf{Y})^{-1},$$

$$(\mathbf{Y}^\dagger \mathbf{Y})^{-1} \mathbf{Y}^\dagger \mathbf{Y} \mathbf{B} = (\mathbf{Y}^\dagger \mathbf{Y})^{-1} \mathbf{Y}^\dagger (\bar{\mathbf{w}})^{-1} \mathbf{Y} \mathbf{W},$$

$$\mathbf{B} = (\mathbf{Y}^\dagger \mathbf{Y})^{-1} \mathbf{Y}^\dagger (\bar{\mathbf{w}})^{-1} \mathbf{Y} \mathbf{W}. \quad (2.8b)$$

Although (2.8b) presents a numerical solution, the computation of the term  $(\mathbf{Y}^\dagger \mathbf{Y})^{-1} \mathbf{Y}^\dagger (\bar{\mathbf{w}})^{-1} \mathbf{Y}$  becomes expensive for reasonably higher degrees of spherical harmonic degrees, for e.g.  $l > 100$ .

### Smoothed field

Inserting equations (2.6) and (2.1a) into (2.5b) gives

$$\begin{aligned} \bar{f}(\theta, \lambda) &= \frac{1}{4\pi} \int_{\Omega'} \sum_{l,m} Y_{lm}(\theta, \lambda) \sum_{n,k} B_{lm}^{nk} Y_{nk}^*(\theta', \lambda') \sum_{n',k'} F_{n'k'} Y_{n'k'}(\theta', \lambda') d\Omega', \\ &= \sum_{l,m} Y_{lm}(\theta, \lambda) \sum_{n,k} B_{lm}^{nk} \sum_{n',k'} F_{n'k'} \frac{1}{4\pi} \int_{\Omega'} Y_{nk}^*(\theta', \lambda') Y_{n'k'}(\theta', \lambda') d\Omega', \\ &= \sum_{l,m} Y_{lm}(\theta, \lambda) \sum_{n,k} B_{lm}^{nk} \sum_{n',k'} F_{n'k'} \delta_{nn'} \delta_{kk'}, \\ &= \sum_{l,m} Y_{lm}(\theta, \lambda) \sum_{n,k} B_{lm}^{nk} F_{nk}, \end{aligned} \quad (2.9a)$$

$$\bar{F}_{lm} = \sum_{n,k} B_{lm}^{nk} F_{nk}, \quad (2.9b)$$

which is the smoothed field obtained by using the spherical harmonic coefficients of the smoothing kernel. The same can be expressed in matrix form as follows:

$$\begin{aligned} \bar{\mathbf{f}} &= \mathbf{b} \mathbf{f}, \\ &= \mathbf{Y} \mathbf{B} \mathbf{Y}^\dagger \mathbf{Y} (\mathbf{Y}^\dagger \mathbf{Y})^{-1} (\mathbf{Y}^\dagger \mathbf{Y})^{-1} \mathbf{Y}^\dagger \mathbf{Y} \mathbf{F}, \\ &= \mathbf{Y} \mathbf{B} \mathbf{F}, \end{aligned} \quad (2.10a)$$

$$\bar{\mathbf{F}} = \mathbf{B} \mathbf{F}. \quad (2.10b)$$

## §2.2 ALTERNATIVE REPRESENTATION OF WEIGHTING FUNCTIONS

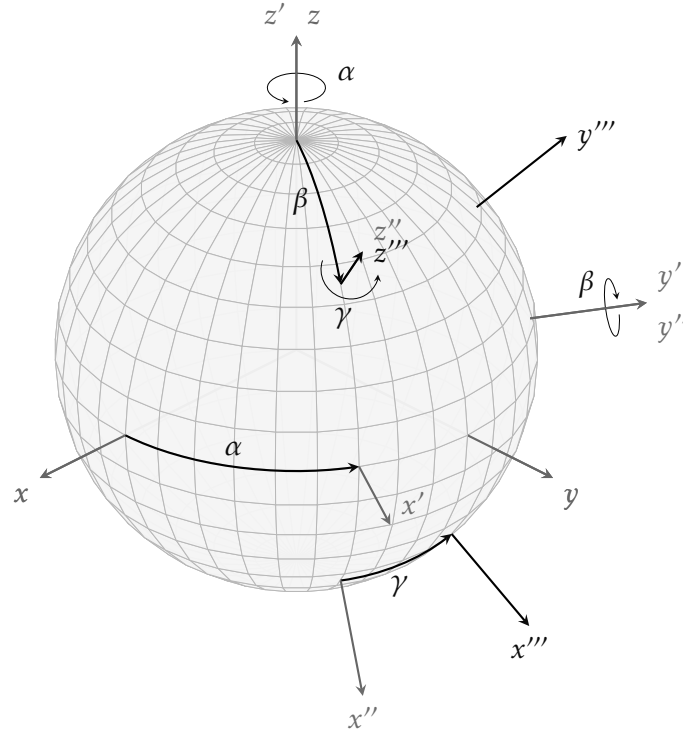
An alternative representation of (2.3a) can be obtained by taking the calculation point as the pole of the sphere  $\Omega'$ . This accounts for a rotation of the coordinate system of the sphere  $\Omega'$ , and the rotation of the coordinate system is carried out using the *Euler rotations* (cf. Figure 2.1),  $\mathcal{R}(\alpha, \beta, \gamma)$ , where

$$\alpha = [0, 2\pi), \text{ rotation about the initial } x\text{-axis,} \quad (2.11a)$$

$$\beta = [0, \pi], \text{ rotation about the new } y\text{-axis, and} \quad (2.11b)$$

$$\gamma = [0, 2\pi), \text{ rotation about the final } z\text{-axis.} \quad (2.11c)$$

$$\Rightarrow \mathcal{R}(\alpha, \beta, \gamma) = \mathcal{R}_{z''}(\gamma) \mathcal{R}_{y'}(\beta) \mathcal{R}_z(\alpha). \quad (2.11d)$$



**Figure 2.1:** Euler rotations on the sphere:  $\{x, y, z\} \xrightarrow{\mathcal{R}_z(\alpha)} \{x', y', z'\} \xrightarrow{\mathcal{R}_{y'}(\beta)} \{x'', y'', z''\} \xrightarrow{\mathcal{R}_{z''}(\gamma)} \{x''', y''', z'''\}.$

This rotation also corresponds to a transformation of the spherical harmonics, which is accomplished by the use of *Wigner-D functions* [e.g., Edmonds, 1960].

$$Y_{nq}(\psi, \pi - A) = \sum_k D_{nqk}(\lambda, \theta, 0) Y_{nk}(\theta', \lambda'), \quad (2.12a)$$

$$\begin{aligned} &= \sum_{r,k} D_{nqr}(0, \theta, 0) D_{nrk}(\lambda, 0, 0) Y_{nk}(\theta', \lambda'), \\ &= \sum_r D_{nqr}(0, \theta, 0) Y_{nr}(\theta', \Delta\lambda), \end{aligned} \quad (2.12b)$$

$$Y_{nk}(\theta', \lambda') = \sum_q D_{nqk}^*(\lambda, \theta, 0) Y_{nq}(\psi, \pi - A),$$

$$= \sum_q D_{nkq}(0, -\theta, -\lambda) Y_{nq}(\psi, \pi - A), \quad (2.12c)$$

where  $D_{nkq}(0, -\theta, -\lambda)$  are the fully normalised Wigner- $D$  symbols with the three Euler rotation angles ( $\alpha = 0$ ,  $\beta = -\theta$ ,  $\gamma = -\lambda$ ). The Wigner- $D$  symbol is defined as

$$D_{nqk}(\alpha, \beta, \gamma) = e^{-iq\gamma} d_{nqk}(\beta) e^{-ik\alpha}, \quad (2.13a)$$

$$D_{nqk}^*(\alpha, \beta, \gamma) = e^{iq\gamma} d_{nqk}(\beta) e^{ik\alpha}, \quad (2.13b)$$

$$d_{nqk}(\beta) = (-1)^{k-q} \sqrt{\frac{(n-q)!}{(n-k)!} \frac{(n+q)!}{(n+k)!}} \sum_{t=t_1}^{t_2} \binom{n+k}{t} \binom{n-k}{n-q-t} (-1)^t c^{2n-p} s^p, \quad (2.13c)$$

$$\text{with } c = \cos \frac{\beta}{2}, \quad (2.13d)$$

$$s = \sin \frac{\beta}{2}, \quad (2.13e)$$

$$p = k - q + 2t, \quad (2.13f)$$

$$t_1 = \max(0, q - k), \quad (2.13g)$$

$$t_2 = \min(n - k, n + q). \quad (2.13h)$$

For a complete overview on different normalisation conventions and the methods of computation used for the Wigner- $D$  functions, consult Sneeuw [1991].

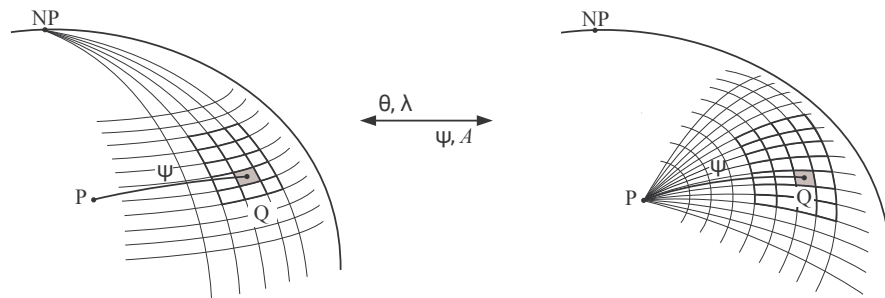
Inserting (2.12c) into (2.3a) gives

$$w(\theta, \lambda, \psi, A) = \sum_{l,m} Y_{lm}(\theta, \lambda) \sum_{n,k} W_{lm}^{nk} \sum_q D_{nkq}^*(0, -\theta, -\lambda) Y_{nq}^*(\psi, \pi - A), \quad (2.14a)$$

$$= \sum_{l,m} Y_{lm}(\theta, \lambda) \sum_{n,q} Y_{nq}^*(\psi, \pi - A) \sum_k W_{lm}^{nk} D_{nkq}^*(0, -\theta, -\lambda). \quad (2.14b)$$

Such an expression was already presented to the geodetic community by Rummel and Schwarz [1977], where they use expression (2.14a) to compute non-homogeneous weighting functions for use in collocation studies. Also, Martinec and Pěč [1985] provide another expression for representing the two-point weighting function, which arise by the use of *bipolar spherical harmonics* and *Clebsch-Gordan coefficients* as used in the quantum mechanics and astronomy communities. Here, we will follow the expressions and methods of Rummel and Schwarz [1977].

The convenience of the representation shown in (2.14a) is that, as mentioned before, all the points on the sphere can be referred and/or visualised as points at certain spherical distances and azimuths. The representation shown in equation (2.14a) allows an intuitive understanding of the behaviour of the weighting function in terms of the distribution of the weights over the whole sphere, and will make the job of classifying, designing and analysing a lot more easier. This will become more clear as we proceed with the discussion in the subsequent sections and chapters.



**Figure 2.2:** Alternative representation of weighting functions. Here, NP is the north pole, P is the calculation point and Q is a data point, and P is related to Q with the spherical distance  $\psi$  and azimuth  $A$ .

### §2.3 CLASSIFICATION OF SMOOTHING KERNELS

It should also be noted here that smoothing with a two-point weighting function does not result in a convolution in the spatial domain (*in the classical Fourier sense*), because every single point on the sphere has its own smoothing kernel. Smoothing in the spatial domain becomes a convolution operation, only when *homogeneity* (location independence) is enforced on the smoothing kernel i.e. every point on the sphere has one and the same smoothing kernel. This statement provides a basis for a broader classification of smoothing kernel types, where the kernels can be classified as *homogeneous* if the kernel remains the same for all points on the sphere, and *inhomogeneous* if the kernel changes for different points on the sphere. Homogeneous smoothing kernels are also referred to as *translation invariant* smoothing kernels.

A further classification of the kernels comes from the *rotational invariance* of the weights of the kernel. Here, the kernels whose weights are directional invariant, i.e. the weighting structure of the smoothing kernel is the same in every direction, are called *isotropic*, and those kernels whose weights are directionally variant are called *anisotropic*. A third classification is also possible, mainly for anisotropic kernels, which is based on the symmetry of the kernels across a great circle section. A general two-point smoothing will be completely anisotropic, and hence, asymmetric across a great circle section, while isotropic smoothing kernels will be radially symmetric. Nevertheless, symmetry can also be enforced on anisotropic smoothing kernels, which eventually would mean that the kernel is not completely anisotropic. This classification terminology is in fact used by Klees et al. [2008] to name the different types of filters that they derive, compute and compare.

It is evident from the classification criteria that homogeneity/inhomogeneity is a *global property*, whereas isotropy/anisotropy (and symmetry/asymmetry) is a *local property*. Further, the properties of inhomogeneity and anisotropy are an expression of the four degrees of freedom—co-latitude ( $\theta$ ), longitude ( $\lambda$ ), spherical distance ( $\psi$ ) and azimuth ( $A$ )—accorded to the general two-point kernel. In other words, the general two-point smoothing kernel does not have any restrictions in the values that it can take based on location ( $\theta, \lambda$ ), spherical distance and azimuth. However, for the homogeneous kernels or the isotropic kernels there are certain restrictions. By applying these restrictions either individually or as a combination a variety of kernels can be generated, and in the following sections the restrictions are applied to the general two-point kernel.

Rummel and Schwarz [1977] showed that the restrictions on the degrees of freedom can be imposed by integrating along each of them, and we will follow their method here. In fact, they provide a detailed derivation of most of the weighting functions that we discuss here, but we repeat it here for the sake of consistency and completeness. The aim of this exercise is to show the type of spectrum that has to be expected for each of the type of smoothing kernels that will be generated after applying the restrictions. A good understanding of the spectrum allows for a better understanding of the smoothing effects associated with the smoothing kernels in question. At the end of the section the spectra of all the different forms of smoothing kernels is visualised in Figure 2.3 for a quick overview.

### Homogeneous smoothing kernels

Homogeneous windows are characterised by the invariance of the window shape and the weight distribution under translations and rotations on the sphere. Smoothing with the homogeneous windows is essentially a convolution (in the classical sense). These convolutions can be performed either using an isotropic or an anisotropic kernel, and Jekeli [1981] refers to the convolutions with homogeneous isotropic kernels as *convolution of the first kind* and those with homogeneous anisotropic kernels as *convolution of the second kind*. Here, the general form of the isotropic and anisotropic homogeneous windows will be described and discussed.

#### Isotropic

The weights of homogeneous isotropic windows on the sphere depend only on the spherical distance  $\psi$  between the window location and the points on the sphere, which implies that they are independent of the location and direction. They are the simplest class of windows defined on the sphere, and they can be derived from the general two-point function as follows:

$$w(\psi) = \frac{1}{8\pi^2} \int_{\Omega} \int_A w(\theta, \lambda, \psi, A) dA d\Omega,$$

inserting (2.14a) on the right hand side gives

$$\begin{aligned} w(\psi) &= \frac{1}{8\pi^2} \int_{\Omega} \int_A \sum_{l,m} Y_{lm}(\theta, \lambda) \sum_{n,k} W_{lm}^{nk} \sum_q D_{nkq}^*(0, -\theta, -\lambda) Y_{nq}^*(\psi, \pi - A) dA d\Omega, \\ &= \frac{1}{4\pi} \int_{\Omega} \sum_{l,m} Y_{lm}(\theta, \lambda) \sum_{n,k} W_{lm}^{nk} \sum_q D_{nkq}^*(0, -\theta, -\lambda) \bar{P}_{nq}(\cos \psi) \delta_{q0} d\Omega, \\ &= \frac{1}{4\pi} \int_{\Omega} \sum_{l,m} Y_{lm}(\theta, \lambda) \sum_{n,k} W_{lm}^{nk} D_{nk0}^*(0, -\theta, -\lambda) \bar{P}_{n0}(\cos \psi) d\Omega, \\ &= \frac{1}{4\pi} \int_{\Omega} \sum_{l,m} Y_{lm}(\theta, \lambda) \sum_{n,k} W_{lm}^{nk} D_{n0k}(\lambda, \theta, 0) \bar{P}_{n0}(\cos \psi) d\Omega, \\ &= \frac{1}{4\pi} \int_{\Omega} \sum_{l,m} Y_{lm}(\theta, \lambda) \sum_{n,k} W_{lm}^{nk} \frac{1}{\sqrt{2n+1}} Y_{nk}^*(\theta, \lambda) \sqrt{2n+1} P_n(\cos \psi) d\Omega, \\ &= \sum_{l,m} \sum_{n,k} W_{lm}^{nk} P_n(\cos \psi) \delta_{ln} \delta_{mk}, \end{aligned}$$



$$= \sum_l P_l(\cos \psi) \sum_m W_{lm}^{lm} = \sum_l W'_l P_l(\cos \psi). \quad (2.15)$$

The final equation (2.15) is the spectrum of a homogeneous isotropic weighting function as derived from an inhomogeneous anisotropic weighting function, which suggests that the spectrum is purely degree dependent. The other implication of degree dependence is that the values  $W'_l$  are all real-valued as opposed to  $W_{lm}^{nk}$ , which are complex-valued.

Now, to derive the smoothing kernel,  $b(\psi)$ , from the weighting function we have to compute the normalisation factor  $\bar{w}(\psi)$ .

$$\bar{w}(\psi) = \frac{1}{4\pi} \int_{\Omega'} w(\psi) d\Omega',$$

inserting (2.15), the spectrum of  $w(\psi)$

$$= \frac{1}{4\pi} \int_{\Omega'} \sum_l P_l(\cos \psi) \sum_m W_{lm}^{lm} d\Omega'$$

rewriting  $P_l(\cos \psi)$  using (A.3a)

$$\begin{aligned} &= \frac{1}{4\pi} \int_{\Omega'} \sum_{l,k} \frac{1}{2l+1} Y_{lk}(\theta, \lambda) Y_{lk}^*(\theta', \lambda') \sum_m W_{lm}^{lm} d\Omega' \\ &= \sum_{l,k} \frac{1}{2l+1} Y_{lk}(\theta, \lambda) \frac{1}{4\pi} \int_{\Omega'} Y_{lk}^*(\theta', \lambda') d\Omega' \sum_m W_{lm}^{lm}, \\ &= \sum_{l,k} \frac{1}{2l+1} Y_{lk}(\theta, \lambda) \delta_{l0} \delta_{k0} \sum_m W_{lm}^{lm} = W_{00}^{00}. \end{aligned} \quad (2.16a)$$

$$\Rightarrow b(\psi) = \frac{w(\psi)}{\bar{w}(\psi)} = \sum_l P_l(\cos \psi) \frac{W'_l}{W_{00}^{00}}, \quad (2.16b)$$

$$B_l = \frac{W'_l}{W_{00}^{00}}. \quad (2.16c)$$

The normalisation factor for the weighting function clearly indicates the homogeneity of the weighting as it is independent of the point where the weighting function is located.

Smoothing a field  $f(\theta, \lambda)$  with a homogeneous isotropic smoothing kernel,  $b(\psi)$ , is done as follows:

$$\begin{aligned} \bar{f}(\theta, \lambda) &= \frac{1}{4\pi} \int_{\Omega'} f(\theta', \lambda') b(\psi) d\Omega', \\ &= \frac{1}{4\pi} \int_{\Omega'} \sum_{l,m} F_{lm} Y_{lm}(\theta', \lambda') \sum_n B_n P_n(\psi) d\Omega', \\ &= \frac{1}{4\pi} \int_{\Omega'} \sum_{l,m} F_{lm} Y_{lm}(\theta', \lambda') \sum_n \frac{B_n}{2n+1} \sum_k Y_{nk}(\theta, \lambda) Y_{nk}^*(\theta', \lambda') d\Omega', \end{aligned}$$

$$\begin{aligned}
&= \sum_{l,m} F_{lm} \sum_n \frac{B_n}{2n+1} \sum_k Y_{nk}(\theta, \lambda) \frac{1}{4\pi} \int_{\Omega'} Y_{lm}(\theta', \lambda') Y_{nk}^*(\theta', \lambda') d\Omega', \\
&= \sum_{l,m} F_{lm} \sum_n \frac{B_n}{2n+1} \sum_k Y_{nk}(\theta, \lambda) \delta_{ln} \delta_{mk}, \\
&= \sum_l \frac{B_l}{2l+1} \sum_m F_{lm} Y_{lm}(\theta, \lambda), \tag{2.17a}
\end{aligned}$$

$$\bar{F}_{lm} = \frac{B_l}{2l+1} F_{lm}. \tag{2.17b}$$

### Anisotropic

The weights of homogeneous anisotropic windows depend both on the spherical distance  $\psi$  and the azimuth  $A$  between the window location and the points on the sphere. These windows can be derived by averaging the general two-point weighting function over all the window locations on the sphere.

$$\begin{aligned}
w(\psi, A) &= \frac{1}{4\pi} \int_{\Omega} w(\theta, \lambda, \psi, A) d\Omega, \\
&= \frac{1}{4\pi} \int_{\Omega} \sum_{l,m} Y_{lm}(\theta, \lambda) \sum_{n,k} W_{lm}^{nk} \sum_q D_{nkq}^*(0, -\theta, -\lambda) Y_{nq}^*(\psi, \pi - A) d\Omega, \\
&= \frac{1}{2} \int_{\theta} \sum_{l,m} \bar{P}_{lm}(\cos \theta) \sum_{n,k} W_{lm}^{nk} \delta_{mk} \sum_q d_{nkq}(-\theta) Y_{nq}^*(\psi, \pi - A) \sin \theta d\theta,
\end{aligned}$$

using (A.16b), (A.15b) and (A.15c)  $\bar{P}_{lm}(\cos \theta)$  can be written as a Wigner- $d$  symbol,

$$\begin{aligned}
&= \frac{1}{2} \int_{\theta} \sum_{l,m} \sqrt{2l+1} d_{l0m}(\theta) \sum_n W_{lm}^{nm} \sum_q d_{nqm}(\theta) Y_{nq}^*(\psi, \pi - A) \sin \theta d\theta, \\
&= \sum_l \sqrt{2l+1} \sum_{n,m} W_{lm}^{nm} \sum_q Y_{nq}^*(\psi, \pi - A) \frac{1}{2} \int_{\theta} d_{l0m}(\theta) d_{nqm}(\theta) \sin \theta d\theta,
\end{aligned}$$

inserting (B.4) for the integral gives

$$\begin{aligned}
&= \sum_l \sqrt{2l+1} \sum_{n,m} W_{lm}^{nm} \sum_q I_{l0m}^{nqm} Y_{nq}^*(\psi, \pi - A), \\
&= \sum_{n,q} Y_{nq}^*(\psi, \pi - A) \sum_{l,m} \sqrt{2l+1} W_{lm}^{nm} I_{l0m}^{nqm}, \\
&= \sum_{n,q} Y_{nq}^*(\psi, \pi - A) W'_{nq}. \tag{2.18}
\end{aligned}$$

Equation (2.18) is the spherical harmonic transform of the homogeneous anisotropic weighting function. The smoothing kernel  $b(\psi, A)$  of the homogeneous anisotropic weighting function  $w(\psi, A)$  is given by

$$b(\psi, A) = \frac{w(\psi, A)}{\bar{w}(\psi, A)}, \tag{2.19a}$$

where

$$\begin{aligned}
\bar{w}(\psi, A) &= \frac{1}{4\pi} \int_{\Omega'} w(\psi, A) d\Omega', \\
&= \frac{1}{16\pi^2} \int_{\Omega'} \int_{\Omega} w(\theta, \lambda, \psi, A), \\
&= W_{00}^{00},
\end{aligned} \tag{2.19b}$$

substituting (2.18) and (2.19b) in (2.19a) gives

$$\begin{aligned}
b(\psi, A) &= \sum_{n,q} Y_{nq}^*(\psi, \pi - A) \frac{W_{nq}'}{W_{00}^{00}}, \\
&= \sum_{n,q} B_{nq} Y_{nq}^*(\psi, \pi - A).
\end{aligned} \tag{2.19c}$$

Smoothing a field  $f(\theta, \lambda)$  with the smoothing kernel  $b(\psi, A)$  is done as follows:

$$\begin{aligned}
\bar{f}(\theta, \lambda) &= \int_{\Omega'} f(\theta', \lambda') b(\psi, A) d\Omega', \\
&= \frac{1}{4\pi} \int_{\Omega'} \sum_{l,m} F_{lm} Y_{lm}(\theta', \lambda') \sum_{n,q} B_{nq} Y_{nq}^*(\psi, \pi - A) d\Omega', \\
&= \frac{1}{4\pi} \int_{\Omega'} \sum_{l,m} F_{lm} Y_{lm}(\theta', \lambda') \sum_{n,q} B_{nq} \sum_k D_{nqk}^*(\lambda, \theta, 0) Y_{nk}^*(\theta', \lambda') d\Omega', \\
&= \sum_{l,m} \sum_{n,q} F_{lm} B_{nq} \sum_k D_{nqk}^*(\lambda, \theta, 0) \frac{1}{4\pi} \int_{\Omega'} Y_{lm}(\theta', \lambda') Y_{nk}^*(\theta', \lambda') d\Omega', \\
&= \sum_{l,m} \sum_{n,q} F_{lm} B_{nq} \sum_k D_{nqk}^*(\lambda, \theta, 0) \delta_{ln} \delta_{mk}, \\
&= \sum_{l,m} F_{lm} \sum_q B_{lq} D_{lqm}^*(\lambda, \theta, 0), \\
&= \sum_{l,m} F_{lm} B_{lm}(\theta, \lambda),
\end{aligned} \tag{2.20a}$$

$$\bar{F}_{lm}(\theta, \lambda) = F_{lm} B_{lm}(\theta, \lambda). \tag{2.20b}$$

Equation (2.20a) is the spherical harmonic spectrum of a field smoothed using a homogeneous anisotropic smoothing kernel, where  $B_{lm}(\theta, \lambda)$  signify that the spectrum of the anisotropic kernel,  $B_{lk}$ , has to be rotated to the computation point  $(\theta, \lambda)$  prior to filtering. Due to the rotation, every point has its own filtered spectrum,  $\bar{F}_{lm}(\theta, \lambda)$ . Jekeli [1981] also derives an identical equation [pg. 10, equation (29)], but proceeds further to derive the spectrum of  $\bar{f}(\theta, \lambda)$  in terms of surface spherical harmonics rather than Wigner- $D$  functions. The problem with (2.20a) is that for every point on the sphere a rotation matrix must be computed, which is an expensive computation compared to the spherical harmonic synthesis computation. However, the symmetries between Wigner- $D$  coefficients help in speeding up the calculation

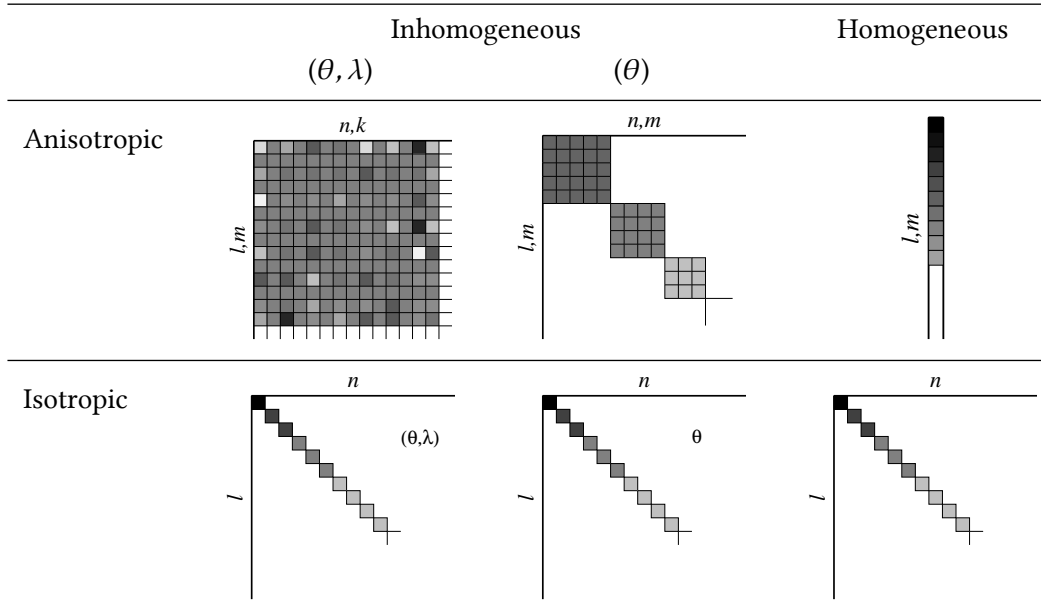
manifold, and with modern computer power this should not be an issue. Nevertheless, we find that such kernels have not been used before in geodesy.

**Table 2.2:** Deriving different types of weighting functions from the general two-point weighting function. The corresponding spectra of all the weighting functions are also provided.

		Isotropic	Anisotropic
Homogeneous		$w(\psi) = \frac{1}{8\pi^2} \int_{\Omega, A} w(\theta, \lambda, \psi, A) dA d\Omega$ $= \sum_{l=0}^L \frac{2l+1}{2} W_l P_l(\cos \psi)$	$w(\psi, A) = \frac{1}{4\pi} \int_{\Omega} w(\theta, \lambda, \psi, A) d\Omega$ $= \sum_{n,k} W_{nk} Y_{nk}^*(\psi, \pi - A)$
Inhomogeneous	Latitude dependent	$w(\theta, \psi) = \frac{1}{4\pi^2} \int_{\lambda, A} w(\theta, \lambda, \psi, A) dA d\lambda$ $= \sum_{l,m,n} \bar{P}_{lm}(\cos \theta) W_{lm}^{nm} \times$ $\bar{P}_{nm}(\cos \theta) \bar{P}_n(\cos \psi)$	$w(\theta, \psi, A) = \frac{1}{2\pi} \int_{\lambda} w(\theta, \lambda, \psi, A) d\lambda$ $= \sum_{l,m,n} Y_{lm}(\theta, \lambda) W_{lm}^{nm} Y_{nm}^*(\theta', \lambda')$
	Location dependent	$w(\theta, \lambda, \psi) = \frac{1}{2\pi} \int_A w(\theta, \lambda, \psi, A) dA$ $= \sum_{l,m,n,k} Y_{lm}(\theta, \lambda) W_{lm}^{nk} \times$ $Y_{nk}^*(\theta, \lambda) \bar{P}_n(\cos \psi)$	$w(\theta, \lambda, \psi, A) = \sum_{l,m,n,q} Y_{lm}(\theta, \lambda) Y_{nq}^*(\psi, \pi - A) \times$ $\sum_k W_{lm}^{nk} D_{nkq}^*(0, -\theta, -\lambda)$

### Inhomogeneous smoothing kernels

Inhomogeneous windows appear in smoothing, when different calculation points have different smoothing kernels centred on them, which in other words mean that they are calculation point-dependent. Therefore, at any point of time the location of the kernel has to be specified. These type of kernels are, in general, derived from covariance functions (stochastic information) of the field. Unlike homogeneous windows, where there were only two types of windows (isotropic and anisotropic), here a number of possibilities are available to design the kernels due to the fact that four variables ( $\theta$ ,  $\lambda$ ,  $\psi$ , and  $A$ ) are involved in the definition. Martinec and Pěč [1985] explore these possibilities in terms of covariance functions on the sphere, and here those possibilities are revisited and extended for the case of smoothing kernels.



**Figure 2.3:** The different classes of the weighting windows can be derived by averaging the general form over the calculation points  $(\theta, \lambda)$  and over the azimuth  $A$ . While the special forms of weighting windows need not always be derived in this manner, such averaging immediately clarifies spectral structure of the special forms. The knowledge of the respective spectra is an important aide in the design of filters.

#### Location-dependent and isotropic

Inhomogeneous isotropic windows are generated by choosing different smoothing radii for different points on the sphere. This is achieved by integrating the general two-point kernel over the azimuth.

$$w(\theta, \lambda, \psi) = \frac{1}{2\pi} \int_0^{2\pi} w(\theta, \lambda, \psi, A) dA, \quad (2.21a)$$

$$\begin{aligned}
&= \frac{1}{2\pi} \int_0^{2\pi} \sum_{l,m} Y_{lm}(\theta, \lambda) \sum_{n,k} W_{lm}^{nk} \sum_q D_{nkq}^*(0, -\theta, -\lambda) Y_{nq}^*(\psi, \pi - A) dA, \\
&= \sum_{l,m} Y_{lm}(\theta, \lambda) \sum_{n,k} W_{lm}^{nk} \sum_q D_{nkq}^*(0, -\theta, -\lambda) \bar{P}_{nq}(\cos \psi) \delta_{q0}, \\
&= \sum_{l,m} Y_{lm}(\theta, \lambda) \sum_{n,k} W_{lm}^{nk} D_{nk0}^*(0, -\theta, -\lambda) \bar{P}_{n0}(\cos \psi), \\
&= \sum_{l,m} Y_{lm}(\theta, \lambda) \sum_{n,k} W_{lm}^{nk} \frac{Y_{nk}^*(\theta, \lambda)}{\sqrt{2n+1}} \bar{P}_n(\cos \psi), \\
&= \sum_{l,m} Y_{lm}(\theta, \lambda) \sum_{n,k} W_{lm}^{nk} Y_{nk}^*(\theta, \lambda) P_n(\cos \psi), \\
&= \sum_n W_n(\theta, \lambda) P_n(\cos \psi). \quad (2.21b)
\end{aligned}$$

Equation (2.21b) is the spectrum for a location-dependent isotropic weighting function, and that of the smoothing kernel is given by

$$b(\theta, \lambda, \psi) = \frac{w(\theta, \lambda, \psi)}{\bar{w}(\theta, \lambda, \psi)}, \quad (2.22a)$$

$$\begin{aligned} &= \frac{1}{\bar{w}(\theta, \lambda, \psi)} \sum_n W_n(\theta, \lambda) P_n(\cos \psi), \\ &= \sum_n B_n(\theta, \lambda) P_n(\cos \psi), \end{aligned} \quad (2.22b)$$

with

$$\begin{aligned} \bar{w}(\theta, \lambda, \psi) &= \frac{1}{4\pi} \int_{\Omega'} w(\theta, \lambda, \psi) d\Omega', \\ &= \frac{1}{8\pi^2} \int_{\Omega'} \int_0^{2\pi} w(\theta, \lambda, \psi, A) dA d\Omega', \\ &= \frac{1}{2\pi} \int_0^{2\pi} \sum_{l,m} W_{lm}^{00} Y_{lm}(\theta, \lambda) dA, \\ &= \sum_{l,m} W_{lm}^{00} Y_{lm}(\theta, \lambda). \end{aligned} \quad (2.22c)$$

Smoothing a field with the kernel (2.22b) gives

$$\begin{aligned} \bar{f}(\theta, \lambda) &= \int_{\Omega'} f(\theta', \lambda') b(\theta, \lambda, \psi) d\Omega', \\ &= \frac{1}{4\pi} \int_{\Omega'} \sum_{l,m} F_{lm} Y_{lm}(\theta', \lambda') \sum_n B_n(\theta, \lambda) P_n(\cos \psi) d\Omega', \\ &= \frac{1}{4\pi} \int_{\Omega'} \sum_{l,m} F_{lm} Y_{lm}(\theta', \lambda') \sum_n \frac{B_n(\theta, \lambda)}{2n+1} \sum_k Y_{nk}(\theta, \lambda) Y_{nk}^*(\theta', \lambda') d\Omega', \\ &= \sum_{l,m} F_{lm} \sum_n \frac{B_n(\theta, \lambda)}{2n+1} \sum_k Y_{nk}(\theta, \lambda) \delta_{ln} \delta_{mk}, \\ &= \sum_{l,m} \frac{B_l(\theta, \lambda)}{2l+1} F_{lm} Y_{lm}(\theta, \lambda), \end{aligned} \quad (2.23a)$$

$$\bar{F}_{lm}(\theta, \lambda) = \frac{B_l(\theta, \lambda)}{2l+1} F_{lm}. \quad (2.23b)$$

*Latitude-dependent and isotropic*

The inhomogeneity of the weighting function in (2.21a) can be restricted only to the latitude and this results in

$$\begin{aligned}
 w(\theta, \psi) &= \frac{1}{2\pi} \int_0^{2\pi} w(\theta, \lambda, \psi) d\lambda, \\
 &= \sum_{l,m} \sum_{n,k} W_{lm}^{nk} P_n(\cos \psi) \frac{1}{2\pi} \int_0^{2\pi} Y_{lm}(\theta, \lambda) Y_{nk}^*(\theta, \lambda) d\lambda, \\
 &= \sum_n \sum_{l,m} \bar{P}_{lm}(\cos \theta) W_{lm}^{nm} \bar{P}_{nm}(\cos \theta) P_n(\cos \psi), \\
 &= \sum_n W_n(\theta) P_n(\cos \psi),
 \end{aligned} \tag{2.24a}$$

$$\tag{2.24b}$$

and the smoothing kernel of the latitude-dependent isotropic function is

$$b(\theta, \psi) = \frac{w(\theta, \psi)}{\frac{1}{4\pi} \int_{\Omega'} w(\theta, \psi) d\Omega'}, \tag{2.25a}$$

$$\begin{aligned}
 &= \sum_n \frac{W_n(\theta)}{\bar{w}(\theta, \psi)} P_n(\cos \psi), \\
 &= \sum_n B_n(\theta) P_n(\cos \psi), \text{ and}
 \end{aligned} \tag{2.25b}$$

$$\begin{aligned}
 \bar{w}(\theta, \psi) &= \frac{1}{4\pi} \int_{\Omega'} w(\theta, \psi) d\Omega', \\
 &= \frac{1}{16\pi^3} \int_{\Omega'} \int_0^{2\pi} \int_0^{2\pi} w(\theta, \lambda, \psi, A) d\lambda dA d\Omega', \\
 &= \frac{1}{4\pi^2} \int_0^{2\pi} \int_0^{2\pi} \sum_{lm} W_{lm}^{00} Y_{lm}(\theta, \lambda) d\lambda dA, \\
 &= \frac{1}{2\pi} \int_0^{2\pi} \sum_{lm} W_{lm}^{00} \bar{P}_{lm}(\cos \theta) \delta_{m0} dA, \\
 &= \sum_l W_{l0}^{00} \bar{P}_l(\cos \theta).
 \end{aligned} \tag{2.25c}$$

A field smoothed with the latitude-dependent isotropic kernel, will lead to the following spectrum

$$\bar{f}(\theta, \lambda) = \int_{\Omega'} f(\theta', \lambda') b(\theta, \psi) d\Omega', \tag{2.26a}$$

$$\begin{aligned}
&= \frac{1}{4\pi} \int_{\Omega'} \sum_{l,m} F_{lm} Y_{lm}(\theta', \lambda') \sum_n B_n(\theta) P_n(\cos \psi) d\Omega', \\
&= \frac{1}{4\pi} \int_{\Omega'} \sum_{l,m} F_{lm} Y_{lm}(\theta', \lambda') \sum_n \frac{B_n(\theta)}{2n+1} \sum_k Y_{nk}(\theta, \lambda) Y_{nk}(\theta', \lambda') d\Omega', \\
&= \sum_{l,m} F_{lm} \sum_n \frac{B_n(\theta)}{2n+1} \sum_k Y_{nk}(\theta, \lambda) \frac{1}{4\pi} \int_{\Omega'} Y_{lm}(\theta', \lambda') Y_{nk}(\theta', \lambda') d\Omega', \\
&= \sum_{l,m} F_{lm} \sum_n \frac{B_n(\theta)}{2n+1} \sum_k Y_{nk}(\theta, \lambda) \delta_{ln} \delta_{mk}, \\
&= \sum_{l,m} \frac{B_l(\theta)}{2l+1} F_{lm} Y_{lm}(\theta, \lambda) \tag{2.26b}
\end{aligned}$$

$$\bar{F}_{lm}(\theta) = \frac{B_l(\theta)}{2l+1} F_{lm}. \tag{2.26c}$$

### *Latitude-dependent and anisotropic*

The general two-point kernel is a completely inhomogeneous and completely anisotropic kernel (i.e., asymmetric), which has been discussed in detail in the section 2.1. Klees et al. [2008] describe an optimal filter for GRACE data, and their anisotropic asymmetric filter (ANS) is an example of the general two-point kernel. Also, Kusche [2007] designs a kernel that is a general two-point kernel, but the anisotropy is only partial due to the kernel symmetry in the spatial domain. Later Kusche et al. [2009] designed a latitude-dependent anisotropic kernel that was shown to be as effective as the earlier general two-point kernel design in filtering noise. The reason was attributed to the observation pattern in satellite geodesy, which has a constant sampling space in the longitude direction. Thus, the latitude-dependent anisotropic kernel has a special place in satellite geodetic studies [e.g., Sneeuw, 2000].

As in the isotropic case, anisotropic weighting functions can also be made latitude-dependent only. Again, it is accomplished by averaging the general two-point weighting function over the longitudes of the calculation points.

$$\begin{aligned}
w(\theta, \psi, A) &= \frac{1}{2\pi} \int_0^{2\pi} w(\theta, \lambda, \psi, A) d\lambda, \tag{2.27a} \\
&= \frac{1}{2\pi} \int_0^{2\pi} \sum_{l,m} Y_{lm}(\theta, \lambda) \sum_{n,k} W_{lm}^{nk} \sum_q D_{nkq}^*(0, -\theta, -\lambda) Y_{nq}^*(\psi, \pi - A) d\lambda, \\
&= \sum_{l,m} \bar{P}_{lm}(\cos \theta) \sum_{n,k} W_{lm}^{nk} \sum_q d_{nkq}(-\theta) Y_{nq}^*(\psi, \pi - A) \frac{1}{2\pi} \int_0^{2\pi} e^{im\lambda} e^{-ik\lambda} d\lambda, \\
&= \sum_{l,m} \bar{P}_{lm}(\cos \theta) \sum_{n,k} W_{lm}^{nk} \sum_q d_{nkq}(-\theta) Y_{nq}^*(\psi, \pi - A) \delta_{mk}, \\
&= \sum_{l,m} \bar{P}_{lm}(\cos \theta) \sum_n W_{lm}^{nm} \sum_q d_{nmq}(-\theta) Y_{nq}^*(\psi, \pi - A),
\end{aligned}$$



$$= \sum_{l,m} \bar{P}_{lm}(\cos \theta) \sum_n W_{lm}^{nm} \sum_q D_{nmq}^*(0, -\theta, 0) Y_{nq}^*(\psi, \pi - A), \quad (2.27b)$$

The above spectrum of the weighting function can be further simplified by rotating back the spherical harmonics  $Y_{nq}^*(\psi, \pi - A)$  using  $D_{nmq}^*(0, -\theta, 0)$  as in (2.12b) as shown in the following derivation.

$$\begin{aligned} w(\theta, \psi, A) &= \sum_{l,m,n} \bar{P}_{lm}(\cos \theta) W_{lm}^{nm} Y_{nm}^*(\theta', \Delta\lambda), \\ &= \sum_{l,m,n} \bar{P}_{lm}(\cos \theta) W_{lm}^{nm} \bar{P}_{nm}(\cos \theta') e^{-im(\Delta\lambda)}, \\ &= \sum_{l,m,n} \bar{P}_{lm}(\cos \theta) W_{lm}^{nm} \bar{P}_{nm}(\cos \theta') e^{-im(\lambda' - \lambda)}, \\ &= \sum_{l,m,n} \bar{P}_{lm}(\cos \theta) e^{im\lambda} W_{lm}^{nm} \bar{P}_{nm}(\cos \theta') e^{-im\lambda'}, \\ &= \sum_{l,m} Y_{lm}(\theta, \lambda) \sum_n W_{lm}^{nm} Y_{nm}^*(\theta', \lambda'). \end{aligned} \quad (2.27c)$$

The spectrum of the latitude-dependent weighting function has two forms (2.27c) and (2.27d), and the former is the same as that derived by Rummel and Schwarz [1977] for their weighting function  $C(\theta_P, \theta_Q, \Delta\lambda)$  in equation (30). Therefore, the functions  $w(\theta, \psi, A)$  and  $w(\theta, \theta', \Delta\lambda)$  are one and the same, and the difference is only in the representation, which comes from the fact that whether the kernel is rotated such that the pole is at the calculation point or not. Although the  $w(\theta, \psi, A)$  is an attractive and appealing representation, the representation  $w(\theta, \theta', \Delta\lambda)$  reveals a peculiar behaviour of the latitude-dependent anisotropic kernel. Since the kernel depends on the difference between the longitudes of the two points, at the pole  $\Delta\lambda$  becomes zero due to convergence of the longitudes. Furthermore, the associated Legendre functions at the poles are order independent. Therefore, the kernel at the pole becomes completely isotropic. This can be visualised mathematically as follows:

$$\begin{aligned} w(\theta, \psi, A) &= w(\theta, \theta', \Delta\lambda), \\ &= \sum_{l,m} \bar{P}_{lm}(\cos \theta) e^{im\Delta\lambda} \sum_n W_{lm}^{nm} \bar{P}_{nm}(\cos \theta'), \end{aligned} \quad (2.27c)$$

when  $\theta = 0$

$$w(0, \theta', \Delta\lambda) = \sum_{l,m} \bar{P}_{lm}(1) e^{im\Delta\lambda} \sum_n W_{lm}^{nm} \bar{P}_{nm}(\cos \theta'),$$

using (A.7b) and (A.10a)

$$\begin{aligned} &= \sum_{l,m} \delta_{m0} \sqrt{2l+1} e^{im\Delta\lambda} \sum_n W_{lm}^{nm} \bar{P}_{nm}(\cos \theta'), \\ &= \sum_{l,n} \sqrt{2l+1} W_{l0}^{n0} \bar{P}_{n0}(\cos \theta'), \\ w(0, \theta') &= \sum_{l,n} \sqrt{(2l+1)(2n+1)} W_{l0}^{n0} P_n(\cos \theta'), \end{aligned}$$

also when  $\theta = 0$ ,  $\theta'$  becomes the spherical distance  $\psi$  between the two points, and therefore the above equation can be re-written in the following form:

$$w(0, \psi) = \sum_{l,n} \sqrt{(2l+1)(2n+1)} W_{l0}^{n0} P_n(\cos \psi), \quad (2.28a)$$

which reveals the isotropic nature of the latitude-dependent anisotropic weighting function at the pole (cf. Figure 3.4).

The smoothing kernel associated with (2.27d) is given as

$$\begin{aligned} b(\theta, \psi, A) &= \frac{w(\theta, \psi, A)}{\frac{1}{4\pi} \int_{\Omega'} w(\theta, \psi, A) d\Omega'}, \\ &= \sum_{l,m} Y_{lm}(\theta, \lambda) \sum_n \frac{W_{lm}^{nm}}{\bar{w}(\theta, \psi, A)} Y_{nm}^*(\theta', \lambda'), \\ &= \sum_{l,m} Y_{lm}(\theta, \lambda) \sum_n B_{lm}^{nm} Y_{nm}^*(\theta', \lambda'), \end{aligned} \quad (2.29) \quad (2.30)$$

where  $\bar{w}(\theta, \psi, A)$  will have the same form as in (2.25c).

An interesting case develops when the off-diagonal elements of each of the  $m$  blocks of the spectrum of the weighting function become zero. Then the spectrum of the weighting function takes the following form:

$$w(\theta, \psi, A) = \sum_{l,m} Y_{lm}(\theta, \lambda) W_{lm}^{lm} Y_{lm}^*(\theta', \lambda'), \quad (2.31a)$$

and the normalisation factor becomes

$$\begin{aligned} \frac{1}{4\pi} \int_{\Omega'} w(\theta, \psi, A) d\Omega' &= \sum_{l,m} Y_{lm}(\theta, \lambda) W_{lm}^{lm} \frac{1}{4\pi} \int_{\Omega'} Y_{lm}^*(\theta', \lambda') d\Omega', \\ &= \sum_{l,m} Y_{lm}(\theta, \lambda) W_{lm}^{lm} \delta_{l0} \delta_{m0}, \\ &= W_{00}^{00}, \end{aligned} \quad (2.31b)$$

which implies that the sum of the weighting function is independent of the latitude. The underlying meaning is that no matter which latitude the kernel is located, the sum of the weights of the function must be a constant. This is an important design criteria in the design of such latitude-dependent anisotropic weighting functions. Therefore, the smoothing kernel becomes

$$\begin{aligned} b(\theta, \psi, A) &= \sum_{l,m} Y_{lm}(\theta, \lambda) \frac{W_{lm}^{lm}}{W_{00}^{00}} Y_{lm}^*(\theta', \lambda'), \\ &= \sum_{l,m} Y_{lm}(\theta, \lambda) B_{lm}^{lm} Y_{lm}^*(\theta', \lambda'). \end{aligned} \quad (2.31c)$$

Latitude-dependent anisotropic smoothing kernels are the most widely designed kernels in the GRACE community, for example, Han et al. [2005]; Chen et al. [2006]; Swenson and Wahr

[2006b]; Kusche et al. [2009]. This should not be surprising, because of the equispaced observations of the satellite geodetic observables in the longitude directions lend themselves to latitude-dependent anisotropic smoothing kernels.

Smoothing a field with these kernels is carried out in the following equations:

$$\bar{f}(\theta, \lambda) = \frac{1}{4\pi} \int_{\Omega'} f(\theta', \lambda') b(\theta, \psi, A) d\Omega', \quad (2.32a)$$

$$\begin{aligned} &= \sum_{p,q} F_{pq} \sum_{l,m} Y_{lm}(\theta, \lambda) \sum_n B_{lm}^{nm} \frac{1}{4\pi} \int_{\Omega'} Y_{pq}(\theta', \lambda') Y_{nm}^*(\theta', \lambda') d\Omega', \\ &= \sum_{l,m} Y_{lm}(\theta, \lambda) \sum_n B_{lm}^{nm} F_{nm} \end{aligned} \quad (2.32b)$$

$$\bar{F}_{lm} = \sum_n B_{lm}^{nm} F_{nm}. \quad (2.32c)$$

Similarly, if the smoothing kernel has a diagonal form as in (2.31c), then the spectrum of the smoothed field will be

$$\bar{f}(\theta, \lambda) = \sum_{l,m} Y_{lm}(\theta, \lambda) B_{lm}^{lm} F_{lm}, \quad (2.33a)$$

$$\bar{F}_{lm} = B_{lm}^{lm} F_{lm}. \quad (2.33b)$$

## §2.4 AMPLITUDE AND PHASE SPECTRUM OF THE FILTERED FIELD

The spherical harmonic spectrum  $F_{lm}$  of a field  $f(\theta, \lambda)$  is a complex number, and so it can be re-written in terms of the magnitude and argument of a complex number as follows:

$$F_{lm} = A_{lm} e^{i\phi_{lm}}, \quad (2.34a)$$

$$A_{lm} = |F_{lm}| = \sqrt{\text{Re}(F_{lm})^2 + \text{Im}(F_{lm})^2}, \quad (2.34b)$$

$$\phi_{lm} = \arg(F_{lm}) = \arctan\left(\frac{\text{Im}(F_{lm})}{\text{Re}(F_{lm})}\right). \quad (2.34c)$$

Further, substituting (2.34a) in (2.1a) gives

$$\begin{aligned} f(\theta, \lambda) &= \sum_{l,m} A_{lm} e^{i\phi_{lm}} \bar{P}_{lm}(\cos \theta) e^{i(m\lambda)}, \\ &= \sum_{l,m} A_{lm} \bar{P}_{lm}(\cos \theta) e^{i(m\lambda + \phi_{lm})}. \end{aligned} \quad (2.34d)$$

In harmonic analysis, the representation in (2.34a) is called amplitude and phase spectrum of the field. The amplitude and phase spectrum is not a frequently used representation for spherical harmonic spectra in geodesy. It is quite often used in the Fourier analysis of time-series, where the idea of phase of the frequency is easily interpretable. Whereas the phase of the spherical harmonic spectrum has a spatial connotation to it, and therefore, it is not straightforward to interpret it. Notwithstanding these difficulties in interpretation, we

form the amplitude and phase spectrum of the filtered spectrum  $\bar{F}_{lm}$ .

$$\bar{F}_{lm} = \sum_{n,k} B_{lm}^{nk} F_{nk} = \bar{A}_{lm} e^{i\bar{\phi}_{lm}},$$

$$\bar{A}_{lm} = |\bar{F}_{lm}| = \left[ \text{Re} \left( \sum_{n,k} B_{lm}^{nk} F_{nk} \right)^2 + \text{Im} \left( \sum_{n,k} B_{lm}^{nk} F_{nk} \right)^2 \right]^{\frac{1}{2}}, \quad (2.35a)$$

$$\bar{\phi}_{lm} = \arg(\bar{F}_{lm}) = \arctan \left( \frac{\text{Im} \left( \sum_{n,k} B_{lm}^{nk} F_{nk} \right)}{\text{Re} \left( \sum_{n,k} B_{lm}^{nk} F_{nk} \right)} \right). \quad (2.35b)$$

From (2.35a) and (2.35b), we see that the amplitude and phase change completely after the spectrum is filtered. Further, the filtered and unfiltered spectra share a non-linear relationship between them. However, they represent only the general case of filtering with the spectrum of a completely inhomogeneous and anisotropic smoothing kernel. Now, we will extend this to the different classes of filters and see what happens to the amplitude and phase of the corresponding filtered spectra.

#### *Homogeneous and isotropic*

The spectrum of the field filtered with a homogeneous isotropic smoothing is given by

$$\bar{F}_{lm} = \frac{B_l}{2l+1} F_{lm}. \quad (2.17b)$$

A point to be noted here is that  $B_l$  is a real-valued variable, because the smoothing kernel  $b(\psi)$  and the Legendre polynomials  $P_l(\psi)$  in (2.16b) are both real-valued functions. Thus,  $B_l$  are real numbers and act as scaling factors for the complex coefficients  $F_{lm}$ , and therefore the amplitude spectrum takes the following form:

$$\begin{aligned} \bar{A}_{lm} &= \left| \frac{B_l}{2l+1} F_{lm} \right|, \\ &= \left| \frac{B_l}{2l+1} \right| |F_{lm}|, \\ &= \frac{|B_l|}{2l+1} A_{lm}, \end{aligned} \quad (2.36a)$$

where  $|B_l|$  denotes the absolute value of the spectral weight  $B_l$ . Now the phase spectrum of the filtered field is

$$\bar{\phi}_{lm} = \arg \left( \frac{B_l}{2l+1} F_{lm} \right),$$

after factoring out  $2l+1$ , we get

$$= \arctan \left( \frac{\text{Im}(B_l F_{lm})}{\text{Re}(B_l F_{lm})} \right) = \arctan \left( \frac{B_l \text{Im}(F_{lm})}{B_l \text{Re}(F_{lm})} \right), \quad \because B_l \text{ is a real number.}$$

Although the weights  $B_l$  are scalar and get factored out, the phase is still affected by the sign of the weights  $B_l$ . This is written as follows

$$\begin{aligned}
 &= \arctan\left(\frac{\operatorname{sgn}(B_l) \operatorname{Im}(F_{lm})}{\operatorname{sgn}(B_l) \operatorname{Re}(F_{lm})}\right), \\
 &= \arg(\operatorname{sgn}(B_l) F_{lm}). \\
 \therefore \quad \bar{\phi}_{lm} &= \begin{cases} \phi_{lm}, & B_l \geq 0 \\ \phi_{lm} - \pi, & B_l < 0 \end{cases}, \tag{2.36b}
 \end{aligned}$$

which clearly indicates that the homogeneous isotropic smoothing kernel affects both the amplitude and phase of the spherical harmonic spectrum. Nevertheless, the phase is unaffected if the spectral weights of the homogeneous isotropic filter are all positive, but it is rotated by an angle of  $\pi$  for the degrees whose spectral weights are negative. Finally, the smoothed field in terms of amplitude and phase spectrum reads as

$$\begin{aligned}
 \bar{f}(\theta, \lambda) &= \sum_{l,m} \bar{A}_{lm} \bar{P}_{lm}(\cos \theta) e^{i(m\lambda + \bar{\phi}_{lm})}, \\
 &= \sum_{l,m} \frac{|B_l|}{2l+1} A_{lm} \bar{P}_{lm}(\cos \theta) e^{im\lambda} \begin{cases} e^{i\phi_{lm}}, & B_l \geq 0 \\ e^{i(\phi_{lm} - \pi)}, & B_l < 0 \end{cases}. \tag{2.36c}
 \end{aligned}$$

#### Homogeneous and anisotropic

Again, we start with the spectrum of the smoothed field, (2.20b),

$$\begin{aligned}
 \bar{F}_{lm}(\theta, \lambda) &= B_{lm}(\theta, \lambda) F_{lm}, \tag{2.20b} \\
 \bar{A}_{lm}(\theta, \lambda) &= |\bar{F}_{lm}(\theta, \lambda)|, \\
 &= |B_{lm}(\theta, \lambda) F_{lm}|
 \end{aligned}$$

where  $B_{lm}(\theta, \lambda)$  and  $F_{lm}$  are both complex, and hence  $A_{lm}$  and  $\bar{A}_{lm}$  are related as follows:

$$\begin{aligned}
 \bar{A}_{lm}(\theta, \lambda) &= |B_{lm}(\theta, \lambda)| |F_{lm}|, \\
 &= |B_{lm}(\theta, \lambda)| A_{lm}, \tag{2.37a}
 \end{aligned}$$

Now, the phase of the spectrum of the smoothed field is given by

$$\begin{aligned}
 \bar{\phi}_{lm}(\theta, \lambda) &= \arg(\bar{F}_{lm}), \\
 &= \arg(B_{lm}(\theta, \lambda) F_{lm}), \\
 &= \arg(B_{lm}(\theta, \lambda)) + \arg(F_{lm}).
 \end{aligned}$$

Setting  $\arg(B_{lm}(\theta, \lambda))$  as  $\Phi_{lm}(\theta, \lambda)$  we get

$$\bar{\phi}_{lm} = \Phi_{lm}(\theta, \lambda) + \phi_{lm}. \tag{2.37b}$$

In the above equation, it is evident that the phase of  $F_{lm}$  is further rotated by  $\Phi_{lm}(\theta, \lambda)$ . This is in contrast to the isotropic filter, where there was either no rotation or a rotation

of  $\pi$ . However, here there is a range of rotations from 0 to  $2\pi$ . Also, the phase of the unsmoothed and the smoothed spectra are linearly related.

Rewriting the smoothed field in terms of the amplitude and phase spectrum, we get

$$\begin{aligned}\bar{f}(\theta, \lambda) &= \sum_{l,m} \bar{A}_{lm}(\theta, \lambda) e^{i\bar{\phi}_{lm}(\theta, \lambda)}, \\ &= \sum_{l,m} |B_{lm}(\theta, \lambda)| A_{lm} e^{i(\phi_{lm} + \Phi_{lm}(\theta, \lambda))}.\end{aligned}\tag{2.37c}$$

#### *Location-dependent and isotropic*

Starting with the filtered spectrum (2.23b) we have,

$$\bar{F}_{lm}(\theta, \lambda) = \frac{B_l(\theta, \lambda)}{2l+1} F_{lm},\tag{2.23b}$$

where the coefficients  $B_l(\theta, \lambda)$ , by virtue of (2.22b), will all be real-valued numbers. Therefore, they will behave similar to the homogeneous isotropic kernel.

$$\begin{aligned}\bar{A}_{lm}(\theta, \lambda) &= \left| \frac{B_l(\theta, \lambda)}{2l+1} F_{lm} \right|, \\ &= \frac{|B_l(\theta, \lambda)|}{2l+1} A_{lm},\end{aligned}\tag{2.38a}$$

$$\begin{aligned}\bar{\phi}_{lm}(\theta, \lambda) &= \arg\left(\frac{B_l(\theta, \lambda)}{2l+1} F_{lm}\right), \\ &= \arg(\text{sgn}(B_l(\theta, \lambda)) F_{lm}), \\ &= \begin{cases} \phi_{lm}, & B_l(\theta, \lambda) \geq 0 \\ \phi_{lm} - \pi, & B_l(\theta, \lambda) < 0 \end{cases}.\end{aligned}\tag{2.38b}$$

Therefore the smoothed field becomes

$$\begin{aligned}\bar{f}(\theta, \lambda) &= \sum_{l,m} \bar{A}_{lm} \bar{P}_{lm}(\cos \theta) e^{i(m\lambda + \bar{\phi}_{lm})}, \\ &= \sum_{l,m} \frac{|B_l(\theta, \lambda)|}{2l+1} A_{lm} \bar{P}_{lm}(\cos \theta) e^{im\lambda} \begin{cases} e^{i\phi_{lm}}, & B_l(\theta, \lambda) \geq 0 \\ e^{i(\phi_{lm} - \pi)}, & B_l(\theta, \lambda) < 0 \end{cases}.\end{aligned}\tag{2.38c}$$

#### *Latitude-dependent and isotropic*

The latitude-dependent isotropic smoothing kernels will show a similar behaviour as the location-dependent isotropic smoothing kernel, because  $B_l(\theta)$  is also a real-valued number that forms a real-valued function  $b(\theta, \psi)$  with the Legendre polynomials  $P_l(\cos \psi)$ . Therefore,

$$\bar{F}_{lm} = B_l(\theta) F_{lm},\tag{2.26c}$$

$$\bar{A}_{lm}(\theta) = |B_l(\theta)| A_{lm},\tag{2.39a}$$

$$\bar{\phi}_{lm} = \begin{cases} \phi_{lm}, & B_l(\theta) \geq 0 \\ \phi_{lm} - \pi, & B_l(\theta) < 0 \end{cases}\tag{2.39b}$$

$$\bar{f}(\theta, \lambda) = \sum_{l,m} \frac{|B_l(\theta)|}{2l+1} A_{lm} \bar{P}_{lm}(\cos \theta) e^{im\lambda} \begin{cases} e^{i\phi_{lm}}, & B_l(\theta) \geq 0 \\ e^{i(\phi_{lm}-\pi)}, & B_l(\theta) < 0 \end{cases}. \quad (2.39c)$$

#### Latitude-dependent and anisotropic

The general form of the filtered spectrum of the field smoothed with a latitude-dependent anisotropic kernel (2.32c) has the same form as the field filtered with a location-dependent anisotropic filter kernel (2.9b), and therefore, the amplitude and phase have the same behaviour.

$$\bar{F}_{lm} = \sum_n B_{lm}^{nm} F_{nm}, \quad (2.32c)$$

$$\bar{A}_{lm} = |\bar{F}_{lm}|, \quad (2.40a)$$

$$\bar{\phi}_{lm} = \arg(\bar{F}_{lm}), \quad (2.40b)$$

$$\bar{f}(\theta, \lambda) = \sum_{l,m} \bar{A}_{lm} \bar{P}_{lm}(\cos \theta) e^{i(m\lambda + \bar{\phi}_{lm})}. \quad (2.40c)$$

In the special case that the spectrum is diagonal-only (cf. (2.33b)), two cases arise depending on whether the  $B_{lm}^{lm}$  is a real number, i.e., real-valued [e.g., Han et al., 2005] or complex. The filtered spectrum is given by

$$\bar{F}_{lm} = B_{lm}^{lm} F_{lm}. \quad ((2.33b))$$

If the spectral weights are complex, then the amplitude and phase are given by

$$\bar{A}_{lm} = |B_{lm}^{lm}| A_{lm}, \quad (2.41a)$$

$$\bar{\phi}_{lm} = \arg(B_{lm}^{lm} F_{lm}) = \Phi_{lm}^{lm} + \phi_{lm}, \quad (2.41b)$$

where  $\Phi_{lm}^{lm}$  is the phase of  $B_{lm}^{lm}$ . In the case that  $B_{lm}^{lm}$  are real then the amplitude and phase behave the same way as in the case of homogeneous isotropic filters (cf. (2.36)).

$$\bar{A}_{lm} = |B_{lm}^{lm}| A_{lm}, \quad (2.42a)$$

$$\bar{\phi}_{lm} = \begin{cases} \phi_{lm}, & B_{lm}^{lm} \geq 0 \\ \phi_{lm} - \pi, & B_{lm}^{lm} < 0 \end{cases}, \quad (2.42b)$$

$$\bar{f}(\theta, \lambda) = \sum_{l,m} |B_{lm}^{lm}| A_{lm} \bar{P}_{lm}(\cos \theta) e^{im\lambda} \begin{cases} e^{i(\phi_{lm} + \Phi_{lm}^{lm})}, & B_{lm}^{lm} \in \mathbb{C}, \\ e^{i\phi_{lm}}, & B_{lm}^{lm} \in \mathbb{R} \mid B_{lm}^{lm} \geq 0, \\ e^{i(\phi_{lm} - \pi)}, & B_{lm}^{lm} \in \mathbb{R} \mid B_{lm}^{lm} < 0, \end{cases} \quad (2.42c)$$

In the preceding discussion we saw how the different filters affect both the amplitude and phase. The amplitude is always affected due to filtering, and in most cases this amounts to scaling of the unfiltered amplitude. In others the relationship is non-linear. The phase of the spectrum is also affected due to filtering, which in the case of isotropic filter kernels have a distinct character: The phase is rotated by an angle of  $\pi$  if the spectral weight is negative

and is unaffected when the spectral weight is positive. In the case of anisotropic kernels there is an additional phase rotation if the amplitude of the filtered and unfiltered fields are linearly related. This linear and non-linear relationships should not come as a surprise as they are inherent in the definitions of the polar form of the spectrum. We will discuss this concept further and explicate the influence of the polar form in the choice of filters in chapters 5 and 6.



OUR aim in this chapter will be to demonstrate the design of a few well-known smoothing kernels. We know, now, that every smoothing kernel provides a weight to the data point depending on its distance and orientation from the calculation point, but with the sole aim of getting a smoothed value. We will start our discussion by looking to trivial designs of smoothing kernels, which leads us to a *qualitative bound* for the quality, *smoothness*. Within these bounds a number of kernels can be designed, and we will discuss three ways of designing the kernels: *deterministic*, *stochastic* and *empirical/data-driven* methods. Thereafter, we will demonstrate the deterministic designs of the common homogeneous isotropic smoothing kernels used in the GRACE community, wherein it will become clear that they are the easiest class of smoothing kernels to design. We will then extend the design ideas to latitude-dependent anisotropic smoothing kernels, where we will also introduce the stochastic and data-driven methods.

### §3.1 SOME TRIVIAL DESIGNS OF SMOOTHING KERNELS

The easiest smoothing kernel can be designed by taking a weighting function that provides the same weights for all the data points without any discrimination. Therefore, such a function will be a homogeneous isotropic kernel that can be formulated as follows:

$$w_{\Omega}(\psi) = 1, \quad \forall \psi \in [0, \pi]. \quad (3.1a)$$

Now, using the above equation in (2.5a), we get

$$\bar{f}(\theta, \lambda) = \frac{\frac{1}{4\pi} \int_{\Omega'} f(\theta', \lambda') w_{\Omega}(\psi) d\Omega'}{\frac{1}{4\pi} \int_{\Omega'} w_{\Omega}(\psi) d\Omega'}, \quad (3.1b)$$

$$= \frac{\frac{1}{4\pi} \int_{\Omega'} f(\theta', \lambda') d\Omega'}{\frac{1}{4\pi} \int_{\Omega'} d\Omega'}, \quad (3.1c)$$

$$\bar{f}_{\Omega}(\theta, \lambda) = F_{00}. \quad (3.1d)$$

which is the same as the spatial mean of the field. It is also obvious from the above equations that

$$b_{\Omega} = w_{\Omega}. \quad (3.2)$$

The other trivial smoothing kernel design is the one that provides weight only to the calculation point, and therefore, reproduces the unsmoothed value of the calculation point. Such a smoothing kernel is the *Dirac's delta function* on the sphere

$$w_{\delta}(\psi) = \delta(\psi) = \delta(\theta, \lambda, \theta', \lambda'), \quad (3.3a)$$

where  $\delta(\cdot, \cdot)$  is the Dirac's delta function on the sphere [Freedman and Schreiner, 2009].

$$\frac{1}{4\pi} \int_{\Omega'} \delta(\psi) d\Omega' = \begin{cases} 1, & \psi = 0 \Rightarrow (\theta, \lambda) = (\theta', \lambda') \\ 0, & \text{elsewhere} \end{cases}, \quad (3.3b)$$

and its spectrum is

$$\delta(\psi) = \sum_{l,m} Y_{lm}(\theta, \lambda) Y_{lm}^*(\theta', \lambda'). \quad (3.3c)$$

Smoothing a field  $f(\cdot)$  with the  $w_{\delta}$  gives

$$\bar{f}(\theta, \lambda) = \frac{\frac{1}{4\pi} \int_{\Omega'} f(\theta', \lambda') w_{\delta}(\psi) d\Omega'}{\frac{1}{4\pi} \int_{\Omega'} w_{\delta}(\psi) d\Omega'}, \quad (3.3d)$$

$$\bar{f}_{\delta}(\theta, \lambda) = f(\theta, \lambda) = \sum_{l,m} F_{lm} Y_{lm}(\theta, \lambda). \quad (3.3e)$$

Again from the above equations, similar to (3.2), it can be deduced that the smoothing function which reproduces the calculation point is also the same as its weighting function:

$$b_{\delta} = w_{\delta}. \quad (3.4)$$

Although these two weighting functions are trivial from the design point of view, their smoothing kernels, and subsequently their smoothed values, set up a platform for understanding the design of smoothing kernels. The smoothed values  $\bar{f}_{\Omega}(\cdot)$  and  $\bar{f}_{\delta}(\cdot)$  form a *qualitative* bound for the smoothed values  $\bar{f}(\cdot)$ , and therefore, also for the smoothing kernels: There cannot be a smoother value than  $\bar{f}_{\Omega}(\cdot)$ , and a more unsmoothed value than  $\bar{f}_{\delta}(\cdot)$ . In a similar vein, no smoothing kernel can smoothen a field  $f(\cdot)$  smoother than  $b_{\Omega}(\psi)$ , and similar is the argument for  $b_{\delta}(\psi)$ . Therefore, any smoothing kernel that we design will generate a smoothed field  $\bar{f}(\cdot)$ , whose smoothness will linger between  $\bar{f}_{\Omega}(\cdot)$  and  $\bar{f}_{\delta}(\cdot)$ .

Another interesting aspect to these two trivial smoothing kernels are the corresponding smoothed spectra, (3.1d) and (3.3e). While the spectrum of  $\bar{f}_{\Omega}(\cdot)$  is just the degree zero value  $F_{00}$  that of  $\bar{f}_{\delta}(\cdot)$  is the complete set  $F_{lm}$ . In other words, the mean value of the entire spherical domain  $\Omega$  is concentrated in one spherical harmonic coefficient,  $F_{00}$ , while the value

of a point  $(\theta, \lambda)$  is distributed over the entire spectrum  $F_{lm}$ . This is indeed the *principle of uncertainty* in signal processing [Strang, 1986, pg. 313–314], which states that a function cannot be simultaneously localised both in the signal domain and the spectral domain. This is extended to the case of the sphere by Freedman and Schreiner [2009, sec. 7.3, pg. 343–357]. Thus, it should be noted that all the smoothing kernels that will be developed will lie between these two trivial kernels.

### The ideal low-pass filter

In practice, it is rather straightforward to realise the smoothing kernel  $b_\Omega$ , but not so with  $b_\delta$  as they require infinite number of degrees to reproduce the point value. For this reason,  $b_\delta$  is often approximated by expanding the spherical harmonics to a finite value of spherical harmonic degree, which then becomes

$$b_\delta \approx \delta_L(\psi) = \sum_{l=0}^L \sum_{m=-l}^l Y_{lm}(\theta, \lambda) Y_{lm}^*(\theta', \lambda'). \quad (3.5a)$$

The approximate kernel is called the *Shannon kernel* [Freedman and Schreiner, 2009]. The first thing that we observe about  $\delta_L(\psi)$  in (3.5a) is that it is band-limited ( $\{l \in \mathbb{N} | 0 \leq l \leq L\}$ ), and the kernel  $\delta_L(\psi)$  can be rewritten in terms of the spectrum of  $\delta(\psi)$  as

$$\delta_L(\psi) = \sum_{l,m} B_l Y_{lm}(\theta, \lambda) Y_{lm}^*(\theta', \lambda'), \quad (3.5b)$$

where

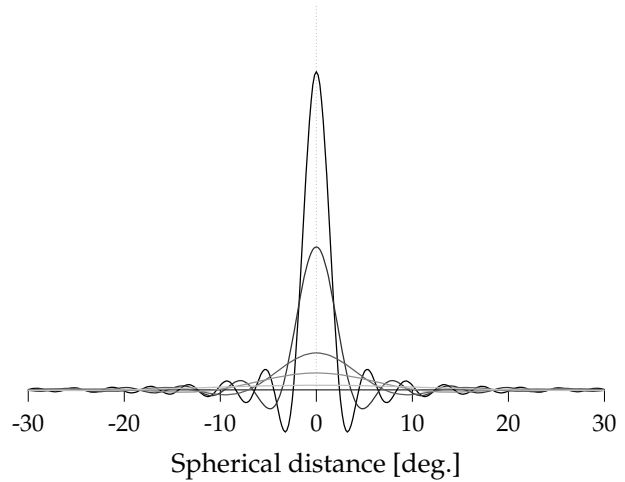
$$B_l = \begin{cases} 1, & \{l \in \mathbb{N} | 0 \leq l \leq L\} \\ 0, & \text{otherwise} \end{cases} \quad (3.5c)$$

are the spectral weights that relate the kernel  $\delta_L(\psi)$  with  $\delta(\psi)$ . These weights act as a filter and suppress the degrees higher than  $l = L$ , which is why it is also called a box-car filter. By virtue of its filtering characteristics it produces a filtered value  $\bar{f}(\cdot)$  of  $f(\cdot)$ , and since it omits the higher frequencies,  $\bar{f}(\cdot)$  is a *low-pass* filtered smooth value. Here again, we note that even in the band-limited case,  $\delta_L(\psi)$  will form the bound for the most unsmoothed value for the given band-limit, because it uses all the information provided within the band-limit ( $0 \leq l \leq L$ ). This characteristic of the box-car makes it the *ideal low-pass filter* in the spherical harmonic spectral domain [Jekeli, 1981].

In the end, we are able to merge together two synonymous ideas – low-pass filtering and smoothing – into a single idea: smoothing blurs the (noisy) high frequency details, which is also the effect of low-pass filters. The above discussion has given us an important hint for designing the smoothing kernel, and that is a smoothing operator is the same as a low-pass filter and it must, therefore, suppress the higher frequencies. Nevertheless, we must first identify whether there is a need for designing a new filter when we have an ideal low-pass filter in hand.

The need arises from the spatial form of the ideal low-pass filter (Figure 3.1), which does not become zero but oscillates around it. These oscillations are an artefact of the truncation of the spectrum at degree  $L$  as harmonic functions cannot handle sudden jumps in the weights, and these oscillations are the well known *Gibbs phenomenon* [Hamming, 1989]. Due to these

**Figure 3.1:** Shannon kernel  $\delta_L(\psi)$  for  $L = 10, 20, 30, 60, 90$  (light to dark colour order). Notice the oscillating nature of the kernel around zero.



oscillating weights the ideal low-pass filter changes the sign of the signal, and, further, as they take a long distance to dampen, they bring data from locations that are far off from the calculation point. In chapters 4 and 5 it will be demonstrated that these are undesirable characteristics, and therefore, the ideal low-pass filter is not “ideal”. Thus, there is a need for designing smoothing kernels, keeping in mind the qualitative bound and the idea of low-pass filtering while designing them.

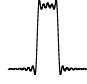


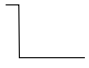
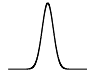




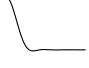
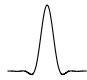

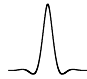

### §3.2 CLASSIFICATION OF FILTER DESIGN

Filters on the sphere have been designed in different ways, which can largely be classified into *deterministic* [e.g., Jekeli, 1981; Sardeshmukh and Hoskins, 1984; Zhang et al., 2009]; *stochastic* [e.g., Swenson and Wahr, 2002; Kusche, 2007; Klees et al., 2008]; *data-driven* [e.g., Swenson and Wahr, 2006b; Wouters and Schrama, 2007; Rangelova et al., 2007]; and *variational calculus* [Khalid et al., 2011] methods. This classification is based on the principles behind the design of the filters, but another attempt has been made by Werth et al. [2009] to classify filter design based on the parameters used.

#### Deterministic filtering

Deterministic filter design is by far the most widely used method for designing filters, and it is characterised by analytical functions that determine the weights of filter functions either in the spatial domain or in the spectral domain. The earliest known deterministic kernels come from Pellinen [1966]; Jekeli [1981], who adapted the deterministic filters from harmonic analysis on the line to smooth gravity anomalies; and Sardeshmukh and Hoskins [1984] designed a few kernels for filtering atmospheric fields. However, after the launch of the GRACE satellite mission a number of deterministic filters have been proposed [e.g., Longuevergne et al., 2010; Zhang et al., 2009; Han et al., 2005], but the most prominent of them all, in GRACE data processing, has been the homogeneous and isotropic *Gaussian* smoothing operator designed by Jekeli [1981]. In table 3.1, formulae, spatial cross-sections and spectral weights of a few other well-known homogeneous isotropic deterministic windows used in physical geodesy and allied fields are depicted.

**Table 3.1:** Definitions, and spectral and spatial cross-sections of some deterministic homogeneous isotropic windows.

Filter	Definition	Spatial	Spectral
Pellinen	$B_l = \frac{1}{2l+1} \frac{P_{l-1}(\cos \psi_0) - P_{l+1}(\cos \psi_0)}{1 - \cos \psi_0}$		
Box-car	$B_l = \begin{cases} 1, & l \in \mathbb{N} \cap [0, l_c] \\ 0, & \text{otherwise} \end{cases}$		
Gauss	$b(\psi) = \frac{a}{\sinh a} e^{a \cos \psi}, \quad a = \frac{\ln(n)}{1 - \cos \psi_0}, \quad n \in \mathbb{R}_{>1}$		
Diffusion	$B_l = \exp \left\{ - \left( \frac{l(l+1)}{l_c(l_c+1)} \right)^k \right\}, \quad k \in \mathbb{N}^*$		
Spatial sine	$w(\psi) = \begin{cases} \cos^k \left( \frac{\pi \psi}{2 \psi_0} \right), & \psi \in \mathbb{R} \cap [0, \psi_0], \quad k \in \mathbb{N}^* \\ 0, & \text{otherwise} \end{cases}$		
Spectral cosine	$B_l = \begin{cases} 1, & l \in \mathbb{N} \cap [0, l_s] \\ \cos^k \left( \frac{\pi}{2} \frac{l - l_s}{l_c - l_s} \right), & l \in \mathbb{N} \cap (l_s, l_c], \quad k \in \mathbb{N}^* \\ 0, & \text{otherwise} \end{cases}$		
Butterworth	$B_l = \frac{1}{\sqrt{1 + \left( \frac{l}{l_c} \right)^{2k}}}, \quad k \in \mathbb{N}^*$		

### Stochastic filter design

Stochastic filtering, unlike deterministic filtering, utilises the behaviour of signal and noise described by their respective covariances to filter out noise. However, the difficulty in designing the stochastic filters lies in the knowledge of signal and noise covariances. In GRACE data processing, Swenson and Wahr [2002] demonstrated the stochastic filter design principles by fine-tuning filter kernels according to a given error budget, which included satellite error and leakage error. This they demonstrated for the case of regional averages, where they used Gaussian functions of different filter radii as the signal covariance model. This was extended by Seo and Wilson [2005] to use signal covariance information from geophysical models. Sasgen et al. [2006] used these principles but modelled the signal covariance of the time-variable gravity field as a *power law*, similar to the *Kaula* rule for static gravity field [Kaula, 1966, pg. 98]. The power law signal covariance model is a homogeneous isotropic covariance model derived from the observation that the power of the gravity field signal

decreases exponentially with increasing spherical harmonic degree. Sasgen et al. [2006] also modelled their noise covariance in terms of a homogeneous isotropic function, and both the signal and noise covariance modelling was carried out using GRACE data. Kusche [2007] used a fully populated noise covariance matrix, although simulated, in place of the isotropic noise covariance of Sasgen et al. [2006]. Stochastic filtering with fully populated noise and signal covariance matrices was successfully demonstrated by Klees et al. [2008], who computed the signal covariance matrix from the complete GRACE dataset by iterative techniques.

### Data-driven filtering methods

Data-driven methods of filtering are those in which the filter designed is dataset-specific. Such a filter designed for one dataset might not filter other datasets with the same efficacy. In the GRACE community, the most widely used *destriping* filter proposed by Swenson and Wahr [2006b] is a modified form of moving polynomial smoothing, also known as the *Suavity's-Golay* filter [Savitzky and Golay, 1964]. Other data-driven filters used in the GRACE community are *principal component analysis* (PCA) [Wouters and Schrama, 2007; Rangelova et al., 2007] and *independent component analysis* (ICA) [Frappart et al., 2011], which are standard tools in climate data analysis. PCA and ICA are empirical techniques based on orthogonal data transformation principles, and are mainly used for studying the patterns underlying the datasets. In addition to these methods Davis et al. [2008] employ a statistical filter on the time-series of GRACE data, where they statistically test the goodness of fit of *a priori* known periodic components and linear trend to the time-series of the dataset.

### Filter design by variational calculus methods

Variational calculus methods of filtering are a standard feature of geophysical inversion techniques [Wu et al., 2009]. In fact the stochastic filter design is a variational calculus method, but here we distinguish them both for the sake of convenience. We will only denote filters that use stochastic information—signal and noise covariance information—as stochastic filters. Variational calculus principles have also been used to design filters that do not use any stochastic information. For example, Khalid et al. [2011] designed a homogeneous isotropic low-pass filter by formulating the filtering problem on the sphere as a *Slepian* problem on the sphere [Albertella et al., 1999]. The central idea is to concentrate the smoothing of the data within the prescribed filter radius in order to avoid leakage problems. Nevertheless, the design process of such a filter is complex, and for this reason Khalid et al. [2011] provide an analytic expression after non-linear fitting to a series of such low-pass filters.

In the following sections we will discuss the principle behind the design of the three of the most commonly used filters in the GRACE community: the Gaussian smoothing operator [Jekeli, 1981], the *destriping* filter [Swenson and Wahr, 2006b] and the *DDK* filter [Kusche, 2007]. Further, we will use these three filters to expound the filter behaviour in the succeeding chapters.

## §3.3 GAUSSIAN SMOOTHING OPERATOR

The Gaussian function on the sphere, which is the basis of the Gaussian smoothing operator, is introduced by Fisher [1953] in the context of statistical analysis of directional data. However, Fisher et al. [1987] inform that it was already introduced in a more general form as early as

1905 by Paul Langevin in the context of magnetism studies. Jekeli [1981] introduced it as a smoothing operator among others for smoothing observed gravity anomalies on the sphere, and thereafter Wahr et al. [1998] modified it to the needs of the GRACE data processing.

The Gaussian weighting function on the sphere is written as

$$w(\psi) = e^{-a(1-\cos\psi)} = e^{-2a \sin^2 \frac{\psi}{2}}, \quad (3.6a)$$

but it degenerates to

$$w(\psi) = e^{-a \frac{\psi^2}{2}}, \quad \psi \text{ is small}, \quad (3.6b)$$

which is the well known form of the Gaussian distribution function. For this reason, Fisher [1953] argues that the form in (3.6a) should in fact be the superset of the Gaussian functions, and he further reduces the form in (3.6a) to

$$w(\psi) \propto e^{a \cos \psi}. \quad (3.6c)$$

In addition he also imposes the condition that  $a \geq 0$  for the function to generate a bell shaped curve. Comparing (3.6a) and (3.6c) it is clear that the proportionality constant is  $e^{-a}$ . Therefore, rewriting (3.6a) we get

$$w(\psi) = e^{-a} e^{a \cos \psi}. \quad (3.6d)$$

Now, the corresponding smoothing operator is given by

$$b(\psi) = \frac{a}{\sinh a} e^{a \cos \psi}, \quad (3.6e)$$

with the normalising constant being

$$\bar{w}(\psi) = \frac{1}{4\pi} \int_{\Omega'} e^{-a} e^{a \cos \psi} d\Omega' = \frac{1}{a} e^{-a} \sinh a. \quad (3.6f)$$

From the above set of equations, it is clear that the weight of the Gaussian smoothing operator depends on the parameter  $a$  and the cosine of the spherical distance  $\psi$  between the calculation and data point, where the parameter  $a$  has a similar function as the variance in the case of the univariate Gaussian distribution. Thus, it is clear that  $a$  controls the width, and hence the shape, of the operator. One of the most important characteristics of this operator is that it becomes zero only asymptotically, thus remains positive. Another important characteristic is that the shapes of both its spatial and its spectral form remain the same [Wahr et al., 1998].

In order to construct this window, the value of the parameter  $a$  needs to be ascertained. Wahr et al. [1998] compute the value of  $a$  by fixing a distance at which the weight function drops to one-half of the weight of the smoothing operator at the calculation point. Here, this computation will be demonstrated, but for any desired fraction ( $1/n$ ) of the weight at the calculation point ( $w(\psi=0)$ ). Let  $\psi_0$  be the distance at which the Gaussian weight function drops to the desired fraction  $1/n$  of  $w(0)$ . Assuming the weight at the calculation point as

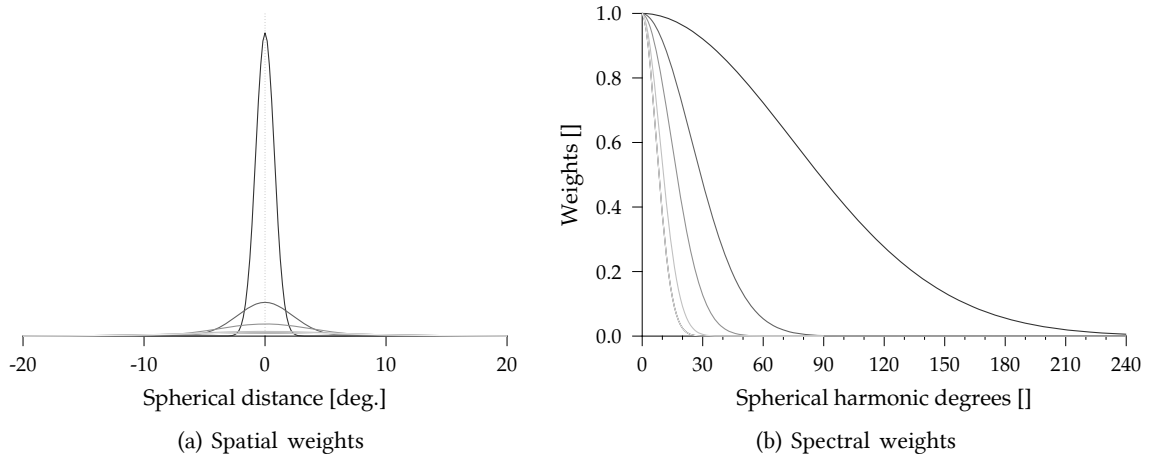
unity we can write,

$$\begin{aligned} w(\psi_0) &= \frac{1}{n} = e^{-a} e^{a \cos \psi_0}, \\ -\ln(n) &= -a + a \cos \psi_0, \\ \therefore a &= \frac{\ln(n)}{1 - \cos \psi_0}. \end{aligned} \quad (3.7)$$

Since by design the Gaussian weights  $w(\psi)$  are positive, the value of  $n$  will also always be a positive (integer) value. Further, as the value of  $(1 - \cos \psi_0)$  will also be positive, (3.7) satisfies the condition that  $a \geq 0$ . The spherical distance  $\psi_0$  then becomes the *smoothing radius*. It should be clear now that the control variable  $a$  is conveniently defined by the two parameters:  $n$  and  $\psi_0$ . Thus, the Gaussian smoothing operator can be mathematically summarised as

$$b(\psi) = \frac{a}{\sinh a} e^{a \cos \psi}, \quad \text{with } a = \frac{\ln(n)}{1 - \cos \psi_0}. \quad (3.8)$$

Figure 3.2 shows the spatial and the corresponding spectral weights of the Gaussian smoothing kernel for a few smoothing radii. The bell-shape of the Gaussian smoothing kernels and also their asymptotic behaviour is clearly visible.



**Figure 3.2:** Spatial and spectral weights of the Gaussian smoothing operators with  $n = 2$  and  $\psi_0 = 0.9^\circ, 2.7^\circ, 4.5^\circ, 7.2^\circ, 9^\circ$  (dark to light colours).

The spectrum of the Gaussian smoothing kernel is given by

$$B_l = \frac{1}{2} \int_0^\pi \frac{a}{\sinh a} e^{a \cos \psi} P_l(\cos \psi) d\psi, \quad (3.9a)$$

$$B_0 = 1,$$

$$B_1 = \coth a - \frac{1}{a},$$

$$B_{l+1} = -\frac{2l+1}{a} B_l + B_{l-1}. \quad (3.9b)$$

The spectrum does not have a closed form expression, but it follows the above recursion.



In practice, the above recursion degenerates quickly that the values of  $B_{l+1}$  start to become higher than  $B_l$  and also start to oscillate around zero (cf. Table 3.2). Therefore, we numerically integrate (3.9a) after taking the Gauss-Neumann samples of the Legendre polynomials ( $P_l(\cos \psi)$ ) and the Gaussian smoothing operator ( $b(\cdot)$ ), which is generally stable up to machine precision.

**Table 3.2:** Comparison of the Gaussian smoothing window spectral weights computed using the recursion in (3.9b) with those by numerical integration. Here the spectral weights of a smoothing radius of  $8^\circ$  is shown.

Degree	Recursion	Numerical integration
0	1.0	1.0
1	0.98593	0.98596
2	0.95838	0.95847
3	0.91850	0.91867
4	0.86791	0.86818
5	0.80858	0.80897
10	0.45932	0.46012
20	0.05206	0.05241
30	0.00152	0.00154
40	$1.2077 \cdot 10^{-5}$	$1.2373 \cdot 10^{-5}$
50	$2.8244 \cdot 10^{-8}$	$2.9254 \cdot 10^{-8}$
60	$4.3860 \cdot 10^{-8}$	$2.1952 \cdot 10^{-11}$
75	$-1.4308 \cdot 10^{-2}$	0.0
90	$4.1008 \cdot 10^4$	0.0

### §3.4 DESTRIPIING FILTER

Swenson and Wahr [2006b] identified that the stripe-like errors in the temporal gravity variations estimated from GRACE observations (see Figure 1.2) are caused by the correlation between the spherical harmonic coefficients that are of the same order and parity, irrespective of the degree (cf. Figure 3.3). They also note that such a behaviour is evident only for orders  $m \geq 8$ . This correlation was later attributed to the near polar orbit geometry of the GRACE satellite pair by Kusche et al. [2009]. Since spherical harmonics are orthogonal functions, ideally, their coefficients must not have any correlation between them. Thus, the correlated coefficients need to be decorrelated to get rid of the noise. This they achieved by modelling the correlation by a moving polynomial average, which is then subtracted from the coefficients to obtain the decorrelated coefficients. Here we will explain the procedure in detail.

Let  $F_{lm}$  be the spherical harmonic coefficients estimated from GRACE observations that are correlated, and  $F'_{lm}$  be the estimate of  $F_{lm}$  after fitting a polynomial to the points around  $F_{lm}$  that have the same order  $m$  and the same parity as  $(l-m)$ . Then the “destriped” spherical harmonic coefficient  $\bar{F}_{lm}$  is given as

$$\bar{F}_{lm} = F_{lm} - F'_{lm}, \quad \text{where} \quad (3.10a)$$

$$F'_{lm} = \sum_{n=0}^p \sum_{\omega=-w}^w Q_n (l + 2\omega)^n, \quad (3.10b)$$

where  $Q_n$  are the unknown polynomial coefficients,  $l$  the spherical harmonic degree and  $p$

the order of the polynomial.  $Q_n$  is estimated from a system of equations after choosing the window  $w$  around the coefficient  $F_{lm}$ . This procedure of computing  $F'_{lm}$  is indeed the Savitzky-Golay filter [Savitzky and Golay, 1964], and the system of equations are given as

$$\begin{bmatrix} F_{(l-2w)m} \\ F_{(l-2(w-1))m} \\ \vdots \\ F_{(l-2)m} \\ F_{lm} \\ F_{(l+2)m} \\ \vdots \\ F_{(l+2(w-1))m} \\ F_{(l+2w)m} \end{bmatrix} = \begin{bmatrix} 1 & l-2w & \cdots & (l-2w)^{p-1} & (l-2w)^p \\ 1 & l-2(w-1) & \cdots & (l-2(w-1))^{p-1} & (l-2(w-1))^p \\ \vdots & \vdots & \ddots & \vdots & \vdots \\ 1 & l-2 & \cdots & (l-2)^{p-1} & (l-2)^p \\ 1 & l & \cdots & l^{(p-1)} & l^p \\ 1 & l+2 & \cdots & (l+2)^{p-1} & (l+2)^p \\ \vdots & \vdots & \ddots & \vdots & \vdots \\ 1 & l+2(w-1) & \cdots & (l+2(w-1))^{p-1} & (l+2(w-1))^p \\ 1 & l+2w & \cdots & (l+2w)^{p-1} & (l+2w)^p \end{bmatrix} \begin{bmatrix} Q_0 \\ Q_1 \\ \vdots \\ Q_{p-1} \\ Q_p \end{bmatrix}$$

Writing the above system in matrix notation we get

$$\mathbf{F}_{lm} = \mathbf{V}_{lm} \mathbf{Q}_{lm},$$

where  $\mathbf{F}_{lm}$  is the vector of data points within the chosen window,  $\mathbf{V}_{lm}$  is the design matrix, which has the form of a *Vandermonde matrix*,  $\mathbf{Q}_{lm}$  is the vector of polynomial coefficients and the subscripts  $lm$  indicate that these matrices and vectors are for the data points centred around the spherical harmonic  $lm$ . Now, by introducing a selection matrix  $\mathbf{M}_{lm}$  we can rewrite the left hand side with the vector of full set of spherical harmonic coefficients  $\mathbf{F}$  as

$$\mathbf{M}_{lm} \mathbf{F} = \mathbf{V}_{lm} \mathbf{Q}_{lm}.$$

The purpose of the selection matrix is to select only the coefficients  $\mathbf{F}_{lm}$  from the complete set  $\mathbf{F}$ . Continuing, the estimate of  $\mathbf{Q}_{lm}$  is then given as

$$\hat{\mathbf{Q}}_{lm} = (\mathbf{V}_{lm}^T \mathbf{V}_{lm})^{-1} \mathbf{V}_{lm}^T \mathbf{M}_{lm} \mathbf{F}. \quad (3.10c)$$

With the help of the estimate  $\mathbf{Q}_{lm}$ , we can now compute the smoothed value  $F'_{lm}$  of the coefficient  $F_{lm}$  as

$$F'_{lm} = \mathbf{v}_{lm} \hat{\mathbf{Q}}_{lm}, \quad (3.10d)$$

where  $\mathbf{v}_{lm}$  is the row vector corresponding to the coefficient  $F_{lm}$  in the matrix  $\mathbf{V}_{lm}$ . Finally, combining (3.10a), (3.10c) and (3.10d), we get

$$\bar{F}_{lm} = F_{lm} - \mathbf{v}_{lm} (\mathbf{V}_{lm}^T \mathbf{V}_{lm})^{-1} \mathbf{V}_{lm}^T \mathbf{M}_{lm} \mathbf{F}. \quad (3.10e)$$

Putting

$$\mathbf{B}'_{lm} = \mathbf{v}_{lm} (\mathbf{V}_{lm}^T \mathbf{V}_{lm})^{-1} \mathbf{V}_{lm}^T \mathbf{M}_{lm}, \quad (3.10f)$$

we get

$$\bar{F}_{lm} = F_{lm} - \mathbf{B}'_{lm} \mathbf{F}. \quad (3.10g)$$

Extending the above equation for the complete set of spherical harmonic coefficients we get

$$\begin{aligned} \bar{\mathbf{F}} &= \mathbf{F} - \mathbf{B}' \mathbf{F}, \\ &= (\mathbf{I} - \mathbf{B}') \mathbf{F}, \\ &= \mathbf{B} \mathbf{F}, \end{aligned} \quad (3.10h)$$

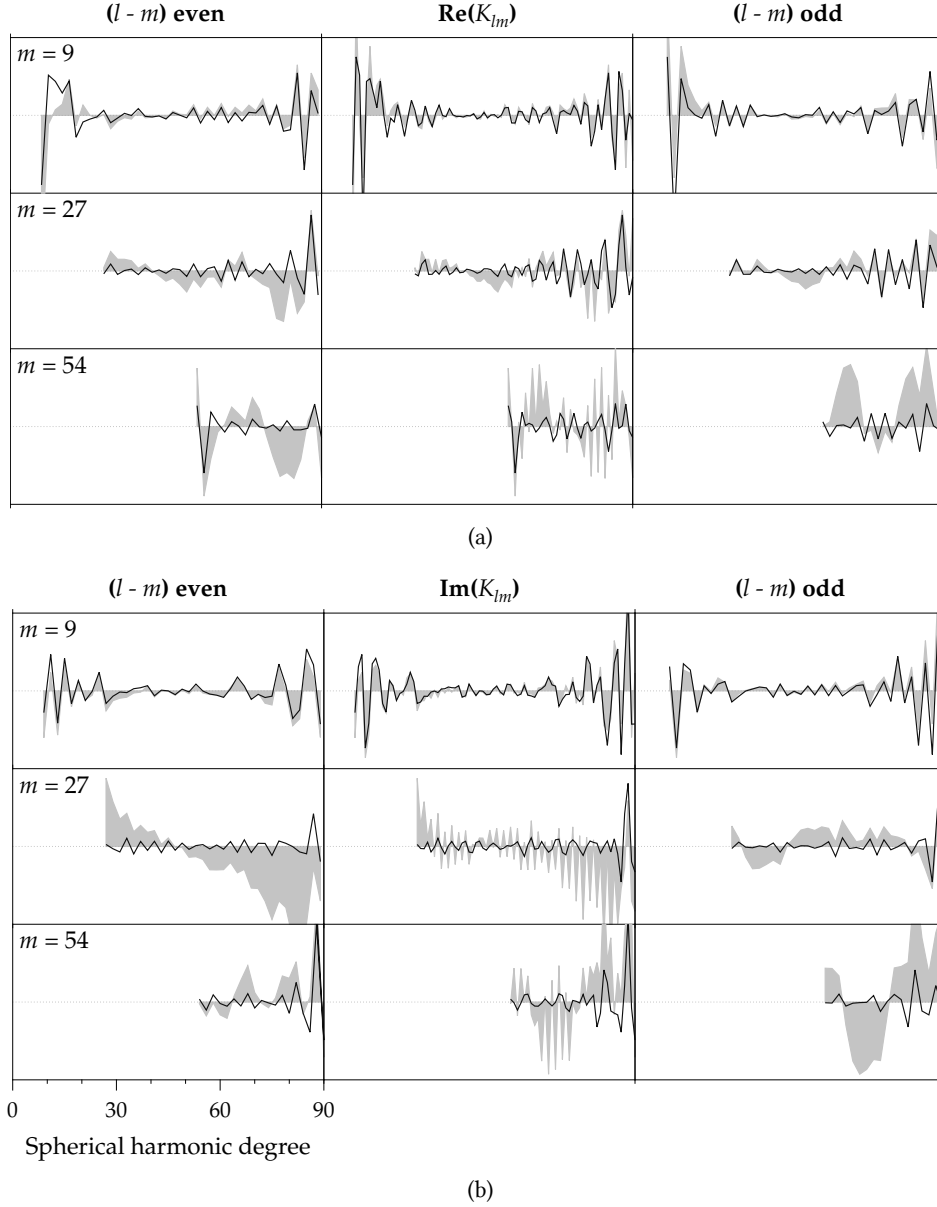
where the term  $\mathbf{B} = (\mathbf{I} - \mathbf{B}')$  is the required destriping filter matrix. Since, the destriping filter is constructed only for the individual orders, the filter matrix has an order-leading block-diagonal structure (cf. Figure 2.3). Thus, the destriping filter is a latitude dependent inhomogeneous anisotropic filter.

The spherical harmonic coefficients for a few orders, before and after applying the destriping filter, is depicted in Figure 3.3. The window size for the destriping filter used here was determined by an empirical formula provided by Duan et al. [2009] and a second degree polynomial was used for modelling the correlations. A minimum window size of 5 is used and typical window sizes hover between 5 and 8. The destriping procedure was carried out for orders  $m \geq 8$  as suggested by Swenson and Wahr [2006b], which implies that the coefficients with order  $m < 8$  are left untouched. Such moving polynomial methods suffer from edge effects, especially when  $(l - 2w) < m$  or  $(l + 2w) > L$ . In such cases a minimum window size of 5 is used to obtain the smoothed value.

It is evident from both the cosine (Figure 3.3(a)) and the sine (Figure 3.3(b)) plots that order  $m = 9$  is not affected by correlation, but there is still some signal reduction happening there. As the orders increase it is clear that the correlation also increases. The destriping filter does an effective job of removing the correlations, especially the even parity sine coefficients of order  $m = 27$ . Nevertheless, the method also suffers from mismodelling problems, for example, whenever there is a trough between two peaks, invariably excess signal is removed from the trough and thereby changing the sign of the coefficient (cf. both cosine and sine coefficients of order  $m = 54$  around degree 80).

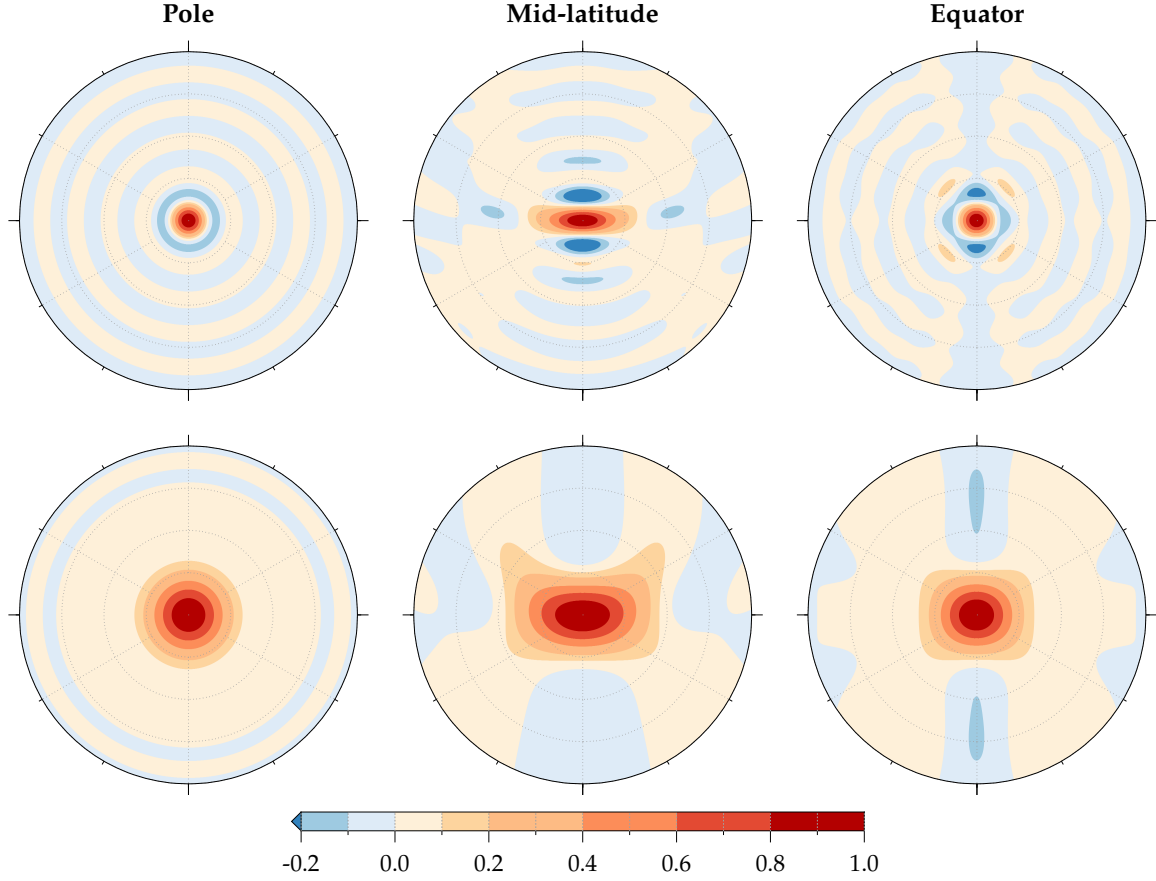
So far we have been looking at the spectrum of the destriping filter and its efficacy in decorrelating the GRACE coefficients. The intention behind decorrelating the coefficients was to rid the spatial fields of the stripes. The spatial structure of the destriping filter in fact reveals this attribute, where we see that the filter is elongated in the east-west direction (cf. top panel of Figure 3.4) in order to smoothen the stripes that alternate in sign in the east-west direction (Figure 1.2). In order to decorrelate the signals in the north-south direction, which share the same sign, the filter alternates the sign by providing negative weights in that direction. However the east-west elongation of the kernel is more pronounced at the mid-latitude than at the equator as the kernel tends towards isotropy at the equator. Due to the block diagonal structure of the destriping filter we see that the kernel is isotropic at the pole and changes with the latitude.

The destriping filter works like a preprocessor requiring further filtering with an isotropic filter like the Gaussian filter. The kernel dilates significantly at all the latitudes after cascading it with the Gaussian smoothing kernel (cf. bottom panel of Figure 3.4). Due to the isotropic



**Figure 3.3:** Spherical harmonic coefficients of the temporal gravity field for a particular harmonic order  $m$  before (gray) and after (black) applying the destriping filter. The middle column denotes the full set of coefficients for a particular order and the left column denotes even parity of  $(l - m)$  coefficients and the right column the odd parity coefficients.

nature of the Gaussian smoothing kernel the east-west elongation is retained. Since the weights of the Gaussian kernel are all positive the negative weights of the destriping kernel are also retained. Although the spectrum of the Gaussian filter is diagonal, cascading works only in one direction due to the non-commutative nature of matrix multiplication. In other words, first filtering the GRACE spectrum with the Gaussian filter and then destriping it will not give the same results as first destriping the GRACE spectrum and then filtering it with a Gaussian filter.



**Figure 3.4:** Spatial structure of the destriping filter and the filter after combining with a Gaussian filter of radius  $3.5^\circ$  and  $n = 2$ . Notice the east-west symmetry of the smoothing kernel in the mid-latitude and equator, and additionally also in the north-south direction at the equator. At the pole the smoothing kernel is isotropic due to the block-diagonal structure of the destriping filter spectrum.

### §3.5 REGULARIZATION FILTER

The regularization filter proposed by Kusche [2007] reformulates the filtering problem into an estimation problem with stochastic constraints. The reformulation is based on the principles of *Bayesian regularization* [Koch and Kusche, 2002]. Given the monthly estimates of spherical harmonic spectrum of the temporal gravity field variations  $\hat{\mathbf{F}}$ , whose stochastics are described by the covariance matrix  $\mathbf{Q}$ , then the linear stochastic model can be written as

$$\mathbf{E}\{\hat{\mathbf{F}}\} = \mathbf{F}; \quad \mathbf{D}\{\hat{\mathbf{F}}\} = \sigma^2 \mathbf{Q}, \quad (3.11a)$$

where  $\mathbf{F}$  is the unknown true value of  $\hat{\mathbf{F}}$ ,  $\mathbf{E}\{\cdot\}$  is the expectation operator,  $\mathbf{D}\{\cdot\}$  is the dispersion operator and  $\sigma^2$  is the variance component of  $\mathbf{Q}$ . If there is *a priori* knowledge about the stochastic behaviour of  $\mathbf{F}$  provided by the signal covariance matrix  $\mathbf{S}$ , then the linear model in (3.11a) can be extended as

$$\mathbf{E}\left\{\begin{pmatrix} \hat{\mathbf{F}} \\ \mathbf{F}_0 \end{pmatrix}\right\} = \begin{bmatrix} \mathbf{I} \\ \mathbf{I} \end{bmatrix} \mathbf{F}; \quad \mathbf{D}\left\{\begin{pmatrix} \hat{\mathbf{F}} \\ \mathbf{F}_0 \end{pmatrix}\right\} = \begin{bmatrix} \sigma^2 \mathbf{Q} & 0 \\ 0 & \sigma_0^2 \mathbf{S} \end{bmatrix}, \quad (3.11b)$$

where  $\mathbf{F}_0$  is one of the possible realisations of  $\mathbf{F}$ , which is again unknown and  $\sigma_0^2$  is the

variance component of the signal covariance matrix  $\mathbf{S}$ . These set of equations can be cast into an objective function with the aim of minimising the norm of the residuals:

$$\bar{\mathbf{F}} : \min_{\mathbf{F}} \frac{1}{\sigma^2} \|\mathbf{F} - \hat{\mathbf{F}}\|_{\mathbf{Q}^{-1}}^2 + \frac{1}{\sigma_0^2} \|\mathbf{F} - \mathbf{F}_0\|_{\mathbf{S}^{-1}}^2. \quad (3.11c)$$

The solution that minimises the objective function is given by

$$\bar{\mathbf{F}} = (\gamma \mathbf{S}^{-1} + \mathbf{Q}^{-1})^{-1} (\mathbf{Q}^{-1} \hat{\mathbf{F}} + \gamma \mathbf{S}^{-1} \mathbf{F}_0), \quad (3.11d)$$

$$\gamma = \frac{\sigma^2}{\sigma_0^2}. \quad (3.11e)$$

Both the inputs  $\hat{\mathbf{F}}$  and  $\mathbf{F}_0$  contribute to the final estimate, but their contribution is controlled by the size of the variance components, which are the squared norm of the residuals [Bouman and Koop, 1998]. In practice, the values of  $\mathbf{F}_0$  and  $\mathbf{S}$  are not known. In the case of  $\mathbf{F}_0$ , it is generally assumed to be  $\mathbf{0}$  [Sneeuw, 2000], and therefore (3.11d) reduces to

$$\bar{\mathbf{F}} = (\gamma \mathbf{S}^{-1} + \mathbf{Q}^{-1})^{-1} \mathbf{Q}^{-1} \hat{\mathbf{F}}. \quad (3.11f)$$

In the above equation there is only contribution from  $\hat{\mathbf{F}}$ , and therefore, any information that is too noisy or lacking in  $\hat{\mathbf{F}}$  will not be replaced hence resulting in a solution  $\bar{\mathbf{F}}$  that is replete of some details and effectively smooth. The contribution of  $\hat{\mathbf{F}}$ , and hence the smoothness of  $\bar{\mathbf{F}}$ , is directly controlled by the value of  $\gamma$ : The larger the value of  $\gamma$ , the smoother the value of  $\bar{\mathbf{F}}$ . This can be visualised mathematically by taking the expectation of (3.11d) [Sneeuw, 2000]:

$$\begin{aligned} \mathbf{E}\{\bar{\mathbf{F}}\} &= \mathbf{E}\left\{(\gamma \mathbf{S}^{-1} + \mathbf{Q}^{-1})^{-1} (\mathbf{Q}^{-1} \hat{\mathbf{F}} + \gamma \mathbf{S}^{-1} \mathbf{F}_0)\right\}, \\ \mathbf{E}\{\bar{\mathbf{F}}\} &= (\gamma \mathbf{S}^{-1} + \mathbf{Q}^{-1})^{-1} (\mathbf{Q}^{-1} \mathbf{E}\{\hat{\mathbf{F}}\} + \gamma \mathbf{S}^{-1} \mathbf{E}\{\mathbf{F}_0\}), \\ \mathbf{F} &= (\gamma \mathbf{S}^{-1} + \mathbf{Q}^{-1})^{-1} (\mathbf{Q}^{-1} \mathbf{F} + \gamma \mathbf{S}^{-1} \mathbf{F}). \end{aligned} \quad (3.11g)$$

Putting

$$\mathbf{R}_x = (\gamma \mathbf{S}^{-1} + \mathbf{Q}^{-1})^{-1} \gamma \mathbf{S}^{-1}, \quad (3.11h)$$

$$\mathbf{R}_y = (\gamma \mathbf{S}^{-1} + \mathbf{Q}^{-1})^{-1} \mathbf{Q}^{-1}, \quad (3.11i)$$

where  $\mathbf{R}_x$  and  $\mathbf{R}_y$  are called the constraint and the data *redundancy* matrices, respectively. Their diagonal elements indicate the relative contribution of the data and the constraints to the final solution [Sneeuw, 2000]. Inserting (3.11i) and (3.11h) into (3.11g) we get

$$\mathbf{F} = \mathbf{R}_y \mathbf{F} + \mathbf{R}_x \mathbf{F} \quad \Rightarrow \quad \mathbf{R}_y + \mathbf{R}_x = \mathbf{I}. \quad (3.11j)$$

Equation (3.11j) demonstrates that contributions from both the data and the constraints flow into the estimate  $\bar{\mathbf{F}}$ . As we assumed the realisation of  $\mathbf{F}$ ,  $\mathbf{F}_0$  to be  $\mathbf{0}$ , we get, after comparing (3.11f) and (3.11i)

$$\bar{\mathbf{F}} = \mathbf{R}_y \hat{\mathbf{F}}. \quad (3.11k)$$

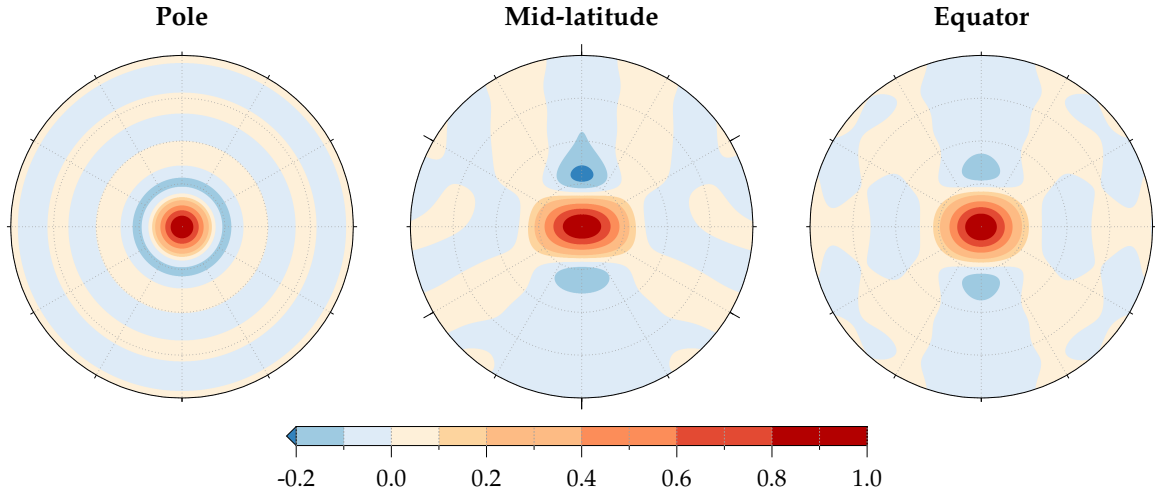
Thus, (3.11k) clearly shows that the final estimate  $\bar{\mathbf{F}}$  will only have contribution from  $\hat{\mathbf{F}}$ , but that after being constrained by the stochastic constraints  $\mathbf{S}$ . This implies that in essence we will get a filtered estimate  $\bar{\mathbf{F}}$  of the spectrum  $\mathbf{F}$ .

In order to construct the regularization filter we need the signal and noise covariance matrix. In general, the noise covariance is readily available if the data are estimates from a linear least squares estimation, but the signal covariance matrices are more often than not unavailable. In the case of GRACE data analysis both the covariance matrices are not available. Although, the spherical harmonic coefficients of the monthly gravity field snapshots from GRACE are estimated via least squares, the covariance matrices are not always disseminated by the data centres for reasons of size of those matrices. Nevertheless, the estimated standard deviations are provided with the data. Kusche [2007] proposed to simulate the covariance via the *energy balance approach* [Gerlach et al., 2003], and demonstrated the ability of the simulated covariance matrix to filter out noise. A clear account of the procedure to simulate the GRACE variance-covariance matrix is given by Lorenz [2009, sec. 4.2]. In contrast, Klees et al. [2008] used covariances from in-house least squares estimates of the monthly GRACE gravity field harmonic spectra.

Due to the unprecedented nature of the data that was produced by GRACE, the signal covariances of the temporal gravity field variations remained elusive. Nevertheless, the signal covariance of the static gravity field was very well studied. It was established by Kaula [1966] that the power spectrum of the signal covariance of the static gravity field has a *power-law* behaviour, whose power decreases with increasing degree. Taking this cue, Sasgen et al. [2006] computed the signal covariance of the temporal variations of the gravity field by fitting a power law to the GRACE spherical harmonic power spectra. On the other hand, Kusche [2007] computed the same from geophysical models. A fully populated signal covariance matrix was computed iteratively by Klees et al. [2008].

Another aspect of the regularization filter that we have not discussed so far is the ratio  $\gamma$ , also known as the *regularization parameter*. From least squares estimation it is well known that the inverse of the covariance matrices are used as weight matrices. With this in mind, looking at (3.11f) we can see that if the ratio  $\gamma$  is greater than 1 then the signal covariance is weighted more than the noise covariance, and hence less contribution from  $\hat{\mathbf{F}}$ , and *vice versa*. Since  $\gamma$  is the ratio of the squared norm of the residuals from the data ( $\sigma^2$ ) and *a priori* information ( $\sigma_0^2$ ) (cf. (3.11e)), it will be a large value if the data is noisy resulting in larger residuals and thereby a larger value for  $\sigma^2$  compared to  $\sigma_0^2$ . Thus, the regularization parameter acts as a tuning parameter that decides the level of filtering of the data. This idea is illustrated in terms of a multi-resolution concept by Kusche [2007]. The optimum value of the regularization parameter is estimated via variance component estimation [Lorenz, 2009], but can also be tweaked to the desired smoothness as demonstrated by Kusche [2007].

Figure 3.5 shows the spatial structure of the regularization filter for nine different calculation points spread over three different latitudes and three different longitudes. By virtue of using a fully populated covariance matrix, the resultant smoothing operator will be an inhomogeneous anisotropic kernel, that means the smoothing operator should change for every single location. However, as Kusche et al. [2009] observed the covariance structure of the GRACE observed temporal gravity field variations is order-leading block-diagonal dominant due to its orbit configuration. Therefore, even if one would use a fully populated covariance matrix the smoothing operator will be a latitude dependent anisotropic kernel. This is clear in the



**Figure 3.5:** Spatial structure of the regularization filter for the month of September 2004 at three different latitudes. Due to the dominance of the order-leading block-diagonal elements of the filter spectrum, the regularization filter also shows latitude-dependent anisotropy. Notice the symmetry of the smoothing kernels similar to that of the destriping filters (Figure 3.4).

smoothing operator at the pole (Figure 3.5), where we see that the smoothing operator is isotropic, which is the case for a latitude dependent anisotropic kernel. Despite this fact, Lorenz [2009] found benefit in using the full covariance matrix for filtering the GRACE datasets.

In this work we will follow the method of Sasgen et al. [2006] to model the signal covariance, and there we will demonstrate its cyclo-stationary nature. Since, the idea of cyclo-stationarity requires the knowledge of the signal content in GRACE data, we will demonstrate the signal covariance modelling in chapter 6. For computing the noise covariance matrix we will follow the method of Lorenz [2009], and for the regularization parameter we will use the approach of [King et al., 2006] by comparing regularized solutions of different  $\gamma$  values with GPS deformation time-series to find out the optimum value.



GIVEN the existence of different possible filters and a variety of filter design options, we are at a juncture, where we have the problem of *choosing the appropriate filter*. It has been one of the never-ending problems in the application of GRACE data to study various geophysical phenomena [e.g., Seo and Wilson, 2005; Werth et al., 2009; Longuevergne et al., 2010; Lorenz et al., 2014]. It is in this context that we will develop metrics for evaluating the performance of a given filter, which will eventually provide us with a generic impression of the effect of the filter on any given dataset. Further, it will also provide us a good understanding of the mechanics of the filter. These metrics have largely been inspired by the metrics developed for data windows in one dimensional Fourier analysis by Harris [1978].

The performance metrics that are developed here use the energy associated with the filter kernel and/or the weighted field as the basis. Energy and power are the only quantities that have a straight-forward and simple relationship between the spatial and spectral representations of a smoothing kernel due to *Parseval's theorem*. Energy of a smoothing kernel at the calculation point,  $E(\theta, \lambda)$ , is given as

$$E(\theta, \lambda) = \int_0^{2\pi} \int_0^\pi b^2(\theta, \lambda, \psi, A) \sin \psi \, d\psi \, dA, \quad (4.1a)$$

$$= 2 \int_0^{2\pi} E(\theta, \lambda, A) \, dA, \quad (4.1b)$$

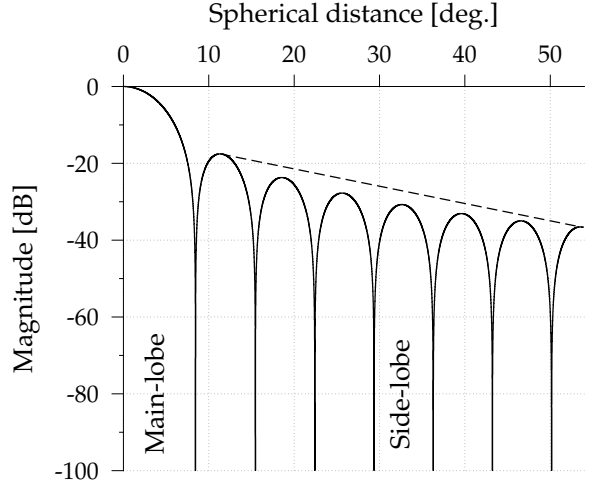
$$= 4\pi \sum_{lm} \sum_{nk} \sum_{pq} Y_{lm}(\theta, \lambda) B_{lm}^{nk} B_{nk}^{pq} Y_{pq}(\theta, \lambda), \quad (4.1c)$$

where  $E(\theta, \lambda, A)$  is the energy associated with the kernel along the azimuth  $A$ . Another commonly used quantity in signal processing literature is the *power* associated with the function, which is the average energy over the unit sphere. The power of a function defined on the unit sphere is

$$P(\theta, \lambda) = \frac{1}{4\pi} E(\theta, \lambda), \quad (4.2a)$$

and

$$P(\theta, \lambda, A) = \frac{1}{2} E(\theta, \lambda, A), \quad (4.2b)$$



**Figure 4.1:** Anatomy of a smoothing kernel along a particular azimuth.

When the filter spectrum is synthesised to the spatial domain, the smoothing operator demonstrates a certain structure. This structure is clearly evident when the filter is depicted in the *log-normal scale*. The log-normal magnitude of the smoothing kernel weights is given as

$$\tilde{b}(\theta, \lambda, \psi, A) \text{ [dB]} = 20 \log_{10} \left( \frac{b(\theta, \lambda, \psi, A)}{b(\theta, \lambda, 0, 0)} \right) \quad (4.3a)$$

$$= 10 \log_{10} \left( \frac{b^2(\theta, \lambda, \psi, A)}{b^2(\theta, \lambda, 0, 0)} \right) \quad (4.3b)$$

In Figure 4.1, the log-normal scale plot of the box-car smoothing operator along a particular azimuth is shown, where we see that the kernel has a dominant *main-lobe* and the oscillating ripples as its *side-lobes*. The magnitude and the geometry of the main-lobe and the side-lobes will impact the way the signal is being smoothed, and therefore, also energy associated with the smoothed signal. In the sequel we will demonstrate as to how the anatomy of the smoothing kernel enables us to understand the mechanics of filtering leading us to evaluate its performance.

#### §4.1 DAMPING FACTOR

Any filtering applied to a field, dampens the amplitude to a certain extent. The first measure that already provides an overview of the smoothing window is the damping factor [Kusche, 2007]. It is defined as the ratio between the energy of the smoothed and the non-smoothed fields:

$$\alpha = \frac{\int_{\Omega} \bar{f}^2(\theta, \lambda) d\Omega}{\int_{\Omega} f^2(\theta, \lambda) d\Omega} = \frac{\sum_{l,m} \bar{F}_{lm}^2}{\sum_{l,m} F_{lm}^2} = \frac{\sum_{l,m} \left( \sum_{n,k} B_{lm}^{nk} F_{nk} \right)^2}{\sum_{l,m} F_{lm}^2}. \quad (4.4)$$

The damping factor provides a *coarse* estimate of the amount of damping of the signal amplitude due to smoothing. The term *coarse* is used in order to emphasise the point that the damping factor indicates only an average value for the amplitude damping of the

smoothed field. This is easier to understand in the spectral domain, where every single frequency (spherical harmonic degree) will have its own specific damping value irrespective of the type of smoothing window used, and the damping factor provides an average value for all frequencies put together. In the following equation this idea is explicitly illustrated by the homogeneous isotropic filter coefficients:

$$\alpha = \frac{\sum_{l,m} B_l^2 F_{lm}^2}{\sum_{l,m} F_{lm}^2}. \quad (4.5)$$

The damping factor takes an interesting form if the field that is being smoothed is band-limited and has a white spectrum, i.e., the degree variance of the spherical harmonic expansion of the field has the same magnitude for any given spherical harmonic degree ( $\sum_m F_{lm}^2 = \kappa^2$ ). Applying this restriction to equation (4.5) and referring  $\alpha$  as  $\alpha_w$  gives,

$$\alpha_w = \frac{\sum_{l=0}^L B_l^2 \kappa^2}{\sum_{l=0}^L \kappa^2} = \frac{\sum_{l=0}^L B_l^2}{L+1} \quad (4.6)$$

where  $L$  is the maximum degree of expansion of the band-limited function. A careful look at equation (4.6) will show that it describes the average power of the spherical harmonic coefficients of the smoothing window. While (4.5) is a field-specific quantity, (4.6) is a general quantity as it gives the potential damping due to the filter being used. Further, it should also be clear from (4.6) that the computation of  $\alpha_w$  is only possible for the degree-dependent homogeneous isotropic filters.

### Processing gain

Processing gain is the ratio between the signal-to-noise ratios of the unsmoothed and the smoothed fields. This measure explains how much improvement in terms of signal-to-noise ratio is achieved by smoothing the field, which is the reason that this measure is referred to as *processing gain*.

$$\alpha_G = \frac{\text{SNR}(\bar{f}(\Omega))}{\text{SNR}(f(\Omega))}, \quad \text{where} \quad \text{SNR} = \frac{\text{Signal power}}{\text{Noise power}}, \quad (4.7a)$$

$$\alpha_G = \frac{\int_{\Omega} \bar{f}^2(\theta, \lambda) d\Omega}{\int_{\Omega} f^2(\theta, \lambda) d\Omega} \bigg/ \frac{\int_{\Omega} \bar{\epsilon}^2(\theta, \lambda) d\Omega}{\int_{\Omega} \epsilon^2(\theta, \lambda) d\Omega}, \quad (4.7b)$$

where  $\epsilon(\theta, \lambda)$  is the noise associated with the unsmoothed field  $f(\theta, \lambda)$  and  $\bar{\epsilon}(\theta, \lambda)$  is the noise associated with the smoothed field  $\bar{f}(\theta, \lambda)$ .

### Processing loss

A certain amount of the signal is lost when a field is filtered. *Processing loss* measures the amount of signal energy lost due to filtering, and it is defined as the ratio between the difference in the signal energy before and after smoothing and the signal energy before smoothing.

$$\alpha_L = 1 - \frac{\int_{\Omega} \bar{f}^2(\theta, \lambda) d\Omega}{\int_{\Omega} f^2(\theta, \lambda) d\Omega} = 1 - \alpha \quad , \quad (4.8)$$

where  $\alpha$  is the damping factor. As can be seen from (4.8) processing loss purely describes the energy loss in the signal and there is no reference to the reduction in noise. Further, equation (4.8) is a field-specific quantity. Again, by restricting the signal spectrum to be a white spectrum processing loss can be expressed as a general quantity, and it will be explicitly denoted as  $\alpha_\ell$ . The general processing loss is given as

$$\alpha_\ell = 1 - \alpha_w . \quad (4.9)$$

Values close to 1 indicate heavy processing loss and values closer to zero indicate nearly no loss.

### §4.2 MAIN-LOBE HALF-WIDTH

As we saw in the design of filter kernels, especially in the deterministic design, there is either a smoothing radius that defines the set of data points that will be weighted more than the others, or a spherical harmonic degree beyond which the frequencies are down-weighted, which eventually corresponds to a spatial wavelength. In the case of the stochastic filter this is controlled by the regularization parameter. No matter the type of design every filter has a region, where most of the smoothing occurs and this is called the *main-lobe* of the filter. The main-lobe is accompanied by the side-lobes that are generally the ripples from the Gibbs phenomenon due to sharp jumps in the weights of the smoothing kernel, either in the spatial or the spectral domains. These ripples start to form at around the sharp changes, which in this case would be around the intended smoothing radius. However, the ripples need not always be due to sharp changes in the weights, but can also be due to the design of the filter/smoothing kernel. For example, in stochastic filters the side-lobes are mainly due to negative covariances, which means that care must be taken to interpret the side-lobes. So, a typical smoothing kernel will have a central main-lobe surrounded by side-lobes of varying magnitudes (Figure 4.1). Since we expect that most of the smoothing to take place within the main-lobe, it becomes important to ascertain how much of the filter area is under the main-lobe and what is the areal extent of this main-lobe. Thus, the main-lobe plays a central role in analysis of filters.

In general, the first zero-crossing of the smoothing kernel is taken as the half-width of the main-lobe. This definition has been taken from one-dimensional Fourier analysis. There, Oppenheim et al. [1999, section 7.2] demonstrate that the full-width of the main-lobe of the spectral transfer function of a box-car data window corresponds to the width between the

ripples immediately before and after the discontinuity in the reconstructed window. However, there are exceptions to this “typical” anatomy of the smoothing kernel, for example the Gaussian smoothing kernel (cf. Figure 5.1), which does not have a side-lobe as the function slowly decays to zero but never crosses it. Only in practical cases, where the spectrum of the Gaussian function is truncated according to the required band-width, the reconstructed Gaussian function exhibits some ripples (cf. Figure 3.2). In such cases, the first zero crossing rule cannot be applied as this might produce very big numbers for the main-lobe width that are unrealistic. This calls for some alternative methods to ascertain the main-lobe width.

### Spatial variance of the smoothing kernel

A possible definition for the main-lobe width can be the spatial variance of the energy of the smoothing kernel. It is calculated by taking the second moments of the integrand of the energy function normalised by the total energy of the smoothing kernel in the cartesian coordinate system.

$$\mathcal{S} = \int_{\Omega'} \mathbf{u} \mathbf{u}^T \frac{b^2(\mathbf{x}, \mathbf{u})}{E(\mathbf{x})} d\Omega', \quad (4.10a)$$

where

$$\mathbf{x} = \begin{bmatrix} x \\ y \\ z \end{bmatrix} = \begin{bmatrix} \sin \theta \cos \lambda \\ \sin \theta \sin \lambda \\ \cos \theta \end{bmatrix}, \quad \text{and} \quad (4.10b)$$

$$\mathbf{u} = \begin{bmatrix} u \\ v \\ h \end{bmatrix} = \begin{bmatrix} \sin \psi \cos(\pi - A) \\ \sin \psi \sin(\pi - A) \\ \cos \psi \end{bmatrix}, \quad (4.10c)$$

which leads to the following mappings and changes:

$$\begin{aligned} (\theta, \lambda) &\longrightarrow (x, y, z) \longrightarrow \mathbf{x} \in \Omega \\ (\psi, A) &\longrightarrow (u, v, h) \longrightarrow \mathbf{u} \in \Omega' \end{aligned}$$

$$\Rightarrow b(\theta, \lambda, \psi, A) \longrightarrow b(\mathbf{x}, \mathbf{u}).$$

By virtue of the normalisation, the area under the energy integrand becomes unity. This allows us to interpret it as a probability density function on the sphere. The incentive of such an interpretation is that we can apply methods of directional statistics [e.g., Fisher et al., 1987] on the energy integrand. In fact (4.10a), is a continuous form of the spatial variance formulation used in directional statistics [Fisher et al., 1987]. However, there are minor differences in the way those methods are adapted here. In directional statistics, in general, the distribution of the directions is not known and also the mean direction. In our case, both the distribution (cf. (4.10a)) and also the mean direction (direction cosines of the calculation point) are all known. And, here we only seek to compute the variance of the distribution located at the calculation point. To proceed, we also abbreviate the infinitesimal

element of the density function, following Fisher [1953]:

$$d\hat{E} = \frac{b^2(\theta, \lambda, \psi, A)}{E(\theta, \lambda)} d\Omega' = \frac{b^2(\mathbf{x}, \mathbf{u})}{E(\mathbf{x})} d\Omega', \quad (4.10d)$$

$$\therefore \mathcal{S} = \int_{\Omega'} \mathbf{u} \mathbf{u}^T d\hat{E}. \quad (4.10e)$$

The spatial variance obtained from (4.10e) is a  $3 \times 3$  matrix of the following form:

$$\mathcal{S} = \begin{bmatrix} \sigma_u^2 & \sigma_{uv} & \sigma_{uh} \\ \sigma_{vu} & \sigma_v^2 & \sigma_{vh} \\ \sigma_{hu} & \sigma_{hv} & \sigma_h^2 \end{bmatrix}, \quad (4.11a)$$

where

$$\begin{aligned} \sigma_u^2 &= \int_{\Omega'} \sin^2 \psi \cos^2(\pi - A) d\hat{E}, \\ \sigma_v^2 &= \int_{\Omega'} \sin^2 \psi \sin^2(\pi - A) d\hat{E}, \\ \sigma_h^2 &= \int_{\Omega'} \cos^2 \psi d\hat{E}, \\ \sigma_{uv} &= \sigma_{vu} = \int_{\Omega'} \sin^2 \psi \cos(\pi - A) \sin(\pi - A) d\hat{E}, \\ \sigma_{hv} &= \sigma_{vh} = \int_{\Omega'} \cos \psi \sin \psi \sin(\pi - A) d\hat{E}, \\ \sigma_{uh} &= \sigma_{hu} = \int_{\Omega'} \cos \psi \sin \psi \cos(\pi - A) d\hat{E}. \end{aligned} \quad (4.11b)$$

$$(4.11c)$$

In order to describe the spatial variance of the density function, we need the entire matrix  $\mathcal{S}$  if all of its elements have a value significantly greater than zero. Interestingly, the eigenvalues of  $\mathcal{S}$  that describes the variance in the direction of  $u$ - and  $v$ -axes provide the semi-major and semi-minor axes of an ellipse that best describe the density function. The eigenvalues are found by rotating the density function around the  $h$ -axis by an angle  $\gamma$ , which is given as

$$\gamma = \frac{1}{2} \arctan\left(\frac{2\sigma_{uv}}{\sigma_u^2 - \sigma_v^2}\right). \quad (4.12a)$$

Computing the rotation matrix

$$\mathbf{R}_h(\gamma) = \begin{bmatrix} \cos \gamma & -\sin \gamma & 0 \\ \sin \gamma & \cos \gamma & 0 \\ 0 & 0 & 1 \end{bmatrix}, \quad (4.12b)$$

and rotating the matrix  $\mathcal{S}$ , we get the required spatial variance matrix  $\Sigma_M$ :

$$\Sigma_M = \mathbf{R}_h^\top \mathcal{S} \mathbf{R}_h. \quad (4.12c)$$

The values of the elements  $\Sigma'_{11}$  and  $\Sigma'_{22}$  of  $\Sigma_M$  provide the semi-major and semi-minor axes of the elliptical confidence region that we seek.

$$\sigma_{11} = \arcsin\left(\sqrt{\Sigma'_{11}}\right), \quad (4.12d)$$

$$\sigma_{22} = \arcsin\left(\sqrt{\Sigma'_{22}}\right), \quad (4.12e)$$

where  $\sigma_{11}$  is the semi-major axis of the spatial variance ellipse in radians and  $\sigma_{22}$  the semi-minor axis. The procedure described above is the same as the one used for finding the semi-major and semi-minor axes of error ellipses in adjustment theory, and also the principal component analysis technique in the two-dimensional case. Thus, we can now describe the spatial variance of the density function, and therefore the smoothing kernel, by the set of values  $\sigma_{11}$ ,  $\sigma_{22}$  and  $\gamma$ . It should also be noted here that the value  $\sigma_h^2$ , which is unaffected by the above rotation, also provides a value that describes the overall dispersion of energy under the signal. This is because it is the integral of squared distances of the energy distribution as can be seen from (4.11b).

$$\sigma_E = \arccos(\sigma_h). \quad (4.13)$$

*Remark* Fisher et al. [1987] discuss another statistic to describe the spread of the density function. It is intriguing to note that it is based on the *first-order* moment of the density function, which they denote as the *resultant length*. The resultant length is calculated as follows:

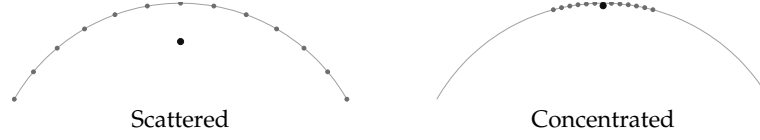
$$\bar{R} = \|\bar{\mathbf{u}}\|, \quad \text{where } \bar{\mathbf{u}} = \int_{\Omega'} \mathbf{u} d\hat{E}. \quad (4.14a)$$

Since we are interested mainly in the main-lobe width and not just the localising ability of the smoothing kernel, we will transform the resultant length to spherical distance:

$$\psi_E = \arccos(\bar{R}). \quad (4.14b)$$

The value of the resultant length is between zero and one ( $0 \leq \bar{R} \leq 1$ ). A value close to one indicates that the energy of the smoothing kernel is localised into a small area, and hence, the smoothing kernel has a narrow main-lobe width. And, *vice versa* is the case when the smoothing kernel is close to zero. The resultant length was already introduced by Narcowich and Ward [1996] in the context of spherical basis functions, which was later used by Kusche [2007].

The drawback of the resultant length is that it describes only one aspect of the spatial variance: energy localisation. It does not give us an idea of the shape of the smoothing kernel we are working with, because the same amount of localisation can be achieved by a wide variety of shapes. This drawback of the resultant length must be borne in mind, if it is used as the sole measure for describing the spatial variance of the smoothing kernel.



**Figure 4.2:** Depiction of the concept of resultant length. The gray dots depict the weights as distribution of points – the higher the weight the denser the distribution and *vice versa*, and the black dot is the resultant length. The resultant length is the radius of the black dot from the centre of the sphere, and it is short when the weights are dispersed and long when they are concentrated.

### Half-width of the fraction of maximum

It is defined as the half-width from kernel location along a particular azimuth at which the kernel attains a certain fraction of the peak value of the kernel.

$$b(\theta, \lambda, \psi_M, A) = \frac{1}{n} b(\theta, \lambda, 0, 0) \quad (4.15)$$

This definition is a generalisation of *half-width at half of maximum* definition used by Jekeli [1981] for defining the smoothing radii of Gaussian smoothing kernels, which is similar in character to the definition of correlation length of the empirical covariance functions designed in collocation studies [e.g., Moritz, 1989]. Half-width at half of maximum corresponds to -6 dB in terms of normalised magnitude, which is used by Harris [1978] to define the resolution of windowing functions in one-dimensional Fourier analysis. This is the most convenient and pragmatic of all the definitions for main-lobe half-width as it simply corresponds to one of the isolines of the smoothing kernel weights. For a smoothing kernel like Pellinen, whose weights are either zeros or ones, this definition is not applicable.

### Half-width at fraction of energy

It is defined as the half-width at which the filter has accumulated a desired fraction of total energy contained in the function.

$$\int_0^{\psi_M(A)} b^2(\theta, \lambda, \psi, A) \sin \psi \, d\psi = \frac{1}{n} E(\theta, \lambda, A) \quad (4.16)$$

This definition is a utilitarian definition as it is possible to prescribe the main-lobe half-width for a smoothing kernel based on the desired amount of accumulated beyond a certain distance from the calculation point. This definition is (again) an isoline of the accumulated energy of the kernel along each azimuth. This definition shares a lot of similarities with the idea of spatial leakage (cf. section 4.5), and therefore, it can be used to define a main-lobe width that has a tolerable level of spatial leakage.

## §4.3 MAIN-LOBE ENERGY CONCENTRATION

The main-lobe is the region where most of the smoothing takes place, and therefore the energy contained within this main-lobe is a direct measure of the amount of smoothing that is taking place in the main-lobe. It is computed by taking the ratio between the integral of the kernel energy within the main-lobe region ( $\Omega_M$ ) and the total energy of the smoothing



kernel:

$$\beta^2(\theta, \lambda) = \int_0^{2\pi} \int_0^{\psi_M(A)} \frac{b^2(\theta, \lambda, \psi, A)}{E(\theta, \lambda)} \sin \psi \, d\psi = \int_0^{2\pi} \beta^2(\theta, \lambda, A) \, dA. \quad (4.17a)$$

Similarly, a quantity that relates to the field being smoothed can also be applied, but here the quantity will only deal with signal and hence, will be referred to as *main-lobe signal concentration*:

$$\beta_f(\theta, \lambda) = \frac{1}{\Omega_M} \int_0^{2\pi} \int_0^{\psi_M(A)} \frac{f(\psi, A) b(\theta, \lambda, \psi, A)}{\bar{f}(\theta, \lambda)} \sin \psi \, d\psi \, dA. \quad (4.17b)$$

#### §4.4 SPATIAL RESOLUTION

Spatial resolution defines the smallest possible feature that can be identified distinctly from its surroundings [Lillesand and Kiefer, 1994]. In signal processing, resolution is in general associated with sampling as expounded by the corresponding sampling theorem, for example, Nyquist-Shannon sampling theorem in the Euclidean space. In physical geodesy, spatial resolution of a gravity field, given in terms of spherical harmonic coefficients up to complete degree  $L$ , is expressed as the *half-wavelength* ( $\psi_{\frac{1}{2}}$ ) of the harmonic  $L$  at the equator.

$$\psi_{\frac{1}{2}} = \frac{\pi a_E}{L} \approx \frac{20,000}{L}, \quad (4.18)$$

where  $a_E$  is the semi-major axis of the ellipsoid approximating the Earth. The value  $\psi_{\frac{1}{2}}$  is the Nyquist-Shannon sampling required along the equator, and also approximately the spacing between the zeros of the Legendre polynomial of degree  $L$ . Due to the isotropic nature of spherical harmonics, this value is assumed to hold over the entire sphere. However, Laprise [1992] points out that the half-wavelength at equator is one of many possible values for the resolution, and also proposes that at best such values can only be used as an upper limit.

When we apply a filter to a band-limited field, we are still left with a field that is band-limited up to  $L$ , but with a different resolution. In one-dimensional Fourier analysis, the resolution of a filter is taken to be the -6 dB point as suggested by Harris [1978]. The -6 dB value is the filter width at half of the amplitude at the peak, however, this definition comes out of intuitive reasoning. In contrast, the optical and remote sensing communities use resolution charts to determine the resolution of lenses, which can be adapted for our problem. The resolution chart consists of a number of vertical and horizontal lines of varying thickness drawn at varying spacings. These charts are then imaged by the sensors and the least distance between the fully resolved lines is taken as the resolution of the lenses [Lillesand and Kiefer, 1994]. We base our method on this technique to determine the resolution of the homogeneous isotropic filters.

## Methodology

We define a scalar field  $g(\theta, \lambda)$  on a unit sphere defined as

$$g(\theta, \lambda) = \sum_{j=P, Q} \delta(\theta, \lambda, \tilde{\theta}_j, \tilde{\lambda}_j), \quad (4.19)$$

where  $\delta(\cdot, \cdot)$  is the *Dirac's pulse* on the sphere [Freeden and Schreiner, 2009], located at the points P and Q, which are separated by a spherical distance of  $\psi_{PQ}$ . Smoothing  $g(\theta, \lambda)$  with a general two-point smoothing kernel gives

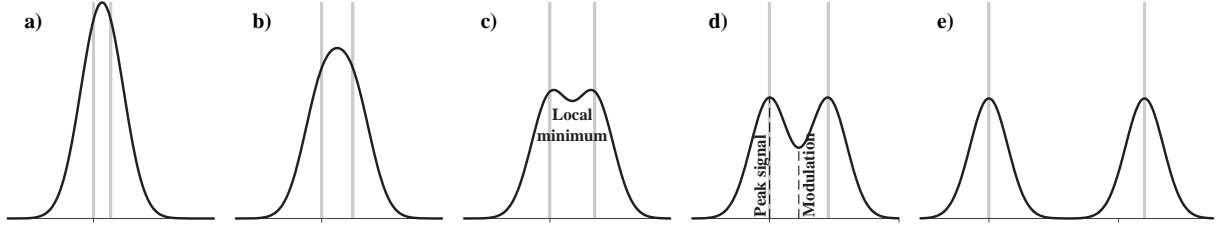
$$\begin{aligned} \bar{g}(\theta, \lambda) &= \frac{1}{4\pi} \int_{\Omega'} b(\theta, \lambda, \theta', \lambda') g(\theta', \lambda') d\Omega', \\ &= \frac{1}{4\pi} \int_{\Omega'} \sum_{l, m} Y_{lm}(\theta, \lambda) \sum_{n, k} B_{lm}^{nk} Y_{nk}^*(\theta', \lambda') \sum_{j, l', m'} Y_{l'm'}(\theta', \lambda') Y_{l'm'}^*(\tilde{\theta}_j, \tilde{\lambda}_j) d\Omega', \\ &= \sum_j \sum_{l, m} B_{lm}^{nk} Y_{lm}(\theta, \lambda) \sum_{n, k} \sum_{l', m'} Y_{l'm'}^*(\tilde{\theta}_j, \tilde{\lambda}_j) \delta_{nl'} \delta_{k, m'}, \\ &= \sum_j \sum_{l, m} Y_{lm}(\theta, \lambda) \sum_{n, k} B_{lm}^{nk} Y_{nk}^*(\tilde{\theta}_j, \tilde{\lambda}_j) \\ \bar{g}(\theta, \lambda) &= \sum_j b(\theta, \lambda, \tilde{\theta}_j, \tilde{\lambda}_j). \end{aligned} \quad (4.20)$$

The above equation shows that the filtered field  $\bar{g}(\theta, \lambda)$  is the sum of the weights at calculation points with respect to the points P and Q.

*Remark* In the case of homogeneous isotropic filters, (4.20) takes an interesting form. The spectrum of the filtered signal  $\bar{g}(\theta, \lambda)$ , when filtered with a homogeneous isotropic filter is given as

$$\begin{aligned} \bar{g}(\theta, \lambda) &= \sum_j b(\theta, \lambda, \tilde{\theta}_j, \tilde{\lambda}_j) = \sum_j b(\psi_j), \\ &= \sum_j \sum_l B_l \sum_m Y_{lm}^*(\tilde{\theta}_j, \tilde{\lambda}_j) Y_{lm}(\theta, \lambda), \\ &= \sum_j \sum_l (2l+1) B_l P_l(\cos \psi_j), \quad \because (A.3a), \\ &= \sum_j \sum_l B_l \sum_m Y_{lm}(\tilde{\theta}_j, \tilde{\lambda}_j) Y_{lm}^*(\theta, \lambda), \\ \bar{g}(\theta, \lambda) &= \sum_j b(\tilde{\theta}_j, \tilde{\lambda}_j, \theta, \lambda). \end{aligned} \quad (4.21)$$

This clearly shows that the  $\bar{g}(\theta, \lambda)$ , is equivalent to the sum of the homogeneous isotropic kernels located at the points P and Q. In other words, the smoothing operation of a field like  $g(\theta, \lambda)$  with a homogeneous isotropic kernel is commutative. Commutativity of the smoothing operation on the sphere is only possible when the spectrum of the field as well as the filter are both degree dependent.



**Figure 4.3:** Methodology for determining the resolution of homogeneous isotropic filters. The light gray lines indicate the unfiltered input signal and the dark gray lines indicate the filtered output. The level of distinction between the two peaks in the filtered and resolved field can be quantified by the quantity modulation. The method is illustrated using the Gaussian smoothing kernel.

After filtering, we scrutinise the filtered field to see if the two Dirac's pulses are resolved. If they are not resolved, we increase the separation  $\psi_{PQ}$  between the signals until they can be seen distinctly in the filtered field. The sequence is depicted in Figure 4.3. This method was also employed by Harris [1978] to demonstrate the spectral resolution of different filter windows in the harmonic analysis of time-series.

### Modulation transfer functions

The concept of spatial resolution does not merely stop at the point where we are able to identify the two signals as distinct. It continues with the question of how distinct are those signals from each other before and after filtering. At the point of resolution, the two signals are distinct, but as we separate the two signals a bit further, then they are readily recognisable as two different entities (cf. Figure 4.3). Therefore, there is a need for quantifying the level of distinctness of the resolved signals in comparison with the unfiltered signals. Again, this has already been treated by the remote sensing community, where they use the concept of *modulation transfer function* (MTF) to quantify the distinction between the two signals.

Originally, in the unfiltered field, there is no signal in the region between the points P and Q, but due to filtering we initially see only one 'peak' (Figure 4.3a and 4.3b) and then a 'valley' between the two resolved 'peaks' (Figure 4.3c). As we separate the signals farther apart, beyond the point of resolution, the valley deepens (Figure 4.3d). We will denote the ordinate of the local minimum in the valley as *modulation*, which when zero indicates completely resolved signals (Figure 4.3e).

The modulation is rather straight-forward to compute in the case of homogeneous isotropic smoothing kernels. Since they are rotationally symmetric functions, the mid-point along the geodesic between the two functions will be the only unique point. Further, it is at this point the local minimum in the valley will always occur. Thus, modulation of the homogeneous isotropic filtered field  $g(\cdot)$  is

$$\text{Modulation} = 2b \left( \frac{\psi_{PQ}}{2} \right). \quad (4.22)$$

Since the modulation and peak signal values are subjective to the filter function, we need to devise a relative measure that enables us to compare the different filters. We denote such

a measure as the *modulation transfer*. It is defined as

$$\text{MT} = 1 - \frac{\text{Modulation}}{\text{Peak signal}}. \quad (4.23)$$

As the name suggests modulation transfer indicates how the original modulation between the two signals is transferred to the filtered field. The modulation transfer takes a value zero until the signals are resolved, because the peak signal always resides at the mid-point until the signals are resolved. As soon as the signals are resolved the valley starts appearing at which point the peak signal and modulation cease to be at the same point. This means that modulation takes a value that is smaller than the peak signal. As we increase the distance between P and Q, the modulation starts decreasing. Therefore, the value of modulation transfer starts to increase. Numerically speaking, the signals are said to be resolved as soon as modulation transfer takes a value greater than zero.

Plotting the modulation transfer against the signal separation for a given set of filter parameters we get a unique curve, which we denote as the *modulation transfer function* (MTF) (Figure 5.2). The important feature of the MTF curve is the slope of the curve between 0 and 1 modulation transfer, which directly depends on the speed at which the filter function decays from peak value to zero. This is indicated by (4.22), where filters which decay slowly to zero (e.g., Gaussian) will not reduce quickly to zero modulation, and therefore, the corresponding MTF will have a gentle slope and *vice versa* (cf. Figure 5.2).

#### §4.5 SPATIAL LEAKAGE

The intention of prescribing a smoothing radius is to dictate the use of data points within the given radius to arrive at a smoother value for the calculation points. Ideally, this radius is the intended resolution. However, for some designs there is still some significant filter energy left beyond the point of resolution. This energy as we saw in the modulation transfer function is what dictates the slope of the MTF curve. Thus, we will define spatial leakage as the fraction of energy contributed to the total energy by the smoothing kernel beyond the point of resolution. Thus, the total energy contained in the filter is the sum of leakage and the energy within the unresolvable part of smoothing kernel:

$$\xi^2(\theta, \lambda) = \int_0^{2\pi} \int_{\psi_o(A)}^{\pi} \frac{b^2(\theta, \lambda, \psi, A)}{E(\theta, \lambda)} d\Omega, \quad (4.24a)$$

where  $\psi_o(A)$  is the anisotropic spatial resolution distance. The above set of equations describe, in general, the potential spatial leakage of the smoothing kernel. However, the idea of spatial leakage can also be reformulated to account for the field that is being smoothed. Such a type of spatial leakage will be referred to as *field-specific spatial leakage*:

$$\xi_f(\theta, \lambda) = \int_0^{2\pi} \int_{\psi_o(A)}^{\pi} \frac{f(\psi, A) b(\theta, \lambda, \psi, A)}{\bar{f}(\theta, \lambda)} d\Omega. \quad (4.24b)$$

*Remark* It must be noted that there is a significant difference in the term *leakage* as it was proposed here and the connotation it has in the GRACE community [e.g., Klees et al., 2008].

In the GRACE community, leakage is associated to the mass exchange due to the smoothing operation between two entities under study, for example, catchments in hydrological studies. However, here we attempt at defining leakage as a concept associated solely related to the filter, and therefore it is *agnostic* to the type of application. This also has been our intention while designing this performance metric.

#### §4.6 HIGHEST SIDE-LOBE LEVEL

The side-lobes beside the main-lobes are mostly effects of harmonic transforms of non-smooth spectral filter windows [Hamming, 1989]. Nevertheless, they can also be due to the negative correlation between the points as well as in the case of stochastic filters. In general, if these side-lobes occur due to truncation effects or non-smooth filter windows, they are considered as one of the major contributors to leakage [Harris, 1978], and hence, their suppression is an important design criteria in filter design literature (e.g., Nutall [1981]; Bergen and Antoniou [2004]). The highest side-lobes contribute the most to the leakage of signal, and therefore, measuring their amplitude gives a good idea of the leakage one can expect. This is an important quantity both for noise reduction and resolution reduction as it determines the single largest unwanted contribution from outside the main-lobe. For non-zero-crossing windows, we will take the value of the window immediately after the resolution distance as the highest side-lobe level.

#### §4.7 SIDE-LOBE ROLL-OFF RATIO

The faster the side-lobes decay to zero the lesser the spatial leakage will be. The rate of decay of the side-lobes is measured by the *side-lobe roll-off ratio*. It is defined as the ratio between peak window weights of the first and last side-lobe (cf. figure 4.1). In some windows the side-lobes might not decay linearly, but even in those cases this measure will give a sense of the rate of side-lobe decay. For non-zero-crossing windows, we will take the ratio between window weights at the resolution distance and at the end of the window. It should be noted that the side-lobe roll-off ratio and highest side-lobe level are explanatory metrics for the spatial leakage metric.

IN THIS CHAPTER we will put to test the filters whose designs were discussed in chapter 3 using the performance metrics in chapter 4. For the analysis, we will deal with the isotropic and homogeneous filters separately from the others. The reason for dealing with them separately should become clear as soon as we distinguish the performance metrics, for the sake of convenience, into *global* and *local* performance measures.

We will discuss the performance of the filters one by one starting with the homogeneous isotropic filters. Thereafter, we will continue with the inhomogeneous anisotropic filters, and finally provide remarks on the performance of the filters put to test. Since we draw from our experiences on filtering gravity field data in general and GRACE data in particular, whenever the metrics require the knowledge of the signal or noise they will be drawn from the spherical harmonic models of the gravity field and its temporal variations. Due to this dependence the remarks here will mostly pertain to the signals similar in character to the gravity field and its temporal variations.

In order to illustrate the use of the performance metrics, in this chapter we have used the static gravity field model GO-CONS-GCF-2-DIR-R4 from GOCE [Rummel et al., 2011] data computed by Bruinsma et al. [2013]; and for the temporal variations of the gravity field, we have used GRACE data GFZ release 05, processed by GeoForschungsZentrum (GFZ), Potsdam [Dahle et al., 2013]. The static gravity field model from GOCE will be used mainly for illustrating the spatial resolution, and the other performance metrics will be calculated using the GRACE data. In this analysis a total of nine different filters have been used, of which seven are homogeneous isotropic filters and the other two are latitude dependent anisotropic filters.

## §5.1 HOMOGENEOUS ISOTROPIC FILTERS

The homogeneous isotropic filters have been grouped according to whether their filter design is done in the spatial domain or in the spectral domain. For the filters that have a spectral design (ideal low-pass, diffusion, spectral cosine and Butterworth filters), cut-off degree is one of the parameters, for which we take values from  $l = 10$  to 80 in steps of 10. For the filters that have a spatial design (Pellinen, Gauss and von Hann filters), smoothing radius is the design parameter, and for which we take values between  $1^\circ$  to  $20^\circ$  in uneven steps (cf. Figure 5.2).

### Ideal low-pass filter

In general, gravity field estimates are disseminated as spherical harmonic expansions up to a maximum spherical harmonic degree ( $L$ ), thereby making the field band-limited between the frequencies 0 and  $L$ . As per (2.1a), by definition the spherical harmonic expansion extends up to infinity, but in practice these are developed up to degree  $L$  due to a variety of reasons: spatial sampling, measurement accuracy and computational limits. This band-limitation can be expressed as a *low-pass* filter as shown in Table 3.1. This filter is referred to as the *ideal low-pass filter*, *Shannon window* and *box-car filter*. Due to the nature of its spectrum the filter is homogeneous and isotropic.

#### Anatomy

The spectral design of the filter is straight-forward with the value ‘1’ for all the degrees that need to be retained and zeros for the others (cf. Figure 5.1). The corresponding spatial form of the filter shows that there are many side-lobes of high magnitude and also of similar width to the filter main-lobe. These side-lobes are the oscillations due to the abrupt change in the spectral weights of the filter. Due to the high magnitude of the side-lobes we see that the filter takes significant magnitudes of signal far away from the calculation point in order to perform smoothing. Also, due to the oscillating nature of the smoothing kernel, we see that the sign of the signal is inverted.

#### Spatial resolution

The resolution of any given filter is depicted by its *modulation transfer function* (MTF) (cf. section 4.4). The MTF of the ideal low-pass filter is shown in Figure 5.2 for a range of spherical harmonic degrees. The striking features of the curves are their steep slopes and the oscillation of the modulation transfer values around one. While the steep slope of the MTF indicates that the filters decay to zero very quickly, the oscillation is caused by the well-known ringing effect caused by the truncation of a harmonic series at a finite degree  $L$ . Further, the magnitude of the overshoot remains nearly the same for all the degrees of truncation shown here, but their convergence to unity clearly depends on the number of spherical harmonic degrees involved in the synthesis: the more the harmonic degrees faster the convergence.

Truncating a field of gravity anomalies, expanded up to degree  $L = 260$ , to degree  $L = 60$  we see the smoothing effects of the ideal low-pass filter in Figure 5.3. The ideal resolution of the filter is  $4.54^\circ$ , and we see that it resolves the features that are separated by as much as or more than the ideal resolution. Here, we also see the outcome of the steep MTF, i.e. the filter is able to depict the modulations that are separated by shorter distances, but more than the ideal resolution. Nevertheless, due to its big side-lobes it also overshoots the unfiltered modulation, for example at  $160^\circ$  co-latitude. The panel depicting a portion of the filtered field also shows that the smoothed field faithfully represents the unfiltered field to a large extent.

#### Performance

The performance metrics in Figures 5.5 and 5.6 also show the peculiarities of the ideal low-pass filter. For any given spatial resolution the ideal low-pass filter has the largest variance, the least processing loss, constant spatial leakage and highest side-lobe level. Also the spatial

leakage is the largest for all the filters analysed here. The fact that the ideal low-pass filter takes a lot signal from data points far away from the calculation point affects its variance. The large spatial leakage is explained by the facts that the filter has very high side-lobe level and poor roll-off ratio. On the positive side it is the best filter when it comes to the trade-off between processing loss and processing gain.

### Diffusion filter

The diffusion filter on the sphere was introduced by Sardeshmukh and Hoskins [1984] for smoothing global atmospheric data. The diffusion filter of order  $k = 1$  provides nearly the same weights as that of Gauss filter for a given spatial resolution. This is not surprising as Gaussian functions are used for solving diffusion equations. For the analysis here, though, we will use diffusion filters of order  $k = 2$ .

### *Anatomy*

The spectral form of the diffusion filter gradually reduces to insignificant values, but the spatial form is ridden with a lot of low magnitude ripples (cf. Figure 5.3). The highest side-lobe is less than one order of magnitude and it rolls off very quickly to insignificant magnitudes. Due to the quick damping of the filter weights the signal from data points far away from the calculation point are not taken for computing the filtered field.

### *Spatial resolution*

The MTF of the diffusion filter has moderately steep slope. Due to the presence of ripples in the spatial form, the MTF overshoots but quickly recovers to unity. This quick recovery can be attributed to the steep roll-off of the side-lobes. The filtered gravity anomalies also reiterate the moderately steep slope of the diffusion filter as they depict only the overall profile of the field. All but the features that are separated by distances much greater than the ideal resolution are smothered, resulting in a smooth field.

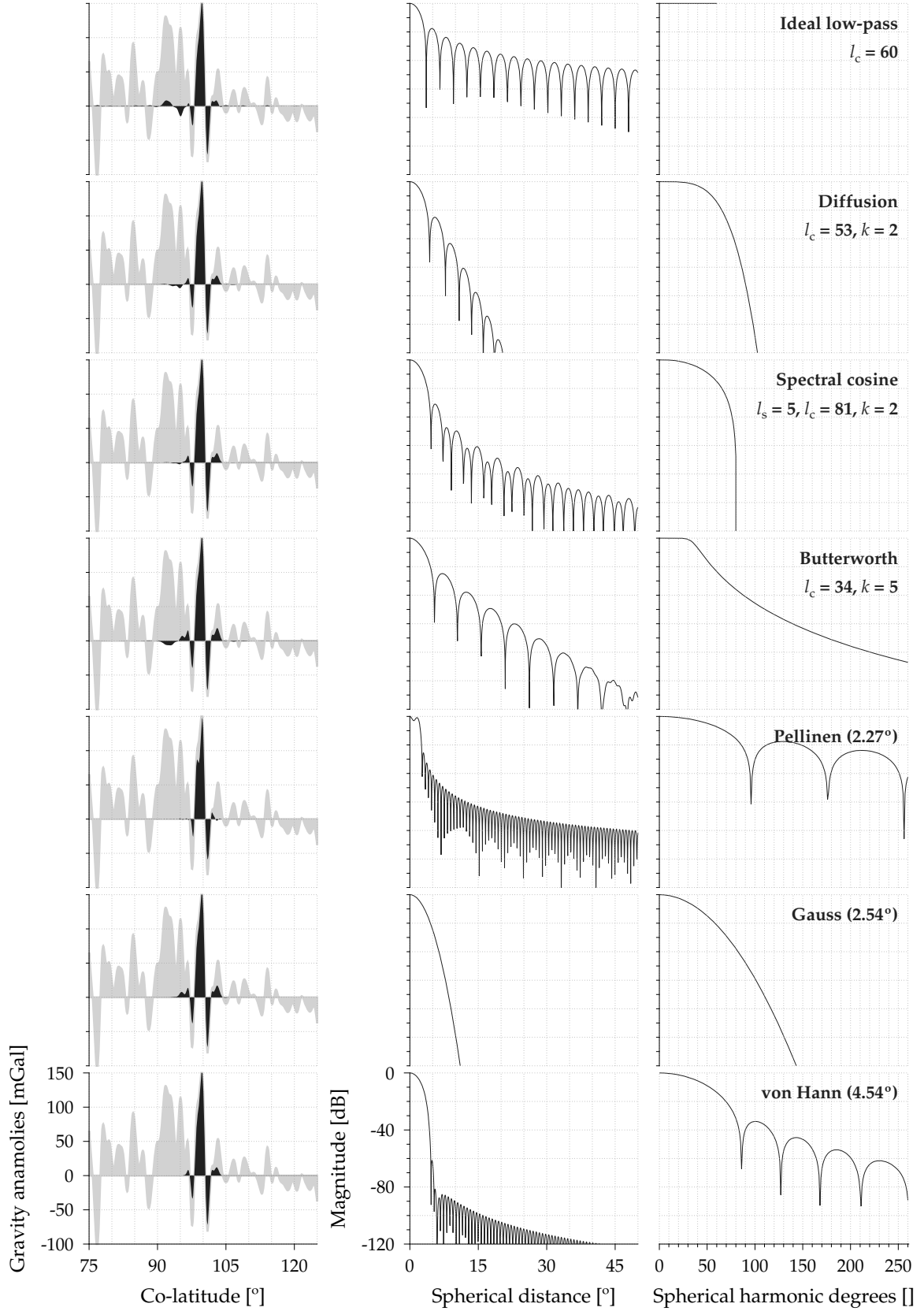
### *Performance*

There are a number of performance metrics in which the diffusion filter displays desirable characteristics. It has a smaller variance for any given spatial resolution and it has good processing gain for gravity field type signals and a highly desirable balance between processing loss and processing gain. It also nearly has a constant highest side-lobe level and a constant spatial leakage. Like in the case of the ideal low-pass filter the leakage is dictated by the highest side-lobe level. Among the filters analysed here it has the steepest roll-off slopes.

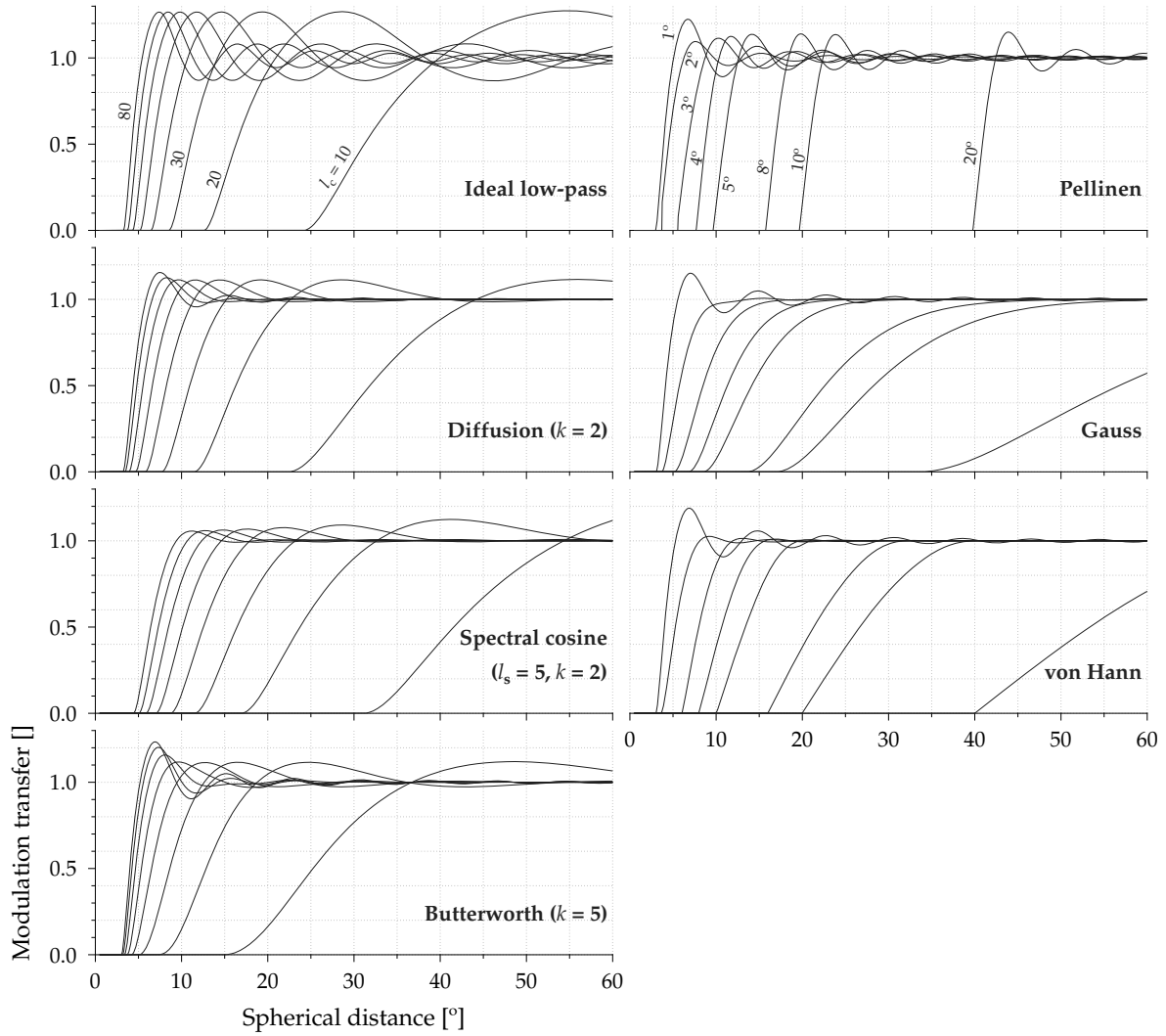
### Spectral cosine filter

The spectral cosine filter is an adaptation of the cosine taper [Harris, 1978], adapted by Longuevergne et al. [2010]. The distinct design of this filter is that it can be used to smooth a particular bandwidth of the spectrum by way of the two parameters start degree  $l_s$  and cut-off degree  $l_c$  (cf. Table 3.1). The parameter  $l_c$  allows for changing the bandwidth of the given field.





**Figure 5.1:** Depiction of the log-magnitude of the filters used in Figure 5.3 and also the amount of signal gathered by a filter to provide the smoothed value at the calculation point (left-most panels)



**Figure 5.2:** Modulation transfer functions of the homogeneous isotropic filters for different filter parameters. Filtering radius is the parameter for the filters on the right-hand-side and spherical harmonic degree for the filters on the left-hand-side.

### *Anatomy*

The spectrum of the spectral cosine filter has a sharp decrease at around the cut-off degree. This sharp decrease results in side-lobes that are less than two orders of magnitude than the peak main-lobe value. This makes sure that not a lot of signal is drawn from data points far away from the calculation point. In comparison with the diffusion filter the spectral cosine has a slightly wider main-lobe. Further, the side-lobes roll-off far more gently than the diffusion filter.

### *Spatial resolution*

Due to the similarities between the main-lobe behaviour of the spectral cosine and the diffusion filters, their modular functions also have similar behaviour if their ideal resolutions match. For example, the spectral cosine filter of order 2 with a cut-off degree of 30 and starting degree of 5, has the nearly the same MTF as a diffusion filter of order 2 with a cut-off degree of 20, except for the level of the modulation overshoot (Figure 5.2). The spectral cosine also has

modulation overshoot due to the presence of negative side-lobes. The longitude profile of the spectral cosine filtered GOCE field shows a lot of similarities with the profile filtered with the diffusion filter. However, the maps of the filtered fields show the dissimilarities quite clearly: the spectral cosine filter smothers the field a bit more than the diffusion filter (Figure 5.3).

### *Performance*

The spatial variance of the spectral cosine filter is very desirable when the bandwidth between the cut-off degree and the starting degree is wide enough. When the smoothing bandwidth becomes smaller there are a lot of high magnitude ripples (not shown here). Also the processing gain and the balance between processing gain and processing loss are at highly desirable levels. It is also quite clear that spatial leakage shoots up as soon as the bandwidth becomes very narrow ( $l_c - l_s = 25$ ) (Figure 5.5). This is also the case with the highest side-lobe level, which also increases with decreasing bandwidth (bottom panel Figure 5.6). Here again, we see that the highest side-lobe influences the spatial leakage (top panel Figure 5.6). From the performance metrics it is obvious that although this filter offers a way to reduce the bandwidth of the field in hand, it cannot reduce it below a certain level (35 degrees for the filter analysed here) without some undesirable results.

### **Butterworth filter**

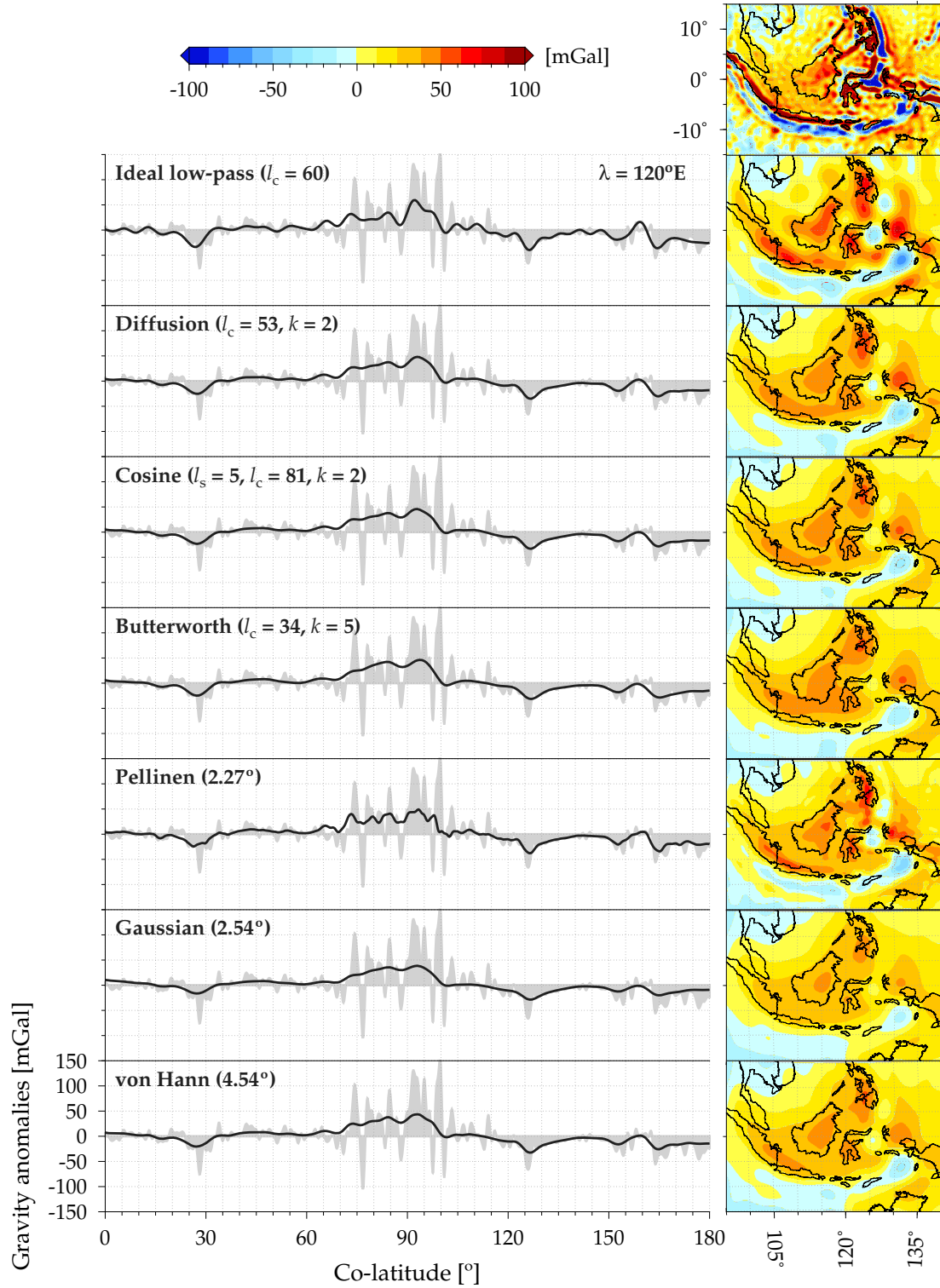
The Butterworth filter is also an adaptation of the filter of the same name in one-dimensional Fourier analysis. This is a two parameter filter like the diffusion filter—cut-off degree  $l_c$  and order  $k$ —with the interesting property that the cut-off degree always receives half the weight of the peak. Another interesting aspect is that a Butterworth filter of very high order approximates an ideal low-pass filter, but such high orders are never used in practice.

### *Anatomy*

The spectral form of the filter has a gradual decrease in weight as the filter approaches the higher degrees and provides equal weight to the degrees lower than the cut-off. This causes the spatial form to have ripples that are as wide as the main-lobe. The side-lobes roll off pretty quickly and their magnitude is less than one order of magnitude of the main-lobe peak. Also, the main-lobe is rather wide compared to the other filters. Due to its high side-lobes it also grabs signal from data points that are far away from the calculation point. Figure 5.1 shows that such signal values are as big as the ideal low-pass filter.

### *Spatial resolution*

Butterworth filters transfer modulation like the diffusion and the spectral cosine filters when the cut-off degree is not very close to the total bandwidth. If the cut-off degree is close to the total bandwidth, then the MTF shares similarities with the ideal low-pass filter with big modulation overshoot and oscillating around unity (Figure 5.2). The longitude profile like in the case of the spectral cosine filter shows normal behaviour, but the spatial plot shows that areas that are disconnected in the other filtered fields are all connected here (Figure 5.3).



**Figure 5.3:** Comparison of unfiltered and filtered GOCE data along a longitudinal profile of  $120^\circ$  E. The filter parameters are given in the brackets adjacent to the label indicating the filter.

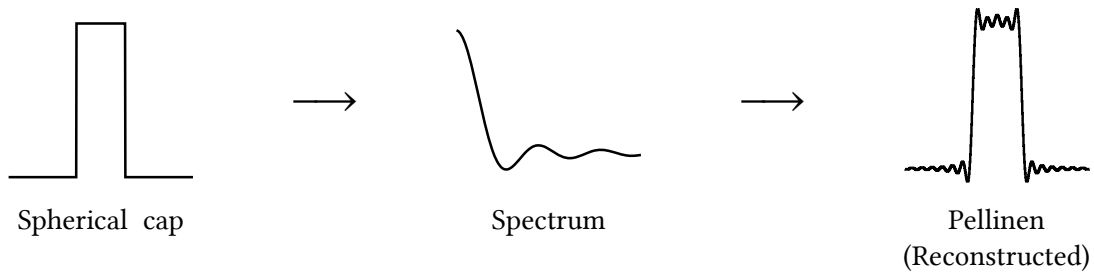
### Performance

The best feature of the Butterworth filter is that it can balance processing gain and processing loss better than all the filters except ideal low-pass filter (Figure 5.5). On the contrary, it has very high spatial leakage, which hovers around a constant value for low spatial resolutions.

The spatial leakage has an intriguing relationship with the highest side-lobe level: the spatial leakage is bounded within a small range, and highest side-lobe level varies heavily irrespective of its resolution (Figure 5.6). The other undesired characteristic of the Butterworth filter is its large variance compared to the other filters compared here, but a lot smaller than the ideal low-pass filter.

### Pellinen filter

The Pellinen filter gets its name from *L. P. Pellinen* who devised a method to calculate [Pellinen, 1966] the Legendre spectrum of the *spherical cap filter*. For this reason, the Pellinen filter is a reconstructed form of the spherical cap filter (cf. Figure 5.4). The spherical cap filter is designed to provide uniform weights for all the data points within the smoothing radius (cf. Table 3.1), which is similar in design, though spatially, to the ideal low-pass filter. Although the weights of the Pellinen filter are not uniform within the prescribed smoothing radius, due to the Gibbs effect (cf. Figure 5.4), it can still be considered as the spatial counterpart of the ideal low-pass filter.



**Figure 5.4:** Depiction of Pellinen filter, which is the reconstruction of a spherical cap from its spectrum. The ripples in the reconstructed form is the well-known Gibbs effect.

### Anatomy

The Pellinen filter displays the Gibbs phenomenon in its full form. The log-magnitude of the filter shows plenty of ripples, and also a few within the smoothing radius (cf. Figure 5.1). Although there are ripples, their magnitude is mostly two to three orders of magnitude of the main-lobe. Not only does the spatial form contain ripples, but also the spectral form, and their magnitude is close to one order of magnitude less than the main-lobe magnitude. In comparison with the spectra of other filters, the side-lobe magnitude of the Pellinen is the highest. Due to this reason it cannot be strictly classified as a low-pass filter. More precisely, because they retain a large part of the higher harmonic degrees, they cannot be classified as low-pass filters in its strictest sense. This brings up the problem of differentiating smoothing and low-pass filters. Based on the above observation it can be said that not all smoothing operations enable low-pass filtering, but all low-pass filtering naturally enables smoothing. The anatomy of the Pellinen filter reinforces the uncertainty principle that in order to constrict the signal within a small space a large part of the spectrum must be used.

### Spatial resolution

The ideal spatial resolution of the spherical cap filter is twice the radius of the spherical cap, and will have a right angular modulation transfer function. It means that all the features that

are separated by twice the spherical cap radius will be resolved with the same modulation as the unfiltered field. However, the reconstructed spherical cap also has the same ideal resolution as the spherical cap filter, but the modular transfer function is not right angular. The Pellinen filter has the steepest modulation transfer function of all the filters analysed here (cf. Figure 5.2).

The impact of the steep modulation transfer function can be seen in the filtered GOCE gravity anomalies (Figure 5.3). The Pellinen filtered field retains a lot more details compared to other filters. The reason for this can be ascribed to the significant power left in the higher harmonics even after filtering (Figure 5.1). However, it is clear from the longitude profile of the filtered field that the peaks and valleys are shifted in space (Figure 5.3). The reason for this might be the interplay between equal weight given to all the data points within the filter radius and the Gibbs effect. For example, the negative peak at around  $97^\circ$  in the longitudinal profile appears at about  $96^\circ$ . The smoothing kernel located at the valley point takes the complete negative peak. The remaining positive values are to some extent compensated by the negative ripples that invert parts of the neighbouring positive peaks to negative values.

Equal weights given to all the data points within the smoothing radius flattens the big peaks and valleys in the smoothed field. This is very obvious in the longitude profile between the co-latitudes  $70^\circ$ – $105^\circ$ . The side effect of this flattening is that the overall profile of the field is not faithfully reproduced.

### *Performance*

The strongest feature of the Pellinen filter is that it has strong localisation properties, because for any given spatial resolution it has the smallest spatial variance. This is also clearly visible in the map of the Pellinen filtered field (right panel of Figure 5.3), where the filtered peaks and valleys are not spread out as in the case of the other filters, but rather confined to a smaller area. This localisation property also explains the coarseness of the filtered field and also the lower levels of spatial leakage. However, in other performance metrics the Pellinen filter falters: for any given spatial resolution it has the least processing gain and also it is the poorest in terms of balancing processing loss and processing gain. Due to the Gibbs effect some of the performance metric curves also show jumps and are jagged unlike the other filters.

### **Spatial cosine filter**

The spatial cosine filter is an adaptation of the cosine taper function from one-dimensional Fourier analysis. Spatial cosine filter like its spectral counterpart (spectral cosine filter) has a cut-off radius ( $\psi_0$ ) and an order ( $k$ ). The spatial cosine filter of order  $k = 2$  is called the von Hann filter [Jekeli, 1981]. For the von Hann and the other cosine taper windows, their weight reduces to half of the peak value at half of the smoothing radius. This is very similar to the definition of the Gauss filter used here. Due to this reason the filtering radii of the von Hann filters analysed here are taken to be twice that of the Gaussian filters analysed here.

### *Anatomy*

There are a number of similarities between the anatomies of the Pellinen and the von Hann filters. Like the Pellinen filter the spectral form of the von Hann filter also has negative

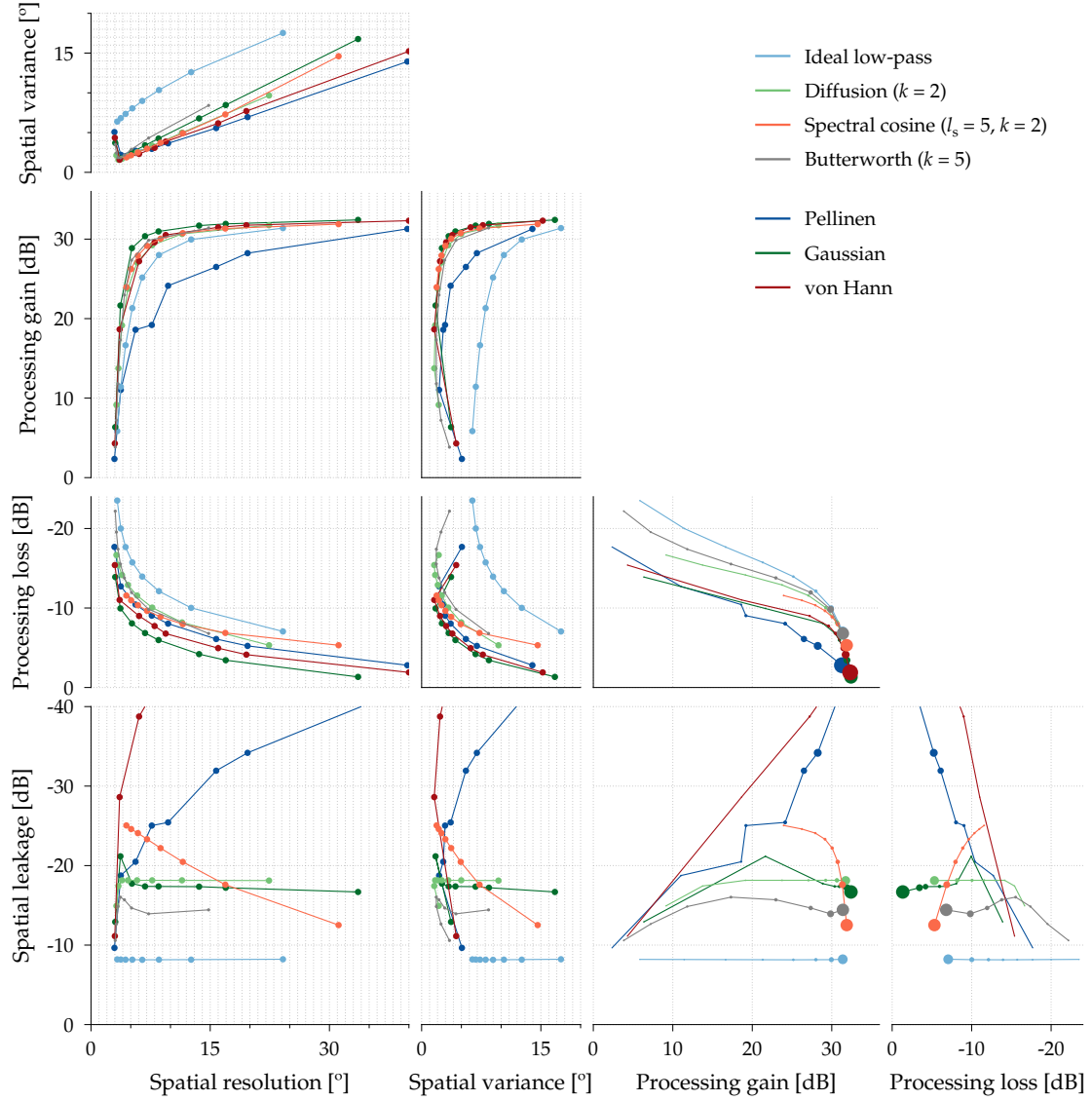
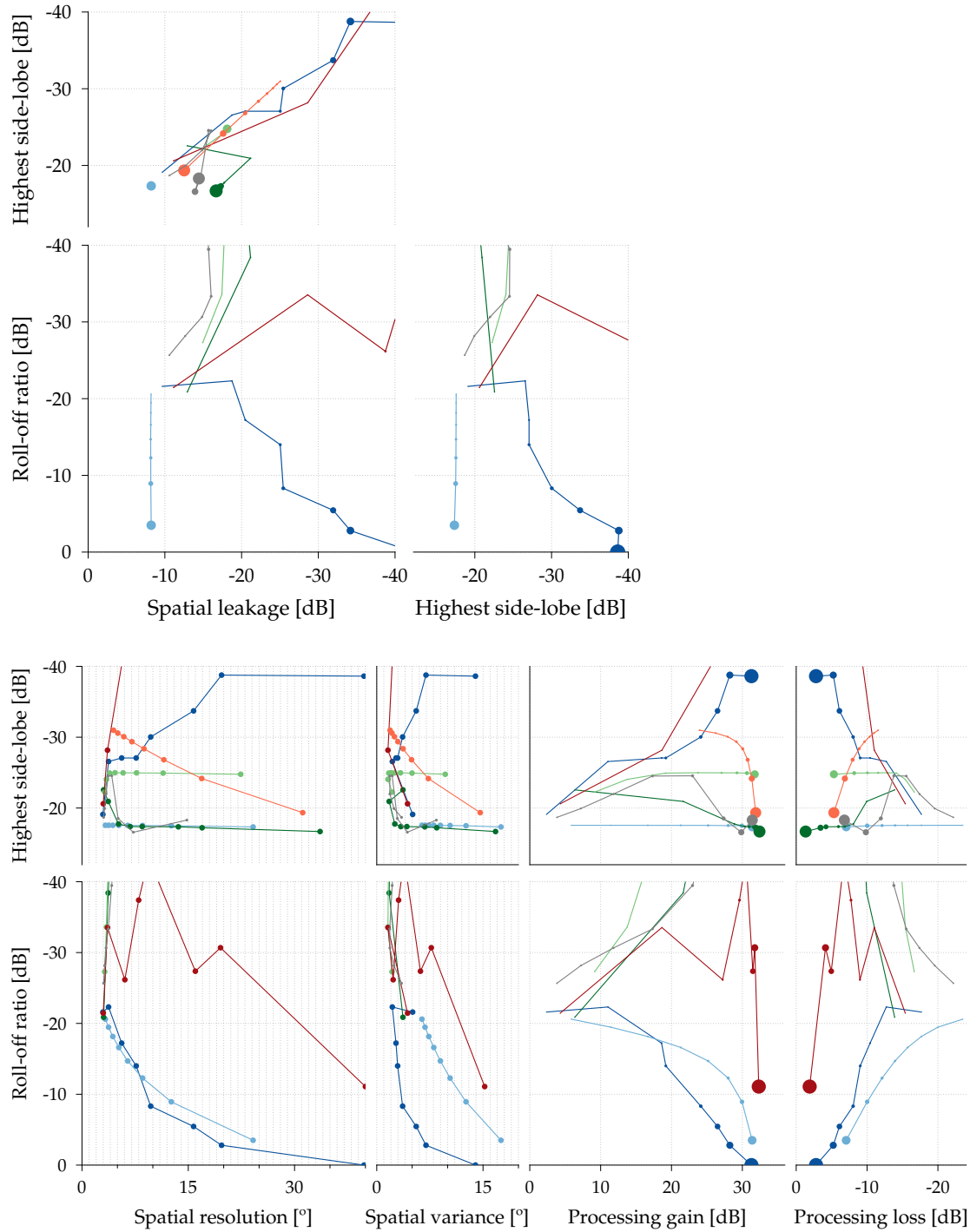


Figure 5.5: Scatterplots of the different performance metrics.

side-lobes but their magnitude is nearly two orders of magnitude less than that at the peak. Also the spatial form of the filter has a lot of side-lobes, but except for the highest side-lobe all of them are four orders of magnitude less than the value of the peak of the main-lobe. From the profile it is also easy to see that the von Hann filter does not take value outside its smoothing radius due to the insignificant filter window weights.

### Spatial resolution

The remarkable feature of the von Hann filter is that the ideal resolution of the filter is its smoothing radius. However, the MTF curves for the von Hann filter show that the resolution is slightly more than the smoothing radius itself, which is due to the presence of the side-lobes in the reconstructed filter. The slope of the MTF curves are moderately steep and reflect the piece-wise nature of the filter as the MT values increase sharply from zero. In contrast to the previously discussed filters the modulation overshoot is only present for filters that have a relatively smaller smoothing radius ( $\psi_0 < 8^\circ$ ). The smoothed longitude profile of the gravity anomalies shows that the von Hann filter is able to transfer the modulations to a



**Figure 5.6:** Scatterplots of the the different performance metrics with high side-lobe level and side-lobe roll-off ratio.

large extent, but damps the output much more than the other filters.

### *Performance*

For any given spatial resolution the von Hann filter provides the lowest spatial leakage (Figure 5.5), and it has also one of the lowest side-lobe levels (bottom panel of Figure 5.6). The filter localises the signal in a desirable manner and it is only superseded by the Pellinen filter. Nevertheless, the filter suffers from significant processing loss and even though it has



a desirable processing gain, it cannot balance between them both. Here again the spatial leakage is strongly influenced by the highest side-lobe level.

### Gauss filter

The Gaussian function is a unique function in that its spatial and spectral forms are both bell-shaped curves that converge to zero asymptotically. Further, the smoothing radius of the generic form of the Gaussian filter is the spread of the filter, but for the sake of convenience the smoothing radius is defined at a certain fraction of the peak value – in geodesy the fraction is taken to be one-half of the peak value.

### Anatomy

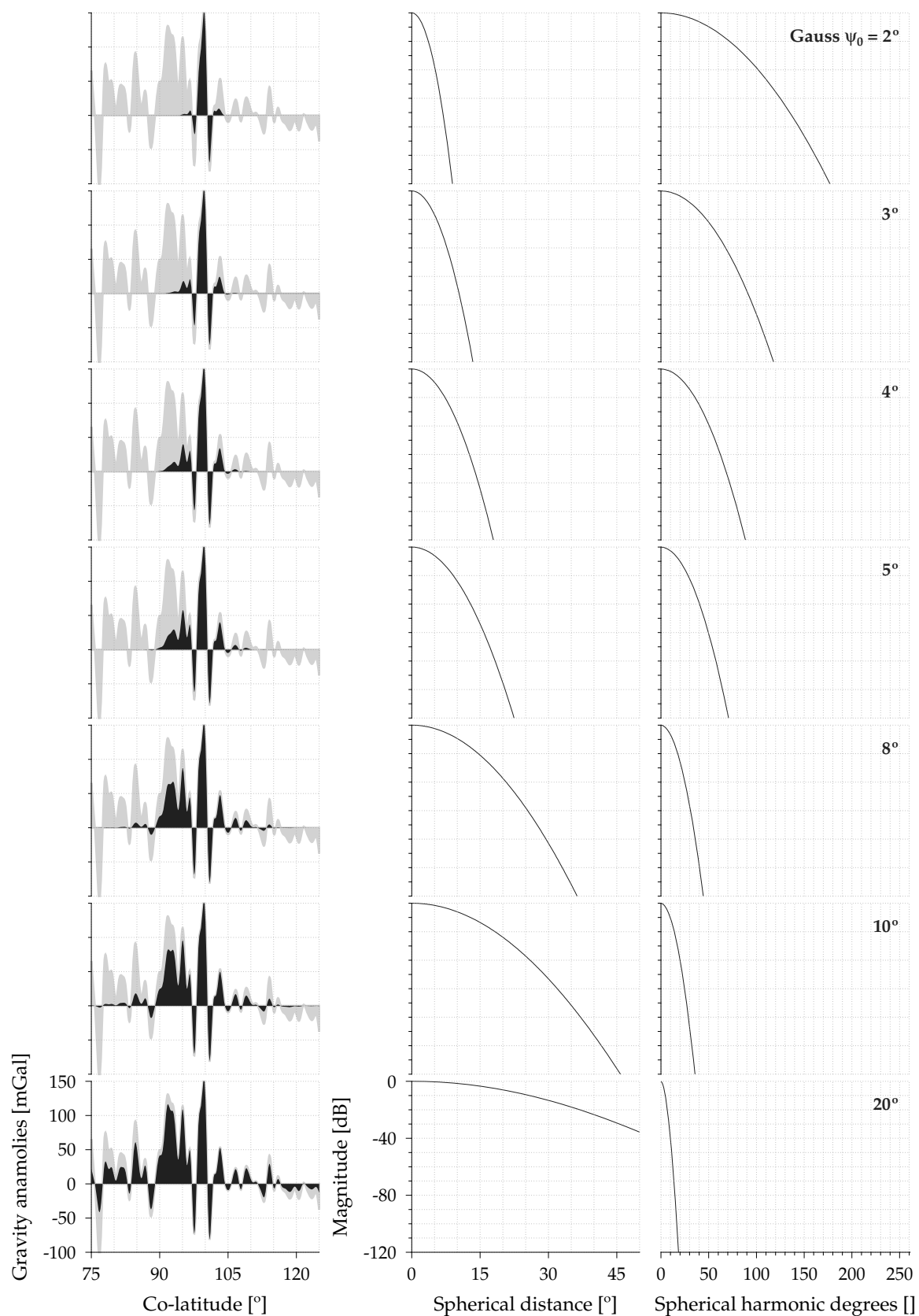
The Gauss filter has one of the most unique and simple anatomies. It is unique, because it is the only filter whose spatial and spectral forms share the same shape and do not have any ripples. And simple, because as mentioned previously, both the spatial and spectral forms of the filter take the shape of a bell (cf. Figure 3.2). In addition to this, the filter kernel and its spectra become zero only asymptotically, which is why the log-magnitude gradually diminishes away to insignificance. It should also be noted that the Gauss filter is predominantly wider than the other filters analysed here.

### Spatial resolution

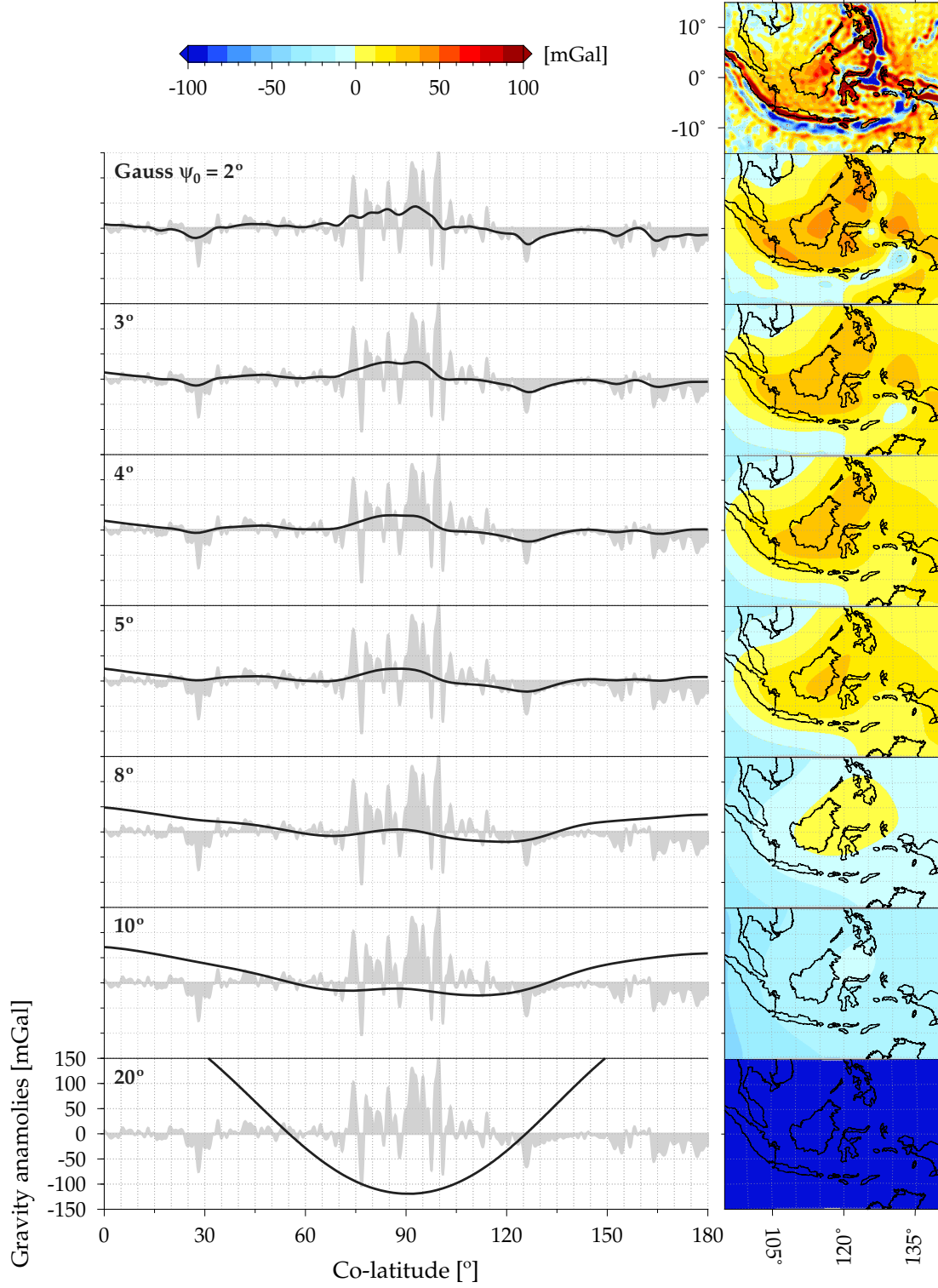
The MTF of the Gaussian filter shows that the resolution is almost double the smoothing radius. It rises from zero and converges to one in an asymptotic manner, while increasing along a gentle slope. Due to these characteristics, the Gaussian filter takes a lot of distance to completely reproduce the input modulation. For example, the Gauss 5° filter – a very widely used smoothing radius in the GRACE community – needs a signal separation of at least 20° to completely resolve the signals (cf. Figure 5.2). This can again be explained by the asymptotic nature of the Gaussian filter, which implies that in realistic signal scenarios the Gauss filter will not be able to reproduce the unfiltered modulations and provide smoother signals.

The profile filtered with the Gauss filter provides the smoothest profile, and therefore, shows very few details. In addition to the lack of details, the amplitude of the filtered field is also considerably reduced. The spatial map of the Gaussian filtered field is replete of any features that are visible in the other filtered fields due to the high level of smoothing. In Figure 5.8 we can see the impact of using different filter radii for filtering the gravity anomalies. Beyond a smoothing radius of 4° the details are completely lost and we see only the long wavelength profile of the field. It is interesting to note that the field filtered with 20° smoothing radius does not have any semblance to the anomalies in the area in view. This can be taken as an indicator to the way filtering works when we deal with a field with details smoothed by a disproportionately large smoothing radius.

*Remark* The smoothing radius of the Gauss filter is chosen as the -6 dB point, which is defined as the filter resolution in one-dimensional signal processing [Harris, 1978]. However, we have demonstrated here that the ideal resolution is far more than the -6 dB point. The ideal resolution point in general lies between  $1/8$  and  $1/10$  of the peak with the fraction decreasing with increasing resolution. To facilitate the user the Gauss smoothing radius can



**Figure 5.7:** Depiction of the log-magnitude of the filters used in Figure 5.3 and also the amount of signal gathered by a filter to provide the smoothed value at the calculation point (left-most panels)



**Figure 5.8:** Comparison of unfiltered and filtered GOCE data along a longitudinal profile of  $120^\circ$  E. The filter parameters are given in the brackets adjacent to the label indicating the filter.

be redefined as  $1/10$  rather than  $1/2$  to directly reflect the ideal resolution of the filter. We can thus rewrite (3.8) as

$$b(\psi) = \frac{a_o}{\sinh a_o} e^{a_o \cos \psi}, \quad \text{with } a_o = \frac{\ln(10)}{1 - \cos \psi_o}. \quad (5.1)$$

### Performance

The strength of the Gauss filter lies in its ability to subdue noise, thereby providing a very good processing gain (Figure 5.5). It is clear that it provides the highest possible processing gain for any given spatial resolution, but this comes at the cost of heavy processing loss. This is also reflected in the poor balance between processing gain and processing loss. The Gauss filter also suffers from poor variance and an undesirable leakage level, which is explained by the highest side-lobe levels\* that are on par with those of the ideal low-pass filter. Despite such high side-lobe levels, the steep roll-off of the filter keeps the spatial leakage under check. For filter radii greater than  $3^\circ$ , the spatial leakage increases only gradually stabilising around -18 dB.

### §5.2 INHOMOGENEOUS ANISOTROPIC FILTERS

The difficulties in analysing inhomogeneous anisotropic filters are immediately apparent from Figures 5.11 and 5.18, where we need to consider the direction of the data points, the location of the calculation points and the different filter parameters. In the case of homogeneous isotropic filters, we could analyse the spatial resolution with other performance metrics and study their inter-relationship. Here, due to the involvement of inhomogeneity and anisotropy we will not be able to make such a study.

In the following sections we will analyse the destriping filter cascaded with a Gauss filter and the regularization filter. Since these filters change their spatial structure with the latitude, we have shown the performance metrics that depend on the calculation point and azimuth for four different co-latitudes ( $0^\circ$ ,  $30^\circ$ ,  $60^\circ$  and  $90^\circ$ ). Those that depend only on the calculation point have been shown for three additional co-latitudes ( $15^\circ$ ,  $45^\circ$  and  $75^\circ$ ). As these filters are symmetric across the equator in the direction of the poles, only the co-latitudes in the northern hemisphere are considered. The performance metrics then hold good for the complementary co-latitudes in the southern hemisphere.

For the cases of the processing gain and processing loss, we will use field-specific quantities rather than those derived from the power-laws. This is because the amplitudes of the unfiltered and filtered coefficients do not share a linear relationship, if an inhomogeneous and anisotropic filter is used (cf. (2.35a)). In the case of the homogeneous isotropic filters, the damping factor we used was

$$\alpha = \frac{\sum_{l,m} B_l^2 F_{lm}^2}{\sum_{l,m} F_{lm}^2}. \quad (4.5)$$

$$= \frac{\sum_l B_l^2 \sum_m F_{lm}^2}{\sum_l \sum_m F_{lm}^2} \approx \frac{\sum_l B_l^2 \sigma_l^2}{\sum_l \sigma_l^2}, \quad (5.2)$$

where we have replaced the degree variances of the field  $\sum_m F_{lm}^2$  with the power-law degree

---

\*It must be recalled that for smoothing kernels that do not have a side-lobe the largest weight outside the ideal resolution is taken as the highest side-lobe level.

variances  $\sigma_l^2$ . The damping factor for the case of the latitude-dependent anisotropic filters reads

$$\alpha = \frac{\sum_{l,m} \left( \sum_n B_{lm}^{nm} F_{nm} \right)^2}{\sum_{l,m} F_{lm}^2}, \quad (5.3)$$

where we cannot replace the degree variance of the field with the power-law based degree variances. This necessitates the computation of the damping factor as follows:

$$\alpha = \frac{\sum_{l,m} \left( \sum_n B_{lm}^{nm} F_{nm} \right)^2}{\sum_l \sigma_l^2}. \quad (5.4)$$

### Destriping filter

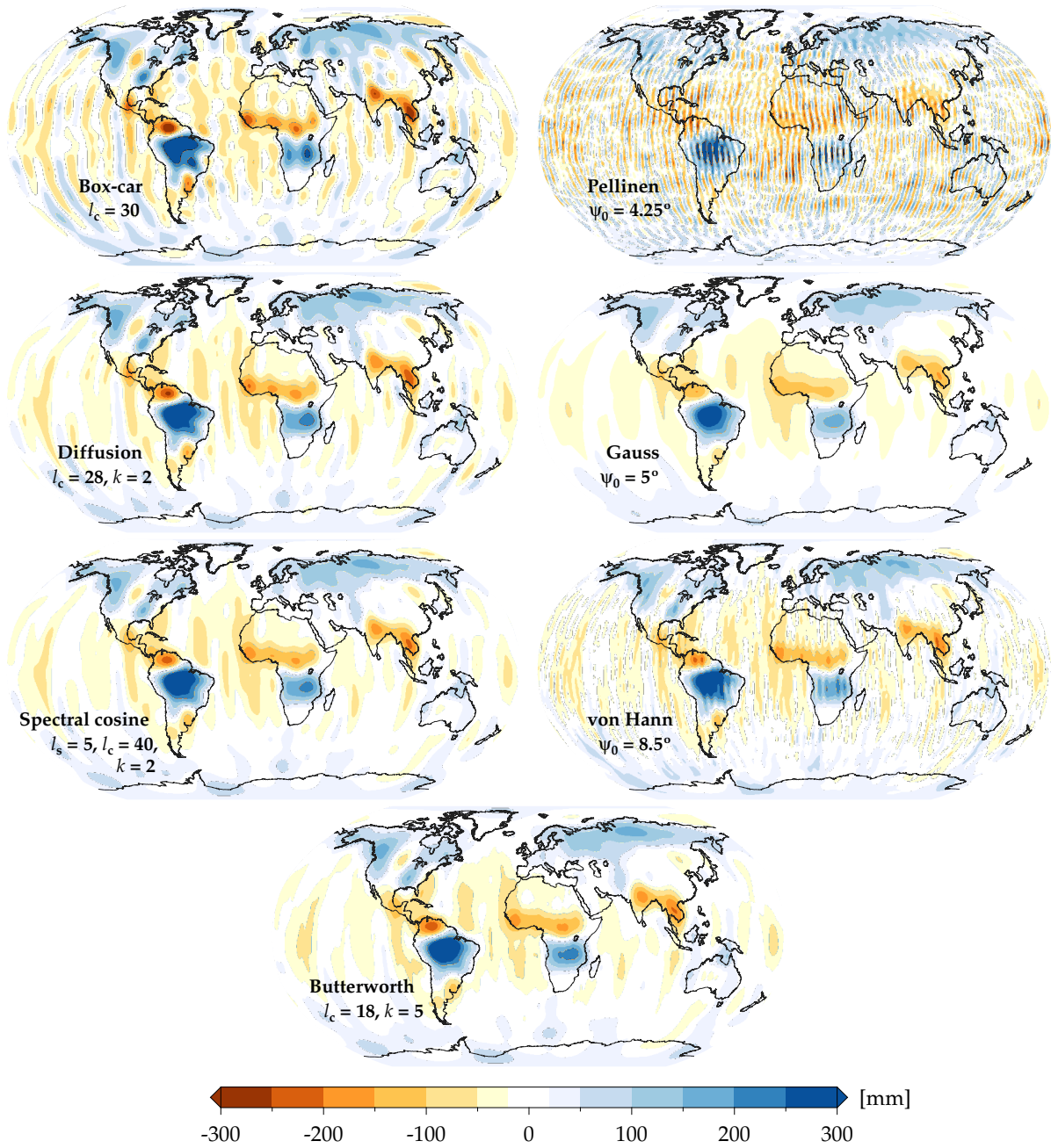
The destriping filter is always used in conjunction with the another low-pass filter (predominantly the Gauss filter), and we termed it a cascading filter (cf. section 3.4). Due to the block-diagonality structure of its spectrum, it is anisotropic and inhomogeneous across the latitudes (Table 2.2 and Figures 5.10 & 5.12).

### Spatial resolution

The spatial resolution of the cascade of destriping and Gauss filters is shown in Figure 5.11, for different smoothing radii of the Gauss filter, and in Figure 5.13, for different parameters (minimum spherical harmonic orders) of the destriping filter. We see that the spatial resolution is affected by both the smoothing radius of the Gauss filter and the order at which destriping is commenced. The influence of the smoothing radius of the Gauss filter is predictable in that the resolution decreases with increasing smoothing radius.

A peculiarity of the latitude dependent kernels shows up in the modulation transfer function at the pole of the destriping filter. The modulation transfer function is isotropic at the poles (Figures 5.11 and 5.13). This is due to an interplay between the isotropy at the poles (cf. (2.28a)) and latitude-only dependence of the smoothing kernel. At every spherical distance the polar kernel interacts with the other kernels at their zero azimuth. Further, at every azimuth for a given spherical distance from the polar kernel the smoothing kernels do not change. Thus, the polar kernel encounters the same weight at a given spherical distance for every azimuth. This is the reason that we get an isotropic MTF for the smoothing kernel at the pole.

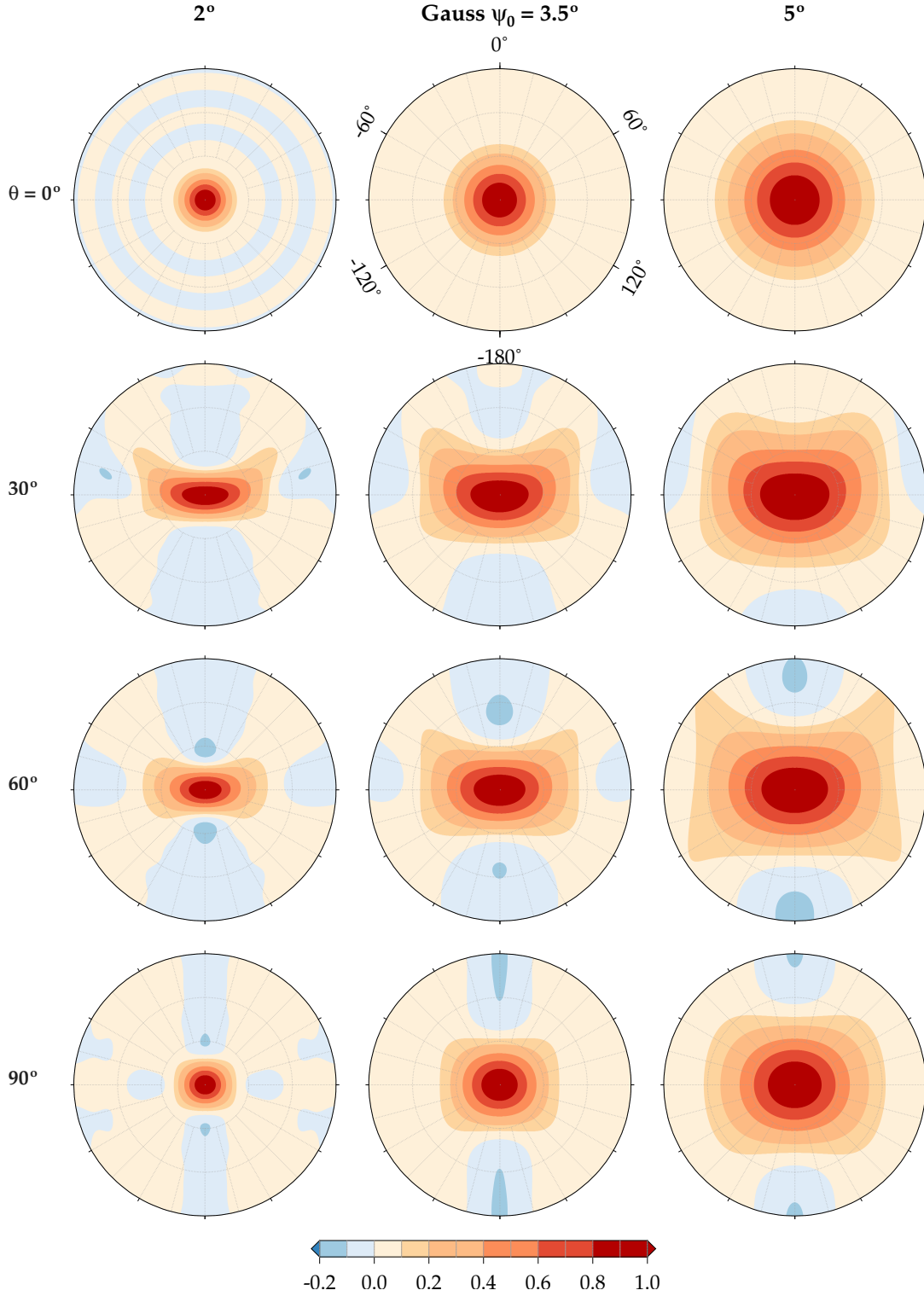
Overall there is a strong congruence between the filter structure and the corresponding MTF in terms of the shape and size of the ideal resolution isoline. However, for the case when destriping commences at order  $m=2$ , the MTF of the smoothing kernel at the pole is at odds with its filter structure. While the filter structure at the pole is the same for the cases of  $m=8$  and 20, the ideal resolution is far more wider than for those two cases (cf. Figure 5.13). By commencing the destriping from order 2 we reduce the weight of the spectrum for



**Figure 5.9:** GRACE data for April 2008 filtered with the homogeneous isotropic filters analysed here. All the filters have the same ideal resolution of  $8.5^\circ$ .

the very low degrees. Therefore, as soon as the tesseral and the sectorial coefficients begin to play a role in the spatial structure of the non-polar calculation points they increase the smoothing. The commencing order for destriping affects the filter structure at almost all the calculation points.

In general, the MTF starts from isotropy at the poles becoming anisotropic at the mid-latitudes, and again tending towards isotropy at the equator. At the mid-latitudes the filters have a very coarse resolution in the east-west direction and, nearly, doubly fine resolution in the north-south direction. The level of anisotropy at the mid-latitudes depends mainly on the commencing order of destriping. Due to the use of the Gaussian filter the MTF has a gradual slope. Further, only in the cases of filter truncation ( $\psi_0 = 2^\circ$  in Figure 5.11) and early

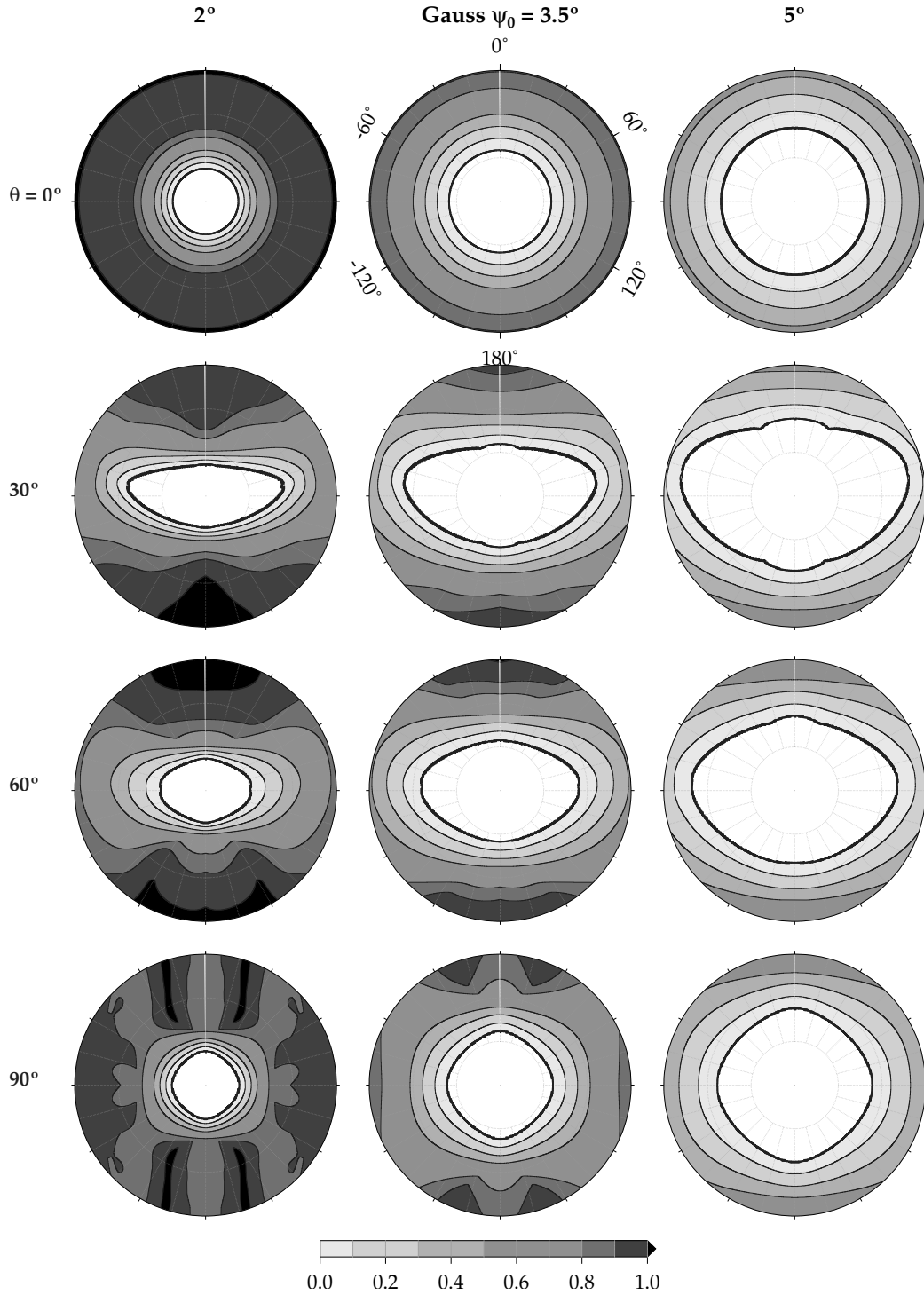


**Figure 5.10:** Smoothing kernels of the destriping and Gaussian filter cascade for different radii at different co-latitude. The gridlines for the spherical distance are  $5^\circ$  apart.

commencement of destriping ( $m = 2$  in Figure 5.13) we see modulation overshoot.

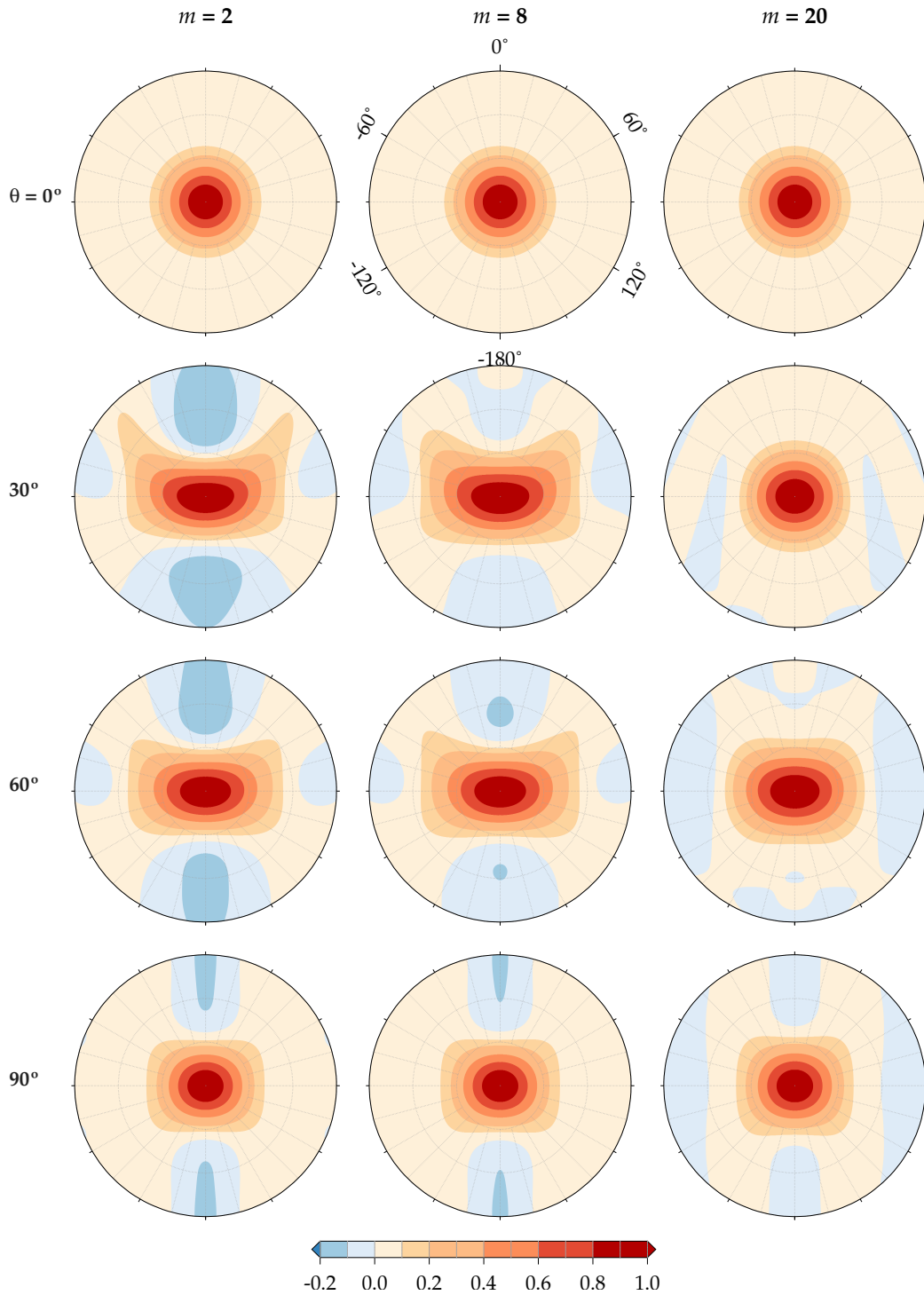
The left panel of Figure 5.16 shows the GRACE fields filtered with the cascade of destriping and Gauss filters. The field filtered with Gaussian filter with  $2^\circ$  smoothing radius shows the need for cascading an additional filter with the destriping filter to subdue all the striping behaviour. Further, the signal intensity and their locations are all affected by the use of

different parameters. For example, the destriping filter commencing at order  $m = 20$  is able to distinguish between the signals of Ganges and south east Asia, but for all the other parameters the destriping filter smothers these two signals. Similarly, when destriping is commenced from order  $m = 2$ , the filtered field does not have any semblance with the other filtered fields in the polar areas.



**Figure 5.11:** Modulation transfer function of the destriping and Gaussian filter cascade for different radii. The gridlines for the spherical distance are  $5^\circ$  apart.

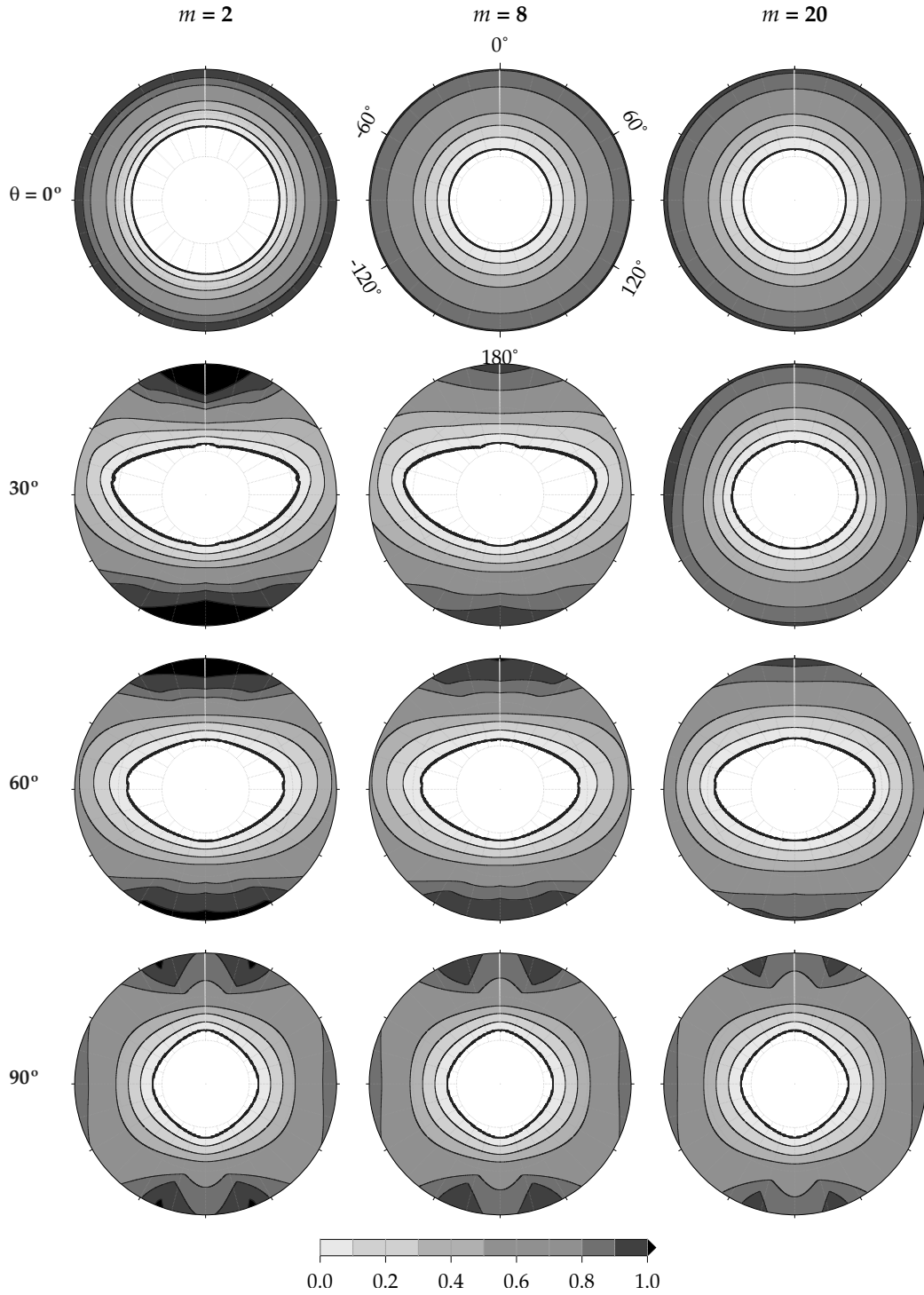




**Figure 5.12:** Smoothing kernels of the destriping and Gaussian filter for different commencing order of destriping. The gridlines for the spherical distance are  $5^\circ$  apart.

### Performance

The cascade of destriping and Gaussian filters have very good processing gain, which apparently is effected by the use of the destriping filter (cf. Figure 5.14). Both processing loss and processing gain are affected by the choice of parameters, especially the choice of commencing order for the destriping filter dictates the amount of loss and gain. Comparing the curve with that of the Gaussian filter, shows the impact of the destriping filter. The destriping filter



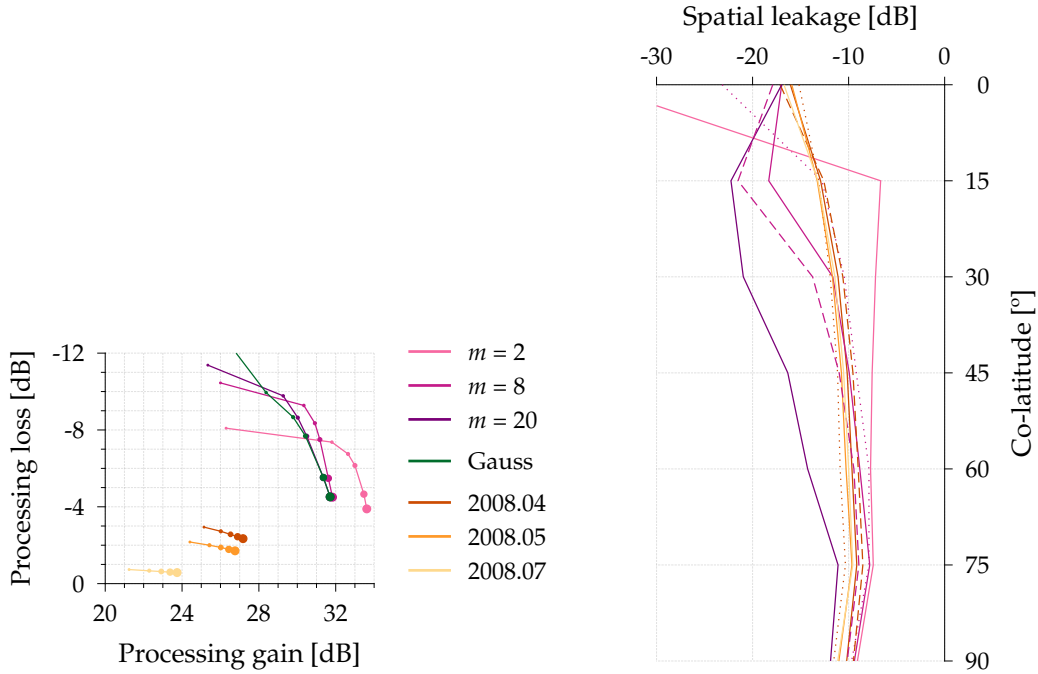
**Figure 5.13:** Modulation transfer function of the destriping and Gaussian filter cascade for different commencing order of destriping. The gridlines for the spherical distance are  $5^\circ$  apart.

definitely improves the processing gain, and at the same time does not lose a lot of signal in comparison with the fields that were filtered only with Gaussian filters. The commencing order of  $m = 8$  provides the best balance between processing loss and processing gain.

Apart from processing gain and processing loss all the other metrics depend on the calculation point. The spatial leakage of the destriping filter plotted as a function of co-latitude (cf. Figure 5.14), shows that most of the variation due to parameter choice is borne

at the poles and the mid-latitudes. Spatial leakage at the equator seems rather stable for the parameter choices made here. It is interesting to note that destriping commencing at order  $m = 2$  has the least leakage at the poles, whereas for the other choices co-latitude  $15^\circ$  has the least spatial leakage.

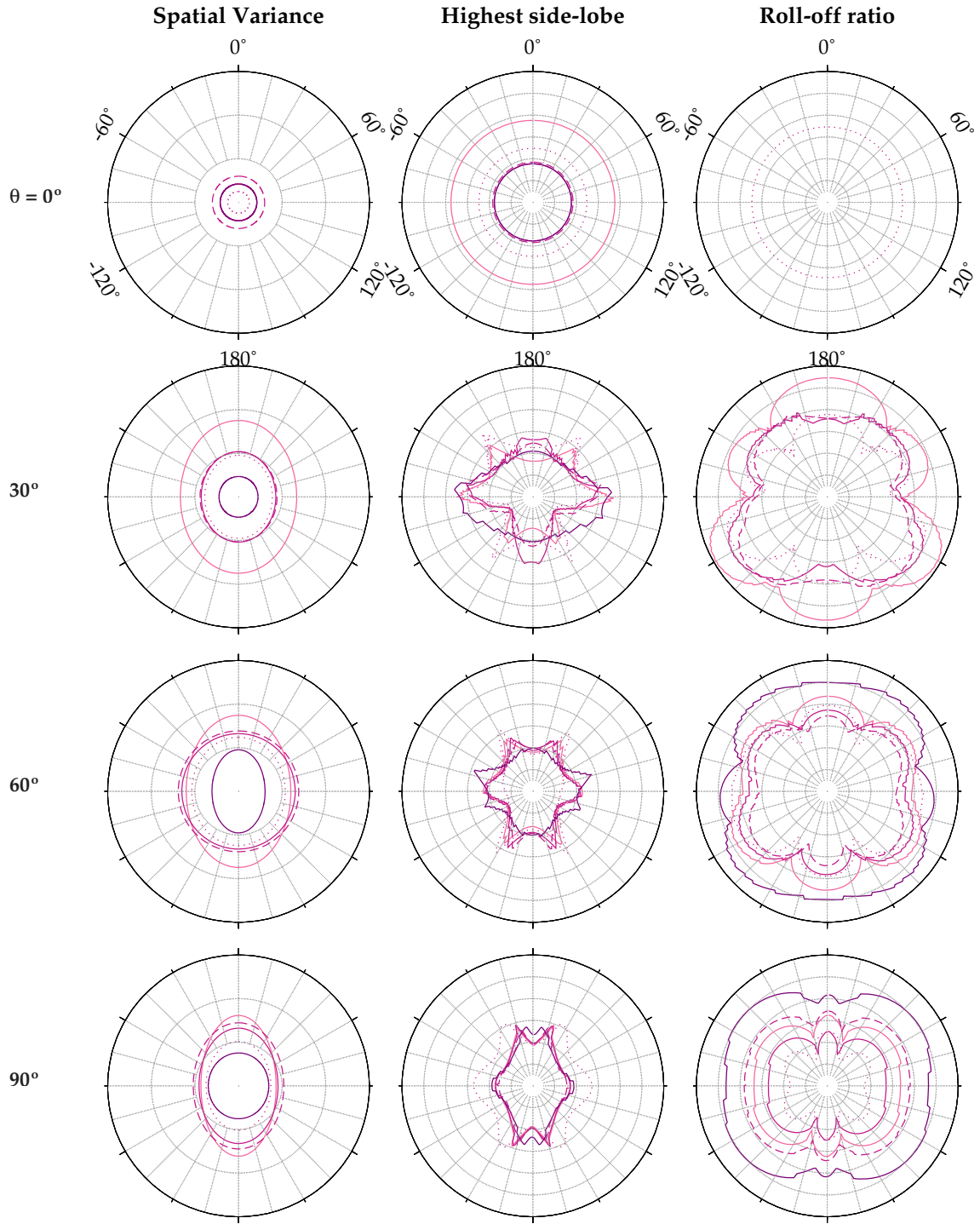
The spatial variance of the destriping and Gaussian filter cascade shows different behaviour for different filter parameters (cf. Figure 5.15). The overall pattern seems to be that the variance is much larger in the north-south direction than the east-west direction. This is caused mainly by the big side-lobes in the north-south direction. Further, there is an alternation of near-isotropy and anisotropy in the variance as one goes from the pole to equator for every given parameter choice. It can also be seen that the spatial variance is directly affected by the highest side-lobe level. The roll-off ratio is not substantial but significant, and it is steepest at the poles and becoming gradual towards the equator. The high leakage at the equator is corroborated by the highest side-lobe level and the side-lobe roll-off as in the case of the homogeneous and isotropic filters.



**Figure 5.14:** Scatterplot of processing loss against processing gain for the anisotropic filters (left panel). Spatial leakage with respect to co-latitude for the different filter parameter choices (right panel). The dotted lines indicate weak smoothing ( $\gamma = 1$  and  $\psi_0 = 2^\circ$ ), the solid lines moderate smoothing ( $\gamma = 3$  and  $\psi_0 = 3.5^\circ$ ) and the dashed lines strong smoothing ( $\gamma = 5$  and  $\psi_0 = 5^\circ$ ).

### Regularization filter

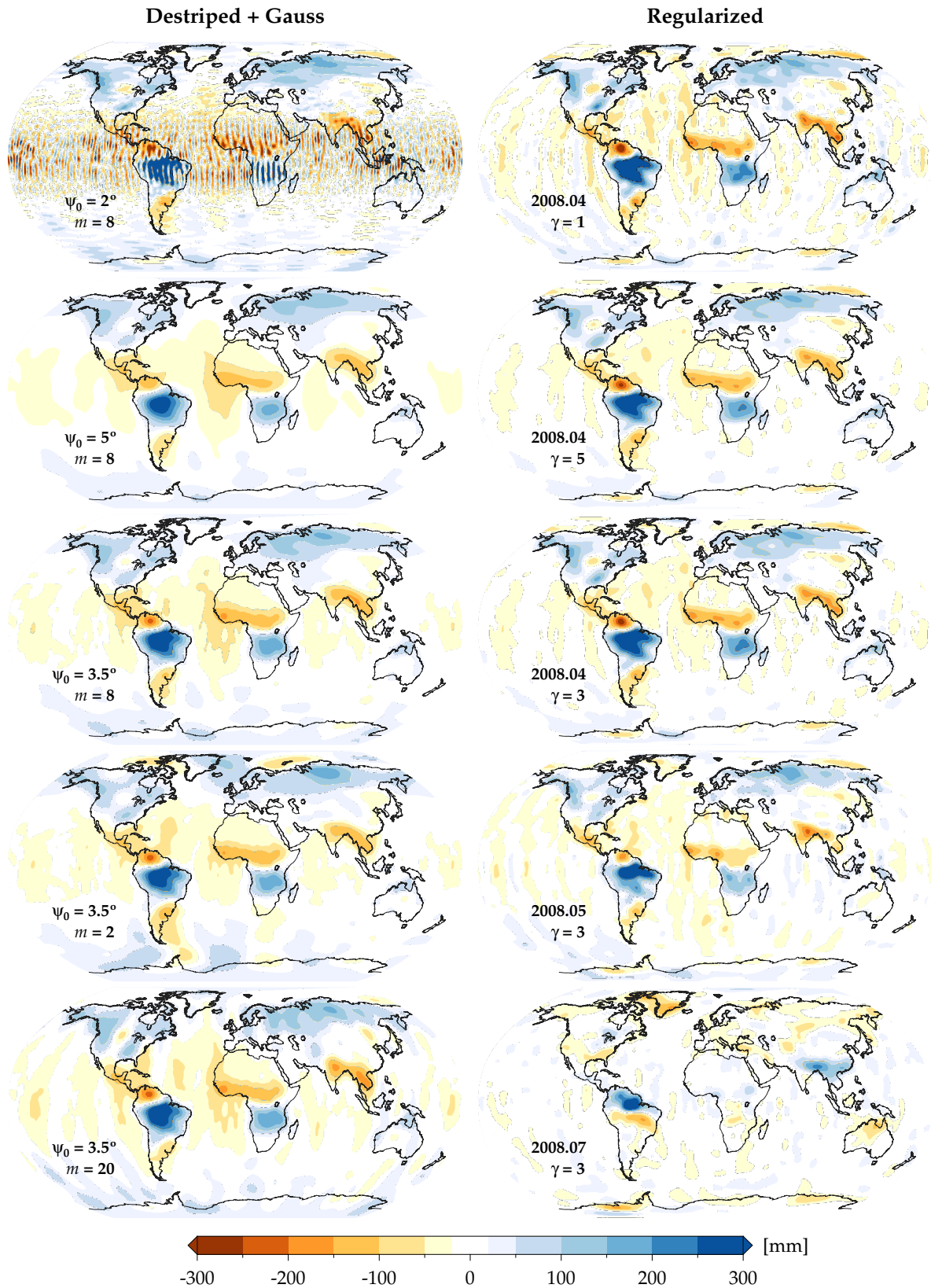
The regularization filter, as described in section 3.5, comes from the minimisation principles, and is reliant on the stochastic information of the field that has to be filtered. The main ingredients of the filter are the signal and noise covariance matrices and the regularization parameter ( $\gamma$ ) that decides the level of smoothing. In the ensuing analysis, we have chosen three levels of smoothing ( $\gamma = 1, 3$  and  $5$ ) and three different months to depict the influence of change in stochastic information.



**Figure 5.15:** Performance metrics for different parameters of the destriping and Gaussian filters. The colours and the line styles are the same as in Figure 5.14. The circular grid lines for the spatial variance are  $5^\circ$  apart. For the highest side-lobe and roll-off the axis in the radial direction goes from 0 in the centre to  $-\infty$  and its grid lines are  $-10$  dB apart.

### *Spatial resolution*

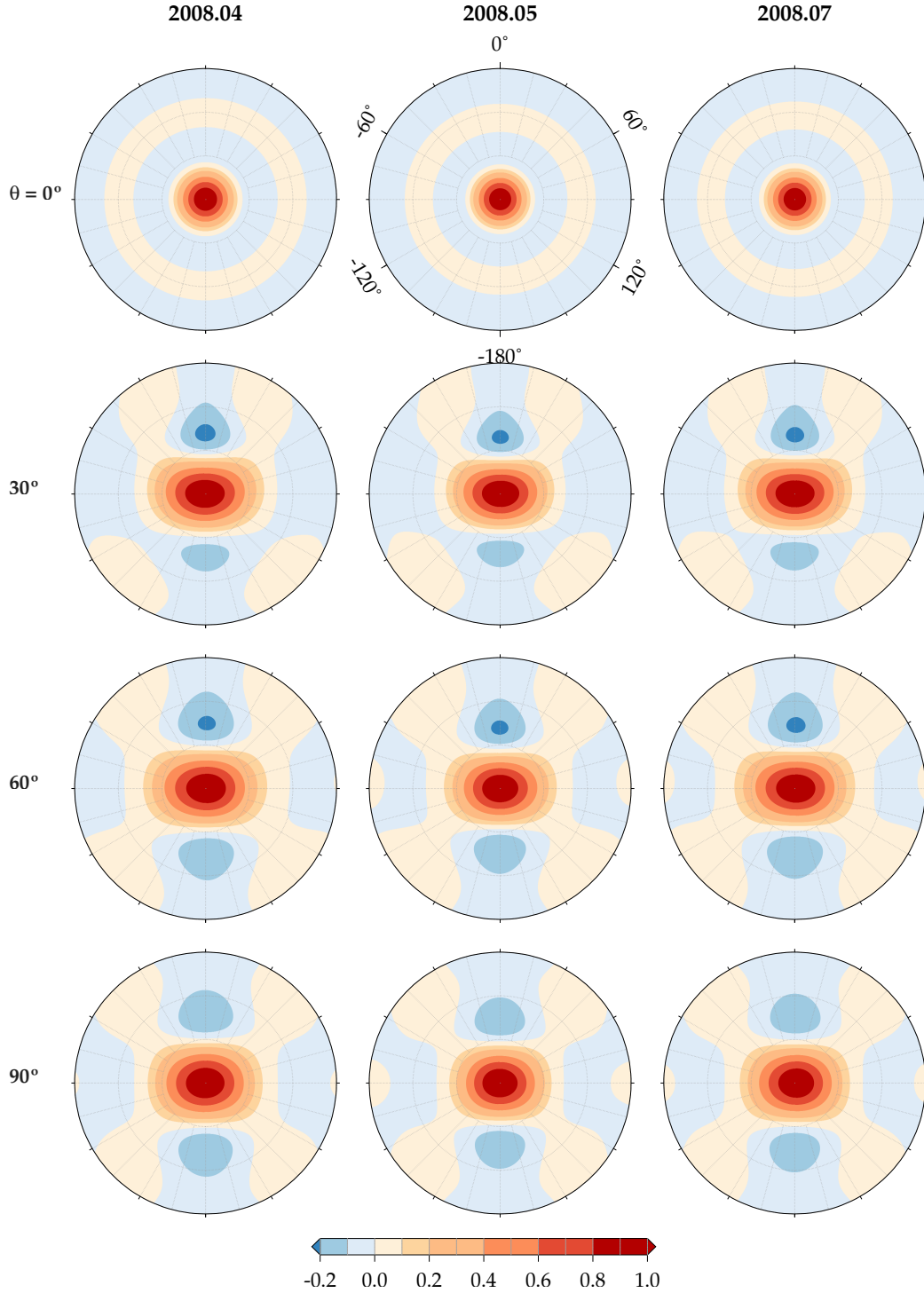
The spatial resolution of the regularization filter is depicted by the MTFs in Figures 5.18 and 5.20. The striking pattern that one can see is the near-isotropy of the resolution in co-latitudes other than the poles, and also the consistency in the shape of the MTF across the co-latitudes irrespective of the choice of the parameter. It is also worth noting that the difference in the



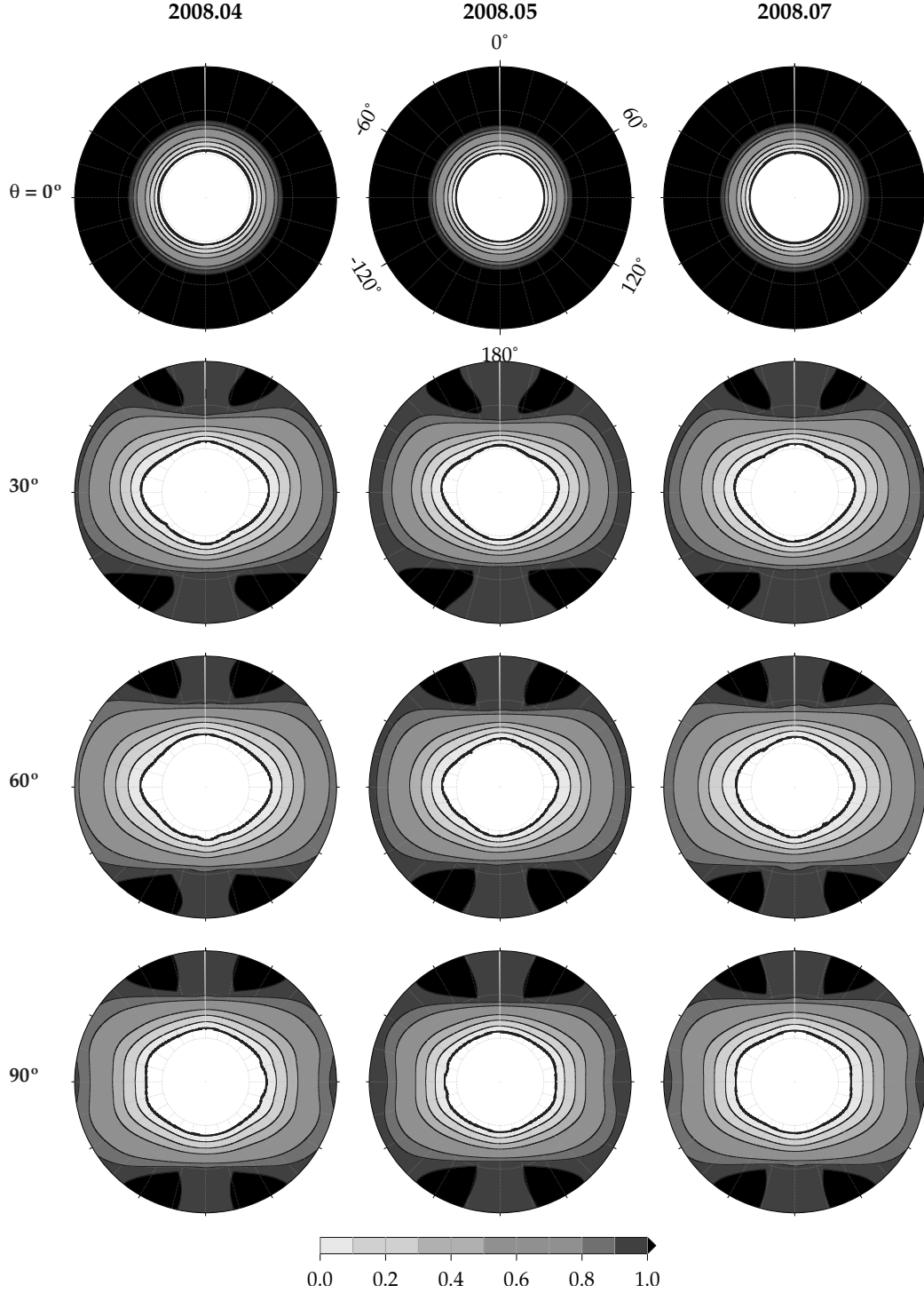
**Figure 5.16:** GRACE observed water storage anomalies filtered using the cascade of destriping and Gaussian filters (left panel) and regularization filter (right panel) for different choices of filter parameters.



resolutions at the poles and at the mid-latitudes is not that drastic. This is clearly reflected in the filter structure as well (Figures 5.17 and 5.19), where the filter structure remains the same starting from the equator through the mid-latitudes. In comparison with the cascade of destriping and Gauss filters, the MTF of the regularization filters are rather uniform in their structure and size in the mid-latitudes up to the equator.



**Figure 5.17:** Smoothing kernels of the regularization filter at different co-latitudes for the different months to depict the variation due to different choice of signal and noise covariances. The gridlines for the spherical distance are 5° apart.



**Figure 5.18:** Modulation transfer function of the regularization filter for the different months to depict the variation in MTF for different choice of signal and noise covariances. The resolution of the filter is anisotropic except at the poles, and it is nearly constant from the mid-latitudes to the equator. The gridlines for the spherical distance are  $5^\circ$  apart.

The fine resolution of the regularization filter is clearly visible in the maps of filtered GRACE fields (Figure 5.16). Comparing the maps of the regularized fields with other filtered fields, the spatial resolution is apparent with the number of features that we can identify. A good example is the band of negative water storage anomalies in central Africa, where we clearly see four different peaks that are well resolved. Similarly, the anomalies in Gangetic

basin in northern India and south east Asia are clearly resolved as two different signals.

The differences between the map with  $\gamma = 1$  and  $\gamma = 3$  are much larger than that between  $\gamma = 3$  and  $\gamma = 5$ , especially the oceans. For the case of  $\gamma = 1$ , the oceans are more noisy compared to the other two smoothing levels. On the continents, the amplitude of the signals are reduced with increasing level of smoothing, but the location of the signals are retained. Having said that, the different smoothing levels do not introduce considerable changes in resolution.

### *Performance*

The regularization filters perform pretty poorly with respect to the processing loss metric (Figure 5.14), which belies their fine resolution. The processing loss for the field of July 2008 is less than -1dB, which means that nearly all of the signal has been removed by smoothing. It is to be borne in mind that we are dealing with gravity field signals, whose lower harmonic degrees have multiple orders of magnitude of power compared to the higher harmonic degrees. Therefore, any filtering in the lower harmonic degrees will severely affect the total power of the signal (cf. Figure 6.4). It is worth noting that there are significant differences in the processing gain and loss between the different months. None of the other filter metrics explain these differences.

The spatial leakage of the filter is concentrated in a thin band that is minimum at the poles and slightly increasing in the mid-latitudes with a decreasing trend again towards the equator. This should not be surprising given the nearly-constant resolution across the co-latitudes. The low spatial leakage at the poles are supported by the low levels of side-lobes and also a healthy side-lobe roll off (cf. Figure 5.21). However, for the other co-latitudes the side-lobe roll off is not as healthy as that at the poles, and also have marginally higher side-lobe levels. This explains the higher spatial leakage at the mid-latitudes.

The highest side-lobe levels and side-lobe roll-off ratios of the regularized filter (Figure 5.21) is a lot higher than those of the cascade of the destriping and Gaussian filters (Figure 5.15). Nevertheless, the spatial leakage values are nearly the same, which only indicates that the energy retained by the main-lobe is considerably higher in the regularized fields than the destriping and Gaussian filter cascade. This instance demonstrates that the performance metrics should be evaluated in a holistic manner.

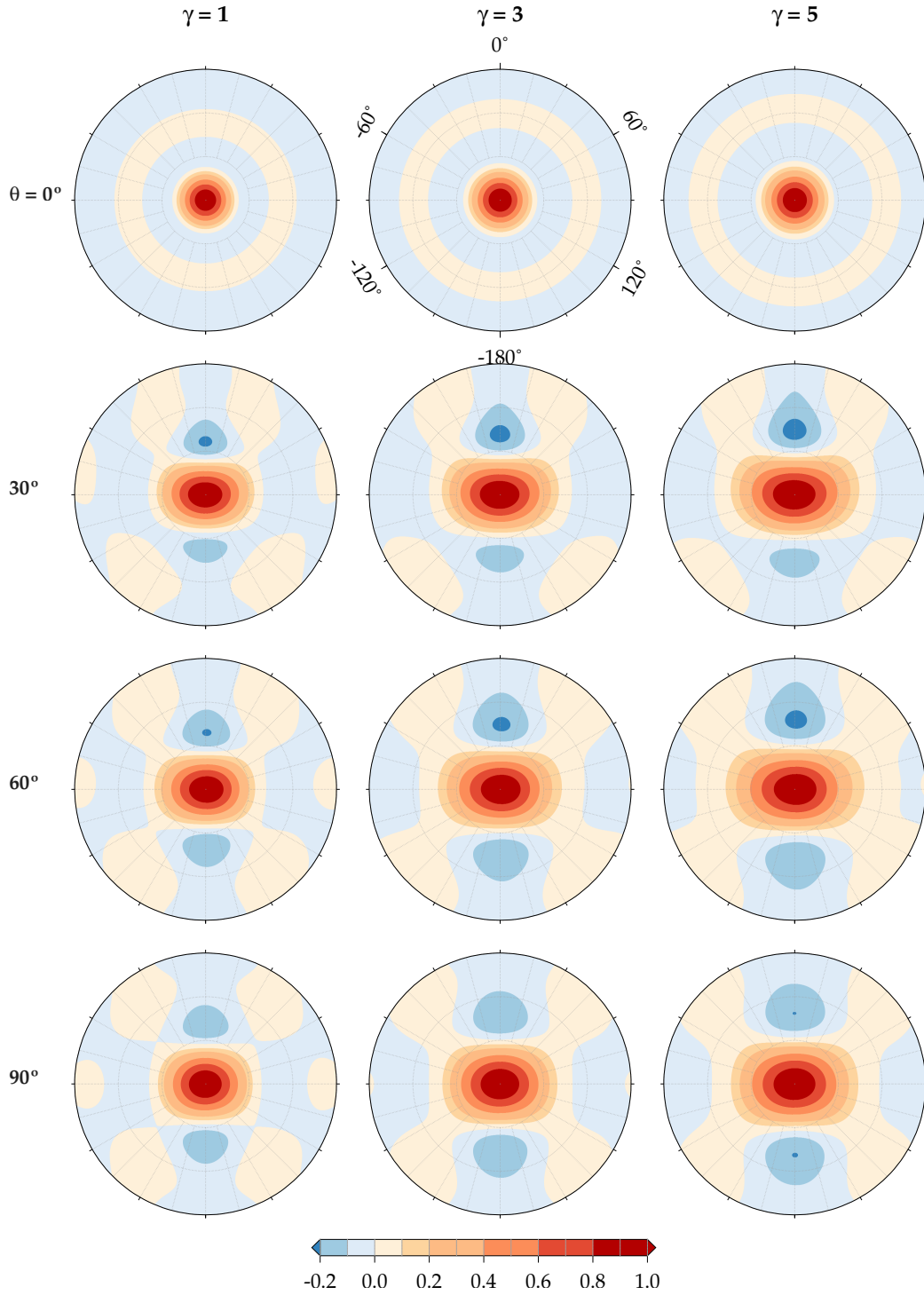
The spatial variance of the regularization filter (left panel of Figure 5.21) demonstrates its strong signal localising abilities. While the choice of parameters does not make a difference at the poles, it makes a significant difference especially in the variance in the north-south directions. Further, the spatial variance keeps increasing in the north-south direction as we move from the poles to the equator. Interestingly, there are hardly any changes to the east-west variances as we move from the mid-latitudes to the equator. This increase in the variance in the north-south direction is clearly supported by the nearly flat side-lobe roll off and high side-lobe levels.

## §5.3 DISCUSSION

### **Spatial resolution**

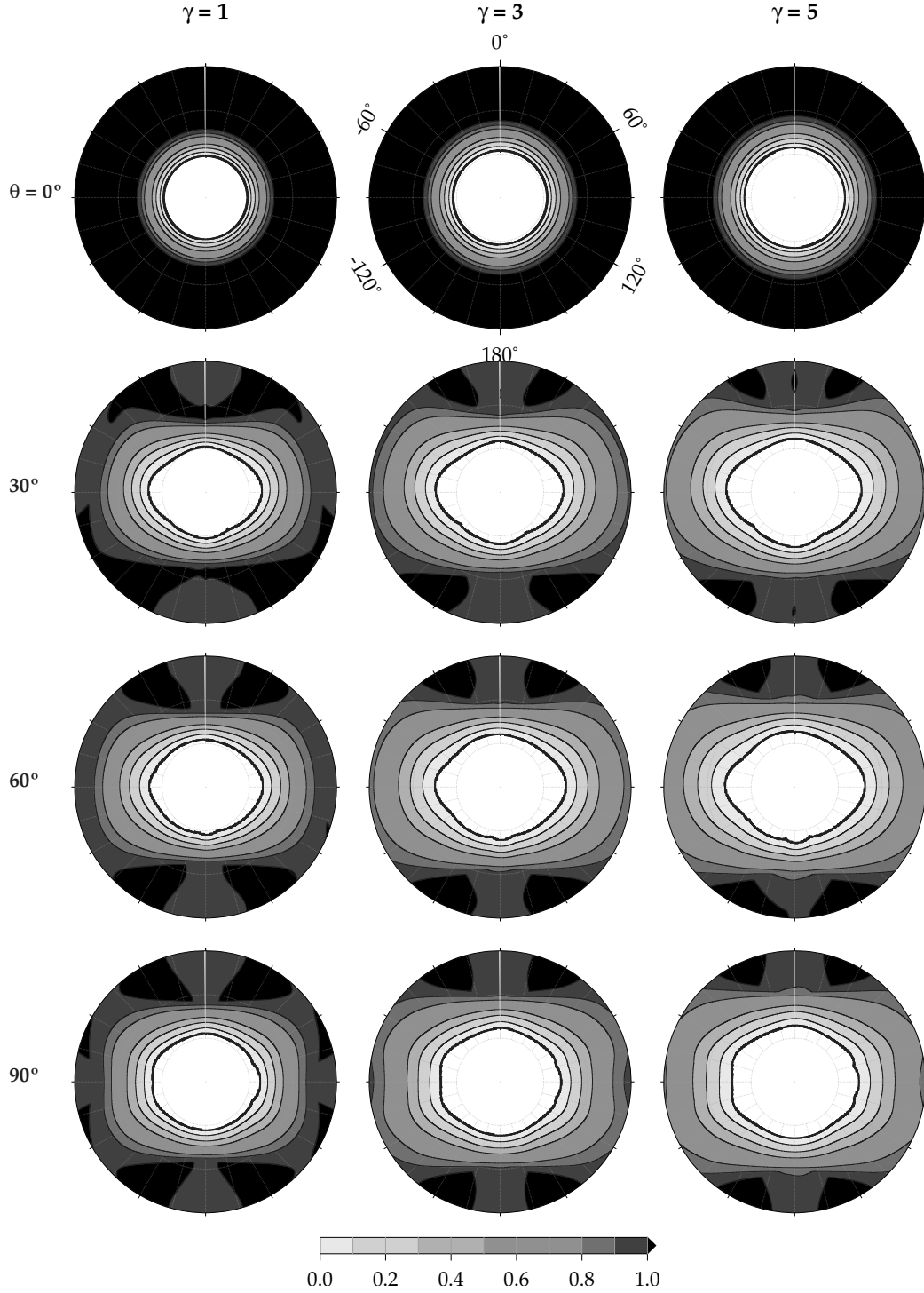
The spatial resolution of filters was considered to be the -6dB point, however all the filters that were analysed here have shown that the filter resolution is far beyond that point. For





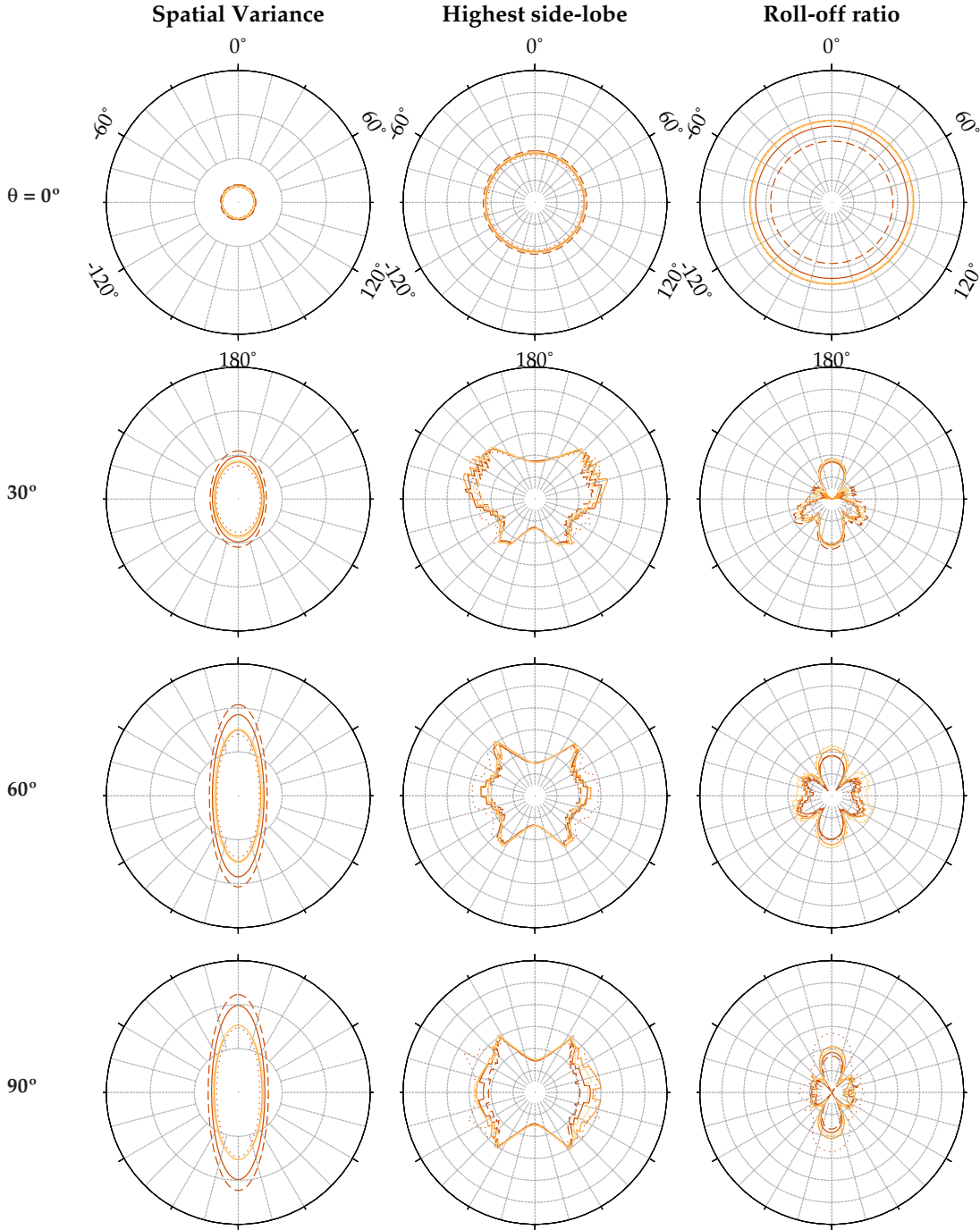
**Figure 5.19:** Smoothing kernels of the regularization filter at different co-latitudes for the different values of the regularization parameter ( $\gamma$ ). The gridlines for the spherical distance are  $5^\circ$  apart.

filters like the Pellinen, the spatial resolution is twice the smoothing radius, which is literally outside the smoothing kernel. In the case of the von Hann filter, the smoothing radius is itself the resolution of the filter. For the Gaussian filter the spatial resolution lay at around  $1/8$  to  $1/10$  of its peak. The spatial resolution points for the diffusion, spectral cosine, Butterworth and the ideal low-pass filter lay in the side-lobe of the respective filter.



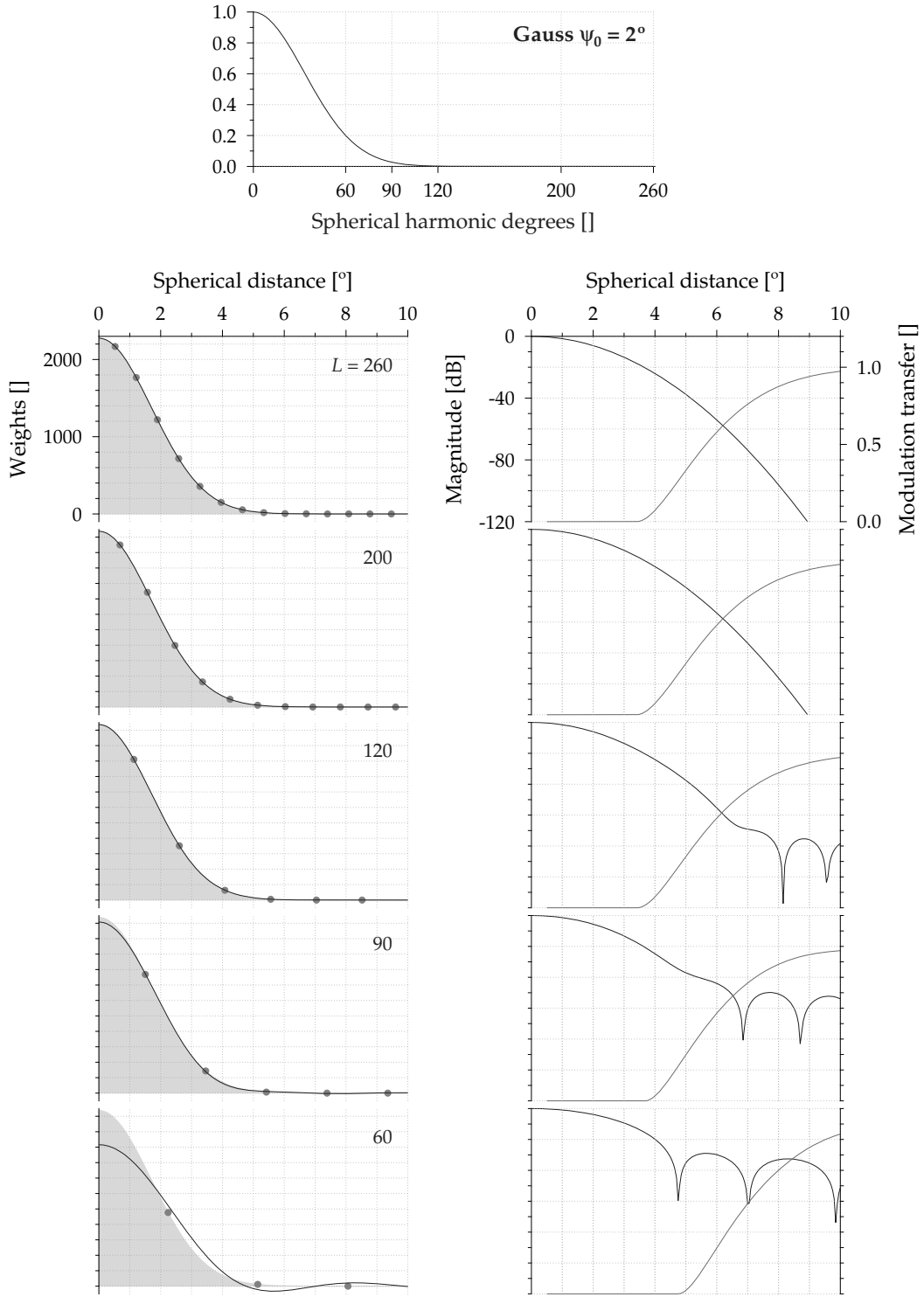
**Figure 5.20:** Modulation transfer function of the regularization filter for the different values of the regularization parameter ( $\gamma$ ). The structure of the MTFs does not change, but only dilates with increase in the size of the regularization parameter. The gridlines for the spherical distance are  $5^\circ$  apart.

In the case of the inhomogeneous anisotropic filters the filter resolution is dependent on the calculation point and also the filter kernels located at each of the other data points. This implies that the spatial resolution is interdependent on the inhomogeneity and anisotropy of the filter under study, which make it complicated and cumbersome to compute their spatial resolution. The filters we studied here were all latitude-dependent, which allowed us to analyse



**Figure 5.21:** Performance metrics for different parameters of the regularization filter. The colours and the line styles are the same as in Figures 5.14. The circular grid lines for the spatial variance are  $5^\circ$  apart. For the highest side-lobe and roll-off the axis in the radial direction goes from 0 in the centre to  $-\infty$  and its grid lines are  $-10$  dB apart.

a variety of filter parameters over a few latitudes. The same might have proven difficult, if not impossible, for a completely inhomogeneous and anisotropic filter. However, such a filter design is not easy to accomplish deterministically. Even stochastic filters for signals of natural phenomena that are completely anisotropic are also ruled out as such stochastics are unrealistic [Rummel and Schwarz, 1977].



**Figure 5.22:** Depiction of the effects of truncating the spectra of filter kernels due to band-limitedness of the field that is to be smoothed. Here, we have used a Gauss filter with a radius of  $\psi_0 = 2^\circ$  ( $n = 2$ ) with different spherical harmonic degrees of truncation.

### Effects of truncating filters

Sometimes, in order to reduce the amount of processing loss, shorter smoothing radii are used to smoothen the given field. If in such cases the smoothing radius is smaller than the resolution of the given bandwidth, then some spurious effects occur. One of the spurious

effects is the modulation overshoot as can be observed in the shortest smoothing radius of the homogeneous isotropic filters in Figure 5.2.

This is far more clearly illustrated in Figure 5.22, where we have taken a Gauss filter with a smoothing radius of  $2^\circ$  and truncate its spectrum at various bandwidths. Here, we see that as long as we truncate the filter at bandwidths whose spatial resolution exceeds that of the filter there are no side-lobes. The side-lobes start to appear as the spatial resolution of the given bandwidth and that of the filter approach each other. Further, the side-lobe levels also keep increasing as the spatial resolutions approach each other.

The other effect of the truncation is the reduction in energy of the main-lobe of the filter. Also the main-lobe cannot be smaller than the main-lobe of the kernel of the given bandwidth. Thus, the properties of the filter in its design form does not hold for the truncated and they would have to be evaluated individually. If on the other hand the filter were sampled with a sampling that is wider than the spatial resolution of the filter (*undersampling*), then we would have an aliased form of the filter spectrum. Therefore, care must be taken when choosing the smoothing radius.

### Alternatives to the Gaussian filter for filtering GRACE data

The main aim of this work is to facilitate the GRACE data user to choose the appropriate filter for his needs. A wide variety of choice is available for the homogeneous isotropic filters as we have demonstrated in this chapter. However, most of the studies in the GRACE community have been mostly reliant on the Gaussian filter. In this section we will try to find homogeneous and isotropic filter alternatives for the Gaussian filter.

Figure 5.9 shows GRACE mass anomalies filtered using homogeneous isotropic filters, where we already see a couple of alternatives to the Gauss filter. The diffusion, spectral cosine and the Butterworth filters provide better results compared to the Gaussian, both in terms of reduction of noise and retention of signal. These are the filters that balance processing gain and processing loss far better than the Gaussian filter. The spectral cosine filter, especially, performs better than the rest, whose filtered field shows details that were seen with the regularization filter in Figure 5.16. For example, the band of negative anomalies in central Africa is very well resolved. In fact the diffusion filter resolves all the signals better, but at the same time also retains more noise.

Similar is the case with the von Hann filter, which despite having comparable properties with the Gaussian is unable to reduce noise. The main problem with the underperformance of the von Hann filter compared to the Gaussian and spectral cosine, even though it has similar performance in terms of the metrics, is primarily due to the Gibbs effect it suffers in the spectral domain. The spectral coefficients of the von Hann in addition to the Pellinen are the only filters that have side-lobes in the spectral domain. The choppy nature of the fields filtered with these filters can be ascribed to their side-lobes.

Finally, based on our analysis, we can say that there are certainly better alternatives to the Gaussian filter, and they must be preferred to the Gaussian filter for filtering GRACE data.

## GRACE OBSERVATIONS OF WATER STORAGE CHANGES: IMPACT OF FILTERING

---

**F**ILTERING THE SPECTRA of the mass anomalies computed from GRACE data brings with it certain side effects that need to be considered in addition to the performance of the filters. These effects are largely related to the nature of the GRACE data and to the type of data analysis carried out in the GRACE community, and hence subjective. Some of the widely studied side effects of filtering are *leakage* of signal between catchments and the *bias* introduced by filtering [e.g., Swenson and Wahr, 2006a; Klees et al., 2007, 2008; Landerer and Swenson, 2012]. In this chapter, first we will introduce the basics of computing mass anomalies from GRACE gravity data. After which we will study the not so well known effects of filtering: changes to signal covariance and those to the amplitude and phase of the spherical harmonic coefficients of the GRACE monthly solutions.

### §6.1 GRAVITY TO MASS

The GRACE satellite mission provides monthly snapshots of the gravity field in terms of spherical harmonic coefficients, from which monthly *geoid anomalies* are calculated by removing a long-term mean of the geoid. This long-term mean is usually the average of the available monthly solutions up to an integer number of years.

$$N(\theta, \lambda)[t] = a_E \sum_{l,m} Y_{lm}(\theta, \lambda) K_{lm}[t], \quad (6.1)$$

$$\Delta N(\theta, \lambda)[t] = N(\theta, \lambda)[t] - \bar{N}(\theta, \lambda) \quad \text{with} \quad (6.2)$$

$$\bar{N}(\theta, \lambda) = \frac{1}{T} \sum_{t=0}^T N(\theta, \lambda)[t] \quad (6.3)$$

in which  $a_E$  is the semi-major axis of the ellipsoid approximating the Earth (6378.1363 km),  $N(\cdot)$  is the geoid height,  $\theta$  and  $\lambda$  are the co-latitude and longitude of a point on Earth,  $t$  is the temporal coordinate,  $T$  is the total number of monthly snapshots within a chosen integer number of years,  $Y_{lm}$  are the geodetic normalised spherical harmonics and  $K_{lm}[t]$  are the monthly spherical harmonic coefficients. Here we have denoted time as a coordinate within square brackets to denote the fact that it is a discrete quantity and only serves as an index. The total change in geoid is then written as

$$\Delta N(\theta, \lambda)[t] = a_E \sum_{l,m} Y_{lm}(\theta, \lambda) \Delta K_{lm}[t]. \quad (6.4)$$

This monthly geoid anomaly is contributed by a) monthly surface mass redistribution and b) the loading effects of the surface mass redistribution. The quantity  $\Delta N(\cdot)[t]$  represents the sum total of all the changes induced by a variety of geophysical phenomena, one of which is the continental water storage anomalies. In order to retrieve the continental water storage anomalies from the monthly geoid anomalies, contributions of the well known phenomena like tides (ocean, solid earth and atmospheric), atmospheric and oceanic mass changes are removed. The remnant signal contains contributions from continental water storage, glacier and (ant)arctic ice mass changes, and solid earth phenomena like glacial isostatic adjustment [Wahr et al., 1998]. This remnant signal of interest can be quantified from the monthly geoid anomalies as follows [Wahr et al., 1998]:

$$\Delta\rho_A(\theta, \lambda)[t] = \frac{a_E \rho_E}{3} \sum_{l=0}^{\infty} \frac{2l+1}{1+k_l} \sum_{m=-l}^l Y_{lm}(\theta, \lambda) \Delta K_{lm}[t], \quad (6.5)$$

where  $\Delta\rho_A(\cdot)[\cdot]$  ( $\text{kg/m}^2$ ) is the surface mass density anomaly,  $\rho_E$  is the average density of Earth ( $5515 \text{ kg/m}^3$ ), and  $k_l$  is the load Love number for the spherical harmonic degree  $l$ . The surface mass density can also be represented in terms of equivalent water height as

$$h_w(\theta, \lambda)[t] = \frac{\Delta\rho_A(\theta, \lambda)[t]}{\rho_w}, \quad (6.6)$$

where  $\rho_w$  is the density of water ( $1000 \text{ kg/m}^3$ ). The quantities  $h_w$  and  $\Delta\rho_A(\theta, \lambda, t)$  only represent mass deviations or anomalies, but they have to be differentiated to arrive at  $\text{d}S/\text{d}t$  storage changes. In practice, this is done by numerical differentiation using a three-point mid-point differentiator.

### Monthly sampling

GRACE, as has been mentioned before, is designed to provide monthly snapshots of the changes in the gravity field, and thus providing a time-series with a sampling rate of one measurement per month. It is important to clarify the time unit month here as it is a crucial element in our understanding of the natural periodicities with which the phenomena observed by GRACE vary. Spectral methods such as fast Fourier transforms (FFT) are used to estimate the periodicities, but FFT can be used only when the dataset is sampled at equal intervals of time. In the case of GRACE the sampling interval, month, is thought of as a constant period of 31 days, and hence an uniform sampling interval is assumed. However, in reality the sampling interval varies between 27 and 31, with the predominant values being 30 and 31, and therefore the sampling interval is *mildly* non-uniform. Tourian [2013, section 4.4.3] discusses the impact of such non-uniform temporal sampling on GRACE data processing.

## §6.2 SIGNAL COVARIANCE OF MASS ANOMALIES

The signal autocovariance of the gravity field [Kaula, 1967] has been the tool of choice for analysing the behaviour of the gravity field. It was established by Kaula [1966] that the autocovariance follows a *power-law* and can be approximated by an analytical expression. Pellinen [1970] demonstrated the ability of such analytical expressions in studying the inestimable parts of the signal. They also have aided in stabilising the ill-posed inverse problem of estimating

the gravity field from the observations of different gravity functionals [e.g., Bouman and Koop, 1998; Sneeuw, 2000].

### Autocovariance functions on the sphere

Covariance functions on the sphere are also two-point functions and have been extensively studied in physical geodesy (e.g., Kaula, 1967; Rummel and Schwarz, 1977). In fact, we took inspiration from [Rummel and Schwarz, 1977] to study the spectral structure of the different forms of smoothing kernels (cf. section 2.3). Kaula [1967] defines the autocovariance function of a field given on the sphere as the covariance of the field with itself at different spatial lags. The spatial lags being the spherical distance between the points whose covariance is sought. Following [Kaula, 1967] it can be mathematically expressed as

$$C(\psi) = \sum_{l=0}^{\infty} \sigma_l^2 P_l(\cos \psi), \quad (6.7)$$

where  $C(\cdot, \cdot)$  is the autocovariance function,  $\psi$  is the spherical distance between the points whose covariance is sought,  $\sigma_l^2$  is the variance of the field for a particular spherical harmonic degree  $l$ , widely known as the *degree variance* and  $P_l(\cdot)$  is the unnormalised Legendre polynomial of degree  $l$ . We have deliberately written the autocovariance as a two-point function to indicate that the spherical distance is between two points, and hence the function is still a two-point function.

Conversely, if we are given a field  $f(\cdot)$  with a covariance  $C(\cdot, \cdot)$ , then the general behaviour of the covariance over the entire region can be studied with the autocovariance function. This can be expressed as follows:

$$D\{f(\cdot)\} = C(\cdot, \cdot), \quad (6.8a)$$

$$= C(\theta, \lambda, \theta', \lambda'), \quad (6.8b)$$

where  $D\{\cdot\}$  is the dispersion operator. Taking the alternative form of the covariance function

$$C(\theta, \lambda, \theta', \lambda') = C(\theta, \lambda, \psi, A), \quad (6.8c)$$

and by integrating it over all the calculation points and the azimuth, we get

$$\frac{1}{8\pi^2} \int_{\Omega} \int_A C(\theta, \lambda, \psi, A) dA d\Omega = C(\psi). \quad (6.8d)$$

This is the autocovariance function of  $f(\cdot)$  and as it is clear from the expression that it has the same form as (6.7). Thus, the spectrum of the  $C(\psi)$  is given as

$$C(\psi) = \sum_{l=0}^{\infty} \sigma_l^2 P_l(\cos \psi), \text{ where} \quad (6.8e)$$

$$\sigma_l^2 = \sum_m |F_{lm}|^2 = \sum_m A_{lm}^2, \quad (6.8f)$$



following equation (22) of Rummel and Schwarz [1977]. Now, at  $\psi = 0$ , we get the variance

$$C(0) = \sum_{l=0}^{\infty} \sigma_l^2 = \sum_{l=0}^{\infty} \sum_{m=-l}^l |F_{lm}|^2, \quad (6.8g)$$

which is the energy contained in the field.

### Eigenvalues of the field of mass anomalies

Following (6.8f), we can compute the degree variances of the spherical harmonic coefficients of the monthly geoid anomalies in (6.4). However, these coefficients are dimensionless with the dimensioning for the geoid being provided by  $a_E$ . Similarly, the dimensioning for the surface mass densities is given by

$$\Lambda_l = \frac{a_E \rho_E}{3} \frac{2l+1}{1+k_l}, \quad (6.9)$$

where  $\Lambda_l$  are also the eigenvalues of the field of surface mass densities. Rummel and van Gelderen [1995] elaborate this idea and also depict the eigenvalues for different functionals of the gravity field. The remarkable character of the eigenvalues is that their spatial transfer functions are all isotropic due to the dependency only on the spherical harmonic degree. For this reason they are called *isotropic transfer functions*. Now, this offers us an opportunity to study the properties of the dimensionless coefficients ( $\Delta K_{lm}$ ) and also along with a particular eigenvalue ( $\Lambda_l$ ).

### Power-law models of degree variances

Due to the heavy noise in the higher harmonic degrees (cf. Figure 1.2), the spherical harmonic coefficients  $\Delta K_{lm}$  cannot be used directly for computing the autocovariance functions. Sasgen et al. [2006] established that the temporal variations of the gravity field also follow power-law, and therefore suggested using power-law models to approximate the degree variances. This is mathematically expressed as

$$\sigma_l^2 = 10^a l^b, \quad (6.10a)$$

taking logarithm on both sides, we get

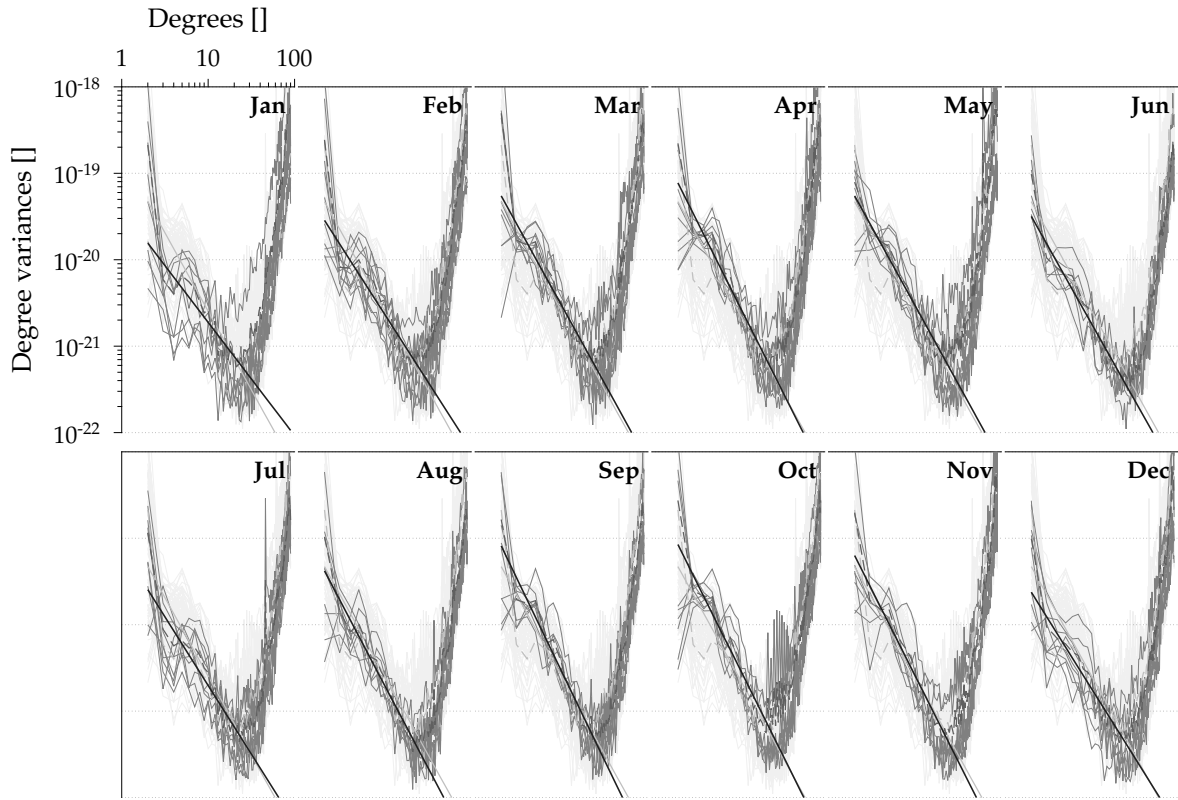
$$2 \log \sigma_l = a + b \log l, \quad (6.10b)$$

where  $a$  and  $b$  are the intercept and slope of the power-law, which are estimated via a least-squares fit to the less noisy degrees ( $3 \leq l \leq 25$ ) of  $\Delta K_{lm}$  (e.g., the straight lines in Figure 6.1). It must be noted that the terms intercept and slope make sense only in the log-log domain.

### Cyclo-stationary autocovariance of the mass anomalies

The mass anomalies depict a strong annual behaviour as shown by the seasonal mean in Figure 6.3. This implies that the degree variances also must indicate a strong annual behaviour, and that the autocovariance function cannot be considered stationary in time. To this end we

look into the degree variances if their values change every month and also repeat after every year. Since the GRACE data is provided as monthly snapshots coinciding with the calendar months, this comparison is made easier.



**Figure 6.1:** Degree variances of the GRACE spherical harmonic spectrum segregated according to the calendar months. The light gray lines indicate the complete set of degree variances and the dark lines are the segregated monthly degree variances. The dashed lines indicate the mean of the degree variances and the solid straight lines the power-law fits to the dashed lines. The power-law fits to the signal degree variances clearly depict a cyclo-stationary behaviour, with the peaks occurring in April and October and the troughs in January and July. These double peaks and troughs indicate the anti-symmetry of the northern and southern hemispheres.



**Figure 6.2:** Intercept and slope of the power-law fits to each of the mean of the degree variances for each calendar month. Here, we clearly see the double peak as in Figure 6.1.

In Figure 6.1 we have segregated the degree variances of each calendar month, and it is amply clear that the annual behaviour of the mass anomalies is reflected in their degree variances as well. The degree variances shift from the lower powers to the higher ones as we go from January to April, and again they decrease in amplitude as we move from April to June. This patterns repeats itself as we move from July to December. Further, the spread of the degree variances is much more, especially in the less noisy harmonics, for the months (January, June, July and December) when the amplitude is lower than for the months (April, May, September and October) when the amplitude is higher.

Instead of fitting a power-law model for the average of the all degree variances, we fit one for the average degree variance of each calendar month. These power-law models show the change in slope from January to June and again from July to December. This is also depicted by the intercept and slope values shown in Figure 6.2. It is noteworthy that we see a double peak in the degree variances. Comparing this behaviour with the mean of the mass anomalies for each calendar month (cf. Figure 6.3), we see that the anomalies change signs with a period of six months across the equator. Since we are dealing with quadratic quantities, the change of signs show themselves as double peaks.

The magnitude of the mass anomalies are low in January and July and high in April and October (Figure 6.3). This should be interpreted as low mass redistribution in the months of January and July and high in April and October. This activity coincides with the onset of the four seasons: Winter – January, Spring – April, Summer – July and Autumn – October. It can be construed that most of the mass redistribution occurs between solstices of winter and summer, with peak redistribution around the vernal and the autumnal equinoxes. Although we took the aid of the mass anomaly maps to elucidate this, the information was already present in the autocovariance function (cf. Figure 6.2).

### Impact of filtering on the autocovariance functions

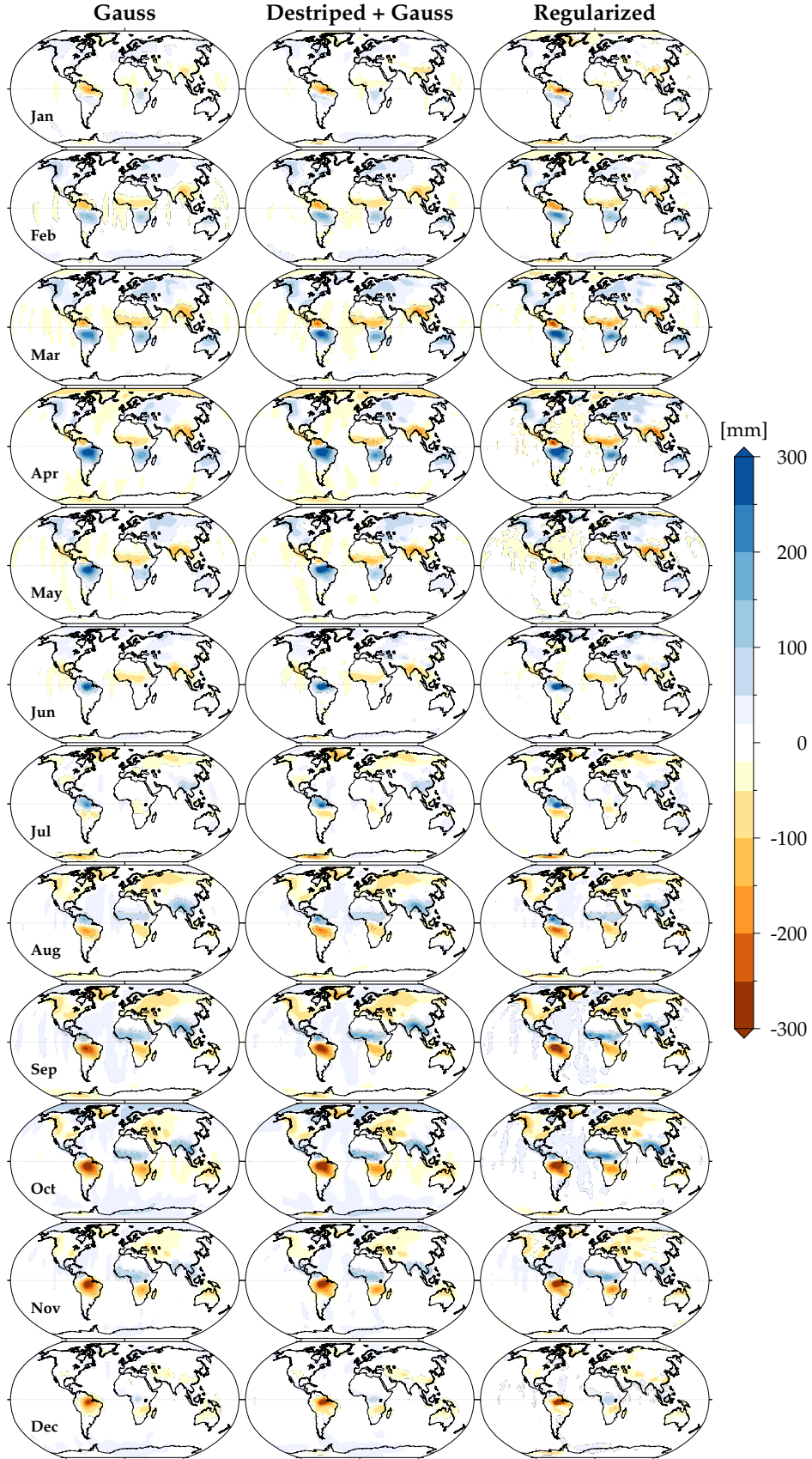
Filtering affects the amplitude of the field being filtered, and therefore, it affects the degree variances as well. The high levels of noise in the spherical harmonic coefficients of the mass anomalies  $\Delta K_{lm}$  damps the signal to a large extent that they diverge significantly from the modelled power-law (cf. Figure 6.4). The extent of smoothing is glaringly obvious in the spatial transfer of the autocovariance. In addition, it is also easy to see how much underestimation and overestimation would occur if the mean of all degree variances is used for the power-law model.

The main culprit behind the oversmoothing of the GRACE data is the noise in the dataset. This can be illustrated clearly with the aid of the regularization filter. Following Klees et al. [2008], we first rewrite the regularization filter as a Wiener filter.

$$\mathbf{B} = \frac{\mathbf{Q}^{-1}}{\gamma \mathbf{S}^{-1} + \mathbf{Q}^{-1}} \quad (3.11j)$$

$$= \frac{\gamma \mathbf{S}}{\gamma \mathbf{S} + \mathbf{Q}}, \quad (6.11)$$

where  $\mathbf{B}$  is the spectral filter matrix,  $\mathbf{S}$  is the signal covariance and  $\mathbf{Q}$  is the noise covariance. The general behaviour of the covariances is described by the degree variances. Therefore, by taking the signal and noise degree variances for  $\mathbf{S}$  and  $\mathbf{Q}$  we can study the impact of



**Figure 6.3:** Seasonal mean of the filtered surface mass changes observed by GRACE. The filter radius of Gauss only filtered solutions was taken as  $\psi_0 = 5^\circ$  and for the destriped and Gauss filtered solutions was taken as  $3^\circ$ . For the regularized solutions  $\gamma = 3$  was chosen.

filtering on each individual harmonic degree.

$$B_l = \frac{\gamma S_l}{\gamma S_l + Q_l}. \quad (6.12)$$

Now, for a spherical harmonic degree of  $l = 60$ ,  $S_l \approx 10^{-21}$  (Figure 6.1) and  $Q_l \approx 10^{-19}$  (Figure 1.2). Here, we see that the noise is two orders of magnitude higher than the signal. Thus,  $B_l$  becomes

$$B_{60} \approx \frac{10^0 10^{-21}}{10^0 10^{-21} + 10^{-19}} = 10^{-2} = 0.01.$$

Using this value to filter  $\Delta K_{lm}$ , we get

$$\begin{aligned} \Delta \bar{K}_{lm} &= B_l \Delta K_{lm} \\ &\approx 10^{-2} 10^{-10} = 10^{-12}. \end{aligned}$$

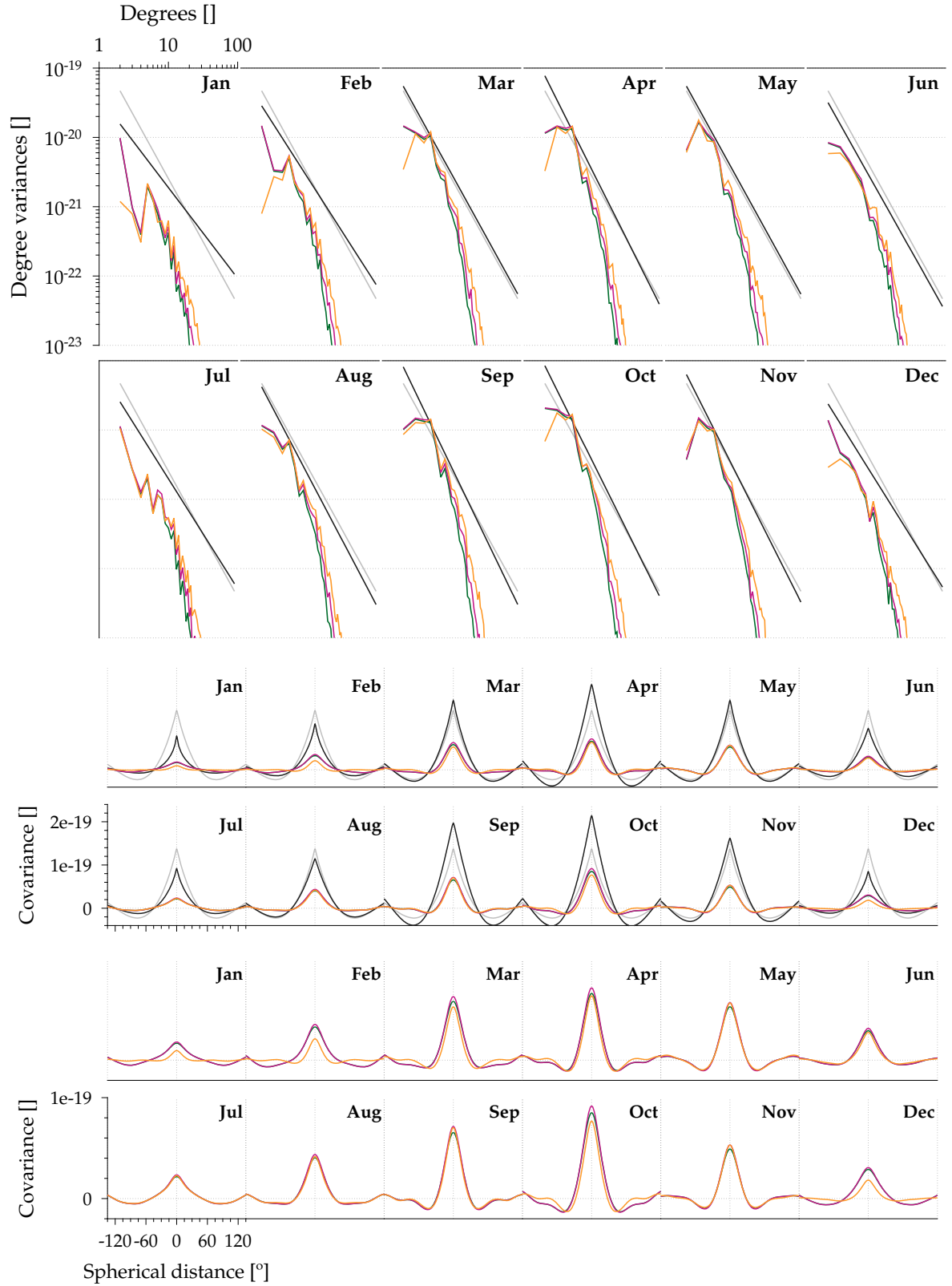
Taking the sum of the square of  $(2l+1)$  values of  $\Delta \bar{K}_{lm}$  we can see that the filtered degree variance of  $l = 60$  will have a value of  $10^{-22}$  which is one order of magnitude less than the *a priori* signal covariance. Thus, the noise in the GRACE data inadvertently allows for oversmoothing.

Filtering, apart from affecting the amplitude, also affects the shape of the spatial transfer of the autocovariance function. The spatial transfer becomes narrower for the months of April and October, and also for these months the negative covariances at a spherical distance of  $60^\circ$  change into positive covariances after filtering (Figure 6.4). Similarly, in the months of January and July the spatial transfer of the filtered degree variances is slightly wider than the power-law model, although, there is no change in sign of the covariances.

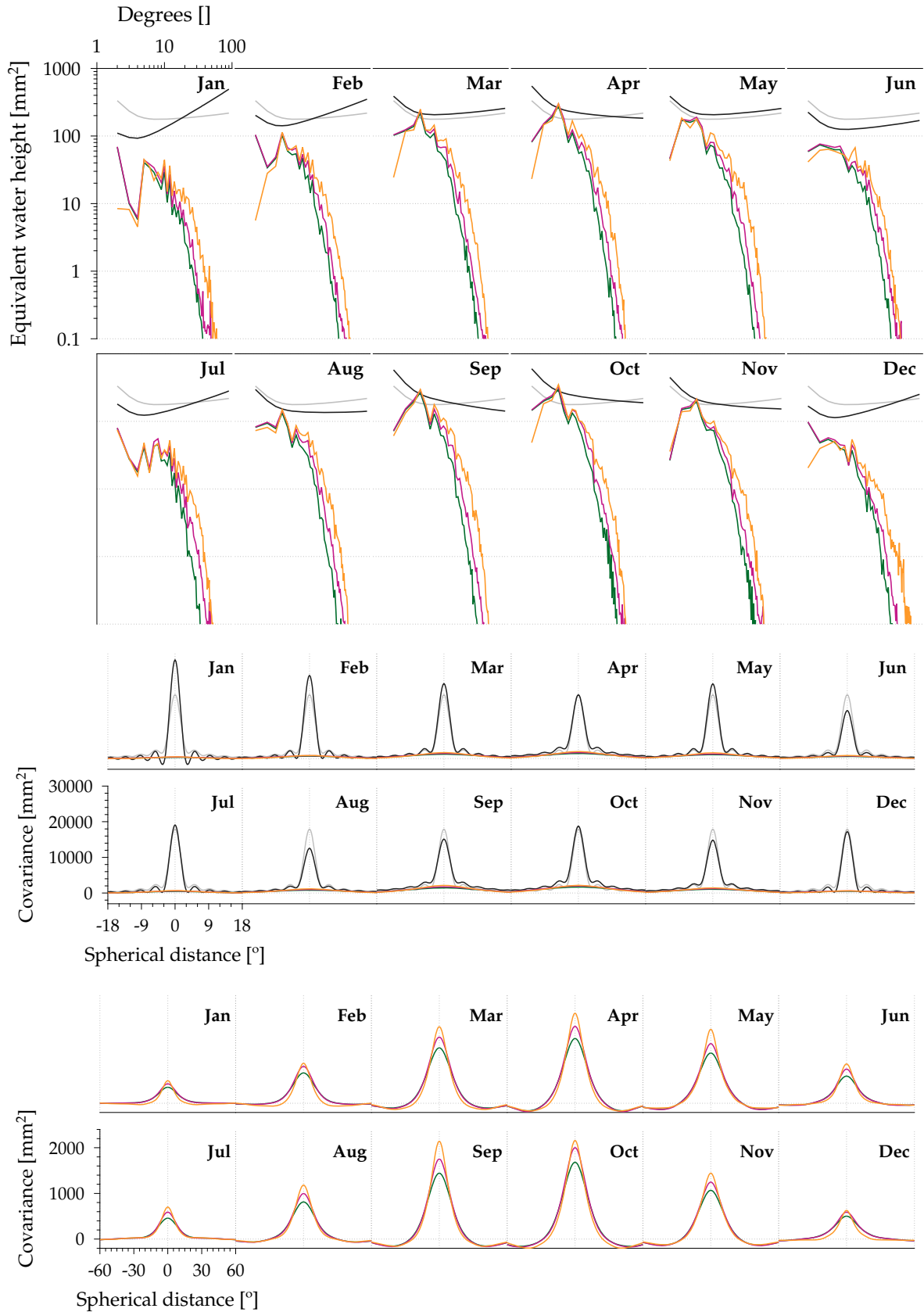
Introducing the eigenvalues of the mass anomalies into the autocovariance functions we see some interesting behaviour, especially of the power-law models (Figure 6.5). The power-law models that were only following a pink spectrum (decreasing power towards the higher harmonic degrees), now also show blue spectra (increasing power towards the higher harmonic degrees) for the months of January, February, March, May, June, July and December. Due to this change in the degree variances, the spatial transfer function also displays a sea of change.

The biggest change between the spatial transfer functions of the dimensionless degree variances and their mass anomaly counterparts is the width of the spatial transfer. While the dimensionless autocovariance had significant covariances as far a spherical distance as  $60^\circ$ , the autocovariance of the mass anomaly drops down to zero at around  $3^\circ$  for most of the months. Another aspect of these spatial transfer functions is that as opposed to the high energy levels of the fields in April and October, the highest energy levels are displayed by the fields in January and July.

The filtered degree variances of the mass anomalies immediately lose their characteristic blueness, and become red as their dimensionless counterparts (Figure 6.5). Due to this dramatic change brought by filtering, the spatial transfer functions also show such dramatic changes. The magnitude of the filtered autocovariance functions is more than an order of magnitude smaller than the unfiltered ones, reducing from  $30,000 \text{ mm}^2$  to  $2,400 \text{ mm}^2$ . At the same time their width has widened more than five times, from a mere  $3^\circ$  to around  $15^\circ$ .



**Figure 6.4:** Comparison of filtered degree variances with the monthly power-law fits (top panel) and the corresponding homogeneous isotropic covariance functions (bottom panel). The dark black lines indicate the cyclo-stationary power-law fits as in Figure 6.1, the light gray line is the power-law fit of the complete set of degree variances, the blue lines are the mean of the Gauss filtered degree variances, purple lines are those of the destriped and Gauss filtered, and the green lines are that of regularized solutions.



**Figure 6.5:** Comparison of filtered degree variances with the monthly power-law fits of the surface mass changes (top panel), and also of the corresponding homogeneous isotropic covariance functions (middle panel). Since the difference between the filtered covariance function and the covariance function of the power-law is substantial, the former are plotted separately (bottom panel). Notice the changes in the range of  $x$ - and  $y$ -axis between the middle and the bottom panels.

Comparing the dimensionless with the dimensioned spatial transfer, also clarifies the difference in the filter abilities. In the case of the dimensionless spatial transfer, the regularization even after having salvaged a large part of the signal from noise in the higher harmonic degrees, it did retain energy levels on par with Gaussian filter and the cascade filter. With the introduction of the eigenvalues, the scenario has been reversed (bottom panel of Figure 6.5). Now we see that the spatial transfer from regularized solutions retain more energy than the other two filtered solutions.

### Implications for the regularization filter

In section 3.5, we discussed the design of the regularization filter, one of whose main ingredients is the signal covariance matrix. There we indicated that we use a power-law model of the dimensionless coefficients  $\Delta K_{lm}$  as the signal covariance matrix. In this work we use only the cyclo-stationary signal covariance model. In the case of GRACE mass anomalies, the noise is highly prohibitive, which does not allow us to benefit from the cyclo-stationary signal covariance models (cf. Figure 6.5). It is also the reason, we depicted the performance metrics of three different months—April, May and July—depict the filter performance at peak, moderate and low signal energy, respectively. Further, here we have used the cyclo-stationary covariance models only for the post-processing of GRACE data, but it might be worthwhile to use them at the GRACE level-1b data processing.

As the regularization filter uses a cyclo-stationary signal covariance and monthly noise covariances the filter becomes time-dependent. This implies that the performance metrics need to be computed for every single month to evaluate their performance, which was amply demonstrated in Figure 5.14. This in addition to inhomogeneity and anisotropy of the filter adds to complexity of filter performance evaluation.

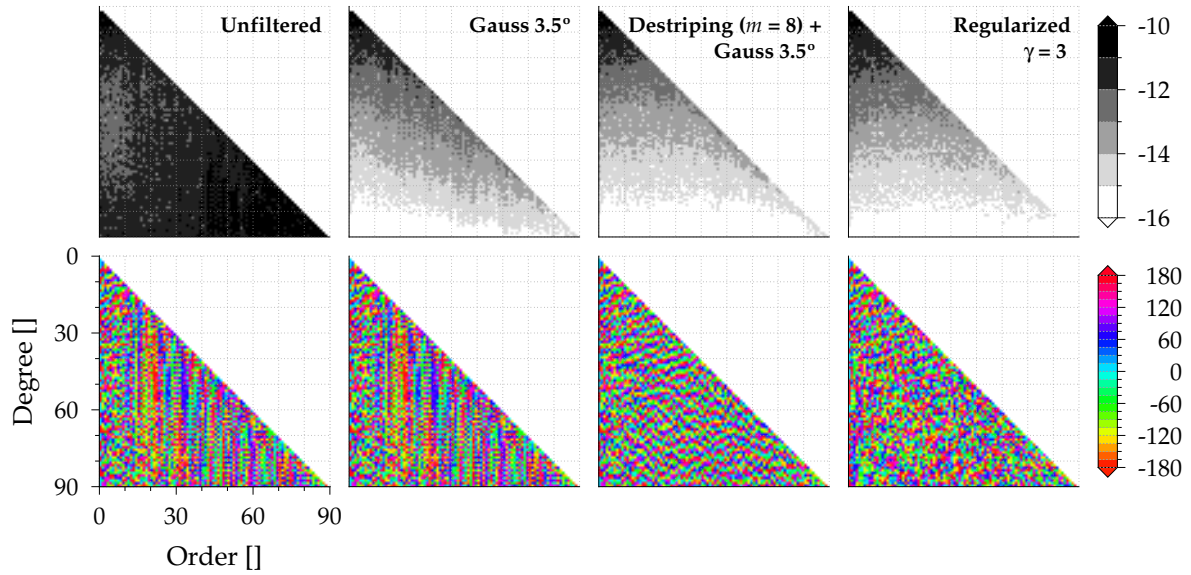
## §6.3 AMPLITUDE AND PHASE OF THE FILTERED GRACE DATA

The polar spectrum of a field provides a different view to analyse the properties of the field. It was established in section 2.4 that apart from isotropic filters and special types of latitude-dependent anisotropic filters, all the other filters change the phase of filtered field. Kaula [1967] indicates that the phase of a harmonic spectrum must be random, because of the orthogonal properties of the harmonic base functions. With this in mind we will look at the phase of the filtered and unfiltered spherical harmonic coefficients of the mass anomalies shown in Figure 6.6.

The phase of the unfiltered mass anomaly spectrum reveals the correlation between the even and odd degrees of a particular order (Figure 6.6). It also reveals the order from which the correlation between the degrees begins. In line with Kaula [1967], the phase of the spectrum until order  $m = 15$  remains random, but beyond that the correlation between the degrees of an order show patterns. It must be noted here that the order  $m = 15$  and its multiples are the resonance orders of GRACE [Seo et al., 2008]. As demonstrated in (2.36), the homogeneous isotropic Gaussian filter does not change the phase of the filtered spectrum.

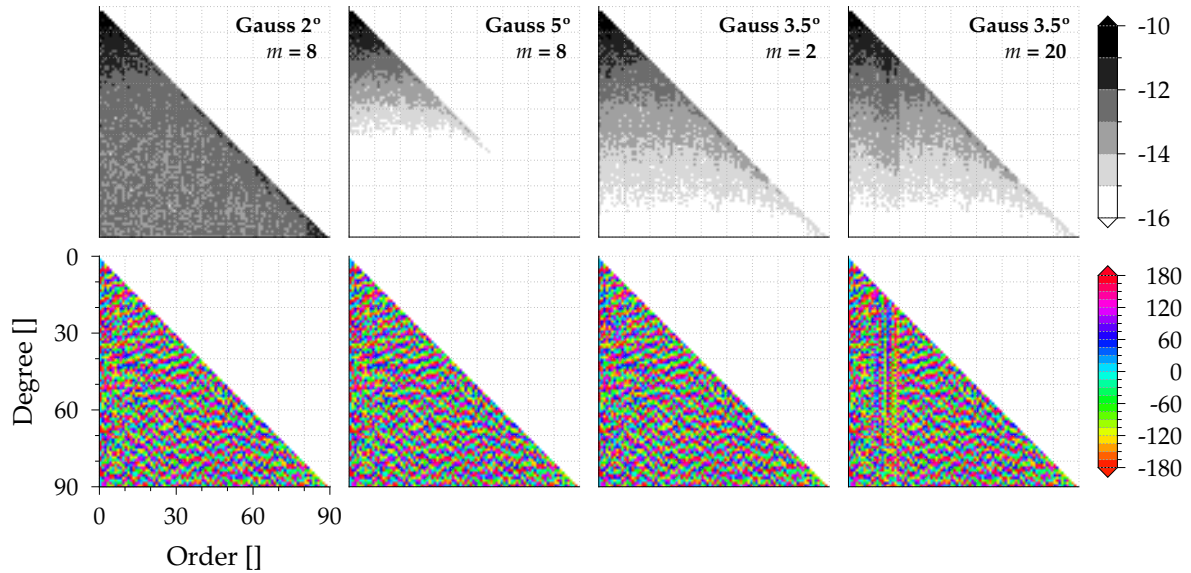
The destriping filter that is specifically designed to remove the correlations, changes the phase of the filtered field. However, it cannot be said that the resultant phase is completely random as there is an apparent wave-like pattern across the orders. Changing the commencing order for the destriping filter either retains the correlations for the orders that are less than the





**Figure 6.6:** Changes in amplitude and phase of the unfiltered and filtered spherical harmonic coefficients of the GRACE gravity field (April 2008), for the three different filters used in this chapter.

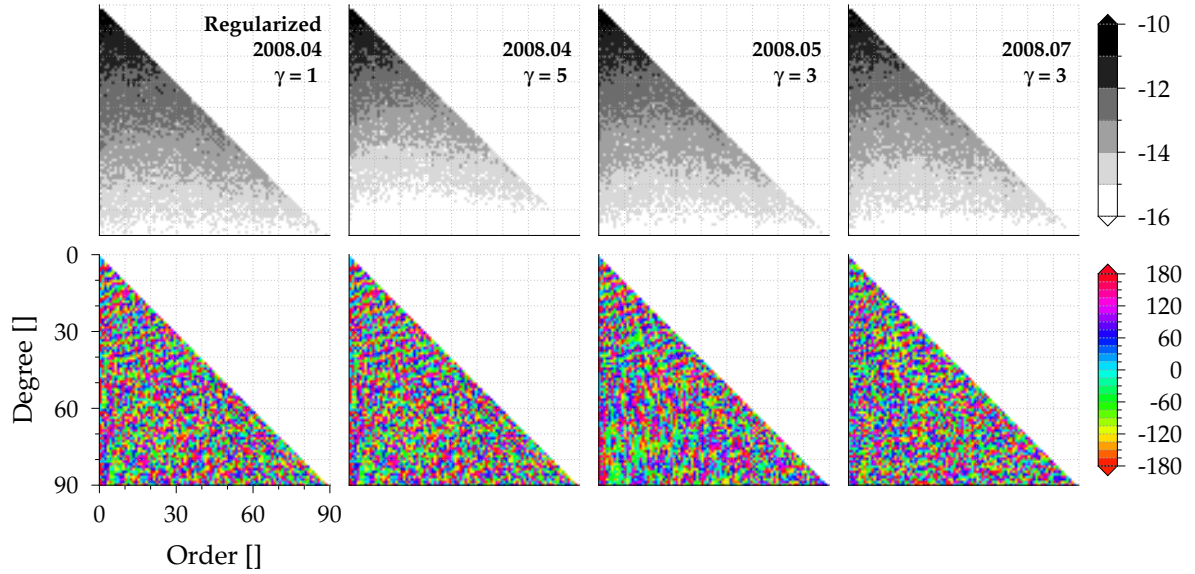
commencing order (Figure 6.7). This is the case of the destriping filter with the commencing order  $m = 20$ , where the correlations between the degrees of orders  $m < 20$  are all retained. Commencing the destriping at order  $m = 2$  or 8 does not bring any drastic changes to the phase of the filtered field. This implies that the destriping filter does not have an adverse effect on orders in which the degrees are not correlated.



**Figure 6.7:** Same as Figure 6.6 for the different parameters of the destriping and Gaussian cascade filter.

The regularization filter as is expected changes the phase of the filtered spectrum, and here the phase is completely random with no obvious patterns (Figure 6.8). Interestingly, changing the regularization parameter does not bring any visible changes to the phase. However, there are considerable differences between the different months. While the phase of the spectrum of May 2008 shows certain patterns, the phase of the spectrum of July 2008 is completely

random.



**Figure 6.8:** Same as Figure 6.6 for the different parameters of the regularization. Here the amplitude and phase spectrum of different monthly fields are also shown.

The amplitude plots indicate the manner of the filtering performed by the filter to suppress noise. The amplitude plot of the unfiltered field shows that the higher harmonics and also the sectorial and near sectorial elements are ridden with noise. The Gaussian filters only damp the amplitude only along the degrees, which indicates how the power increases towards the sectorial elements. The cascade of destriping and Gaussian are able to suppress that to a large extent but we still see the large power in some of the sectorial coefficients. The regularization filter does an even better job of damping the noisy sectorial harmonics and also the higher harmonics, and we also see that overall the amplitude decreases with increasing degree.

## CONCLUDING REMARKS

---

THIS WORK was borne out of the need to choose the appropriate filter for smoothing (noisy) data on the sphere given a wide variety of filters. In order to fulfil this need we set out to understand the mechanics of filtering and also the spatial and spectral structures of the filters. In addition we wanted to put forth some metrics to evaluate the efficacy of filters in a data agnostic (objective) manner. In the following we summarise the findings of this study, after which we will discuss the questions that remain open.

### SUMMARY OF FINDINGS

- i. Data smoothing can be performed by taking weighted averages over the sphere with the use of weighting functions  $w(\theta, \lambda, \theta', \lambda')$ . We distinguish the normalised form of the weighting function as the smoothing operator  $b(\theta, \lambda, \theta', \lambda')$ .
- ii. The smoothing operator is always a two-point function, because the weights are relative between the calculation  $(\theta, \lambda)$  and data  $(\theta', \lambda')$  points.
- iii. Filtering with a general two-point function (inhomogeneous and anisotropic) is still convolution, although with a spatially variable kernel. This spatial operation also leads to convolution in the spectral domain. While the convolution in the spatial domain is continuous, that in the spectral is discrete.
- iv. The key to understanding the smoothing operator is its representation in the local polar coordinate system  $(\theta', \lambda' \rightarrow \psi, A)$ . This change facilitates in understanding the idea of isotropy. Isotropy allows us to describe the spatial structure of the smoothing operator with respect to the data points.
- v. A related idea to isotropy that allows the spatial structure description with respect to the calculation points is homogeneity. The properties, homogeneity and isotropy, together make us understand a wide-variety of smoothing operators, and give us an idea of their respective spectra (cf. Table 2.2). This is crucial for the design of filters and also for designing algorithms for fast numerical computations.
- vi. The homogeneous isotropic filters remain the simplest form of all the filters, both in the spatial and spectral domains, enabling a wide-variety of filter designs. However, latitude-dependent anisotropic filters are innate to filtering satellite gravimetry based spherical harmonic spectra, mainly due to equispaced sampling along the latitude circles.

- vii. The latitude-dependent anisotropic filters have some intriguing aspects. Firstly, their spectrum has a order-leading block-diagonal structure, which is due to the equispaced sampling along the latitude circles. Secondly, because of the sampling and convergence of the longitudes at the poles their spatial structure becomes isotropic.
- viii. By representing the spectra of the field and the smoothing operator in terms of their polar form, we found out that isotropic filters retain the phase of the field after filtering, while anisotropic filters change it. In the filtering of GRACE data with anisotropic filters, the phase of the pre- and post-filtered spectra clearly indicated the decorrelating effect of the filters used.
- ix. Irrespective of the type or design of the smoothing operator the level of smoothing that can be achieved by it is restricted by a qualitative bound. The bound is defined by the global average  $\bar{f}_\Omega(\cdot)$  and the unsmoothed value  $\bar{f}_\delta(\cdot)$  ( $= f(\cdot)$ ). This bound is naturally linked to the uncertainty principle in signal processing.
- x. Designing smoothing operators can be done both spatially and spectrally. The weight functions can be designed as purely deterministic functions, or derived from data-driven and variational calculus methods.
- xi. A number of filters that were analysed in this study have been designed in a deterministic manner, and nearly all of them have a homogeneous isotropic structure. The reason lies in the simplicity of their spectral structure, which makes them fairly straight-forward to design.
- xii. Based on the energy functional and the anatomy of the smoothing operator, metrics for assessing its performance have been developed. Spatial resolution, spatial variance and spatial leakage have all been treated in a novel way.
- xiii. Spatial resolution of a smoothing operator, as we have demonstrated, can only be described in an ideal manner, and hence the use of the term ideal resolution. It was generally accepted that the resolution of the smoothing operator is its -6 dB isoline ( $1/2 b(\theta, \lambda, 0, 0)$ ), but we have demonstrated otherwise. In addition, we have extended and complemented the concept of spatial resolution with the modulation transfer function, whose slope gives an indication of the smoothness of the filtered field.
- xiv. So far, spatial variance has been treated as a uni-dimensional quantity even for anisotropic filters [e.g., Kusche et al., 2009]. Here we derive the spatial variance as a three-dimensional quantity following ideas from spherical statistics.
- xv. In the GRACE community, spatial leakage is treated in a subjective manner, for example, signal exchange between two catchments or signal exchange between ocean and the landmass due to filtering. In this study we define spatial leakage, in an objective way, as the energy that the filter retains beyond the ideal resolution isoline as it directly affects the spatial variance, i.e. the localisation properties of the filter.
- xvi. Inter-comparison of the performance metrics of homogeneous isotropic filters was fairly straightforward compared to the inhomogeneous (and) anisotropic filters. Although the cascade of destriping filter and Gaussian filter was compared with the regularization

filter, it could not be done as comprehensively as in the case of the homogeneous isotropic filters. A clear example is the difficulty in matching the filters according to their spatial, which, in both the cases, is latitude-dependent.

- xvii. There is no single homogeneous isotropic filter that performs best in all the given metrics. For example, while the Gaussian filter has the best processing gain, it is the worst when it comes to processing loss.
- xviii. The performance metrics, especially performance loss and spatial variance, reveal alternatives to the Gaussian filter, which has been the mainstay of GRACE data processing. Diffusion and spectral cosine filters are good alternatives to the Gaussian filter.
- xix. Using filters to smooth band-limited signals, whose spatial resolution is far greater than the smoothing radii of the filter, is not desirable. The properties of the filter in its design form will not hold for the truncated filter, requiring individual evaluation of the truncated filter performance.

## CONCLUSIONS AND OPEN QUESTIONS

Based on the findings of this study it can be said with assurance that good inroads have been made in the filter choice problem. While a clear choice can be made from among the plethora of homogeneous isotropic filters, the same cannot be said for the anisotropic filters. In this study we have only dealt with latitude-dependent anisotropic filters, which has given a fair idea of the challenges that have to be dealt with in evaluating completely inhomogeneous and anisotropic filters. Despite the difficulty in choosing inhomogeneous anisotropic filters, inroads have also been made in understanding the mechanics of such filters. It remains to be seen how this understanding can be translated to inter-comparability and thereby solve the inhomogeneous and anisotropic filter choice problem.

The subtext to the primary aim of solving the filter choice problem was the idea of data agnostic filter performance metrics. With the performance metrics that have been developed here, it can be said with confidence that we have been successful in that attempt. Except for processing gain and processing loss, all the other metrics are data agnostic. Also in the case of processing gain and processing loss, a data agnostic variant was devised, but it is valid only for homogeneous isotropic filters. In a similar vein, for some of the performance metrics data-dependent variants have also been devised. Nevertheless, it should be noted that much of the performance metrics analyse the spatial characteristics of the filter. This must be complemented in the future with performance metrics that evaluate the spectral characteristics of the filter.

The performance metrics devised here need not only be used for evaluating filter performance, but it is also hoped that it will trigger new ways of filter design. For example, filter designs that optimise processing loss and processing gain, or those that optimise the trade-off between spatial resolution and spatial variance. With the knowledge of the spatial structure and spectral form, as expounded here, it should naturally be the next step. Such designs would pre-define the role of the filter thereby making filter choice far more easier. Moreover, such filter designs are the need of the hour for GRACE data processing as there is still room for improvement as demonstrated by the enormous differences between the filtered and unfiltered autocovariance functions.

In this study, the polar form of the spherical harmonics is used as an analysis tool for studying the spectral characteristics of the filters. In the case of GRACE data processing, it turned out to be a vital tool in evaluating the decorrelating capabilities of filters. Further, the polar form made it clear that anisotropic filters will change the phase spectrum to an arbitrary value between  $-\pi$  and  $\pi$ , while isotropic filters will retain the phase spectrum or will shift it by  $\pi$  radians. This is a crucial piece of information for users comparing GRACE data with geophysical model output after filtering both the datasets with the same anisotropic filter. It is worthy to note here that we only know that the phase spectrum changes, but it is yet to be proven whether such a change is critical or not.

## BIBLIOGRAPHY

---

- Albertella, A, Sansò, F and Sneeuw, N (1999). Band-limited functions on a bounded spherical domain: the Slepian problem on the sphere. *Journal of Geodesy*, 73(9):436–447. doi:10.1007/PL00003999.
- Bergen, SWA and Antoniou, A (2004). Design of ultraspherical window functions with prescribed spectral characteristics. *EURASIP Journal on Applied Signal Processing*, 13:2053–2065.
- Bouman, J and Koop, R (1998). Regularization in gradiometric analysis. *Physics and Chemistry of the Earth*, 23(1):41 – 46. doi:http://dx.doi.org/10.1016/S0079-1946(97)00239-5.
- Bruinsma, SL, Förste, C, Abrikosov, O, Marty, JC et al. (2013). The new ESA satellite-only gravity field model via the direct approach. *Geophys Res Lett*. doi:10.1002/grl.50716.
- Chen, J, Wilson, C and Seo, KW (2006). Optimized smoothing of Gravity Recovery and Climate Experiment (GRACE) time-variable gravity observations. *Journal of Geophysical Research*, 111:Bo6,408. doi:doi:10.1029/2005JB004064.
- Cheng, M and Ries, J (2013). *Monthly estimates of C20 from 5 SLR satellites based on GRACE RLO5 models*. GRACE Technical Note 7, Center for Space Research, The University of Texas at Austin.
- Crowley, JW, Mitrovica, JX, Bailey, RC, Tamisiea, ME et al. (2006). Land water storage within the congo basin inferred from grace satellite gravity data. *Geophysical Research Letters*, 33:L19,402. doi:10.1029/2006GL027070.
- Dahle, C, Flechtner, F, Gruber, C, König, D et al. (2013). *GFZ GRACE level-2 processing standards document (for level-2 product release 0005)*. Scientific Technical Report Rev. 1.1, GFZ German Research Centre for Geosciences.
- Davis, JL, Tamisiea, ME, Elósegui, P, Mitrovica, JX et al. (2008). A statistical filtering approach for gravity recovery and climate experiment (grace) gravity data. *Journal of Geophysical Research*, 113(B4). doi:10.1029/2007JB005043.
- Duan, X, Guo, J, Shum, C and Wal, W (2009). On the postprocessing removal of correlated errors in grace temporal gravity field solutions. *Journal of Geodesy*, 83(11):1095–1106. doi:10.1007/s00190-009-0327-0.
- Edmonds, AR (1960). *Angular momentum in quantum mechanics*. 2nd edn. Princeton University Press.
- Fersch, B, Kunstmann, H, Bárdossy, A, Devaraju, B et al. (2012). Continental-scale basin water storage variation from global and dynamically downscaled atmospheric water budgets in comparison with GRACE-derived observations. *Journal of Hydrometeorology*, pp. 1589–1603. doi:10.1175/jhm-d-11-0143.1.
- Fisher, NI, Lewis, T and Embleton, BJJ (1987). *Statistical analysis of spherical data*. Cambridge University Press.
- Fisher, RA (1953). Dispersion on a sphere. *Proceedings of the Royal Society of London Series A, Mathematical and Physical Sciences*, 217(1130):295–305.

- Frappart, F, Ramillien, G, Leblanc, M, Tweed, SO et al. (2011). An independent component analysis filtering approach for estimating continental hydrology in the GRACE gravity data. *Remote Sensing of Environment*, **115**(1):187 – 204. doi:http://dx.doi.org/10.1016/j.rse.2010.08.017.
- Freeden, W and Schreiner, M (2009). *Spherical functions of mathematical geosciences*. Advances in Geophysical and Environmental Mechanics and Mathematics. Springer.
- Gerlach, C, Sneeuw, N, Visser, P and Švehla, D (2003). CHAMP gravity field recovery using the energy balance approach. *Advances in Geosciences*, **1**:73–80. doi:10.5194/adgeo-1-73-2003.
- Gleick, PH, Cooley, H, Famiglietti, JS, Lettenmaier, DP et al. (2013). Improving understanding of the global hydrologic cycle. In: Asrar, GR and Hurrell, JW, eds., *Climate Science for Serving Society*, pp. 151–184. Springer Netherlands. doi:10.1007/978-94-007-6692-1\_6.
- Hamming, RW (1989). *Digital Filters*. 3rd edn. Prentice Hall.
- Han, SC, Shum, CK, Jekeli, C, Kuo, CY et al. (2005). Non-isotropic filtering of GRACE temporal gravity for geophysical signal enhancement. *Geophysical Journal International*, **163**:18–25. doi:10.1111/j.1365-246X.2005.02756.
- Harris, FJ (1978). On the use of windows for harmonic analysis with the discrete Fourier transform. *Proceedings of the IEEE*, **66**(1):51–93.
- Ilk, KH (1983). *Ein Beitrag zur Dynamik ausgedehnter Körper: Gravitationswechselwirkung*. Habilitation dissertation C288, Deutsche Geodätische Kommission.
- Jekeli, C (1981). *Alternative methods to smooth the Earth's gravity field*. Tech. Rep. 327, Department of Geodetic Science and Surveying, The Ohio State University.
- Jin, S, van Dam, T and Wdowinski, S (2013). Observing and understanding the Earth system variations from space geodesy. *Journal of Geodynamics*, **72**:1–10. doi:10.1016/j.jog.2013.08.001.
- Kaula, WM (1966). *Theory of Satellite Geodesy: Applications of Satellites to Geodesy*. Blaisdell Publishing Company.
- (1967). Theory of statistical analysis of data distributed over a sphere. *Reviews of Geophysics*, **5**(1):83–107.
- Khalid, Z, Durrani, S, Kennedy, R and Sadeghi, P (2011). On the construction of low-pass filters on the unit sphere. In: *Acoustics, Speech and Signal Processing (ICASSP), 2011 IEEE International Conference on*, pp. 4356–4359. doi:10.1109/ICASSP.2011.5947318.
- King, M, Moore, P, Clarke, P and Lavallée, D (2006). Choice of optimal averaging radii for temporal GRACE gravity solutions, a comparison with GPS and satellite altimetry. *Geophysical Journal International*, **166**(1):1–11. doi:10.1111/j.1365-246X.2006.03017.x.
- Klees, R, Revtova, EA, Gunter, BC, Ditmar, P et al. (2008). The design of an optimal filter for monthly GRACE gravity models. *Geophysical Journal International*, **175**:417–432. doi:10.1111/j.1365-246X.2008.03922.x.
- Klees, R, Zapreeva, EA, Winsemius, HC and Savenije, HHG (2007). The bias in GRACE estimates of continental water storage variations. *Hydrology and Earth System Sciences*, **11**:1227–1241.
- Koch, KR and Kusche, J (2002). Regularization of geopotential determination from satellite data by variance components. *Journal of Geodesy*, **76**:259–268. doi:10.1007/s00190-002-0245-x.
- Kusche, J (2007). Approximate decorrelation and non-isotropic smoothing of time-variable GRACE-type gravity field models. *Journal of Geodesy*, **81**:733–749. doi:10.1007/s00190-007-0143-3.



- Kusche, J, Schmidt, R, Petrovic, S and Rietbroek, R (2009). Decorrelated GRACE time-variable gravity solutions by GFZ, and their validation using a hydrological model. *Journal of Geodesy*, 83(10):903–913. doi:10.1007/s00190-009-0308-3.
- Landerer, FW and Swenson, SC (2012). Accuracy of scaled GRACE terrestrial water storage estimates. *Water Resources Research*, 48(4). doi:10.1029/2011WR011453.
- Laprise, R (1992). The resolution of global spectral models. *B Am Meteorol Soc*, 73(9):1453–1454.
- Lillesand, TM and Kiefer, RW (1994). *Remote sensing and image interpretation*. 3rd edn. John Wiley & Sons, Inc.
- Longuevergne, L, Scanlon, BR and Wilson, CR (2010). GRACE hydrological estimates for small basins: Evaluating processing approaches on the high plains aquifer, usa. *Water Resources Research*, 46:W11,517. doi:10.1029/2009WR008564.
- Lorenz, C (2009). *Applying stochastic constraints on time-variable GRACE data*. Diplomarbeit, Institute of Geodesy, University of Stuttgart.
- Lorenz, C, Kunstmann, H, Devaraju, B, Tourian, MJ et al. (2014). Large-scale runoff from landmasses: a global assessment of the closure of the hydrological and atmospheric water balances. *Journal of Hydrometeorology*. doi:10.1175/JHM-D-13-0157.1.
- Martinec, Z and Pěč, K (1985). Expansions of the double product of the global gravity field. *Studia Geoph et Geod*, 29:211–219.
- Moritz, H (1989). *Advanced Physical Geodesy*. 2nd edn. Wichmann.
- Murböck, M, Pail, R, Daras, I and Gruber, T (2014). Optimal orbits for temporal gravity recovery regarding temporal aliasing. *Journal of Geodesy*, 88(2):113–126. doi:10.1007/s00190-013-0671-y.
- Narcowich, FJ and Ward, JD (1996). Nonstationary wavelets on them-sphere for scattered data. *Applied and Computational Harmonic Analysis*, 3(4):324 – 336. doi:http://dx.doi.org/10.1006/acha.1996.0025.
- Nutall, AH (1981). Some windows with very good sidelobe behaviour. *IEEE Transactions on Acoustics, Speech, and Signal Processing*, ASSP-29(1):84–91.
- Oppenheim, AV, Schafer, RW and Buck, JR (1999). *Discrete-time Signal Processing*. 2nd edn. Prentice Hall Signal Processing Series.
- Pellinen, L (1966). A method for expanding the gravity potential of the earth in spherical functions. *Transactions of the Central Scientific Research Institute of Geodesy, Aerial Survey and Cartography*, 171:65–116.
- (1970). Estimation and application of degree variances of gravity. *Studia Geophysica et Geodætica*, 14(2):168–173. doi:10.1007/BFo2585615.
- Plag, HP and Pearlman, M (2009). *Global Geodetic Observing System*. Springer Berlin Heidelberg. doi:10.1007/978-3-642-02687-4.
- Rangelova, E, van der Wal, W, Braun, A, Sideris, MG et al. (2007). Analysis of Gravity Recovery and Climate Experiment time-variable mass redistribution signals over North America by means of principal component analysis. *Journal of Geophysical Research*, 112:F03,002. doi:10.1029/2006JF000615.
- Reigber, C, Balmino, G, Schwintzer, P, Biancale, R et al. (2002). A high-quality global gravity field model from CHAMP GPS tracking data and accelerometry (EIGEN-1S). *Geophysical Research Letters*, 29(14):37–1–37–4. doi:10.1029/2002GL015064.

- Rodell, M and Famiglietti, JS (1999). Detectability of variations in continental water storage from satellite observations of the time dependent gravity field. *Water Resources Research*, 35(9):2705–2723. doi:10.1029/1999WR900141.
- Rodell, M, Famiglietti, JS, Chen, J, Seneviratne, SI et al. (2004). Basin scale estimates of evapotranspiration using GRACE and other observations. *Geophysical Research Letters*, 31:L20,504. doi:10.1029/2004GL020873.
- Rodell, M, Velicogna, I and Famiglietti, JS (2009). Satellite-based estimates of groundwater depletion in India. *Nature*, 460:999–1002. doi:10.1038/nature08238.
- Rummel, R (2010). The interdisciplinary role of space geodesy—revisited. *Journal of Geodynamics*, 49(3–4):112–115. doi:10.1016/j.jog.2009.10.006.
- Rummel, R and Schwarz, KP (1977). On the nonhomogeneity of the global covariance function. *Bull Géod*, 51:93–103.
- Rummel, R and van Gelderen, M (1995). Meissl scheme – spectral characteristics of physical geodesy. *Manuscripta Geodaetica*, 20:379–385.
- Rummel, R, Yi, W and Stummer, C (2011). GOCE gravitational gradiometry. *Journal of Geodesy*, 85(11):777–790. doi:10.1007/s00190-011-0500-0.
- Sardeshmukh, PD and Hoskins, BJ (1984). Spatial smoothing on the sphere. *Monthly Weather Review*, 112:2524–2529.
- Sasgen, I, Martinec, Z and Fleming, K (2006). Wiener optimal filtering of GRACE data. *Studia Geoph et Geod*, 50:499–508.
- Savitzky, A and Golay, MJE (1964). Smoothing and differentiation of data by simplified least squares procedures. *Analytical Chemistry*, 36(8):1627–1639. doi:10.1021/ac60214a047.
- Schmidt, R, Flechtner, F, Meyer, U, Neumayer, KH et al. (2008). Hydrological Signals Observed by the GRACE Satellites. *Surveys in Geophysics*, 29(4–5):319–334.
- Schrama, EJO and Wouters, B (2011). Revisiting greenland ice sheet mass loss observed by GRACE. *Journal of Geophysical Research*, 116(B02407). doi:10.1029/2009JB006847.
- Seitz, F, Schmidt, M and Shum, CK (2008). Signals of extreme weather conditions in Central Europe in GRACE 4-D hydrological mass variations. *Earth and Planetary Science Letters*, 268:165–170. doi:10.1016/j.epsl.2008.01.001.
- Seo, KW and Wilson, CR (2005). Simulated estimation of hydrological loads from GRACE. *Journal of Geodesy*, 78(7–8):442–456. doi:10.1007/s00190-004-0410-5.
- Seo, KW, Wilson, CR, Han, SC and Waliser, DE (2008). Gravity recovery and climate experiment (GRACE) alias error from ocean tides. *Journal of Geophysical Research*, 113:B03,405. doi:10.1029/2006JB004747.
- Sneeuw, N (2000). *A semi-analytical approach to gravity field analysis from satellite observations*. Dissertationen Heft Nr. 527, Deutsche Geodätische Kommission, bei der Bayerischen Akademie der Wissenschaften.
- Sneeuw, N, Lorenz, C, Devaraju, B, Tourian, M et al. (2014). Estimating runoff using hydro-geodetic approaches. *Surveys in Geophysics*, 35(6):1333–1359. doi:10.1007/s10712-014-9300-4.
- Sneeuw, NJ (1991). *Inclination Functions: Group Theoretical Background and a Recursive Algorithm*. Tech. Rep. 91.2, Mathematical and Physical Geodesy, Faculty of Geodetic Engineering, Delft University of Technology.

- Strang, G (1986). *Introduction to Applied Mathematics*. Wellesley-Cambridge.
- Swenson, S and Wahr, J (2002). Methods for inferring regional surface-mass anomalies from Gravity Recovery and Climate Experiment (GRACE). *Journal of Geophysical Research*, **107**(B9):2193. doi: 10.1029/2001JB000576.
- (2006a). Estimating large-scale precipitation minus evapotranspiration from GRACE satellite gravity measurements. *Journal of Hydrometeorology*, **7**:252–270. doi:10.1175/JHM478.1.
- (2006b). Post-processing removal of correlated errors in GRACE data. *Geophysical Research Letters*, **33**:L08,402. doi:10.1029/2005GL025285.
- Syed, T, Famiglietti, J and Chambers, D (2009). GRACE-based estimates of terrestrial freshwater discharge from basin to continental scales. *Journal of Hydrometeorology*, **10**:22–40. doi:10.1175/2008JHM993.1.
- Tapley, BD, Bettadpur, S, Watkins, MM and Reigber, C (2004). The Gravity Recovery and Climate Experiment: Mission overview and early results. *Geophysical Research Letters*, **31**(9):L09,607. doi: 10.1029/2004GL019920.
- Tourian, MJ (2013). *Application of spaceborne geodetic sensors for hydrology*. Ph.D. thesis, Universität Stuttgart, Holzgartenstr. 16, 70174 Stuttgart.
- Trenberth, KE, Smith, L, Qian, T, Dai, A et al. (2007). Estimates of the global water budget and its annual cycle using observational and model data. *Journal of Hydrometeorology*, **8**(4):758–769. doi:10.1175/JHM600.1.
- Varshalovich, DA, Moskalev, AN and Khersonskii, VK (1988). *Quantum theory of angular momentum*. World Scientific.
- Wahr, J, Molenaar, M and Bryan, F (1998). Time variability of the Earth's gravity field: Hydrological and oceanic effects and their possible detection using GRACE. *Journal of Geophysical Research*, **103**(B12):30,205–30,229.
- Werth, S, Güntner, A, Schmidt, R and Kusche, J (2009). Evaluation of GRACE filter tools from a hydrological perspective. *Geophysical Journal International*, **179**:1499–1515. doi:10.1111/j.1365-246X.2009.04355.x.
- Wouters, B and Schrama, EJO (2007). Improved accuracy of GRACE gravity solutions through empirical orthogonal function filtering of spherical harmonics. *Geophysical Research Letters*, **34**:L23,711. doi: 10.1029/2007GL032098.
- Wu, X, Blom, RG, Ivins, ER, Oyafuso, FA et al. (2009). Improved inverse and probabilistic methods for geophysical applications of GRACE gravity data. *Geophysical Journal International*, **177**(3):865–877. doi:10.1111/j.1365-246X.2009.04141.x.
- Zhang, ZZ, Chao, BF, Lu, Y and Hsu, HT (2009). An effective filtering for GRACE time-variable gravity: Fan filter. *Geophysical Research Letters*, **36**(17):L17,311. doi:10.1029/2009GL039459.

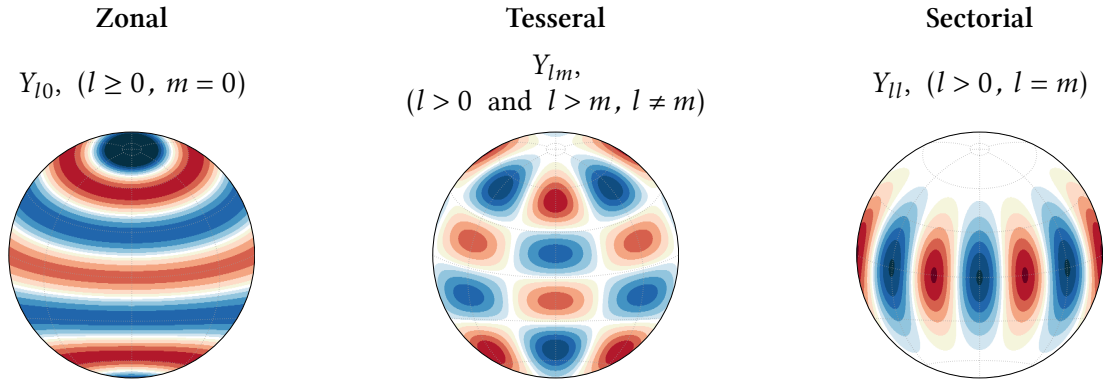
This chapter is intended as a quick formula look-up sheet. All the formulae have been adapted from Varshalovich et al. [1988, chap. 5], and adaptations have been mainly on the normalisation conventions. Some use also have been made of the reports of Sneeuw [1991]; Ilk [1983].

### §A.1 SURFACE SPHERICAL HARMONICS

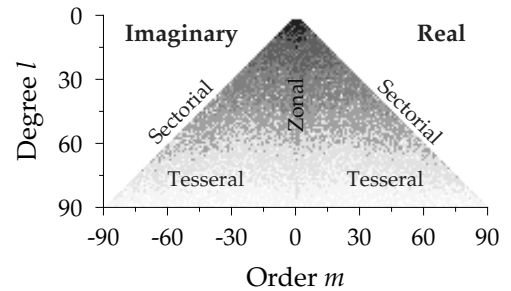
#### Definition

$$Y_{lm}(\theta, \lambda) = \begin{cases} \bar{P}_{lm}(\cos \theta) e^{im\lambda}, & m \geq 0 \\ (-1)^m Y_{l,-m}^*(\theta, \lambda), & m < 0 \end{cases} \quad (\text{A.1a})$$

$$Y_{lm}^*(\theta, \lambda) = \bar{P}_{lm}(\cos \theta) e^{-im\lambda} \quad (\text{A.1b})$$



**Figure A.1:** Spherical harmonic coefficients arranged in matrix form according to their degree and order. The locations of the different structural forms of the spherical harmonics are indicated.



**Orthogonality**

$$\frac{1}{4\pi} \int_{\Omega} Y_{lm}(\theta, \lambda) Y_{l'm'}^*(\theta, \lambda) d\Omega = \delta_{ll'} \delta_{mm'} \quad (\text{A.2})$$

**Addition theorem**

$$P_l(\cos \psi) = \frac{1}{2l+1} \sum_{m=-l}^l Y_{lm}(\theta, \lambda) Y_{lm}^*(\theta', \lambda') \quad (\text{A.3a})$$

$$\cos \psi = \cos \theta \cos \theta' + \sin \theta \sin \theta' \cos \Delta \lambda \quad (\text{A.3b})$$

**Completeness**

$$\sum_{l,m} Y_{lm}(\theta, \lambda) Y_{lm}(\theta', \lambda') = \sum_l (2l+1) P_l(\cos \psi) = \delta(\psi) \quad (\text{A.4})$$

$$\frac{1}{4\pi} \int_{\Omega'} \delta(\psi) d\Omega' = \begin{cases} 1, & \psi = 0 \Rightarrow (\theta, \lambda) = (\theta', \lambda') \\ 0, & \text{elsewhere} \end{cases} \quad (\text{3.3b})$$

**Integral**

$$\frac{1}{4\pi} \int_{\Omega} Y_{lm}(\theta, \lambda) d\Omega = \frac{1}{4\pi} \int_{\Omega} Y_{lm}(\theta, \lambda) Y_{00}(\theta, \lambda) d\Omega = \delta_{l0} \delta_{m0} \quad (\text{A.5})$$

**Integral of triple product**

$$\frac{1}{4\pi} \int_{\Omega} Y_{lm}(\theta, \lambda) Y_{l'm'}(\theta, \lambda) Y_{l''m''}^*(\theta, \lambda) d\Omega = \sqrt{\frac{(2l+1)(2l'+1)}{2l''+1}} C_{l0l'0}^{l''0} C_{lml'm'}^{l''m''} \quad (\text{A.6})$$

**§A.2 ASSOCIATED LEGENDRE FUNCTIONS****Explicit expression**

$$P_{lm}(x) = \frac{1}{2^l l!} (1-x^2)^{\frac{m}{2}} \frac{d^{l+m}}{dx^{l+m}} (x^2-1)^l \quad (\text{A.7a})$$

$$\bar{P}_{lm}(x) = (-1)^m \sqrt{(2l+1) \frac{(l-m)!}{(l+m)!}} P_{lm}(x) = N_{lm} P_{lm}(x) \quad (\text{A.7b})$$

### Orthogonality

$$\frac{1}{2} \int_{-1}^1 P_{lm}(x) P_{nk}(x) \delta_{mk} dx = \frac{1}{2l+1} \frac{(l+m)!}{(l-m)!} \delta_{ln} = N_{lm}^{-2} \delta_{ln} \quad (\text{A.8})$$

### Symmetries

$$P_{lm}(-x) = (-1)^{l+m} P_{lm}(x) \quad (\text{A.9a})$$

$$P_{l,-m}(x) = (-1)^m \frac{(l-m)!}{(l+m)!} P_{lm}(x) \quad (\text{A.9b})$$

### Special cases

$$P_{lm}(1) = \delta_{m0} \quad (\text{A.10a})$$

$$P_{lm}(0) = \begin{cases} \frac{(-1)^{\frac{l-m}{2}}}{2^l} \frac{(l+m)!}{\left(\frac{l-m}{2}\right)! \left(\frac{l+m}{2}\right)!}, & \text{for } l-m \text{ even,} \\ 0, & \text{otherwise.} \end{cases} \quad (\text{A.10b})$$

## §A.3 ROTATION OF SPHERICAL HARMONICS

$$Y_{lm}(\theta', \lambda') = \sum_k D_{lmk}(\alpha, \beta, \gamma) Y_{lk}(\theta, \lambda) \quad (\text{A.11a})$$

$$Y_{lm}^*(\theta', \lambda') = \sum_m D_{lmk}^*(\alpha, \beta, \gamma) Y_{lk}^*(\theta, \lambda) \quad (\text{A.11b})$$

$$Y_{lk}(\theta, \lambda) = \sum_m D_{lkm}^*(\alpha, \beta, \gamma) Y_{lm}(\theta', \lambda') \quad (\text{A.11c})$$

$$D_{lmk}(\alpha, \beta, \gamma) = e^{-im\gamma} d_{lmk}(\beta) e^{-ik\alpha} \quad (\text{2.13a})$$

$$D_{lmk}^*(\alpha, \beta, \gamma) = e^{im\gamma} d_{lmk}(\beta) e^{ik\alpha} \quad (\text{2.13b})$$

$$d_{lmk}(\beta) = (-1)^{k-m} \sqrt{\frac{(l-k)!}{(l-m)!} \frac{(l+k)!}{(l+m)!}} \sum_{t=t_1}^{t_2} \binom{l+m}{t} \binom{l-m}{l-k-t} (-1)^t c^{2l-p} s^p \quad (\text{2.13c})$$

$$\text{with } c = \cos \frac{\beta}{2} \quad (\text{2.13d})$$

$$s = \sin \frac{\beta}{2} \quad (\text{2.13e})$$

$$p = k - m + 2t \quad (\text{2.13f})$$

$$t_1 = \max(0, m-k) \quad (\text{2.13g})$$

$$t_2 = \min(l-k, l+m) \quad (\text{2.13h})$$

$\alpha = [0, 2\pi)$ , rotation about the initial  $x$ -axis

$\beta = [0, \pi]$ , rotation about the new  $y$ -axis

$\gamma = [0, 2\pi)$ , rotation about the final z-axis

### Orthogonality

$$\frac{1}{8\pi^2} \int_0^{2\pi} \int_0^\pi \int_0^{2\pi} D_{lmk}(\alpha, \beta, \gamma) D_{l'm'k'}^*(\alpha, \beta, \gamma) d\alpha \sin\beta d\beta d\gamma = \frac{1}{2l+1} \delta_{ll'} \delta_{mm'} \delta_{kk'}, \quad (\text{A.12a})$$

which leads to the following orthogonality property for the Wigner- $d$  symbols,

$$\frac{1}{2} \int_0^\pi d_{lmk}(\beta) d_{l'm'k'}(\beta) \delta_{kk'} \delta_{mm'} \sin\beta d\beta = \frac{1}{2l+1} \delta_{ll'}. \quad (\text{A.12b})$$

### Product

$$D_{lmk}(\alpha, \beta, \gamma) D_{l'm'k'}(\alpha, \beta, \gamma) = \sum_{l''=|l-l'|}^{l+l'} \sum_{m''=-l''}^{l''} \sum_{k''=-l''}^{l''} C_{lml'm'}^{l''m''} C_{lkl'k'}^{l''k''} D_{l''m''k''}(\alpha, \beta, \gamma), \quad (\text{A.13a})$$

and when  $(\alpha = \gamma = 0)$  a result for Wigner- $d$  symbols can be deduced.

$$d_{lmk}(\beta) d_{l'm'k'}(\beta) = \sum_{l''=|l-l'|}^{l+l'} \sum_{m''=-l''}^{l''} \sum_{k''=-l''}^{l''} C_{lml'm'}^{l''m''} C_{lkl'k'}^{l''k''} d_{l''m''k''}(\beta). \quad (\text{A.13b})$$

### Symmetries

$$D_{lmk}^*(\alpha, \beta, \gamma) = D_{lkm}(-\gamma, -\beta, -\alpha), \quad (\text{A.14a})$$

$$D_{lmk}^*(\alpha, \beta, \gamma) = (-1)^{k-m} D_{l,-m,-k}(\alpha, \beta, \gamma). \quad (\text{A.14b})$$

$$d_{lmk}(\beta) = d_{lkm}(-\beta), \quad (\text{A.15a})$$

$$d_{lmk}(\beta) = (-1)^{k-m} d_{lmk}(-\beta), \quad (\text{A.15b})$$

$$d_{lmk}(\beta) = (-1)^{k-m} d_{lkm}(\beta), \quad (\text{A.15c})$$

$$d_{lmk}(\beta) = d_{l,-k,-m}(\beta), \quad (\text{A.15d})$$

$$d_{lmk}(\beta) = (-1)^{k-m} d_{l,-m,-k}(\beta). \quad (\text{A.15e})$$

### Special cases

$$D_{lm0}(\alpha, \beta, \gamma) = \frac{(-1)^m}{\sqrt{2l+1}} Y_{lm}^*(\beta, \gamma), \quad (\text{A.16a})$$

$$d_{lm0}(\beta) = \frac{(-1)^m}{\sqrt{2l+1}} \bar{P}_{lm}(\cos\beta), \quad (\text{A.16b})$$

$$D_{l00}(\alpha, \beta, \gamma) = d_{l00}(\beta) = P_{l0}(\cos\beta) = P_l(\cos\beta), \quad (\text{A.16c})$$

$$D_{lmk}(0,0,0) = \delta_{mk}, \quad (\text{A.16d})$$

$$d_{lmk}(0) = \delta_{mk}, \quad (\text{A.16e})$$

$$d_{lmk}(\pi) = (-1)^{l+m} \delta_{-m,k} = (-1)^{l-k} \delta_{m,-k}, \quad (\text{A.16f})$$

$$d_{lmk}(\pi - \beta) = (-1)^{l+k} d_{l,-m,k}(\beta) = (-1)^{l-m} d_{l,m,-k}(\beta), \quad (\text{A.16g})$$

$$d_{lmk}(\pi + \beta) = (-1)^{l+m} d_{l,-m,k}(\beta) = (-1)^{l-k} d_{l,m,-k}(\beta). \quad (\text{A.16h})$$

#### §A.4 SPHERICAL HARMONIC SPECTRUM

##### Series expansion

$$f(\theta, \lambda) = \sum_{l=0}^{\infty} \sum_{m=-l}^l F_{lm} \bar{P}_{lm}(\cos \theta) e^{im\lambda} = \sum_{l,m} F_{lm} Y_{lm}(\theta, \lambda) \quad (\text{A.17a})$$

$$F_{lm} = \frac{1}{4\pi} \int_0^{2\pi} \int_0^{\pi} f(\theta, \lambda) \bar{P}_{lm}(\cos \theta) e^{-im\lambda} \sin \theta \, d\theta \, d\lambda \quad (\text{A.17b})$$

$$= \frac{1}{4\pi} \int_{\Omega} f(\theta, \lambda) Y_{lm}^*(\theta, \lambda) \, d\Omega \quad (\text{A.17c})$$

##### Parseval's theorem

$$\frac{1}{4\pi} \int_{\Omega} f^2(\theta, \lambda) \, d\Omega = \sum_{l,m} F_{lm}^2 \quad (\text{A.18})$$

##### Mean value of the field

$$\frac{1}{4\pi} \int_{\Omega} f(\theta, \lambda) \, d\Omega = \frac{1}{4\pi} \int_{\Omega} \sum_{l,m} F_{lm} Y_{lm}(\theta, \lambda) \, d\Omega \quad (\text{A.19a})$$

$$= F_{00} \quad (\text{A.19b})$$

##### Polar form of the spherical harmonic spectrum

$$F_{lm} = A_{lm} e^{i\phi_{lm}} \quad (\text{2.34a})$$

$$A_{lm} = |F_{lm}| = \sqrt{\text{Re}(F_{lm})^2 + \text{Im}(F_{lm})^2} \quad (\text{2.34b})$$

$$\phi_{lm} = \arg(F_{lm}) = \arctan\left(\frac{\text{Im}(F_{lm})}{\text{Re}(F_{lm})}\right) \quad (\text{2.34c})$$

$$\therefore f(\theta, \lambda) = \sum_{l,m} A_{lm} \bar{P}_{lm}(\cos \theta) e^{i(m\lambda + \phi_{lm})} \quad (\text{2.34d})$$



**Power spectral quantities**

$$\sigma_l^2 = \sum_{m=-l}^l |F_{lm}|^2 = \sum_{m=-l}^l A_{lm}^2 \quad \text{Degree variance,} \quad (\text{A.20a})$$

$$\text{RMS}_l = \frac{\sigma_l}{\sqrt{2l+1}} \quad \text{Degree RMS,} \quad (\text{A.20b})$$

$$\text{CUM}_l = \sum_{j=0}^l \sum_{m=-j}^j A_{jm}^2 \quad \text{Cumulative degree variance.} \quad (\text{A.20c})$$

## INTEGRAL OF THE PRODUCT OF WIGNER- $d$ SYMBOLS

---

In this chapter we will compute the integral of the product of two Wigner- $d$  functions.

$$I_{lmk}^{l'm'k'} = \frac{1}{2} \int_0^\pi d_{lmk}(\beta) d_{l'm'k'}(\beta) \sin \beta \, d\beta, \quad (\text{B.1a})$$

where we substitute the product of the Wigner- $d$  symbols with (A.13b),

$$= \frac{1}{2} \int_0^\pi \sum_{l''=|l-l'|}^{l+l'} \sum_{m''=-l''}^{l''} \sum_{k''=-l''}^{l''} C_{lm'l'm'}^{l''m''} C_{lk'l'k'}^{l''k''} d_{l''m''k''}(\beta) \sin \beta \, d\beta. \quad (\text{B.1b})$$

Here we substitute  $d_{l''m''k''}$  with its explicit expression using (2.13c – 2.13h).

$$\begin{aligned} I_{lmk}^{l'm'k'} &= \sum_{l''=|l-l'|}^{l+l'} \sum_{m''=-l''}^{l''} \sum_{k''=-l''}^{l''} C_{lm'l'm'}^{l''m''} C_{lk'l'k'}^{l''k''} \times \\ &\quad (-1)^{k''-m''} \sqrt{\frac{(l''-k'')!}{(l''-m'')!} \frac{(l''+k'')!}{(l''+m'')!}} \sum_{t''=t_1'}^{t_2'} \binom{l''+m''}{t''} \binom{l''-m''}{l''-k''-t''} (-1)^{t''} \times \\ &\quad \int_0^\pi \left( \cos \frac{\beta}{2} \right)^{2l''-p''+1} \left( \sin \frac{\beta}{2} \right)^{p''+1} d\beta, \end{aligned} \quad (\text{B.1c})$$

where we have used the identity  $\sin \beta = 2 \sin \frac{\beta}{2} \cos \frac{\beta}{2}$ . The only thing that remains to be done is to solve for the special trigonometric integral, for which we require the following identities.

$$\begin{aligned} \int \left( \sin \frac{\beta}{2} \right)^u \left( \cos \frac{\beta}{2} \right)^v d\beta &= \frac{-2}{u+v} \left( \sin \frac{\beta}{2} \right)^{u-1} \left( \cos \frac{\beta}{2} \right)^{v+1} + \\ &\quad \frac{u-1}{u+v} \int \left( \sin \frac{\beta}{2} \right)^{u-2} \left( \cos \frac{\beta}{2} \right)^v d\beta, \\ &= \frac{2}{u+v} \left( \sin \frac{\beta}{2} \right)^{u+1} \left( \cos \frac{\beta}{2} \right)^{v-1} + \end{aligned} \quad (\text{B.2a})$$

$$\frac{v-1}{u+v} \int \left( \sin \frac{\beta}{2} \right)^u \left( \cos \frac{\beta}{2} \right)^{v-2} d\beta, \quad (\text{B.2b})$$

Notice that we have two solutions for the integral, but the choice of either solution depends on two conditions: if  $u$  and/or  $v$  are even or odd; and if  $u \geq v$  or *vice versa*. In our case, either both  $u$  and  $v$  are simultaneously even or odd, since this only depends on  $p''$  (cf. (B.1c)), and therefore, we can expect to have four cases and their corresponding solutions.

$$\int_0^\pi \left( \sin \frac{\beta}{2} \right)^u \left( \cos \frac{\beta}{2} \right)^v d\beta = \begin{cases} \frac{\pi}{2^{u+v}} \frac{u!}{\left(\frac{u+v}{2}\right)!} \frac{v!}{\left(\frac{u}{2}\right)! \left(\frac{v}{2}\right)!}, & u \text{ \& } v \text{ are even,} \\ \frac{\left(\frac{u-1}{2}\right)! \left(\frac{v-1}{2}\right)!}{\left(\frac{u+v}{2}\right)!}, & u \text{ \& } v \text{ are odd.} \end{cases} \quad (\text{B.3})$$

Although we expected to have four solutions, we ended only with two as the results (B.3) indicate that the size  $u$  relative to  $v$  is immaterial. For the final solution, we substitute (B.3) in (B.1c), and taking  $u = p'' + 1$ ,  $v = 2l'' - p'' + 1$  and  $u, v \geq 0$ , we get

$$\begin{aligned} I_{lmk}^{l'm'k'} &= \sum_{l''=|l-l'|}^{l+l'} \sum_{m''=-l''}^{l''} \sum_{k''=-l''}^{l''} C_{lml'm'}^{l''m''} C_{lkl'k'}^{l''k''} \times \\ &(-1)^{k''-m''} \sqrt{\frac{(l''-k'')!}{(l''-m'')!} \frac{(l''+k'')!}{(l''+m'')!}} \sum_{t''=t_1'}^{t_2'} \binom{l''+m''}{t''} \binom{l''-m''}{l''-k''-t''} (-1)^{t''} \times \\ &\begin{cases} \frac{\pi}{2^{2(l''+1)}} \frac{(p''+1)!}{(l''+1)!} \frac{(2l''-p''+1)!}{\left(\frac{p''+1}{2}\right)! \left(\frac{2l''-p''+1}{2}\right)!}, & p'' \text{ is odd,} \\ \frac{1}{(l''+1)!} \left(\frac{p''}{2}\right)! \left(\frac{2l''-p''}{2}\right)!, & p'' \text{ is even.} \end{cases} \end{aligned} \quad (\text{B.4})$$

The orthogonality of  $d_{lmk}(\beta)$  given by (A.12b) can be viewed as a special case of  $I_{lmk}^{l'm'k'}$ , because

$$I_{lmk}^{l'mk} = \frac{1}{2} \int_0^\pi d_{lmk}(\beta) d_{l'mk}(\beta) \sin \beta d\beta = \frac{1}{2l+1} \delta_{ll'}. \quad (\text{B.5})$$

We recall that any field  $f(\theta, \lambda)$  given on an unit sphere can be represented in terms of a spherical harmonic series expansion.

$$f(\theta, \lambda) = \sum_{l,m} F_{lm} Y_{lm}(\theta, \lambda) \quad (2.1a)$$

and since  $F_{lm}$  is a complex number it can be rewritten in its polar form as follows:

$$F_{lm} = A_{lm} e^{i\phi_{lm}} \quad (2.34a)$$

inserting (2.34a) into (2.1a), the spherical harmonic synthesis can be expressed in terms of amplitude and phase.

$$\begin{aligned} f(\theta, \lambda) &= \sum_{l,m} A_{lm} e^{i\phi_{lm}} Y_{lm}(\theta, \lambda) \\ &= \sum_{l,m} A_{lm} e^{i\phi_{lm}} \bar{P}_{lm}(\cos \theta) e^{im\lambda} \\ &= \sum_{l,m} A_{lm} \bar{P}_{lm}(\cos \theta) e^{i(m\lambda + \phi_{lm})} \end{aligned} \quad (2.34d)$$

$$= \sum_{l,m} A_{lm} \bar{P}_{lm}(\cos \theta) e^{im(\lambda + \frac{\phi_{lm}}{m})} \quad (C.1a)$$

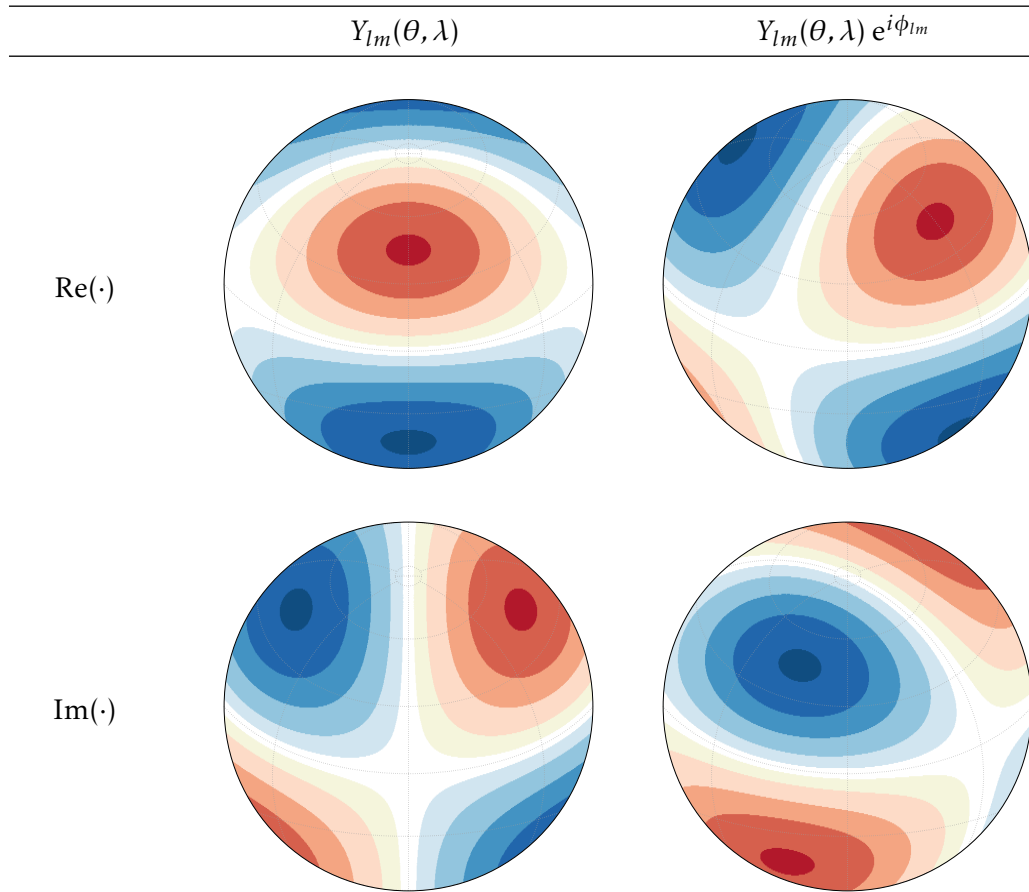
taking  $\lambda_1 = \lambda + \frac{\phi_{lm}}{m}$ ,

$$= \sum_{l,m} A_{lm} \bar{P}_{lm}(\cos \theta) e^{im\lambda_1} \quad (C.1b)$$

$$= \sum_{l,m} A_{lm} Y_{lm}(\theta, \lambda_1) \quad (C.1c)$$

In the above set of equations (C.1), the main ingredient that will help us interpret the polar representation, particularly the phase of the spectrum, is  $\lambda_1$ . The addition of the phase to the longitude of the surface spherical harmonic rotates it by  $\frac{\phi_{lm}}{m}$  (cf. Figure C.1), and therefore (C.1c) can be interpreted as the weighted sum of rotated surface spherical harmonics with the amplitude  $A_{lm}$  as the weights. Another important point that we have to note here is that as we move towards higher spherical harmonic orders the rotation becomes infinitesimal.

For any given spherical harmonic coefficient of degree  $l$  and order  $m$ , the amplitude is



**Figure C.1:** Surface spherical harmonics with (right) and without (left) phase shift. Here we have depicted the phase shift for the spherical harmonics of degree  $l = 2$ , order  $m = 1$  and a phase shift of  $\phi_{lm} = \pi/3$ .

a root-mean-squared positive value. This means that innumerable combinations of real and imaginary parts of a complex number will produce the same amplitude, which renders the amplitude spectrum non-unique. Similarly, the phase is also unique only up to the ratio of the real and imaginary parts. Thus, for a given amplitude there can be innumerable number of phase values, and *vice versa*.

## LIST OF SYMBOLS

---

### Coordinates

$\theta, \lambda$	Spherical coordinates of the unit sphere: co-latitude, longitude
$\psi, A$	Spherical coordinates in the local frame: spherical distance, azimuth
$x, y, z$	Cartesian coordinates
$u, v, h$	Cartesian coordinates in the local frame
$\mathbf{x}, \mathbf{u}$	Position vector in the global and local frame
$t$	Temporal coordinate
$\alpha, \beta, \gamma$	Euler rotation angles
$\Omega, \Omega'$	Domain of the unit sphere
$\Omega_M$	Area under the main-lobe region

### Functions

$f(\theta, \lambda), g(\theta, \lambda)$	Scalar functions defined on the sphere
$w(\theta, \lambda, \theta', \lambda'),$ $w(\theta, \lambda, \psi, A), w(\cdot, \cdot)$	Two-point scalar weight function defined on the unit sphere
$b(\theta, \lambda, \theta', \lambda'),$ $b(\theta, \lambda, \psi, A), b(\cdot, \cdot)$	Smoothing operator defined on the unit sphere, and also the normalized weight function
$\epsilon(\theta, \lambda), \epsilon(\cdot)$	Noise associated with the estimate of $f(\cdot)$
$E(\theta, \lambda), P(\theta, \lambda)$	Energy and power functions
$\delta(\theta, \lambda, \theta', \lambda'), \delta(\psi)$	Dirac's delta function defined on the sphere
$Y_{lm}(\theta, \lambda)$	Surface spherical harmonic function (complex, normalized)
$P_{lm}(\cos \theta), \bar{P}_{lm}(\cos \theta)$	Unnormalized and normalized associated Legendre function
$P_l(\cos \psi), \bar{P}_l(\cos \psi)$	Unnormalized and normalized Legendre polynomials
$d_{lmk}(\beta), D_{lmk}(\alpha, \beta, \gamma)$	Wigner- $d$ and Wigner- $D$ functions. Also known as representation coefficients of the SO(3) group.
$\Delta N(\theta, \lambda)[t]$	Temporal geoid anomalies
$\Delta \rho_A(\theta, \lambda)[t]$	Temporal surface mass changes

$C(\theta, \lambda, \theta', \lambda'), C(\psi)$  Covariance and autocovariance functions

### Coefficients

$F_{lm}$	Spherical harmonic coefficients of $f(\cdot)$
$A_{lm}, \phi_{lm}$	Amplitude and phase of $F_{lm}$
$W_{lm}^{nk}, W_{lm}, W_l$	Spherical harmonic coefficients of the different forms of the weight function $w(\cdot, \cdot)$
$B_{lm}^{nk}, B_{lm}, B_l$	Spherical harmonic coefficients of the different forms of the smoothing operator $b(\cdot, \cdot)$
$C_{lmnk}^{l'm'}$	Clebsch-Gordon coefficients
$\Phi_{lm}^{nk}$	Phase of $B_{lm}^{nk}$
$\Delta K_{lm}[t]$	Dimensionless spherical harmonic coefficients of the temporal geoid anomalies
$k_l$	Load Love numbers
$\sigma_l^2$	Degree variance
$\Lambda_l$	Eigenvalues of the gravity functionals, also known as the isotropic transfer coefficients

### Mathematical notation

$\mathbb{C}$	Set of all complex numbers
$\mathbb{N}, \mathbb{N}^*$	Set of all whole numbers and natural numbers (excludes 0)
$\mathbb{R}, \mathbb{R}_{>1}$	Set of all real numbers and real numbers greater than 1
$\mathbb{Z}$	Set of all integers

### Mathematical operators

$\mathbf{E}\{\cdot\}, \mathbf{D}\{\cdot\}$	Expectation and dispersion operators
$\arg(\cdot)$	Argument of a complex number, also called the phase of the complex number
$\text{sgn}(\cdot)$	Sign operator

## LIST OF ABBREVIATIONS

---

CHAMP	CHAllenging Minisatellite Payload
GRACE	Gravity Recovery and Climate Experiment
GOCE	Gravity field and steady state Ocean Circulation Explorer
GGOS	Global Geodetic Observing System
GPS	Global Positioning System
SLR	Satellite Laser Ranging
MTF	Modulation Transfer Function
SNR	Signal to noise ratio



## ACKNOWLEDGEMENTS

---

**P**HEW! Done it! It is a great feeling to see the labour of love come to fruition. A number of people have been instrumental in making sure that I get to this point. It is my pleasure to pen down their names here for posterity.

This thesis would not have been possible without the guidance and advice of my *Doktorvater* Prof. Sneeuw. I feel privileged to have worked with you, because of the wonderful teacher and scientist that you are. I have learned much more on the white board in your office than through conventional media. It was always a joy to have a discussion with you, be it science, politics, food, or economics. Your attitude towards life and your treatment of your co-workers and students has been inspiring. Without your patience and care, I dare say I would not have reached this stage. Before I meander into an emotional trail, I just want to say thanks for always being there!

Next I would like to thank my co-referee Prof. Michel for accepting to be in the committee, and reviewing my thesis. At this point I also thank Johannes Engels and Prof. Keller for kick-starting my research with their signal processing course. Thanks, especially to Prof. Keller, for being the “mathematical oracle” of my research. Thanks for accepting me as a teaching assistant for your advanced mathematics lectures, which helped me immensely in my research.

The final parts of the thesis were written after I switched to my new job at the Institute of Geodesy at the Leibniz University of Hannover. My heart-felt thanks go to institute’s director Prof. Müller as he graciously allowed me to complete my thesis, and also supported me in presenting my doctoral work at various conferences.

I am deeply indebted to Matthias Weigelt for being the *Doktorbruder*, if I am allowed to invent such a title. Thanks a lot Matt for lending an ear to all my queries/problems both scientific and otherwise; for keeping me grounded; for being my German cultural guide; and for being both a staunch supporter and also a critique. I cannot imagine how I would have managed my stay in Germany without you and your family’s generous help. Your amazing sense of humour has been a reason in retaining sanity in a serious research environment.

Due thanks also go to the other *Doktorbruder* Wouter van der Wal. Initial work for this thesis began with the computer programs you gave me for computing the Gaussian and the destriping filters. Every time I discussed my research accomplishments with you, you came up with thought-provoking but dispiriting questions. Although, it was quite frustrating in the heat of the moment, I am grateful to you for asking them without restraint.

Much of the research in this thesis was carried out as part of the German Research Foundation (DFG) funded project “Direct Water Balance” within the *Mass transport and Mass redistribution in the system Earth* research program. It was enriching to be part of this research program as I had the opportunity to interact with a lot of researchers across Germany. Mohammad J. Tourian and Christof Lorenz were my partners-in-crime in this project. Thanks guys for sharing a great camaraderie, which made the collaboration all the more enjoyable. The speed with which you guys worked was awe-inspiring, and I barely managed to keep pace with you. There was always a healthy competition, which ended up

in a stimulating research atmosphere. Thanks Christof, for flawlessly translating the abstract into German. Thanks go to Dr. Riegger and Prof. Kunstmann, who were the co-investigators of the project. Your friendliness and penchant for learning was infectious. Through the DFG project I had the opportunity to collaborate with Prof. Schuh and Lutz Roesse-Koerner. Thanks a lot for hosting me in Bonn, and also for introducing me to convex optimization.

Thanks go to Qiang for validating my filtered GRACE solutions with GPS data and for the myriad number of questions about GRACE data, which allowed me to dig deep into the details. Also, thank you Qiang for indulging me in badminton, which had the positive effect of keeping me hale and healthy. Thanks to Markus for providing mathematical help, especially with the rotation of spherical harmonics; Matthias Roth for introducing me to software version control; Siavash for his help with empirical orthogonal functions and also introducing me to Persian food and culture; Bramha Dutt for enlightening me on the leakage effects of filters. Thanks to my other office mates Tilo, Shirzad and Wei for a fun-filled work environment. Thanks are also due to Oliver for being my squash partner and also sharing his expertise in regularization methods. Thanks to Ron for providing prompt IT support. Many thanks to Anita for being a kind secretary and for the daily customary discussion on weather. Thanks also to the German Academic Exchange Scholars Rohini, Rajkishan, Gayathri, Bramha Dutt, Sharanya and Sujata, for some of whom I had the privilege of being their mentor. They brought interesting ideas and questions that helped me dust off the rust on my basics.

A big thanks to all the Hannover colleagues, especially Sujata, Akbar, Tamara, Majid, Karim, Guy, Philip, Santosh for their moral support and for sending their good vibes my way during my defence.

Special thanks go to my friends in Germany who have become my extended family over time: Karthik, Gayathri and Vibhu; Bramha Dutt and Medhavi; Alka, Amit and Bhuvvi. Thanks a lot for the unconditional affection and care you have given me over the years. You guys helped me keep home-sickness at bay. I also thank Mr. Krishnapillai and family for the help accorded during my initial days in Stuttgart. Thanks also go to my landlord Mrs. and Mr. Bruder for being a nice neighbour and reinforcing my faith in humanity. It would be unfair if I don't acknowledge my friends from Chennai and Calgary for sharing my aspirations and giving their moral support in my pursuits.

I gratefully acknowledge the initial financial help of my uncles Thirunavukkarasu, Nithyanandam, Muruganandam and aunt Valli, without which it would not have been possible for me to set my feet outside India.

It is not customary to thank your family in the Indian tradition as it will never be enough for the role they play in your life. Nevertheless, thanks to my brother Karthikeyan, who has been my role-model in most of the things that I did since my childhood. His love for science, travel and his work ethic has affected me in positive ways. Without him, I would not have travelled and visited as much of Europe as I have done so far. As long as I remember I have only nagged and annoyed him as is the wont of a little brother. Thanks to my sister-in-law Saranya for avenging it for my brother by constantly nagging me about the status of my thesis. Thanks to my nephew Raghavendra, for being my stress reliever with his effervescent smile.

My vocabulary is insufficient to express the gratitude I feel for my parents. They have constantly backed my decisions and choices, and had unwavering faith in me. It is needless to say that they were my driving force. Thanks for believing in me and for your unconditional love. Towards the end of my doctoral studies I got bitten by the love bug. It was a battle to dedicate time and energy, simultaneously, both for my thesis and my relationship. Thank you Jayani for helping me win the battle unscathed.

To the best of my knowledge I have acknowledged all those who have contributed in the completion of this thesis. If that is not the case then I apologize upfront for the lapse.





“... the scientist. He pores over books night and day, straining his eyes and becoming nearsighted, and if you wonder what on earth he has been working on all that time—it is to become the inventor of eyeglasses to correct nearsightedness.”

– Masanobu Fukuoka  
(*The one-straw revolution*)